Vibration characterisation of aluminium pedestrian bridges

by

Ann Christine Sychterz

A thesis
presented to the University of Waterloo
in fulfillment of the
thesis requirement for the degree of
Master of Applied Science
in
Civil Engineering

Waterloo, Ontario, Canada, 2014

I hereby declare that I am the sole author of this thesis. This is a true copy of the thesis, including any required final revisions, as accepted by my examiners.

I understand that my thesis may be made electronically available to the public.

Abstract

Despite several full-scale applications in Canada, the vibrational characteristics and performance of aluminium pedestrian bridges have not been studied comprehensively in the literature. There is a large degree of variability between design codes and standards, particularly in North America and Europe. This is in part due to a lack of comprehensive experimental test data on full-scale pedestrian bridges. This is compounded by a lack of agreement between researchers on the characterization of pedestrian induced loads and the interaction between loads and the structure. This thesis aims to bridge this gap by building and testing full-scale aluminum pedestrian bridges in a controlled laboratory test program. Results from the experimental program are presented, discussed in detail, and used to estimate the vibration characteristics of an aluminium pedestrian bridge of various lengths. These characteristics include the modal properties —natural frequency, damping ratio, and mode shapes —and human-structure interactions measured using accelerometers, load cells, and strain gauges. Using multiple signal processing techniques, these characteristics were extracted from the data. The results from the pedestrian loading tests were then used to assess the bridge specimens through the above-mentioned design codes. Finite element models of each specimen were built and used for parameter studies and model verification.

These data from full-scale pedestrian bridges are likely to shed new light on their vibrational behaviour and performance, and allow aluminium bridge designers to create competitive alternatives to bridges constructed with conventional materials. It is also anticipated that these tests will form a foundation for future research in the area of pedestrian bridge load modelling.

Acknowledgements

A sincerest thank you to my co-advisors, Dr. Scott Walbridge and Dr. Sriram Narasimhan for their years of guidance and intuition moving through this novel research project. I would like to thank my thesis review committee: Dr. Jeff West and Dr. Don Burn.

This project would not have been possible without the contribution of MAADI Group (Most Advanced Aluminium Design and Inspection Group) including the full-scale Make-A-Bridge aluminium pedestrian bridge lab specimen. A big thank you to the Aluminium Association of Canada for their support on the precursor work leading to this experimental work in the lab. I would like to recognize the Natural Sciences and Engineering Research Council of Canada for making this project possible.

To the Structural Engineering laboratory technicians: Richard Morrison, Rob Sluban, and Michael Burgetz. Your help with building the bridges, designing instrumentation installations, and letting me use power tools has been invaluable.

I would like to acknowledge the members of the Structural Dynamics, Control, and Identification research group; Budhaditya Hazra and Ayan Sadhu, for being an unlimited resource for teaching signal processing concepts and methods. Special thanks goes to my colleague, Pampa Dey, for sharing and continuing this journey through this monumental undertaking of the experimental and theoretical work on this project. To the undergraduate research assistants —Stanley Fong, Melissa Jennings, and Laura Luna —your ever-enthusiastic curiosity was contagious. A warm thanks to all of the pedestrians whom were participants in the walking tests on the lab bridge specimens, especially to Benjamin Scott and Kevin Goorts for your unwavering dependability.

Thank you to all the swing dancers I've met over the years for fuelling my other life passion and being a source of inspiration for my work.

Dedication

To my mum, dad, and aggregate of friends; for the structural integrity of your support and concrete love. I'm glad you've steel got my back and through strain-hardening, permitted me to extrude to farther than my factored ultimate stress.

Table of Contents

List of Tables

List of Figures

Chapter 1

Introduction

1.1 Dynamic behaviour of pedestrian bridges

The dynamic behaviour of pedestrian bridges becomes increasingly important as the span and slenderness increase. This is true not only for vertical vibration modes, but also for lateral sway and torsion modes. Unlike vehicles, pedestrians introduce strong lateral vibration due to the biomechanical alignment of each foot relative to the person's centre of gravity. The vibration of pedestrian bridges is seeing increased interest in recent years due to the increased awareness of issues in the building code-based design of these structures. Concerns with regards to the dynamic design arise when the serviceability of structure is compromised by high amplitude movement of the bridge. This high amplitude movement can occur when the walking speeds of pedestrians match the structure's fundamental frequency, resulting in resonance. Just as wind was responsible for the historic twisting destruction of the Tacoma Narrows Bridge in Washington State, so too has pedestrian traffic caused alarming but not destructive movement of well-known pedestrian bridges such as

the Millennium Bridge in London, England.

In order to appreciate the dynamic interactions that occur in a complex structure, extensive computer simulations using structural engineering software or simplified experimental testing are required. Experimentation has historically been more feasible, which explains why design codes typically use empirical formulae for structural vibration checks. The current simplistic design provisions in several North American and European bridge design codes inhibit proper analysis. With the availability of more computing power, advanced analysis, monitoring and control become the preferred alternatives for addressing vibration issues in structures. Monitoring includes data collection for the characterisation of the bridge's vibrational characteristics and the bridge's behaviour subjected to common pedestrian loading. The advanced analysis encompasses structural dynamics theory with statistical signal processing to extract results from the data. Lastly, these results can be fed back into the system to control the structure by the addition of masses and dampers to alter the structure's properties.

1.2 Aluminium as a building material

The use of aluminium for pedestrian bridge construction can be advantageous due to its relatively high durability and strength-to-weight ratio in comparison with competing construction materials. Transportation and erection of aluminium structural components allow for rapid on-site installation of bridges. Shop welds are more reliable than field welds due to controlled conditions, thus more complex bridge shapes can be pre-assembled and shipped to the site. The reduced weight of the structure allows for non-invasive installation methods that are well-suited to remote or environmentally sensitive regions where access roads or staging areas are not feasible (30).

Aluminium is a relatively new and less understood construction material in comparison to typical concrete and steel structures. The primary advantage of using aluminium over structural steel and concrete, for example, is that it is relatively maintenance-free due to its high corrosion resistance, aesthetically pleasing, and can be transported and installed quickly due to its low self-weight (Figure 1.1).

Figure 1.1: Installation of light-weight aluminium bridge (86)

Other advantages include its high formability, making it easy to extrude complex shapes, and the ease with which it can be recycled at the end of its life. Steel structures can require galvanizing or painting to maintain the structural integrity of the components. Provided that the components are well separated from reactive metals, aluminium construction offers a lower operating and maintenance cost. The use of aluminium in civil structures has been most successful in applications where all or several of these positive attributes (corrosion resistance, lightweight, and extrudability) are exploited (62)(81)(54)(90).

Experiments on vibration properties of full scale bridges and pedestrian walking tests in laboratory conditions have been previously conducted by other research groups. Areas

of knowledge that are have not been documented are fully-instrumented - frequency, load and strain - bridges for structural vibration properties and human-structure interactions. Another gap area is the ability to study the effect of bridge length on the vibration properties. Few experiments from other research groups have been able to replicate the behaviour of a full-scale bridge in a laboratory setting.

1.3 Objectives & scope

The main objectives of the current thesis are:

- to build full-scale instrumented laboratory aluminum bridge specimens that will allow for comprehensive testing under different loading situations, leading to a better understanding of the behaviour and characterisation of full-scale aluminium bridges subjected to pedestrian excitations,
- to complete a modal analysis using statistical signal processes and pedestrian load tests of various crowd sizes and walking speeds on aluminium pony truss pedestrian bridges, with validation from a finite element model, and
- to analyze the aforementioned bridges according to current design codes and standards and comment on their ability to predict the serviceability of aluminium pedestrian bridges.

In addition to the experimental work using the laboratory specimens, there was also on-site testing which was previously documented and not included in this thesis. A 44 m long, welded aluminium pedestrian bridge crossing the Daigneault Creek in Brossard, Québec was subjected to dynamic loading for structure characterisation, (i.e., "heel drop"

tests) and walking tests for further work on human-structure interaction. Though extensive testing was completed for a single pedestrian and pairs of pedestrians, the scope did not include a variety of test subjects nor was a large crowd test possible.

The laboratory bridge specimens were built of a bolted connection aluminium bridge of variable length. Lengths from 10 feet to 75 feet in 5 foot increments were made possible, but only spans of 10 feet, 40 feet, and 70 feet were tested for this thesis. With the laboratory specimens, a broader range of pedestrian characteristics and crowd loading scenarios were tested.

The analysis completed for this study included: finite element models of all possible bridge lengths, statistical signal processing of collected data, and an example tuned mass damper design. There were two benefits to building the finite element models: prediction and validation. Building the computer simulations prior to the construction of the bridges helped guide the experimental setup and understand what results could be expected. Secondly, the finite element models could be re-investigated upon completion of the laboratory work to confirm the analysis of the measured data. If the models prove to be accurate, this method could then be used for future similar structures without having to build the full-scale specimen. The resulting data would then be used to suggest a preliminary damper design using first principles and design guidelines.

The major contribution this thesis has to offer is a data set of acceleration, load, and strain data for various numbers of pedestrians, walking at various paces, with a statistically significant number of trials on three lengths of full-scale bridges. This includes a comprehensive summary of each data type including statistical parameters.

1.4 Organisation

This thesis presents the background information on previous work on pedestrian bridges, pedestrian load models, dynamic design code calculations, signal-processing methods, and damper design basics. The experimental setup of the laboratory work is then presented with details on instrumentation and testing procedures. Next, the results from these tests are presented, divided by data type —acceleration, load, strain, or displacement —and subdivided by bridge span. The analysis section includes the finite element model discussion, signal-processing results, design code review, and damper design.

Chapter 2

Background

2.1 Research on pedestrian bridge vibration

2.1.1 Full-scale structure studies

The most notable instance of dynamic-governed design of a modern pedestrian bridge was the Millennium Bridge, also known as the "wobbly bridge" in London, UK. Since the post-construction study, several other bridges were subjected to field tests for modal characterisation, most notably the M-Bridge, the T-Bridge (59), the Solférino bridge (48), and the Ponte del Mare (22).

The Millennium Bridge has a total span of 332 m, with the largest individual span being in the centre at 144 m (Figure 2.1). Sets of four in-plane cables on each side created the tension ribbon structure to support the 4 m bridge deck every 8 m. This bridge attracted public interest due to its large lateral displacements during inauguration in 2000, assumed to be due to the pedestrian lock-in phenomenon (29). The lock-in effect is the

synchronisation and amplification of the structural vibration due to pedestrians modifying their gait to maintain balance. Despite the structure's adherence to Eurocode 5 for footbridges, AASHTO 1997, the British Building and Construction Standards, and the Ontario Building Code, video footage shows that the bridge had a maximum lateral displacement of 50 mm due to this pedestrian activity. Problematic frequencies for this bridge occurred at 0.48 Hz, 0.78 Hz, 0.95 Hz, and 1.05 Hz. To address the vibration concerns, 37 viscous dampers and 29 pairs of vertical tuned mass dampers (TMD) were installed along the bridge, with the ability to be individually disconnected (63). Modal characterisation tests used a vertical shaker, a horizontal shaker, and slotted bolted connections as friction surface dampers (21)(47). Shortly after the Millennium Bridge studies, an investigation on the Clifton Suspension Bridge in England was performed (51). In tests on this bridge, 27 modes under 3 Hz were identified, with most of those modes being either vertical or torsional. The main objectives in these studies were to understand the reasons for the large amplitude motions resulting from crowd loads.

Figure 2.1: Millennium Bridge, London, UK (28)

In order to mitigate the excessive motions, dampers were installed. Plans show the layout of the dampers installed on the bridge during the improvement (Figure 2.2). Each damper could be independently disconnected from the system so that modal analysis could be conducted with or without damping (63).

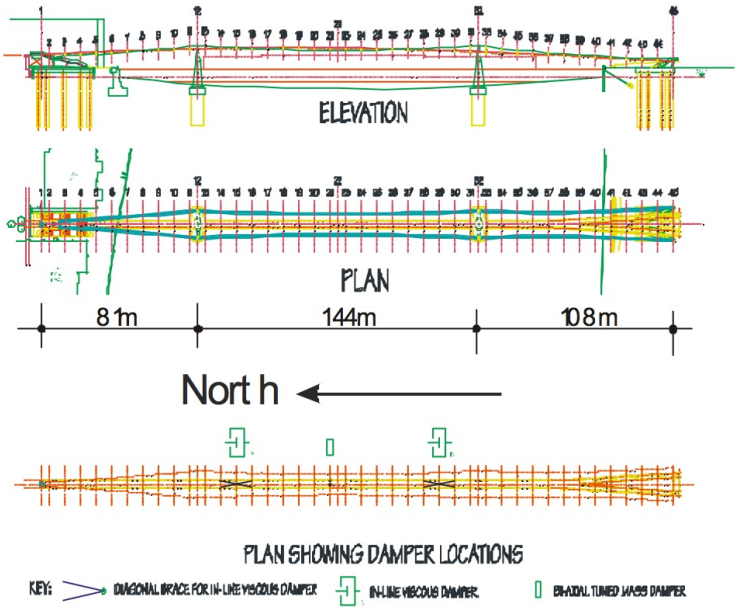

Figure 2.2: Damper layout of the Millennium Bridge (63)

The Millennium Bridge spurred extensive research on the subject of pedestrian induced vibrations during the last decade; despite this, issues surrounding the response of pedestrian induced vibrations in bridges are still not well understood.

The M-Bridge, Maple Valley Great Suspension Bridge in Honshu, Japan, is a suspension bridge consisting of a reinforced concrete tower supporting a deck of two flexible steel H-girders, sway bracing, and steel grating (60). With a main span of 320 m and two back spans of 60 m, the 26.2 m high tower supports a 1.5 m wide deck with a seven-stranded

spiral cable (Figure 2.3). The frequencies excited by pedestrian use were found to be the third mode of 0.88 Hz and the fourth mode of 1.02 Hz. For quick validation of the data, the modal frequencies and damping responses were calculated numerically on site (60). During testing, it was noted that pedestrians could feel the displacement of 10 mm and some were uncomfortable, whereas displacements of 45 mm caused many pedestrians to lose stability, similar to what was seen on the Millennium Bridge. The T-Bridge, also located in Toda City, Japan, is a similar cable-stay bridge, with a main span of 134 m and a tower height of 61.4 m. A box girder deck of width 6.05 m and 1.8 m was laterally excited by pedestrian activity at 0.9 Hz (Figure 2.3).

Figure 2.3: M-Bridge (left) and T-bridge (right), Japan (60)

Documentation from the study at the M-Bridge fully details the arrangement of the modal analysis experiment. Accelerometers were installed in the lateral direction at $L/8$ $L/4$ $3L/8$, $L/2$, and $9L/16$, where L is the bridge span. The accelerometers were connected through amplifiers to an A/D simultaneous transformer, connected to a personal computer (60). In addition to the station bridge setup, the pedestrian was fitted with accelerometers at the waist, powered by a battery in an accompanying backpack. Knowing the bridge's reaction and the imposed pedestrian frequencies allowed the researchers to better under-

stand which frequencies were natural bridge modes and which were forced vibrations. The T-Bridge tests focused on crowd loading of the structure. These tests used photographs from above the crowd to count the number of pedestrians in a given density on the bridge, as well as monitor the walking pace of the pedestrians based on their head movement (60).

A 3-span pedestrian bridge at Texas Technical University connecting the campus to the football stadium experienced large amplitude vibrations from a crowd leaving a game (106). With spans ranging from 34 m to 40 m, the centre span deck is supported by 3 prestressed concrete girders, and the back spans are supported by 2 of the same type of girders (Figure 2.4).

Figure 2.4: Pedestrian bridge at Texas Tech University, USA (106)

This pedestrian bridge was designed prior to the issuance of the AASHTO LRFD bridge code for pedestrian bridges. Despite not being code-prescribed, layered neoprene rubber and steel bearings were installed on all piers (106). The primary lateral frequency that interacted with the crowd excitation was 0.799 Hz at one of the piers, where all three spans exhibited energy at 0.917 Hz. In order to test the pedestrian bridge at Texas Tech University, triaxial accelerometers were installed on the piers and the mid span on

both sides of the bridge. Sampling at 30 Hz, which is greater than 2-3 times the target frequencies, it was found that torsional modes were the most prevalent due to crowd loading (106).

The Ponte del Mare is a suspension bridge over the Pescara River in Italy with two decks; an inner cyclist track of 148 m length and 80 m radius and an outer pedestrian track of 173 m length and 100 m radius (22) (Figure 2.5).

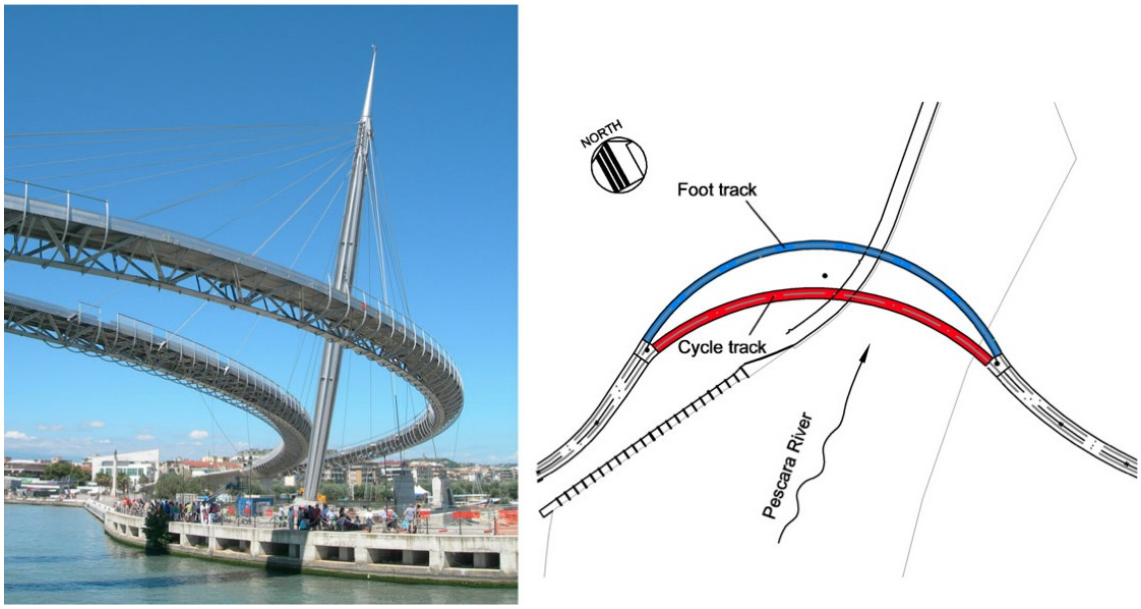

Figure 2.5: Ponte del Mare, Pescara, Italy (22)

Such structures exhibit natural frequencies within close proximity due to flexural-torsional mode coupling, therefore modal identification is particularly challenging. Coupling, the simultaneous presence of two frequencies within close proximity of each other in the frequency domain, was predicted to occur within the structure of each deck and between the two decks. Three types of 'output-only' identification methods were studied; Singular Value Decomposition, Stochastic Subspace Identification (SSI), and Canonical

Variate Analysis. However, the identification results suffered due to the nonstationarity of the data. An Ambient Vibration Survey (AVS) was used to filter ambient noise. This process reduces data resolution that cannot be used for modal identification (63). The lowest natural frequencies were found to be 0.75 Hz, 1.07 Hz, and 1.13 Hz without dampers and 0.92 Hz, 1.08 Hz, and 1.34 Hz with dampers (22). As with the Millennium Bridge, the Ponte del Mare also had dampers that could be individually disconnected in order to conduct modal analysis tests with and without damping. The same set of tests were repeated for both damping scenarios. A finite element model was utilised to select the most effective locations for the piezoelectric accelerometers (Figure 2.6).

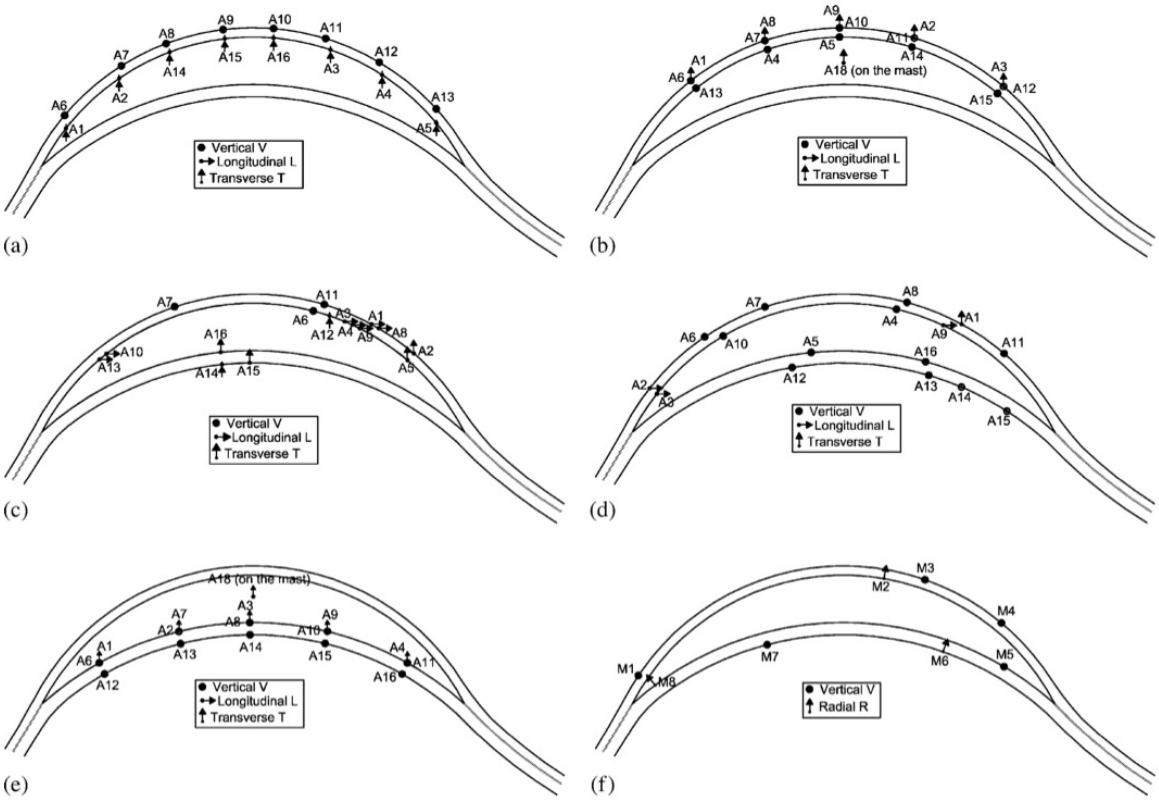

Figure 2.6: Accelerometer layout on the Ponte del Mare (22)

Firstly, ambient tests were conducted at a sampling frequency of 100 Hz for 5 minutes for stabilisation. Free vibration tests involved the sudden release of a large mass tied to the underside of the bridge deck to intensely excite the bridge. These tests were measured with a sampling frequency of 1000 Hz since the test is shorter than that of the ambient tests. A higher sampling frequency was required for an acceptable frequency resolution.

Results from this work showed that with low vibration levels as with those from pedestrian or cyclist loading would not be enough to activate the dampers due to friction and slack in connections. Impact tests for free vibration did activate the dampers and they worked well. Low oscillation amplitudes caused the dampers to create a stiffening effect. The finite element model designed for this work was not reassessed and updated given the collected data.

These studies all focus around an in-place structure, where it is not feasible to complete a rigorous set of repetitive studies due to time and inconvenience to its users. The next step would be to investigate a full-scale structure in a controlled environment, which is what is proposed for this thesis.

2.1.2 Laboratory research

Laboratory experiments provide the controlled environment that allows for repeatable results, especially when there are increased uncertainties in each trial from working with pedestrians.

Rainer (71) conducted tests on a laboratory specimen of a steel undertruss and a concrete deck, simply supported with a temporary support at the midspan. The structure was approximately 17 m long and 2.1 m wide with a force transducer mounted at the temporary centre support. Tests were conducted to determine that the lowest natural

frequency was approximately 12 Hz. The specimen was therefore considered a stiff structure since this is well above the threshold of concern for pedestrian walking frequencies and the first few harmonics. Since the structure was significantly stiffer than the target walking frequencies, it could essentially be regarded as a large load plate. Rainer recorded a single pedestrian walking at frequencies from 1.0 Hz to 3.0 Hz, jumping from 1.0 Hz to 4.0 Hz, and running from 1.6 Hz to 4.0 Hz (71)(70).

Laboratory tests can also be completed in conjunction with a full-scale field study for further understanding. Paired with the investigation of the T-Bridge in Japan, an instrumented laterally moving platform demonstrated that pedestrians synchronise their head movement to the bridge movement. Approximately 20% of the pedestrians started to widen their gate at vibration amplitudes of 10 mm in order to maintain balance (101).

After the vibration issues encountered during the Millennium Bridge inauguration, vertical and lateral vibration tests were conducted by the engineering design firm, Arup (29). A shaketable at the University of Southampton was used for the vertical load testing with a pedestrian walking on the spot (29). At the Imperial College, lateral load tests on a 7.3 m platform were conducted for analyzing the sway observed on the Millennium Bridge (42). The ratio of the maximum periodic walking force to the pedestrian's weight is called the dynamic load factor (DLF). It was determined that the DLF increases with the amplitude of the vibration, but the vibration amplitude was independent of the walking frequency (42)(29). The probability of "lock-in" was also quantified at 30-40% at an amplitude of 5 mm to 80% at an amplitude of 30 mm (42).

Much of the research focus in recent years has been to measure the ground reaction forces (GRFs) using instrumented platforms. A set of 4 m long suspended platforms were built with lateral frequencies of 0.75 Hz, 0.84 Hz, 0.95 Hz, and 1.14 Hz in one study (78). Three walking speeds were performed by each of the four subjects. The speed closest to

the natural frequency of the bridge caused the highest lateral loads due to resonance in the structure. These findings were used to develop a model capable of predicting the equivalent DLF in the non-resonance condition. Other lab setups by other research groups included a treadmill atop a force plate atop a shaketable where the treadmill and lateral shaking were controlled (85).

A second team from the University of Reggio Calabria also completed tests for a range of vibration amplitudes and lateral frequencies from 0.60 Hz - 0.92 Hz (65). This study noted that pedestrians contributed to a negative mass on the system, and that only at one of the vibration frequencies and amplitudes did pedestrians produce a negative damping effect. Similar studies have been repeated with more subjects to verify the statistical significance of these results (42).

These laboratory experiments provided a richer understanding of the vibration behaviour due to pedestrians in a small-scale manner. The common elements were that either the pedestrian was moving over a small platform, or the platform moved under the pedestrian (i.e., a treadmill). Both of these options, however, do not give the full sense of how a pedestrian would walk on a flexible structure.

2.1.3 Analytical research

This section discusses the finite-element modelling for pedestrian bridges (restricted to the Millennium Bridge and the Ponte del Mare), the basic pedestrian load models, serviceability criteria and common means to mitigate vibrations in pedestrian bridges.

Due to the lack of detail in literature of the natural frequencies of the Millennium Bridge, a finite element model was built by Law, Wu, and Chan to investigate the effect of the slotted bolted connection elements (SBCE) under cyclical loading. The slotted bolted

connection allows for movement in the joint and the contact surfaces serve as a frictional damper. Matching the published measured full-scale results very closely, it was observed that the first vertical modes were significantly less than pedestrian walking frequency of approximately 2 Hz. The lateral modes, however, at less than 1 Hz were observed from the model and thought to be the cause of the excessive vibrations in the structure (47). SBCE connections were modelled to have a frictional behaviour, and thus provide an additional avenue for damping. These points were useful for this thesis to understand connections with allowance for movement.

The Ponte del Mare was modelled using ANSYS^{TM} in order to better design the full-scale tests (22). The natural frequencies, mode shapes, and modal damping values were extracted from the model for damper design. To compare the model results to the experimental data, Modal Assurance Criterion (MAC) values were calculated, which are a ratio of measured to calculated mode shape, where the desirable value is 1.0. Results from this study were a mean of 0.86 for the first 12 modes. Future work from this thesis will include MAC values using the measured data.

Given the modal analysis conducted on full-scale pedestrian bridges and finite element models, it was found that the shape of the deck, that is the ratio of length to width, greatly impacted the dynamic performance of the structure. The optimal shape of the deck to reduce the effects of vibration response is proportional to the first lateral mode shape (14). This is also optimal since the first mode is the most influential in the response and thus higher modes have less contribution to the mode shape. It was also determined that the excited modes of vibration are heavily dependent on the crowd size or walking pace of the pedestrian loading on the bridge.

2.2 Dynamic load factors of pedestrian loading

As the interest in vibrations due to walking loads increased, parameters such as the cadence, gait characteristics, and type of movement along the bridge had to be defined (69). The cadence, or gait cycle, is the complete cycle of stepping on the left foot and the right foot. Each leg in this gait cycle has a swing and a stance phase where it is either in motion or in contact with the ground, respectively. The walking step load pattern has two maxima, one at the heel acceptance and one at the toe push-off, and a minima at mid stance (Figure 2.7).

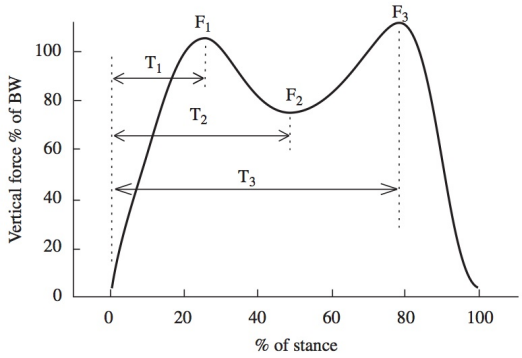

Figure 2.7: Vertical gait load (69)

The intensity of points F_1 and F_3 in Figure 2.7 are expected to increase and the time interval between these peaks to decrease as walking pace increases. Rainer's study (70) collected load data for walking, running, and jumping tests. Harmonics of a frequency are higher frequencies of the original, scaled by an integer. The DLF is then the ratio between this amplified load and the weight of the pedestrian. The DLF of the first four harmonics showed that the first harmonic had the highest energy and was most affected by the gait cycle (Figure 2.8).

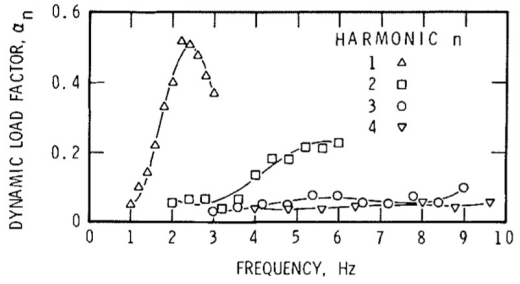

(a) DLF for walking

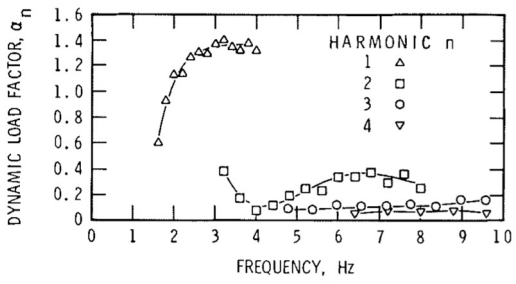

(b) DLF for running

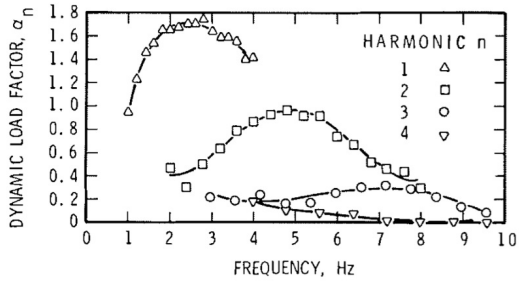

(c) DLF for jumping

Figure 2.8: Dynamic load factors (71)

Gait cycle tests have been performed on several types of surfaces, including transducer-equipped treadmills (77), and very stiff bridge structures (70). Blanchard (12) determined the vertical DLF to be 0.257 given that the natural frequency of the structure is less than 4 Hz, with a reduction factor if the natural frequency is greater than 4 Hz (12). Bachmann and Ammann determined that the vertical DLF is between 0.4 and 0.5 (6) and Young developed the DLFs as a function of the structure harmonic (103). The technical guide for the assessment of vibrational behaviour of footbridges under pedestrian loading by the Service d'Études Techniques des Routes et Autoroutes (SÉTRA) prescribes a design DLF of 0.4 for the first harmonic, and 0.1 for the second and third harmonic (61). Table 2.1 summarises the key dynamic load factors from literature where f is the first natural

frequency of the structure. This will be the basis of comparisons presented later in the current thesis.

Table 2.1: Key dynamic load factors (DLFs) from literature

Author(s)	Dynamic load factor	Activity and direction
Blanchard et al.	$\mathrm{DLF}_1 = 0.257$	walking, vertical
Bachmann and Ammann	$\mathrm{DLF}_1 = 0.4 - 0.5$	walking, vertical
Rainer et al.	DLF_1, DLF_2, DLF_3,DLF_4	dependent on walking, running, jumping, vertical
Young	$\mathrm{DLF}_1 = 0.37(f - 0.95) \leq 0.5$ $\mathrm{DLF}_2 = 0.054 + 0.0044f$ $\mathrm{DLF}_3 = 0.026 + 0.0050f$ $\mathrm{DLF}_4 = 0.010 + 0.0051f$	walking, vertical
SÉTRA	DLF_1=0.4 DLF_2=DLF_3=0.1	walking, vertical

2.3 Pedestrian load models

Pedestrian load models help predict the imposed load for the purpose of predicting the structure response. These models can also be used to solve for the dynamic load factor from the walking pedestrians. The main distinction between the models are whether they are derived analytically or experimentally. Either method of developing load models can be applied in either the time or frequency domain.

Experimental models are more commonly presented in the time-domain and can be either deterministic or probabilistic (53). Models to simulate pedestrian loading of the T-Bridge and the M-Bridge included factors for the large crowd synchronizing with itself and for the crowd synchronizing with the structure (60). The SAMEO model (48) uses the concept of biological oscillators to the application of walking pedestrians. Discrete modelling of the crowd permits flow simulations and boundary conditions of people (19).

The two major analytical load models that are of interest are those that simulate individual pedestrian movement along the bridge; the moving load model and the biomechanical model. The simplest form of a single pedestrian loading is a sinusoid travelling in time along the length of the bridge. This simulates the aggregated loading pattern of a pedestrian walking and does not account for the individual footfalls (Figure 2.9).

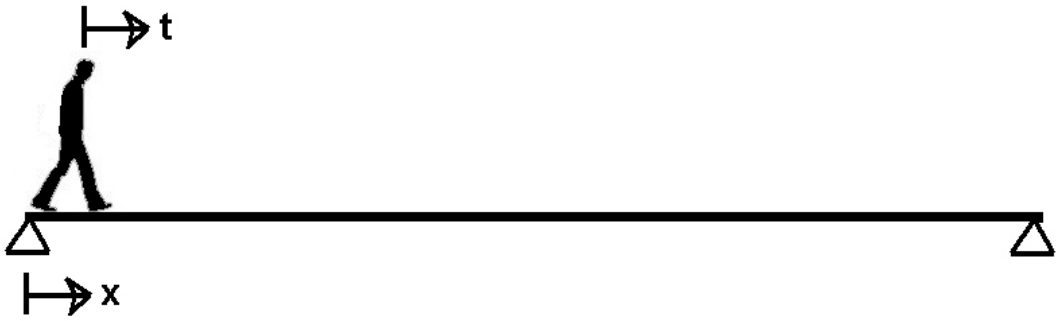

Figure 2.9: Moving load model

The biomecanical model, however, uses the mechanics of walking to determine the response of the flexible structure. The legs of the pedestrian are modelled as a hinged pair of springs and dampers with their own properties separate from the structure (Figure 2.10)(68).

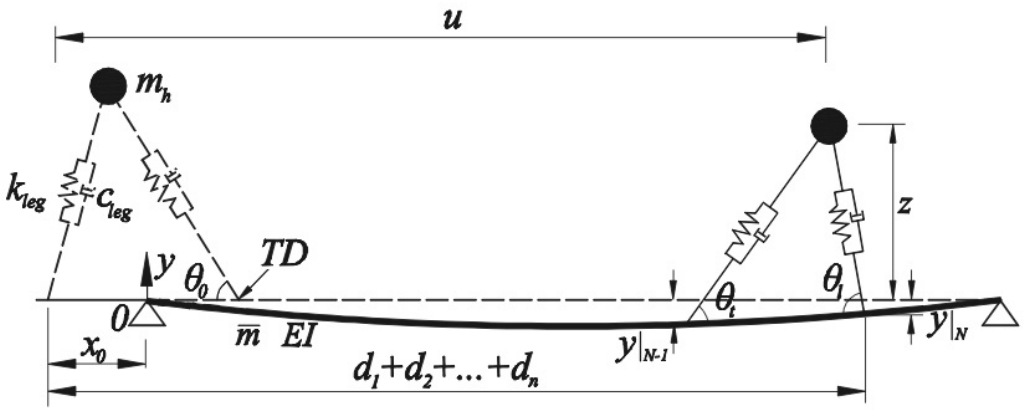

Figure 2.10: Biomechanical model (68)

2.4 Pedestrian bridge codes

2.4.1 CSA S6-06

The Canadian Standards Association, CSA S6-06 Canadian Highway Bridge Design Code (27) contains a section on pedestrian loading and serviceability deflection limits. These limits are valid for structures with natural frequencies below 4 Hz, which is the assumed upper limit of a pedestrian jogging. The assumed forward velocity of the pedestrian is the lesser of 2.5 m/s or $0.9f_1$ m/s. For first flexural frequencies between 4 Hz and 5 Hz, the maximum acceleration can be reduced linearly from 0% at 4 Hz to 70% at 5 Hz or more. Figure 2.11 shows the acceleration limit for dynamic design and compares it with several limits suggested in literature.

A standard 700 N load at the midspan is used to calculate the maximum deflection generated by a pedestrian. This deflection is then used in the calculation of the acceleration

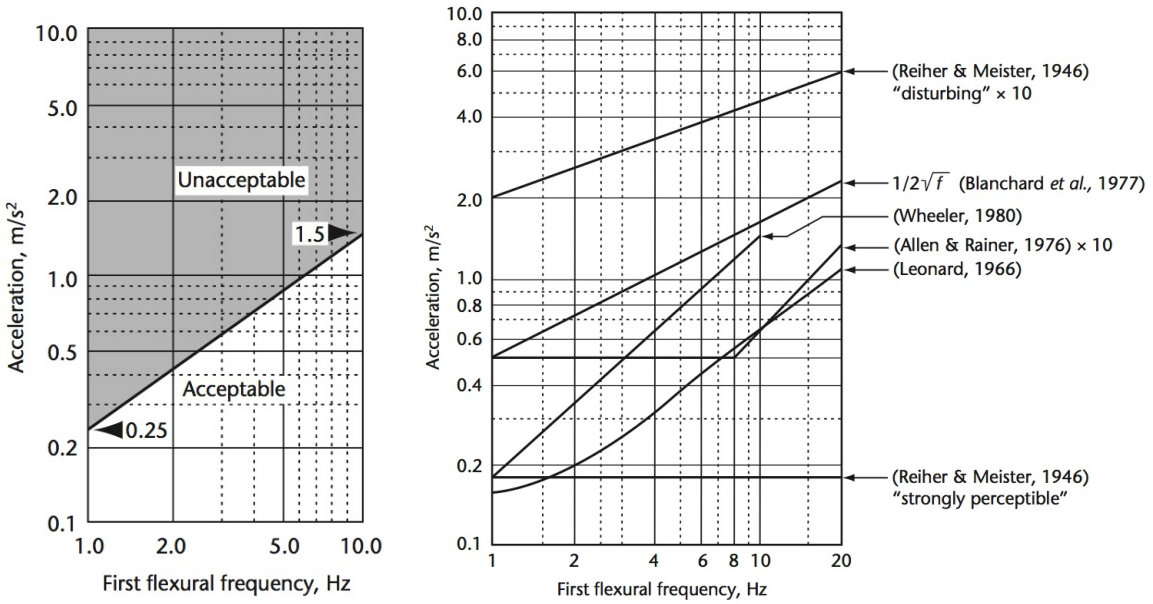

Figure 2.11: CSA S6-06 Figure C3.3 (left): acceleration limit for pedestrian bridge serviceability and Figure C3.4 (right): limits suggested by literature (27)

using the following expression:

$$a = 4\pi^2 f_1^2 w_S K \Psi \tag{2.1}$$

where a = acceleration in m/s^2

f_1 = first flexural frequency in Hz

w_S = maximum static superstructure deflection due to a vertical concentrated force of 700 N in m

K = configuration factor (1 for single span structures)

Ψ = dynamic response factor, a function of damping

Coupling of modes occurs when at least two of the directions of vibration —vertical, lateral, or longitudinal —occur simultaneously due to the relative closeness of those natural

frequencies of the structure. Commentary to the CSA S6-06 advises to avoid mode coupling of the vertical and lateral or longitudinal modes by ensuring that the latter two mode types are not less than 1.5 times the first flexural frequency nor less than 4 Hz. The presence of lateral or longitudinal modes are strongly dependent on the manner of connection of the substructure.

2.4.2 HIVOSS

HIVOSS: Human Induced Vibration of Steel Structures (39) is a set of guidelines specifically for the design of pedestrian bridges and floors. In the outlined design steps, the critical range of natural frequencies for the first vertical and longitudinal modes are:

$$1.25 \text{ Hz} \leq f \leq 2.3 \text{ Hz} \tag{2.2}$$

for the second vertical and longitudinal modes are:

$$1.25 \text{ Hz} \leq f \leq 4.6 \text{ Hz} \tag{2.3}$$

and for the first lateral mode is

$$0.5 \text{ Hz} \leq f \leq 1.2 \text{ Hz} \tag{2.4}$$

The assessment of the appropriate design case includes a qualitative description of the pedestrian traffic, which is then correlated to a traffic class. One of four comfort classes is assigned based on the expected occurrence of this traffic behaviour and sets vertical and lateral acceleration limits (Table 2.2).

Table 2.2: HIVOSS Table 4-4: Defined comfort classes with common acceleration ranges

Comfort Class	Vertical, a_{limit}	Lateral, a_{limit}
CL1	< 0.50 m/s^2	< 0.10 m/s^2
CL2	0.50 - 1.00 m/s^2	0.10 - 0.30 m/s^2
CL3	1.00 - 2.50 m/s^2	0.30 - 0.80 m/s^2
CL4	> 2.50 m/s^2	> 0.80 m/s^2

Damping can occur within the material or the connections of the members of a structure. Damping ratios for serviceability and large vibrations are specified by HIVOSS for applicable materials limited to reinforced concrete, prestressed concrete, steel, and reinforced elastomers. Using a single degree of freedom system (SDOF) method, finite element (FE) method, or response spectra method will yield maximum accelerations. The HIVOSS guidelines specify a pedestrian load within a crowd of 280 N vertical, 140 N longitudinal, and 35 N lateral per pedestrian. The reduction coefficient for the footfall frequency probability is outlined in Figure 2.12.

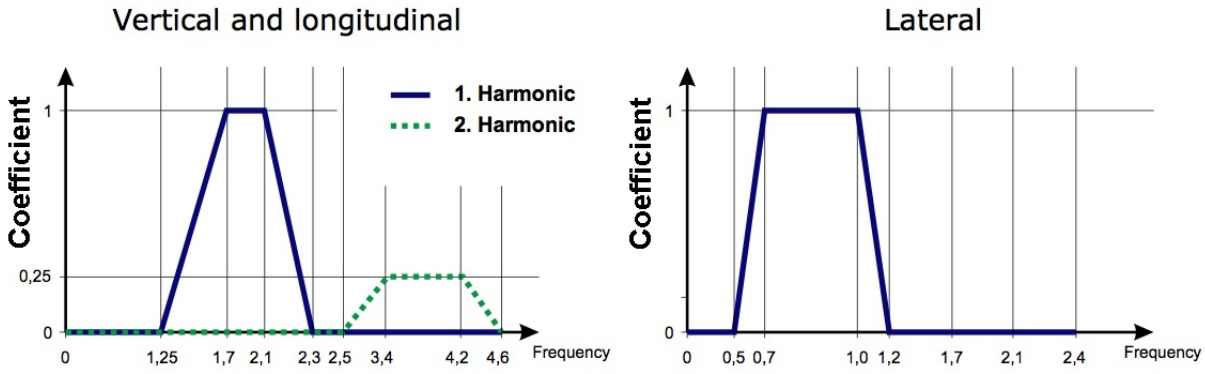

Figure 2.12: HIVOSS load models from Table 4-7 (39)

Calculating the number of effective pedestrians on the bridge is a separate process for the three lighter and the two heavier traffic classes. Checking for the lock-in effect, the synchronisation of pedestrian movement to the bridge sway, is prescribed in the HIVOSS guideline due to its occurrence in precedent cases where pedestrian bridges experienced vibration problems. Lock-in is most likely to occur when lateral accelerations reach 0.1 to 0.15 m/s^2. Lastly, the comfort level of the bridge is determined, where the mass, frequency, or damping can be modified to comply with the above design procedure. The raw measured acceleration data are paired with the natural frequencies calculated from signal-processing methods for a proper dynamic assessment of the bridge.

2.5 Signal-processing methods

Codes and computer simulations serve as tools to determine the prescribed limits and predicted results, respectively, for a given structure. To validate the predictions and ensure the structure falls within acceptable code limits, measured data are required. Much about the structure's dynamic behaviour, its natural frequencies and damping ratio, are embedded in the acceleration data. Processsing of the acceleration data using statistical signal processing tools can extract the embedded properties of the structure (called modal extraction).

The process of modal extraction applies elementary signal processing concepts to the linear d'Alembert's equation of motion, specifically:

$$\begin{aligned} \mathbf{M}\ddot{\mathbf{x}}(t) + \mathbf{C}\dot{\mathbf{x}}(t) + \mathbf{K}\mathbf{x}(t) &= \mathbf{F}(t) \\ \ddot{\mathbf{x}}(t) + 2\omega_n\zeta\dot{\mathbf{x}}(t) + \omega_n^2\mathbf{x}(t) &= \mathbf{F}(t) \end{aligned} \tag{2.5}$$

where ζ is the damping ratio, ω_n is the natural frequency, $\mathbf{F}(t)$ is the applied excitation, and $\mathbf{M}$ is the mass matrix of the system.

The particular method used in this study to separate the source signal is called stochastic subspace identification (SSI) (91). Collected acceleration data are used in the estimation of the state-space solution of the second-order differential equation. Gaussian white noise is superimposed onto the state-space model in the stochastic analysis [2.6]. The state-space model is defined as:

$$\begin{aligned} \dot{\mathbf{x}}(t) &= A(t)\mathbf{x}(t) + B(t)\mathbf{u}(t) \\ \mathbf{y}(t) &= C(t)\mathbf{x}(t) + D(t)\mathbf{u}(t) \end{aligned} \tag{2.6}$$

where $\mathbf{x}$ is the state-vector and A is the system matrix, C is the output matrix. B and D are the input and feedthrough matrices respectively with $\mathbf{u}$ as the input vector, but since zero-mean gaussian noise is being added to the system, the second terms of each of these equations is simplified to a set of gaussian noise vectors.

The eigenvalues Λ, and eigenvectors Θ, are determined from the decomposition of matrix A (66). Given an ordinate number of greater than 2 times the size of matrix A, it is possible to complete the eigenvalue problem. The eigenvalues are used to solve for the natural frequencies of the system.

The specific method of applying SSI for this study is called a Numerical algorithm for Subspace State Space System IDentification (N4SID). This method allows for the response data of the bridge to run through the algorithm and be subjected to singular value decomposition to solve for the natural frequencies, damping, and mode shapes (91).

The basic framework of second-order blind identification (SOBI) (8) is the simultaneous diagonalization of two covariance matrices $\mathbf{R}_{\mathbf{x}}(0)$ and $\mathbf{R}_{\mathbf{x}}(p)$ evaluated at the time-lag zero and p, respectively. This can be written as:

$$\begin{aligned} \mathbf{R}_{\mathbf{x}}(0) &= E\left\{\mathbf{x}(n)\mathbf{x}^T(n)\right\} = \mathbf{A}\mathbf{R}_{\mathbf{s}}(0)\mathbf{A}^T \\ \mathbf{R}_{\mathbf{x}}(p) &= E\left\{\mathbf{x}(n)\mathbf{x}^T(n-p)\right\} = \mathbf{A}\mathbf{R}_{\mathbf{s}}(p)\mathbf{A}^T \end{aligned} \tag{2.7}$$

where:

$$\mathbf{R_s}(p) = E\left\{\mathbf{s}(n)\mathbf{s}^T(n-p)\right\} \tag{2.8}$$

The following three steps set up the essence of SOBI: whitening, orthogonalization, and unitary transformation. Whitening is a linear transformation in which, $\mathbf{R_x}(0) = (1/N)(\sum_{n=1}^{N} \mathbf{x}(n)\mathbf{x}^T(n))$ is first diagonalized using singular value decomposition, $\mathbf{R_x}(0) = \mathbf{V_x}\mathbf{\Lambda_x}\mathbf{V_x}^T$ where $\mathbf{\Lambda_x}$ and $\mathbf{V_x}$ are the eigenvalues and eigenvectors of the co-variance matrix of $\mathbf{R_x}(0)$ respectively. Then, the standard whitening is realized by a linear transformation expressed as:

$$\bar{\mathbf{x}}(n) = \mathbf{Q}\mathbf{x}(n) = \mathbf{\Lambda_x}^{-\frac{1}{2}}\mathbf{V_x}^T\mathbf{x}(n) \tag{2.9}$$

Because of whitening, $\mathbf{R_x}(p)$ becomes $\mathbf{R_{\bar{x}}}(p)$, which is given by the equation:

$$\mathbf{R_{\bar{x}}}(p) = (1/N)(\sum_{n=1}^{N} \bar{\mathbf{x}}(n)\bar{\mathbf{x}}^T(n-p)) = \mathbf{Q}\mathbf{R}_x(p)\mathbf{Q}^T \tag{2.10}$$

Using the Eq. 2.10 and Eq. 2.7, we get:

$$\mathbf{R_{\bar{x}}}(p) = \mathbf{Q}\mathbf{A}\mathbf{R_s}(p)\mathbf{A}^T\mathbf{Q}^T \tag{2.11}$$

The above equation states that by diagonalizing the whitened covariance matrix at a particular time-lag, the unitary matrix product $\mathbf{QA}$ can be determined, resulting in the mixing matrix, $\mathbf{A}$. This process of diagonalization is implemented numerically, and typically involves jointly diagonalizing several covariance matrices at a given lag p (8). The second step, called orthogonalization, is applied to diagonalize the matrix $\mathbf{R_{\bar{x}}}(p)$ whose eigen-value decomposition satisfies:

$$\mathbf{V_{\bar{x}}}\mathbf{R_{\bar{x}}}(p)\mathbf{V_{\bar{x}}}^T = \mathbf{\Lambda_{\bar{x}}} \tag{2.12}$$

Since the diagonal matrix $\mathbf{\Lambda_{\bar{x}}}$ has distinct eigenvalues, the product $\mathbf{QA}$ is a unitary matrix, and the mixing matrix can be estimated by the equation:

$$\hat{\mathbf{A}} = \mathbf{Q}^{-1}\mathbf{V}_{\bar{\mathbf{x}}} = \mathbf{V}_{\mathbf{x}}\mathbf{\Lambda}_{\mathbf{x}}^{1/2}\mathbf{V}_{\bar{\mathbf{x}}} \tag{2.13}$$

where $\hat{\mathbf{A}}$ is the estimated mixing matrix of $\mathbf{A}$. The problem now becomes one of unitary diagonalization of the correlation matrix $\mathbf{R}_{\bar{\mathbf{x}}}(p)$ at one or several non-zero time lags. The determination of the unitary matrix is carried out using a numerical procedure, commonly known as joint approximate diagonalization (8). Denoting $\mathbf{V} = \mathbf{QA}$, $\mathbf{D} = \mathbf{V}^T\widetilde{\mathbf{R}}_{\bar{\mathbf{x}}}(p)\mathbf{V}$, the problem is one of finding the minimum of the performance index J given by:

$$J(\mathbf{V}, \mathbf{p}) = \sum_{p} \sum_{1 \le i \ne j \le n} \left| D_{ij}^{p} \right|^2 \tag{2.14}$$

Then, the unitary matrix $\mathbf{V}$ corresponding to minimum J over fixed h iterations is said to be an approximate joint diagonalizer (8). Once $\hat{\mathbf{A}}$ is estimated, the sources $\hat{\mathbf{s}}$ can be estimated using the pseudo-inverse of Equation 2.5:

$$\hat{\mathbf{s}} = \hat{\mathbf{A}}^{-\mathbf{1}}\mathbf{x} \tag{2.15}$$

2.6 Damper design

Structural dampers offer a means of energy dissipation to mitigate structural vibrations from wind, earthquakes, or other imposed loading. The type of damper varies greatly based on the size constraints of the system and whether the damper passively, actively, or semi-actively responds to the structure's movement. Key examples of dampers are fluid tanks (Figure 2.13a), tuned-mass dampers (Figure 2.13b), viscous dampers (Figure 2.13c),

and frictional dampers (Figure 2.13d); all of which can be instrumented to be passive, active, or semi-active.

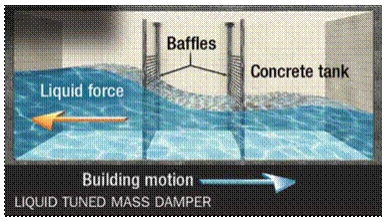

(a) Fluid tank (52)

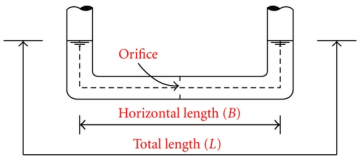

(b) Tuned liquid column damper (37)

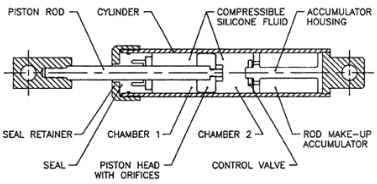

(c) Viscous damper (3)

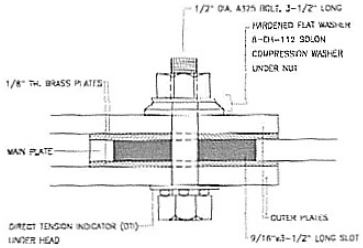

(d) Friction damper (Slotted bolted connection) (36)

Figure 2.13: Types of dampers

In the instance of the fluid tank, the inertia of the fluid is out of phase to the main structure, counteracting the force of the moving structure (83). A tuned-mass damper (TMD) is a mass of a prescribed fraction of the primary structure fitted with springs and dampers will achieve the same result as the fluid tank (38). Viscous dampers are an in-line solution for damping that are analogous to shock absorbers on a vehicle where damping is provided by the flow of a viscous fluid through an orifice, actuated by a piston. A variant of viscous dampers are visco-elastic fluid dampers, which are cost effective and effective, but the modelling is difficult since the stiffness and damping coefficient are dependent on frequency (89). Friction dampers use surface slipping to dissipate energy, such as a

slotted-bolted connection or friction plates (36).

Unlike passive dampers (e.g., fluid, tuned mass and viscous), active dampers are more adaptable to a wide range of frequencies, but conversely they require a fair amount of energy for their operation (92). Real-time data collection and computations for correction are part of the system. Additionally, computer learning techniques may be incorporated in order to predict trends in the structure's behaviour. Corrections can come in the form of displacement control for a frictional damper, orifice diameter control on a viscous damper, or spring stiffness adjustments to a tuned-mass damper.

Semi-active dampers are a compromise between the two previous damper types. They have been developed to keep the cost of energy and computation low, whilst providing damping over a range of frequencies (7). The amount of control provided in a semi-active damper is variable depending on the design, but the concept is to provide corrections to the damper on a less frequent but effective basis.

In the following section, some examples of full-scale damper applications will be described, along with the design principles for the most commonly used damper, the TMD.

2.6.1 Damper studies and applications

The famous Taipei 101 tower in Taiwan has been the subject of many studies due to its incredible height, and thus need for sway mitigation. At the top of the tower is a large, suspended spherical mass, connected to the building structure with viscous dampers. An analytical study was conducted using a model of the tower with semi-active tuned mass dampers (SATMD) and passive tuned mass dampers (PTMD) (102). It was found that when the structure is in resonance, the tuned-mass damper is most effective with a lagging phase shift of 90 degrees. When modelling a SATMD and PTMD frictional damper, both

dampers had a target frequency to structure natural frequency ratio of nearly 1. The damping coefficient, however for the PTMD was approximately 6%, whereas the SATMD damping coefficient was an order of magnitude less (25). Damping for the SATMD was provided by a controllable frictional force, limited by displacement.

Three pairs of viscous dampers were installed on the Ponte del Mare; one set on the outer foot track and two sets on the inner cycling track. Dampers A on the outer track had a damping of 128 kNs/m and stiffness of 127.6 kN/m. Dampers B on the inner track had a damping of 349 kNs/m with the same stiffness as Dampers A. Dampers C had a damping of 794.2 kNs/m and no spring (22). The spring coefficient was deliberately set as low as possible to prevent distortion of natural frequencies and mode shapes, however the dampers were not effective for low-vibration levels. Additionally, the dampers contributed to an increased response for some modes (21). It was found through simulations that the type of numerical representation affects the damping coefficient by manipulating the type of window, and time length (21). Short time Fourier transform (STFT) was the best representation of the estimation factors given the presented bridge structure.

Carpineto (18) observed that pedestrian behaviour affected structural damping, which he used as his starting point for damper design. Pedestrians walking all in the same direction increased the response of the bridge, whereas crowds moving in opposing directions provide natural damping to the system. A system of multiple TMDs were installed on the Singapore Footbridge where the effects of TMDs at $L/2$, and $L/4$ used in isolation were compared to those used simultaneously (18). The total mass of the TMDs was held constant at 1/50th of the mass structure. The TMD at midspan only provided damping to the symmetric modes and none to the anti-symmetric modes since there would be zero displacement at midspan. Dampers at $L/4$ mitigated the anti-symmetric modes in addition to part of the symmetric modes.

Different approaches have been taken to design dampers and their placement. Takewaki developed a gradient-based and optimisation-based approach for determining critical locations for damper placement (89). Conversely, Guo developed a performance spectra for damper design using a graphical design tool to link SDOF responses, residual displacements, peak base shear, and peak base acceleration (96). For frictional dampers however, it was found to be necessary to know the frequencies and their contributions within the excitation signal and the transfer function between the excitation and response (79). In this case, the mean square response, the expectation of the signal squared, must be taken since the frictional damper is a nonlinear system. Theoretically, these methods are elegant, but using experimental results is challenging since the original frequencies and their contributions in the signal are unknown. This requires the solution of the inverse problem from measurement data.

2.6.2 Tuned Mass Damper design principles

The basic steps outlined in *Chapter 4: Tuned mass damper systems* by Connor (26) will be examined for a simply supported beam, which is the model used to analyse the bridge specimens in this study (26). The simply supported beam in Figure 2.14 is the model of the primary structure. The tuned-mass damper is then added to primary structure (Figure 2.15) for the calculation of the combined dynamic behaviour. From the figure, m_d is the mass of the damper, k_d is the stiffness of the damper spring, and c_d is the damping coefficient of the damper. Displacements u^* and u_d are the displacements of the structure and the damper respectively at the damper location x^* along the beam.

Since the structures of this thesis will have inherit damping, the analysis process will include this in the damper design. All of the following calculations are in relation to the

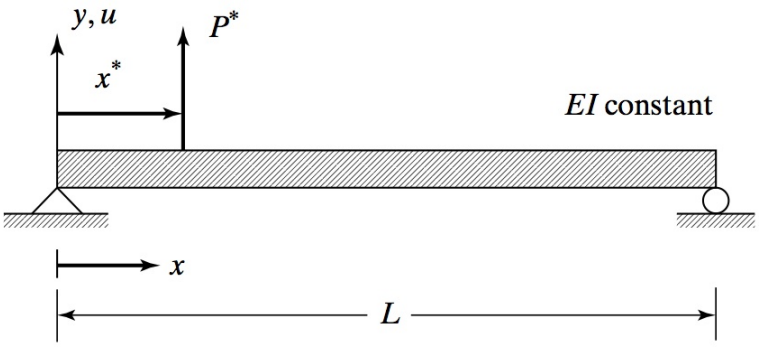

Figure 2.14: Simply supported beam with constant EI and cross section (26)

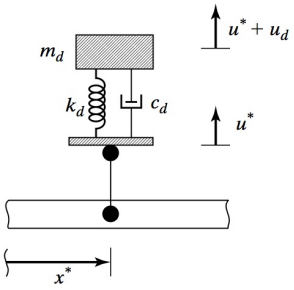

Figure 2.15: Tuned-mass damper connected to beam element (26)

frequency ratio between the system and the damper, f, mass ratio between the damper and the system, $\bar{m}$, the ratio of forcing frequency to system natural frequency, ρ, system damping ratio, ξ, and damper damping ratio, ξ_d.

In a case where a damper is attached to a non-damped primary structure, the damper properties can be analytically determined using Den Hartog's method (26). When the primary structure, however, also includes damping, the process can no longer be solved by this analytical process, and therefore becomes a problem of optimisation. Given initial conditions of the system, the following plots allow for an iterative design process in order to optimize the damper design. The derivation of this optimisation is shown in section 4.4.3 of Connor's book (26).

Firstly, the mass ratio of the damper to the system is determined using Figure 2.16. Optimal condition to solve for mass ratio, $H_5|_{opt}$, occurs when $f = 1$ and the appropriate curve is selected for the system damping value, given by

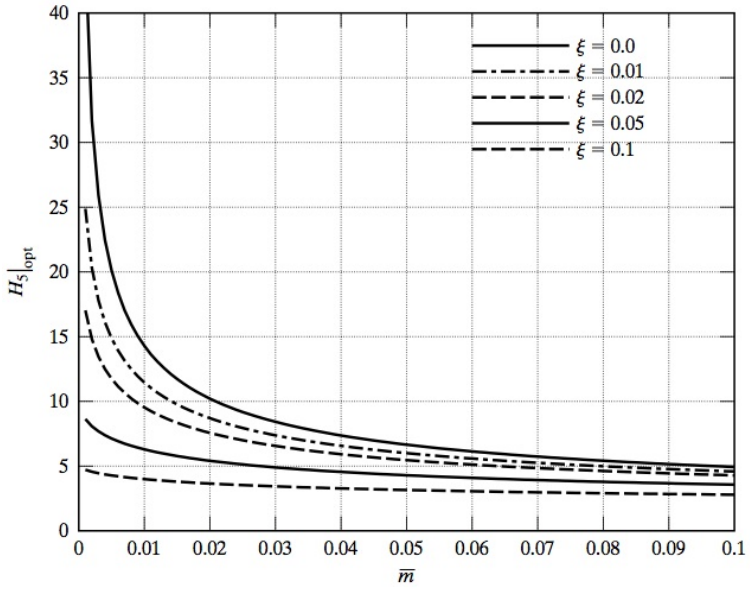

Figure 2.16: Maximum dynamic amplification factor for a SDOF

$$H_5 = \frac{\sqrt{[f^2 - \rho^2]^2 + [2\xi_d \rho f]^2}}{|D_3|} \tag{2.16}$$

where,

$$\begin{aligned} |D_3| = \; & [-f^2\rho^2\bar{m} + (1-\rho^2)(f^2-\rho^2) - 4\xi\xi_d f\rho^2]^2 \\ & +4[\xi\rho(f^2-\rho^2) + \xi_2 f\rho(1-\rho^2(1+\bar{m}))^2] \end{aligned} \tag{2.17}$$

The mass ratio is then used for Figure 2.17 to determine the maximum dynamic amplification factor for the TMD.

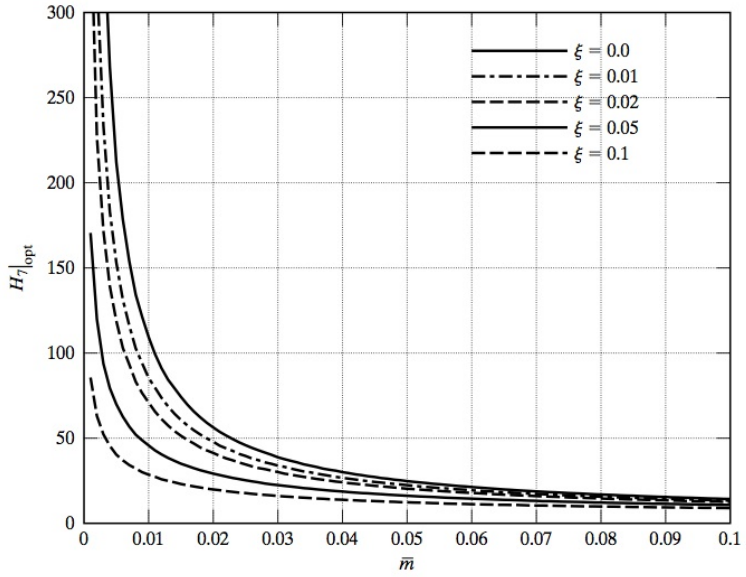

Figure 2.17: Maximum dynamic amplification factor for a TMD

Depending on the nature of the design parameters, Figure 2.18 could be used directly to determine the mass ratio of the TMD to the system. Figures 2.19, 2.20, and 2.21 provide the relationships for optimum TMD tuning frequency, optimum TMD damping ratio, and equivalent damping ratio for an optimally tuned TMD.

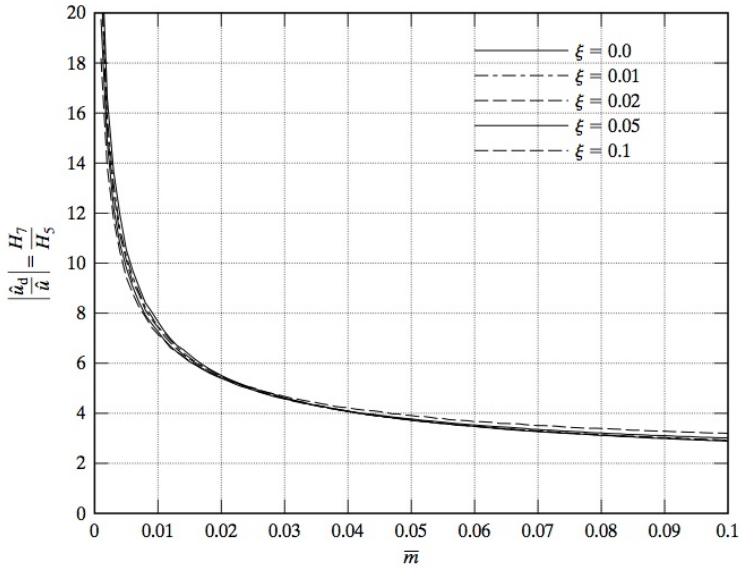

Figure 2.18: Ratio of maximum TMD amplitude to system amplitude

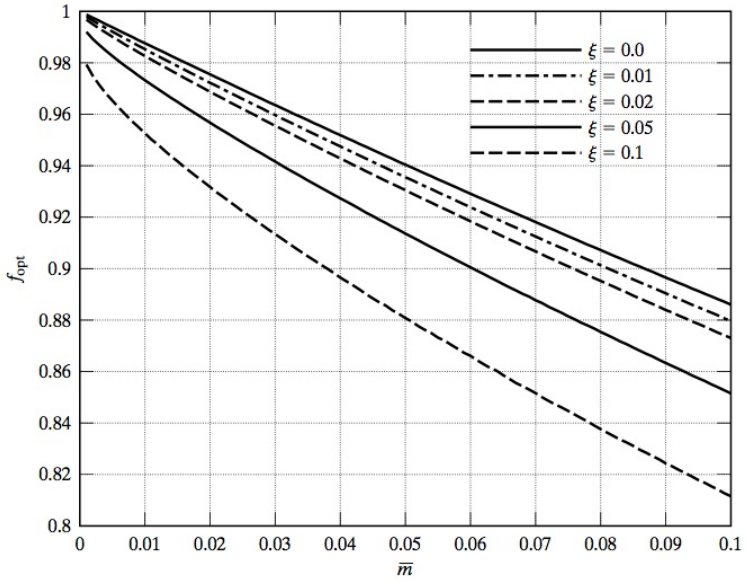

Figure 2.19: Optimal tuning frequency of TMD

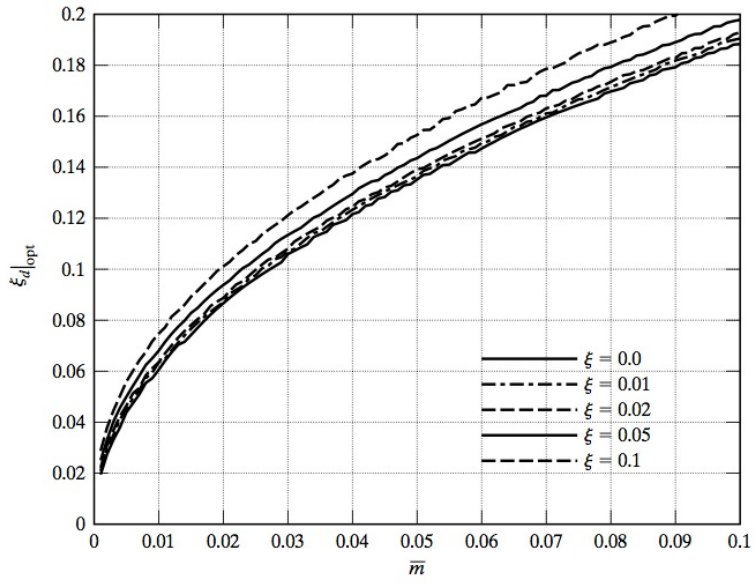

Figure 2.20: Optimal damping ratio of TMD

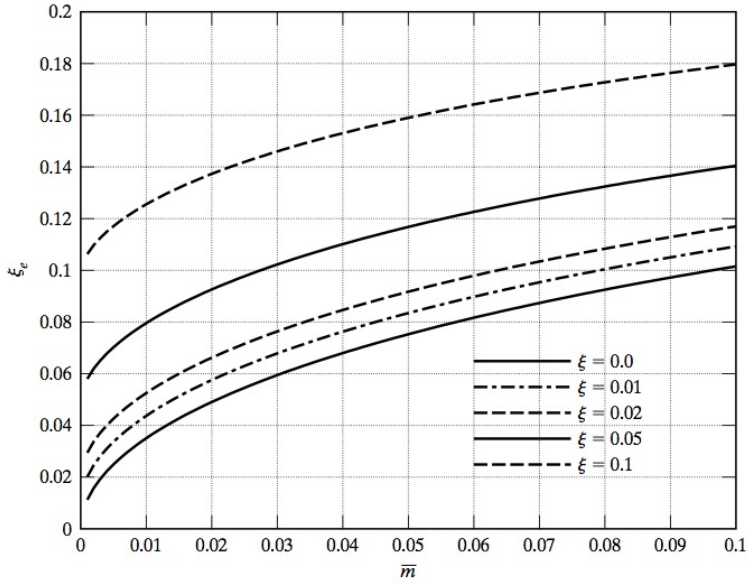

Figure 2.21: Equivalent damping ratio for optimal TMD performance

2.7 Summary of gap areas

Gap areas in prior research remain the:

- examination of a full-scale structure with extensive, statistically significant number of studies on a wide range of pedestrian crowd sizes and walking paces
- analysis of DLFs from pedestrians walking on a full-scale bridge structure with natural frequencies well above pedestrian walking paces
- assessing the performance of non-traditional construction materials (i.e., aluminium) with respect to current dynamic design sections of bridge design codes.

These areas will be addressed in this thesis through the investigation of the dynamic behaviour of three aluminium pedestrian bridges.

Chapter 3

Experimental procedure

3.1 Overview

The goal of the experimental work for this project is to understand the vibrational behaviour of multiple aluminium pedestrian bridge specimens. Thus for each bridge specimen, a common procedure is developed, which consists of:

- Collecting acceleration, load, and strain data from a full-scale bridge specimen under various types of pedestrian-induced loading. Accelerometers are installed vertically and laterally. Triaxial load cells are installed at the four corners of the bridge. Strain gauges are installed on various members in axial tension and bending.
- Using the acceleration data to determine the vibrational properties of natural frequencies, mode shapes, and modal damping using signal-processing techniques.
- Building a finite element (FE) model of the bridge specimen in a structural analysis program based on the bridge manufacturer's design drawings.

- Comparing the results of the FE model analysis to those obtained using the measured data.
- Designing an updated specimen model employing external damping to mitigate vibrational concerns. The damper design is then proposed as a retrofit to the existing structure.

For the purposes of this thesis, the first item will be addressed in the experimental procedure, the results in chapter 4, while the rest will be part of the analysis in chapter 5.

3.2 Instrumentation

3.2.1 Make-A-Bridge

For the purposes of conducting more extensive tests on an aluminium pedestrian bridge, the MAADI Group provided a specimen for controlled laboratory tests. The bridge uses their patented modular Make-A-Bridge system to create the longest span to date with this design. The bridge segments provided were: two 6.096 m (20 ft) spans, two 3.048 m (10 ft) spans, and two 1.524 m (5 ft) end caps. Each bridge length measured 1.353 m (4 ft 5 in) in width and 1.140 m (3 ft 9 in) in height from the centroids of the joints. The bridge lengths tested for this study were 3.048 m (10 ft) (Figure 3.1a), 12.192 m (40 ft) (Figure 3.1b), and 21.336 m (70 ft) (Figure 3.1c). For simplicity of naming convention, each bridge is referred to by their length in bays, thus two-bay, eight-bay, and fourteen-bay bridge. The following figures denote the splice locations where the extruded members were connected with a splice piece inserted inside the top and bottom chords.

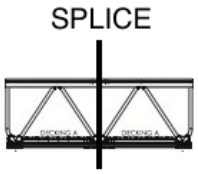

(a) Two-bay bridge

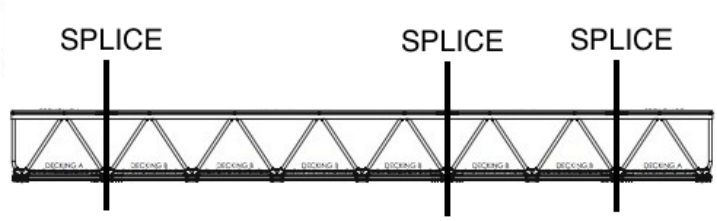

(b) Eight-bay bridge

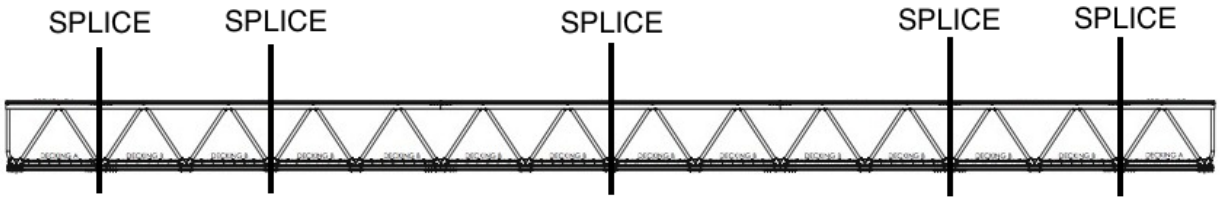

(c) Fourteen-bay bridge

Figure 3.1: Design drawings of Make-A-Bridge

There are six main components to the Make-A-Bridge design which are all fabricated from extruded T6061 aluminium; top chord, bottom chord, diagonal, transversal, deck stringers and decking. With the exception of the stringers that are standard aluminium angles, all of the other components are custom extruded shapes. The assembly is an updated version of that found in patent CA 2688813: Structural assembly for constructing bridges and other structures (Figure 3.2).

The top chord creates the handrail, while the diagonals form the vertical sides of the

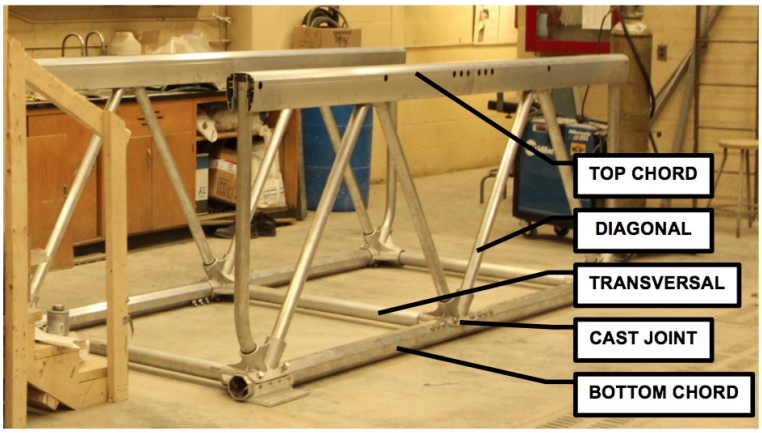

Figure 3.2: Make-A-Bridge parts and assembly

pony truss. The transverse members connect the bottom chords together, forming the cross members of the bridge deck. The ends of the diagonals and transverse members are fitted with neoprene sleeves, which are bolted into a custom-cast aluminium joint. The sleeves are a hard plastic, but since they are not as strong as aluminium, it is possible that they would allow for some movement of the members within the cast joint. All bolts for the construction of these bridges are 5/6" stainless steel. This cast joint is similar to that previously patented, number CA 2607711: Moment-resisting joint and system. These sleeves were coated in silver anti-seize, a viscous liquid, to permit ease of deconstruction. The bottom chords slip into place and are bolted at the joints. The bottom and top chords of adjacent bridge sections are connected by a splice section with three bolts on either side of the splice. The relatively tight fit of the connection essentially results in a moment-resisting connection, however some movement is still possible due to tolerances from machining and fitting the neoprene sleeves. Each deck section measures one truss bay in length with four C-channel stringers running longitudinally along the bridge, and U-bolts secure the deck to the transversal members. Each deck section is individually

attached to the transversals and adjacent deck plates are not directly connected.

Three carts were used to arrange the instrumentation: the load cell workstation (Figure 3.3a), the accelerometer workstation (Figure 3.3b), and the strain gauge workstation (Figure 3.3c). Figure 3.3d shows the arrangement of the carts for the dynamic testing completed on the two, eight, and fourteen-bay bridges. For subsequent strain gauge testing of the eight and fourteen-bay bridges, Figure 3.3e shows the modified arrangement.

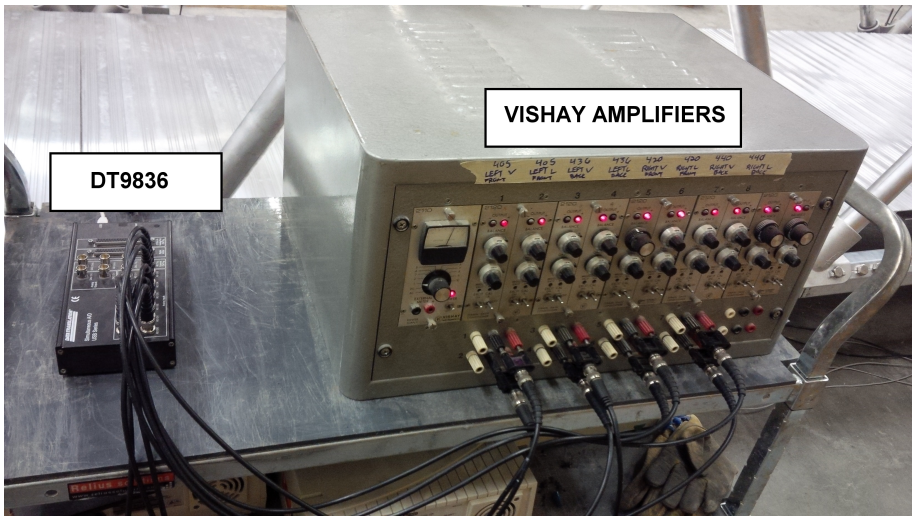

(a) Load cell workstation

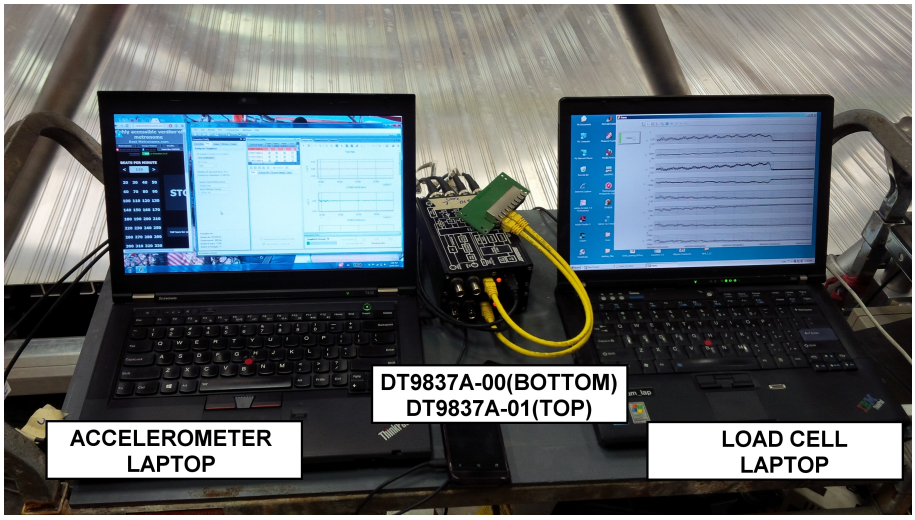

(b) Accelerometer workstation

(c) Strain gauge workstation

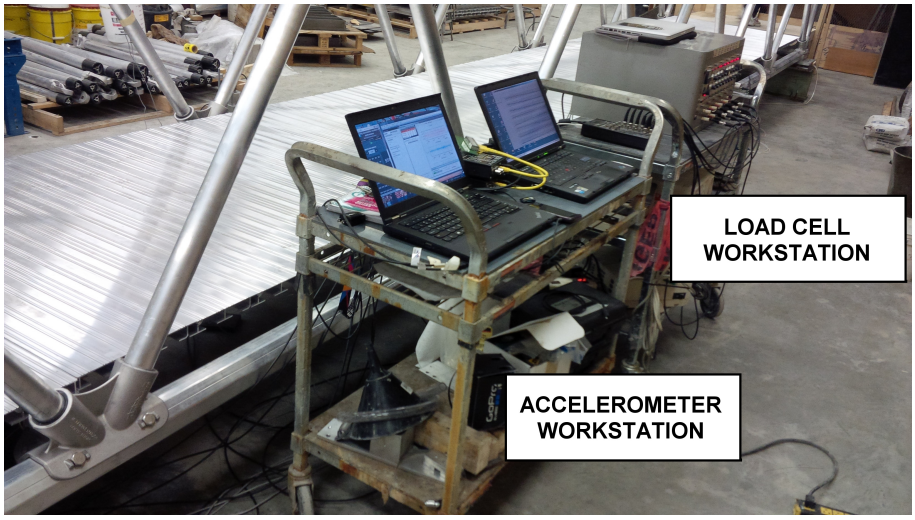

(d) Configuration of the equipment for dynamic testing

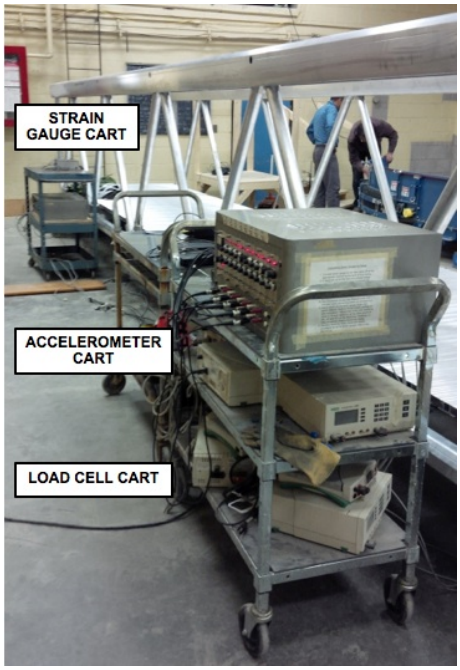

(e) Configuration of the equipment for strain and dynamic testing

Figure 3.3: Instrumentation layout

3.2.2 Load cells and installation

Due to the fact that some of the instrumentation was not hermetically sealed, the bridge was installed indoors, which also reduces thermal effects on the specimen. Underneath each of the four bridge bearing plates, a plate sandwich system was installed that contained a strain-based triaxial load cell; model TR3D-B-4K from Michigan Scientific. These were installed in order to observe the vertical and sidesway (lateral) reaction forces during pedestrian loading. These load cells are capable of up to 18 kN axial force and up to 4.5 mV/V excitation in any of the coordinate directions. This limit is reduced if the orthogonal directions are loaded in unison.

The load cells are sandwiched between two 12 mm thick aluminium mounting plates. A top plate connects the bridge abutment plates at the manufacturer-prescribed location to the top of the load cell with a counterbored M12x1.75 mm bolt. The bottom plate connects the bottom of the load plate with M8 bolts and bolts into a steel W310x129 section at each abutment. (Figure 3.4).

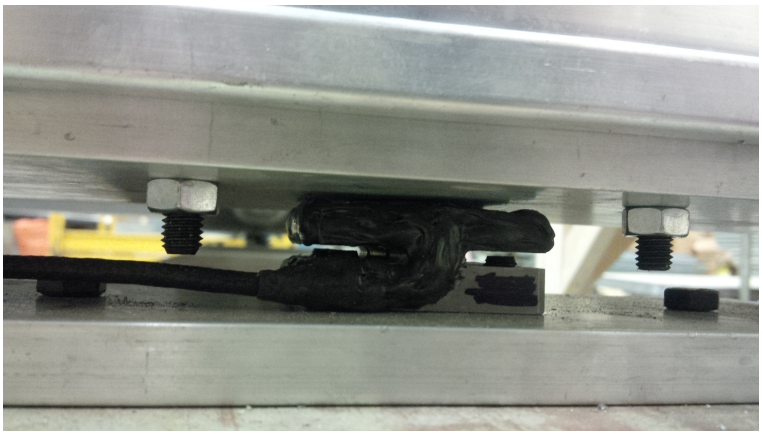

Figure 3.4: Triaxial load cell mounted between steel beam abutment and underside of bridge

The mounting system is intended to simulate stiff abutments for the bridge while raising it off the ground for ease of instrumentation. Since it elevated the bridge above comfortable stepping height, a pair of wooden 4-riser stairs and landings were built to walk on and off the bridge. This was also done to accommodate the flow of crowds for pedestrian walking tests. To create a rigid connection from the bridge to the floor, the bottom flanges of the support beams were bolted down to the floor of the lab using 1/2" threaded rods and 50 mm deep drop-in Hilti anchors drilled into the floor.

Levelling of the bridge was identified as important, and thus threaded rods were installed in holes tapped into the beam so that each of the four corners could be adjusted until the load cells equally divided the bridge self-weight. Non-shrink sand-based grout was then cast between the bottom flange of each support beam and the floor as a filler material to minimise vibration of the support beams. Figure 3.5 shows the abutment beams with the formwork to encase the casted grout to keep the bridge level.

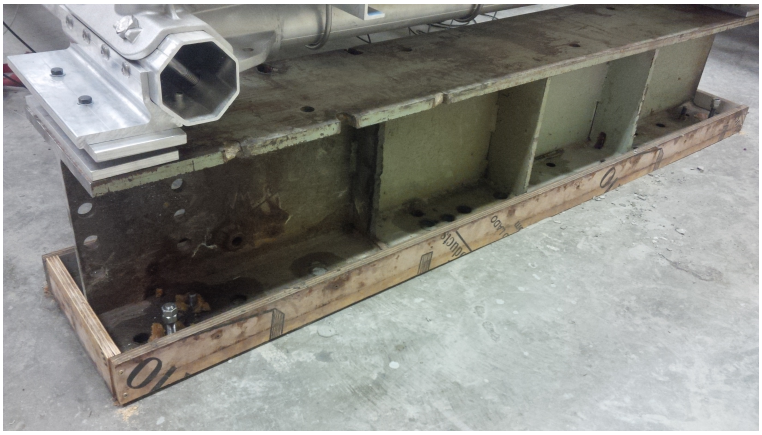

Figure 3.5: Abutment support beams bolted into the floor and grouted

In order to amplify the signal from the load cells, a bank of ten Vishay amplifiers with a full bridge, two parallel sets of two resistors in series, connection for each channel was used

since these devices contribute little to no signal noise. Given an excitation of 8 V, the signal was amplified such that 1 mV = 1 N for ease of interpretation. To check the functionality of the load cells, a 100 k 1% shunt resistor was used to compare to company-printed data sheets specific to each load cell.

Due to the importance of vertical and lateral loads on this bridge specimen, only the vertical, F_z, and lateral, F_y channels of the load cells were wired into the signal amplifiers. A 16-bit 12-channel A/D DAQ, model DT9836 by DataTranslation, was used to collect the load cell data. The data collection software, MeasureFoundry, was used to produce the text files for each trial. Table 3.1 summarises the DAQ channel, Vishay channel, and load cell ID and load cell arrangement.

Table 3.1: Load cell placement and channel allotment

DAQ channel	Vishay channel	Load cell ID	Direction
0	1	405	Vertical
1	2	405	Lateral
2	3	436	Vertical
3	4	436	Lateral
4	5	420	Vertical
5	6	420	Lateral
6	7	440	Vertical
7	8	440	Lateral

3.2.3 Accelerometers

Twelve low-frequency, high-sensitivity model 393B31 accelerometers by PCB Piezotronics were installed along the bottom chords of the bridge at $L/4$, $L/2$, and $3L/4$; a laterally and vertically mounted accelerometer was placed at each attachment point. Each aluminium mounting system consisted of a block, allowing accelerometers to be installed in any axis. This block is screwed into a top plate, 300 mm long, 100 mm wide, and 12 mm thick. Another similar plate sits underneath the beam to which the accelerometers are being installed. Threaded rod and wingnuts secure and tighten the two plates on opposing sides of the beam (Figure 3.6). This connection system was used as it avoided drilling holes, gluing to the bridge itself, or marring the surface.

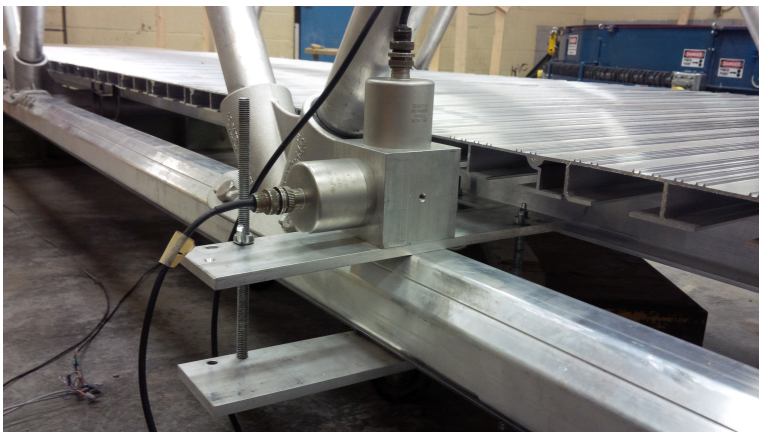

Figure 3.6: Accelerometer mounting system using sandwiching plates

The geometry of the diagonals made installation of the accelerometers close to the joint prohibitive, thus an alternative mounting was developed to hang the sensors below the bottom chord. This mounting configuration was only used for the two-bay bridge, since an offset from the joint in order to use the standard mounting was less significant on the

longer specimens. Figure 3.7 shows the alternative mounting, which consisted of a slotted aluminium block attached with screws to the same accelerometer mounting block; all of which was tightened to the bottom chord using a hose clamp.

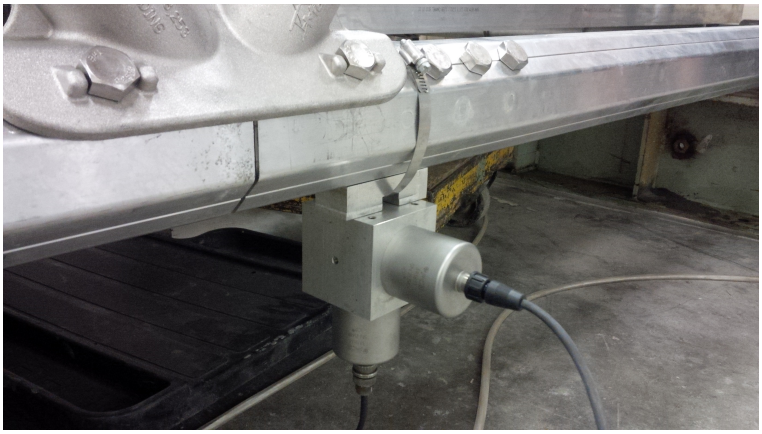

Figure 3.7: Accelerometer mounting system using hose clamp

The accelerometers were ideal for monitoring bridge and pedestrian vibrations since their operable frequency range is 0.1 Hz to 200 Hz with an excitation voltage of 10 V/g with less than 1% non-linearity and 5% sensitivity.

Three daisy-chained 24-bit 4-channel A/D DAQs, model DT9837A by DataTranslation, were used to collect the accelerometer data from another laptop. These pre-amplified DAQs were read by the software VIBpoint, by DataTranslation. Data collection for the load cells and the accelerometers was necessary due to software, DAQ, and CPU usage incompatibilities. However, all tests were coordinated to record concurrently. Table 3.2 summarises the DAQ channel, accelerometer ID, and load cell arrangement.

Table 3.2: Accelerometer placement and channel allotment

DAQ ID	DAQ channel	Accelerometer ID	Calibration (mVs^2/m)	Location	Direction
00	0	25760	989	$L/4$	Vertical
00	1	26263	987	$L/4$	Lateral
00	2	25764	980	$L/4$	Vertical
00	3	25761	977	$L/4$	Lateral
01	0	25151	998	$L/2$	Vertical
01	1	25147	986	$L/2$	Lateral
01	2	26264	1016	$L/2$	Vertical
01	3	26265	998	$L/2$	Lateral
02	0	25688	1003	$3L/4$	Vertical
02	1	25154	988	$3L/4$	Lateral
02	2	25558	1001	$3L/4$	Vertical
02	3	26262	992	$3L/4$	Lateral

3.2.4 Strain gauges and dial gauges

Static deflections of the bridges were recorded to compare with the allowable deflection from CSA S6-06 and to use for code-based dynamic design. The dial gauge used for this purpose was a Baty HL series with an accuracy of 0.01 mm. For a reliable measurement, the dial gauge was used in the middle of its operating range and installed with a magnetic base underneath the bridge (Figure 3.8).

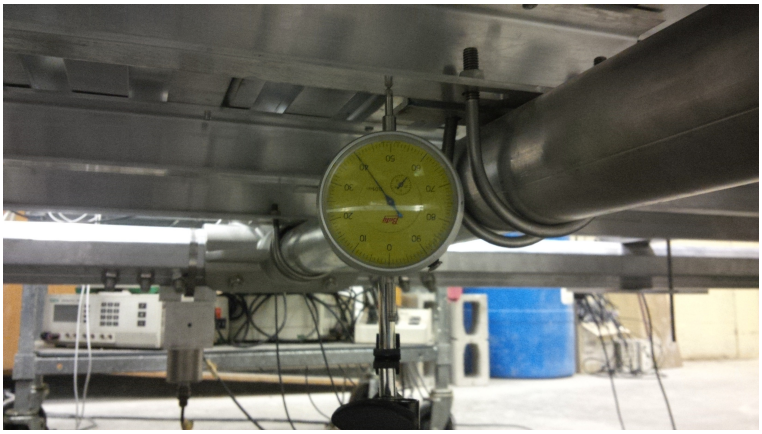

Figure 3.8: Dial gauge for static deflection measurements

The strain gauges used in the second phase of testing were Tokyo Sokki Kenkyujo Co. Ltd, Type FLA-5-23-3L, gauges with a length of 5 mm, and a gauge factor of 2.16 ±1%. In order to measure chord stresses, one bottom chord was selected. A diagonal near the bridge support was selected for measuring stress in the diagonal (Figure 3.9). Each strain channel was excited with 3.5 V and balanced with a 100 k shunt to 2 V. Two strain gauges were placed on opposite sides of each instrumented member so that axial and bending strains could be isolated.

Strain gauges were located at the midspan of the selected members to avoid end effects. These strain gauge channels were added to the eight load cell channels in the DT9837 DAQ system.

3.3 Testing procedure

For modal analysis of the aluminium pedestrian bridge, ambient and free vibration tests were conducted. Pedestrian walking tests were then run to observe human-structure inter-

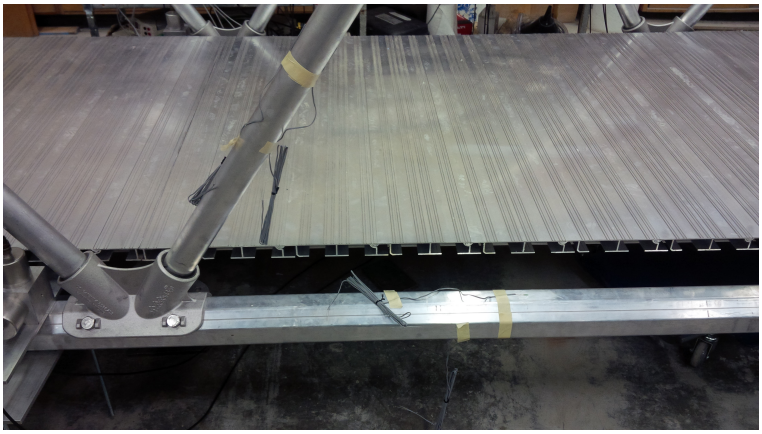

Figure 3.9: Installation of strain gauges on chord member at midspan

action and for validation of future loading models. The pedestrian walking tests were then repeated with the strain gauges for future fatigue work of aluminium structures.

Ambient tests were performed for approximately 60 seconds where no loading was induced on the bridge. These tests were sampled at 500 Hz and were used for verifying baseline noise levels.

Static design checks were in place to ensure the stability of the structure and the accuracy of the finite element model to measured results. A person weighing 700 N stood stationary at midspan where a dial gauge was positioned under the centre of the deck. The difference between the final and initial reading of the dial gauge is the effective static displacement, which can be used as a input for the CSA S6-06 deflection checks.

For the free vibration tests, both vertical and lateral-induced forces were applied. For the vertical impact loading, a dead-blow mallet was dropped from a height of 50 mm to avoid peaking the accelerometers. To excite lateral vibrations, the hammer test was noted to overload the accelerometers and thus an alternative weight-release method was used. For the eight-bay bridge, a rope was tied to the bottom chord of the bridge and pulled

to give an initial displacement. This rope was then suddenly released to cause an impact load and incur free vibration. For the fourteen-bay bridge, a pulley system (Figure 3.10) carrying 100 lbs of weight was used to pre-load the bridge which was then quickly released. All free vibration tests were run for approximately 20 seconds.

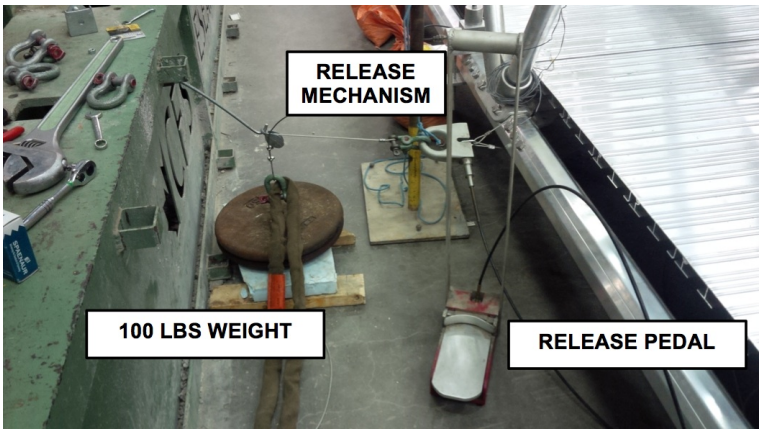

Figure 3.10: Lateral free vibration system for fourteen-bay bridge

For the pedestrian walking tests, previous work on the statistics of walking frequency determined that the mean and standard deviation were 2.0 Hz, steps per second, and 0.3 Hz respectively (70). Thus, in order to obtain the desired level of resolution of the gait analysis, walking frequencies for this study were established from 100 beats per minute (BPM) or 1.67 Hz, to 140 BPM or 2.33 Hz, in increments of 10 BPM. These tests were paired with running tests at 160 BPM, 170 BPM, and 180 BPM, since previous work confirms feasible running cadences for up to 3 Hz (70). The weight of each walking participant was taken as the difference between readings from the load cell when the participant is stationary and after they leave the bridge. In order for future work to be completed on developing a load model for walking pedestrians, the participants' leg length was measured prior to testing. Using a camera aimed at the legs of the participants, stride length could be also

be measured.

Walking tests were conducted for one pedestrian, two pedestrians, and pedestrian densities of 0.2 p/m^2, 0.5 p/m^2, 1.0 p/m^2, and 1.5 p/m^2 as prescribed by the HIVOSS (39) code for traffic classes. Table 3.3 denotes the number of pedestrians present for each crowd test for each specimen.

Table 3.3: Number of pedestrians in crowd tests

Crowd density (p/m^2)	Two-bay bridge	Eight-bay bridge	Fourteen-bay bridge
0.2	1	3	5
0.5	2	7	13
1.0	4	15	26
1.5	6	22	39

For each participant or set of participants, there were 30 trials conducted in order to ensure statistical significance of the results. Additionally, the single pedestrian walking tests were repeated for six individuals; three men three women, one each of below average, average, and above average weight and height.

3.4 Test matrix

Table 3.4 summarises the tests conducted on the bridge specimen for this study where instrumentation is abbreviated for accelerometers (Acc), load cells, (LC), dial gauge (DG) and strain gauges (SG).

Table 3.4: Testing matrix for experimental study

Test name	Duration (sec)	Equipment	Description
Ambient	60	Acc, LC, SG	No bridge excitation
Impact	≈ 20	Acc, LC	Dead-blow mallet
	≈ 20	Acc, LC	Lateral pulley release
Deflection	≈ 20	DG	Midspan deflection from 700 N person
Weight check	≈ 20	Acc, LC	Subject stationary on bridge
Single pedestrian	5+walking+5	Acc, LC, SG	100 BPM to 140 BPM, 10 BPM increment, 160 BPM, 170 BPM, 180 BPM
Two pedestrians	5+walking+5	Acc, LC, SG	Walking synchronously
	5+walking+5	Acc, LC, SG	One at 115 BPM, one at 130 BPM
0.5 p/m^2	5+walking+5	Acc, LC, SG	100 BPM to 140 BPM, 10 BPM increment, 160 BPM, 170 BPM, 180 BPM
1.0 p/m^2	5+walking+5	Acc, LC, SG	100 BPM to 140 BPM, 10 BPM increment, 160 BPM, 170 BPM, 180 BPM
1.5 p/m^2	5+walking+5	Acc, LC, SG	100 BPM to 140 BPM, 10 BPM increment, 160 BPM, 170 BPM, 180 BPM

In this thesis, the units of beats per minute, BPM, and Hertz, Hz, are both used to describe walking frequency. To convert from BPM to Hz, divide the number by 60.

In order to capture the effect of two pedestrians walking synchronously, the test subjects matched each others' steps. To ensure a proper asynchronous test, each pedestrian followed a different walking frequency using independent metronomes.

For the two-bay bridge free vibration tests, five trials were conducted using a dead blow hammer at the midspan. Each walking test was completed twice since statistical significance of the test results was not deemed to be of interest for this span.

For the eight-bay bridge free vibration tests, six vertical impact tests were conducted similar to the two-bay bridge and ten lateral impact trials were run using the laterally-loaded rope. Walking tests were all consisted of 30 trials of each walking pace. In the case of the single pedestrian tests, the testing was repeated for each of the eight participants.

The number and type of tests for the fourteen-bay bridge were identical to those of the eight-bay bridge.

Excitation of the lateral direction was only completed on the eight-bay and fourteen-bay bridges. The lowest crowd density according to HIVOSS guidelines of 0.2 people per square meter was ignored for the two-bay bridge since it was the equivalent of one pedestrian. Conversely, the highest crowd density from HIVOSS, 1.5 people per square meter, was not obtainable on the eight or fourteen bay bridges due to difficulty fitting that number of pedestrians on the bridge.

3.5 Specimen description

This section provides the plans for the instrumentation of each bridge and specific notes about each specimen. Figures 3.11a, 3.11b, 3.11c illustrate the location of each load cell and accelerometer input, identified by DAQ channel number and direction of installation.

Boxed labels refer to the load cells and unboxed labels refer to the accelerometers.

The system coordinates for instrumentation was Z-direction positive upwards, Y-direction across the width of the bridge positive towards the workstation, and the X-direction along the length of the bridge, starting at 0 to the right of the workstation. Figures 3.12a and 3.12b locate the four strain gauges and their respective channels in the DAQ.

The two-bay and eight-bay specimens were installed at the University of Waterloo in room E3-2104 on a slab on grade. Measurements of the space determined that the eight-bay specimen was the largest possible in this space, and thus the fourteen-bay was installed in the adjacent room E3-2102. The 1 m thick concrete strong floor in this structural testing lab is 70 ft (21.336 m) long. The centreline of the support beams on either side of the bridge were aligned with the edge of the strong floor.

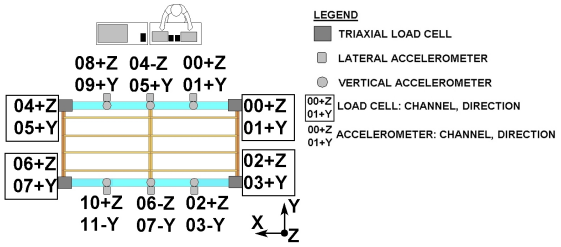

(a) Two-bay bridge

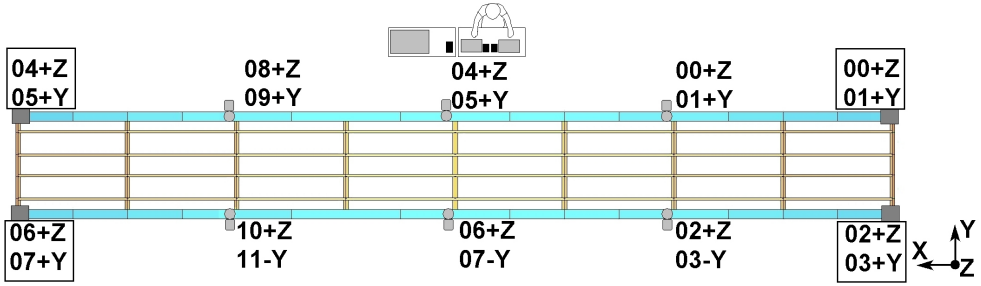

(b) Eight-bay bridge

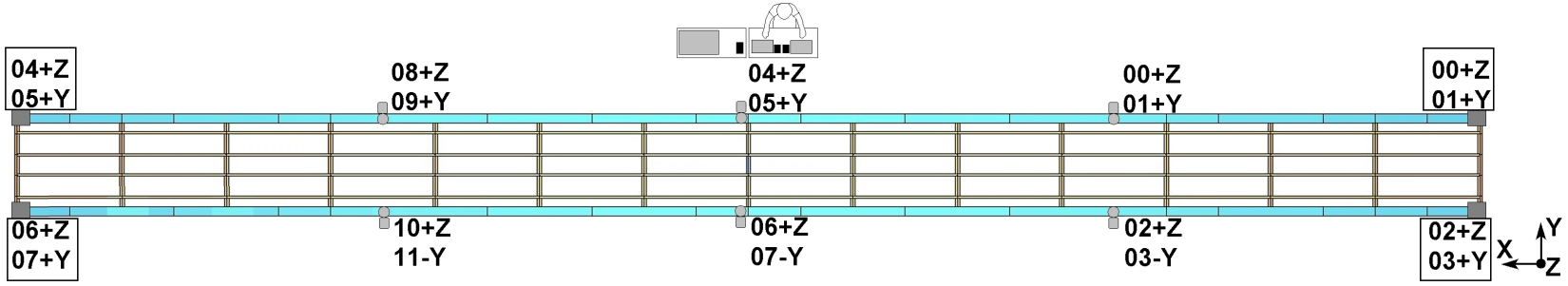

(c) Fourteen-bay bridge

Figure 3.11: Bridge specimen instrumentation setup plan view

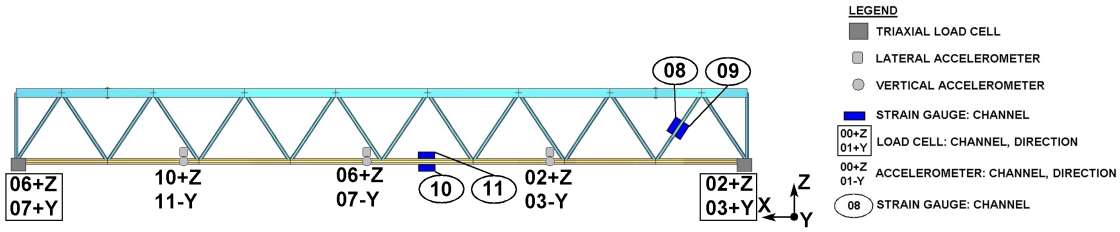

(a) Eight-bay bridge

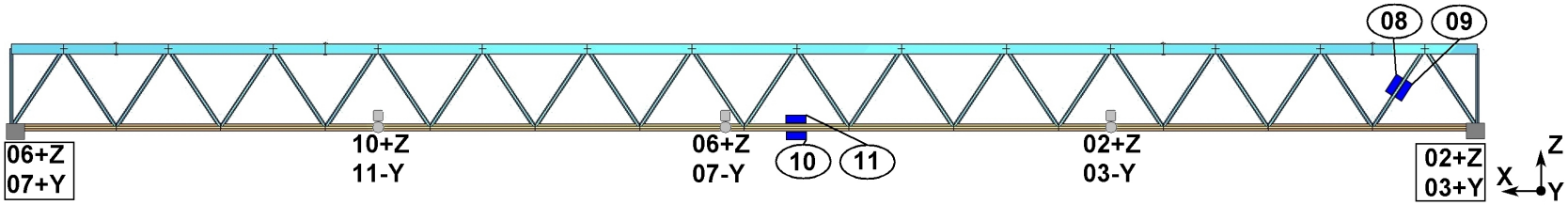

(b) Fourteen-bay bridge

Figure 3.12: Bridge specimen instrumentation setup elevation view

3.5.1 Two-bay bridge

The bridge in its two-bay configuration is 3.048 m long and weighs approximately 280 kg. This is the shortest of the available spans and is constructed by joining the two bridge sections, designated as the end caps, at the midspan of this length. Figure 3.13 is an overall view of the structure in the lab. This was the only setup where the midspan accelerometers were mounted in the downwards position using the hose-clamp mounting system in order to obtain measurements as close to the midspan as possible. The hose clamp mounts were installed to the left of the joints as indicated in the schematics.

Figure 3.13: Two-bay bridge overview

3.5.2 Eight-bay bridge

The bridge in its eight-bay configuration is 12.192 m long and weighs approximately 982 kg. This bridge is constructed by stringing together the endcaps, a 4-bay section, and a 2-bay section. Due to the asymmetry in the assembly, it was predicted this may have an observable impact on the structure. Since the overall length was much greater for this specimen than that of the previous, the sandwich-style mounting systems were used for every location. The mounting was kept as physically close to the left side of the joint as possible as shown in the setup schematic. Figure 3.14 is an overall view of the structure in the lab.

Figure 3.14: Eight-bay bridge overview

3.5.3 Fourteen-bay bridge

The bridge in its fourteen-bay configuration is 21.336 m long and weighs approximately 1600 kg. This bridge is constructed by stringing together the endcaps, a 4-bay section, two 2-bay sections, and a 4-bay section. The sections were assembled in a symmetrical manner

in order to prevent localised anomalies. Additionally, the 2-bay sections were installed in the centre since it was observed that the tolerance gap in joints was a major contributor to the structure's overall maximum deflection under self-weight. The splice gaps were "locked" under self-weight, but their behaviour was not observed during pedestrian loading. The gaps reduced the effective stiffness of the bridge which changes its vibration characteristics. Placing the 4-bay sections towards the abutments was done to ensure that these sections act as cantilevers from the abutments during construction. This was considered in the build process in order to prevent local stresses or deformations. Figure 3.15 is an overall view of the structure in the lab.

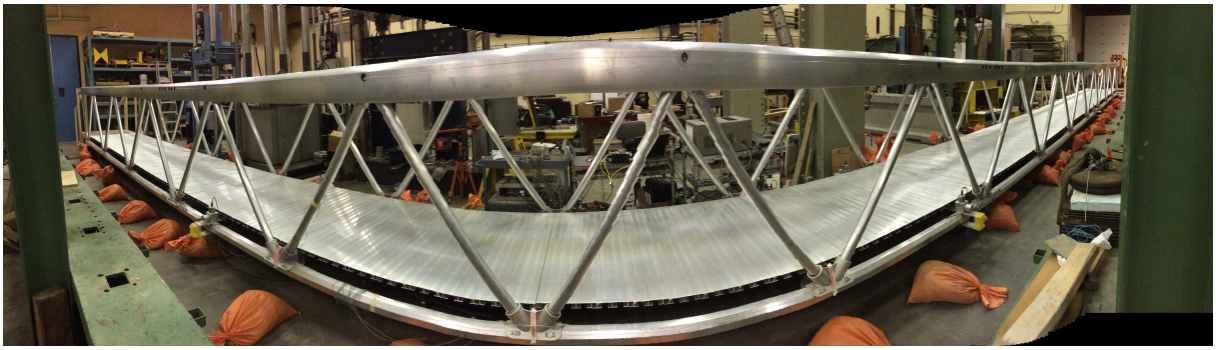

(a) Side-view

(b) End-view

Figure 3.15: Fourteen-bay bridge overview

Chapter 4

Results

This chapter provides sample data sets and key observations for each type of measurement —acceleration, load, strain, and displacement —that was captured using the instrumentation previously mentioned. Within each type of measurement is each applicable bridge specimen. Main highlights of the data and preliminary observations directly inferred from the data are summarized in this section. Since no comparable experiments have been completed, results are compared to the first bridge specimen built, the two-bay bridge, and design codes in Chapter 5. The data from this study are then used for further analysis in Chapter 5.

4.1 Accelerometer results

Through preliminary analysis of the finite element models built prior to experimental work, it was determined that the two-bay bridge would experience the highest frequencies. Within the first twenty modes from the analysis, the natural frequencies reached up to 180

Hz, and it was determined that the accelerometers should be capable of sensing this range. For the purposes of future signal processing, the sampling frequency is twice that of the highest measureable frequency due to a Nyquist value of 2. Thus, accelerations from all bridge specimens were measured at the same sampling frequency of 500 Hz, in order to capture frequencies up to a possible 250 Hz.

In the following sections, sample plots are given to illustrate the results of the accelerometer measurements, the remaining of which can be found in Appendix A. Each plot lists the test type, DAQ channel and geometric configuration of accelerometer.

4.1.1 Impact test acceleration results

Figure 4.1 shows the vertical hammer impact and the lateral pulley release tests for the fourteen-bay bridge.

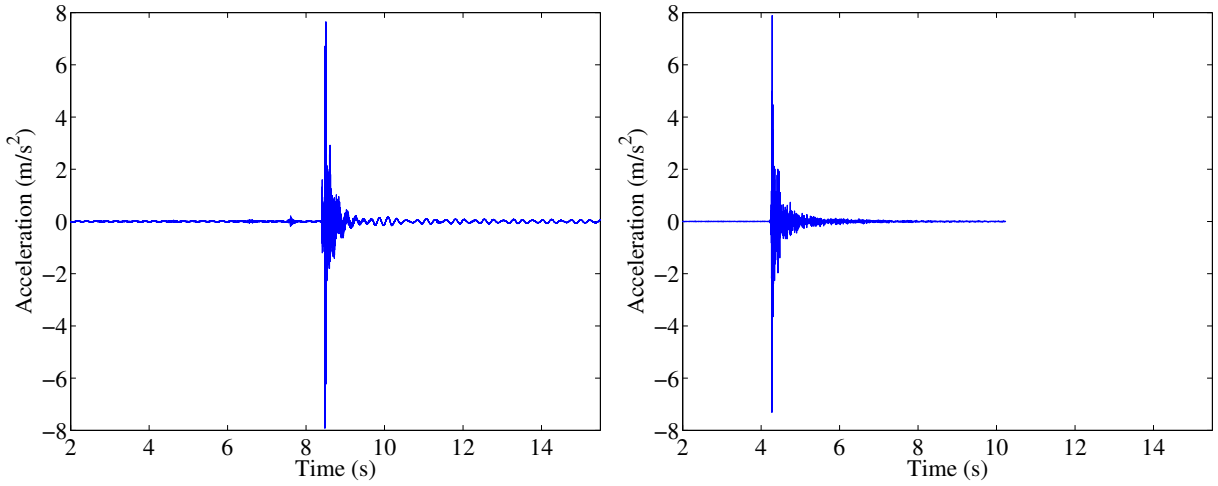

(a) Vertical hammer impact, 04+Z

(b) Lateral pulley release, 05+Y

Figure 4.1: Sample acceleration histories from impact tests

All of the impact tests completed on the bridge specimens —either vertical or lateral —have all shown the same sharp initiation of acceleration, with an exponential decay back to rest. This is what was anticipated from these tests in order to determine the natural frequencies and damping of the structures without pedestrian involvement. The lateral pulley release test was only developed for the fourteen-bay bridge and the eight-bay bridge was manually pulled laterally using a rope. Even though the two-bay bridge did not have a specific lateral test, there was lateral acceleration measured in the lateral accelerometers during the vertical hammer impact test.

4.1.2 Single pedestrian results

For the purposes of discussion on acceleration results of a single pedestrian, the fourteen-bay specimens with pedestrians walking at 120 BPM and running at 180 BPM will be referenced. Figure 4.2 shows the acceleration results from a pedestrian walking at 120 BPM on the fourteen-bay bridge. Figure 4.3 shows the same pedestrian running on the same bridge at 180 BPM.

As the pace of the pedestrian increases, the time interval between the peaks decreases. In the first plots, two peaks per second are observed while in the second, three peaks are observed. The shape of the peaks changes with the increase in pace due to the biomechanical nature of walking compared to running. The attack of the peaks increases with increasing pace due to a more sudden step by the pedestrian.

Additionally, Figures 4.2 and 4.3 show that the vertical accelerations are greater than the lateral accelerations.

As bridge span increased, the accelerations at the same walking pace also increased. For example, the peak accelerations for the 100 BPM walking test for the two-bay, eight-

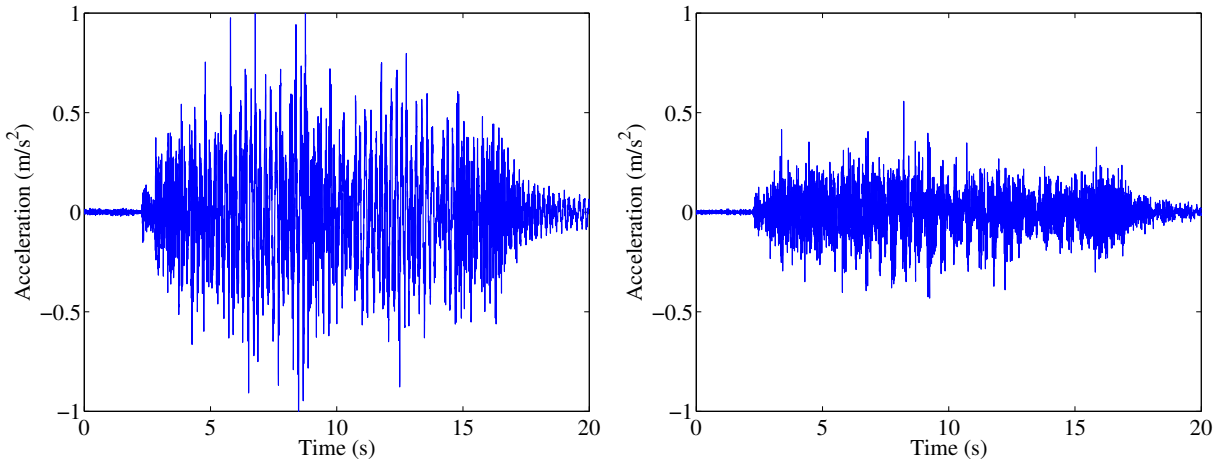

(a) Vertical, 04+Z

(b) Lateral, 05+Y

Figure 4.2: Sample acceleration histories for single person walking at a pace of 120 BPM, weight: 0.65 kN, leg length: 0.95 m, fourteen-bay

bay, and fourteen-bay bridges are 0.54 m/s^2, 0.86 m/s^2, and 1.15 m/s^2 respectively. These results were expected since more movement during pedestrian testing was observed on the eight-bay bridge in comparison to the two-bay bridge. Given a single walking pace over multiple bridge lengths, the imposed frequency will be constant but the amplitude of the vibration increased as the span increases, thus an increase in acceleration.

4.1.3 Pedestrian crowd acceleration results

Figure 4.4 shows the acceleration results for a crowd of 0.5 p/m^2 of the fourteen-bay bridge. Figure 4.5 shows the acceleration results for a crowd of 1.0 p/m^2.

From Figures 4.4 and 4.5, the number of pedestrians was doubled, but the acceleration amplitude was not. This shows that the peak acceleration is not linearly related to the number of pedestrians walking. This was expected from literature that the peak acceler-

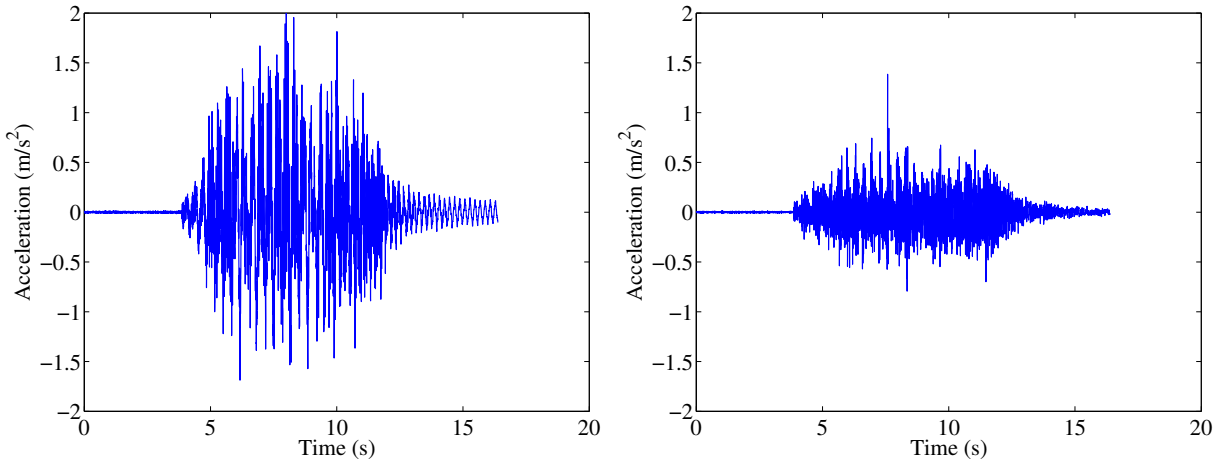

(a) Vertical, 04+Z

(b) Lateral, 05+Y

Figure 4.3: Sample acceleration histories for single person running at a pace of 180 BPM, weight: 0.65 kN, leg length: 0.95 m, fourteen-bay

ation would be approximately proportional to $\sqrt{n}$, where n is the number of pedestrians (51).

Unlike the single pedestrian tests where all of the peaks were evenly spaced, each pedestrian in the crowd walked at different paces and at different phase angles, creating unevenly distributed peaks. Seen in both figures, but particularly evident in the 1.0 p/m^2 test, sudden acceleration peaks occur when pedestrians changed their gait to match the sway of the bridge or had to catch themselves on the handrail. This trend of unevenly-spaced peaks is evident even in the two-pedestrian synchronous and asynchronous walking tests, provided in Appendix A.

The fourteen-bay bridge exhibits a higher acceleration sensitivity than the two-bay or the eight-bay bridges. In particular, the 1.0 p/m^2 test for the fourteen-bay bridge shows a large amplitude, low frequency resonance in the lateral direction, unique to this test on

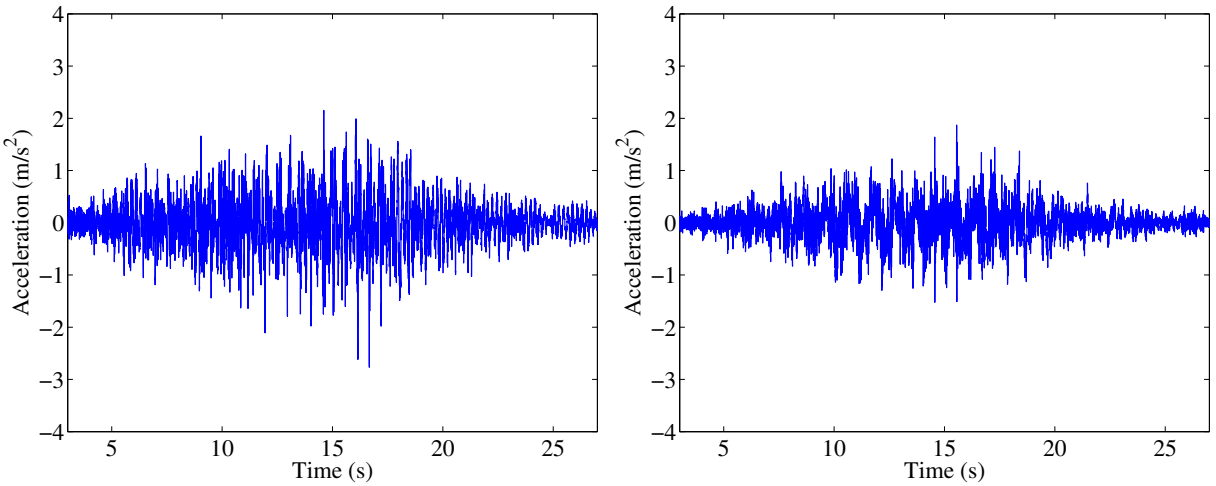

(a) Vertical, 04+Z

(b) Lateral, 05+Y

Figure 4.4: Sample acceleration histories for 0.5 p/m^2 walking, total weight: 9.66 kN, fourteen-bay

this bridge. As the large crowds were introduced, the combined weight of the bridge and pedestrians lowered the natural frequency into the resonance range with pedestrian walking paces. The increase in bridge span increased the lateral sensitivity to acceleration due to the natural frequencies approaching that of the lateral resonance with walking paces.

4.1.4 Peak and RMS acceleration results

The summary of the acceleration data are presented as the mean of the peak accelerations per test, and the mean root mean square (RMS) value of each test.

The root mean square (RMS) of a signal is:

$$RMS = \sqrt{1/n(x_1^2 + x_2^2 + \ldots + x_n^2)} \tag{4.1}$$

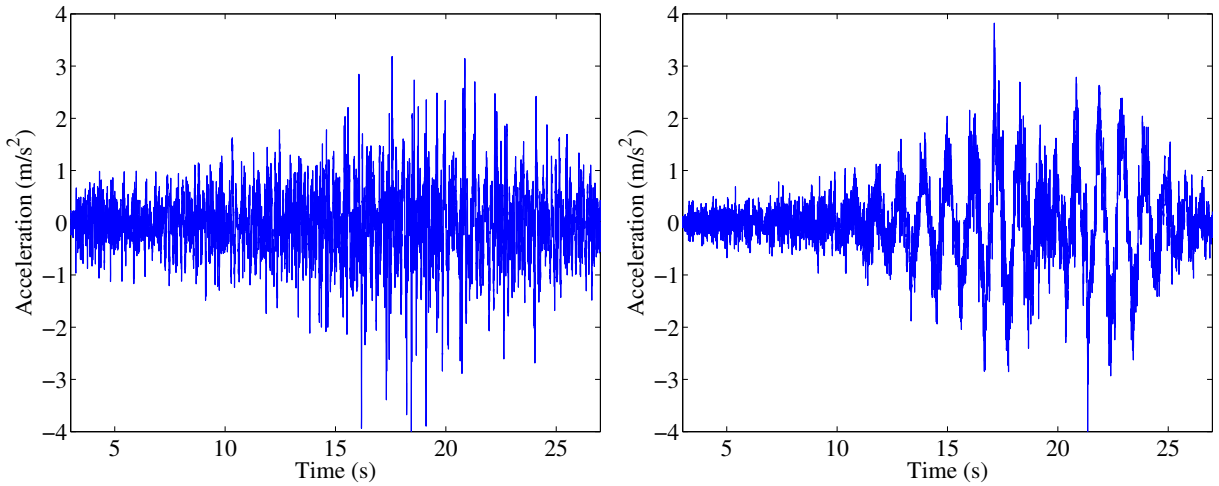

(a) Vertical, 04+Z

(b) Lateral, 05+Y

Figure 4.5: Sample acceleration histories for 1.0 p/m^2 walking, total weight: 20.32 kN, fourteen-bay

where values 1 to n are individual data points in a signal. It is a valuable calculation as it characterises the embedded energy within the signal.

All analyses were completed on all 30 trials of every test. The single pedestrian tests are those noted by the walking pace, the crowd tests by the pedestrian density, the two pedestrian tests by "Sync" and "Async", and the impact tests by "Hammer" and "Lateral". Some tests were not completed for each bridge span (i.e., the 1.5 p/m^2 crowd test was only completed for the two-bay bridge). Figures 4.6 and 4.7 show the mean and standard deviation of the RMS acceleration. Figures 4.8 and 4.9 show the mean and standard deviation of the peak acceleration.

For the single pedestrian, both the RMS and peak accelerations increased with an increase in walking frequency. As the bridge span increased, both the RMS and peak accelerations increased. Given a single walking pace over multiple bridge lengths, the

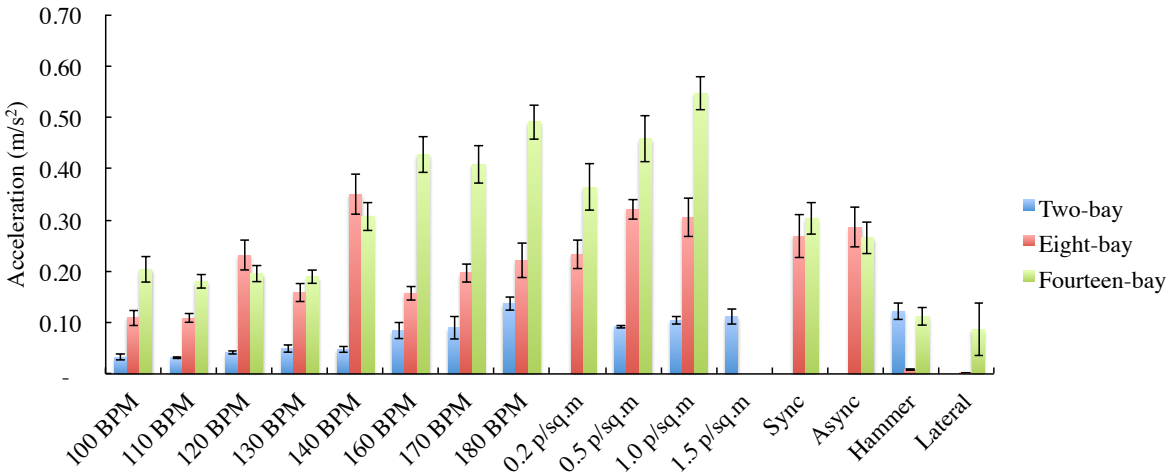

Figure 4.6: RMS acceleration for all bridge spans in vertical direction

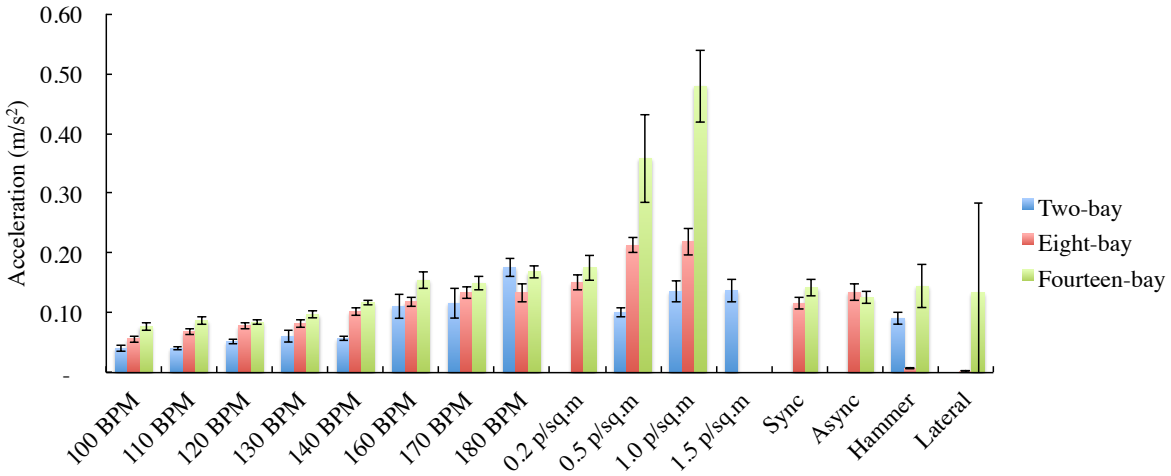

Figure 4.7: RMS acceleration for all bridge spans in lateral direction

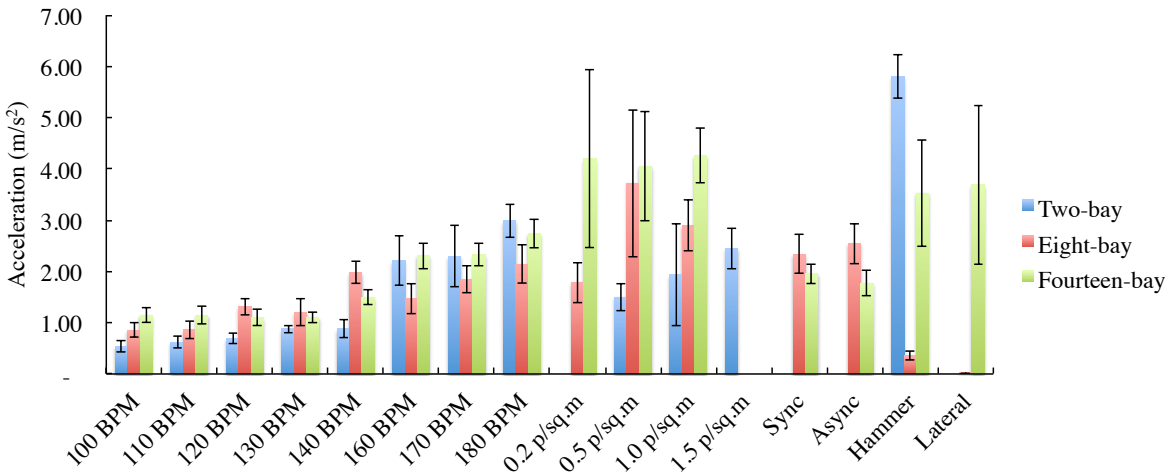

Figure 4.8: Peak acceleration for all bridge spans in vertical direction

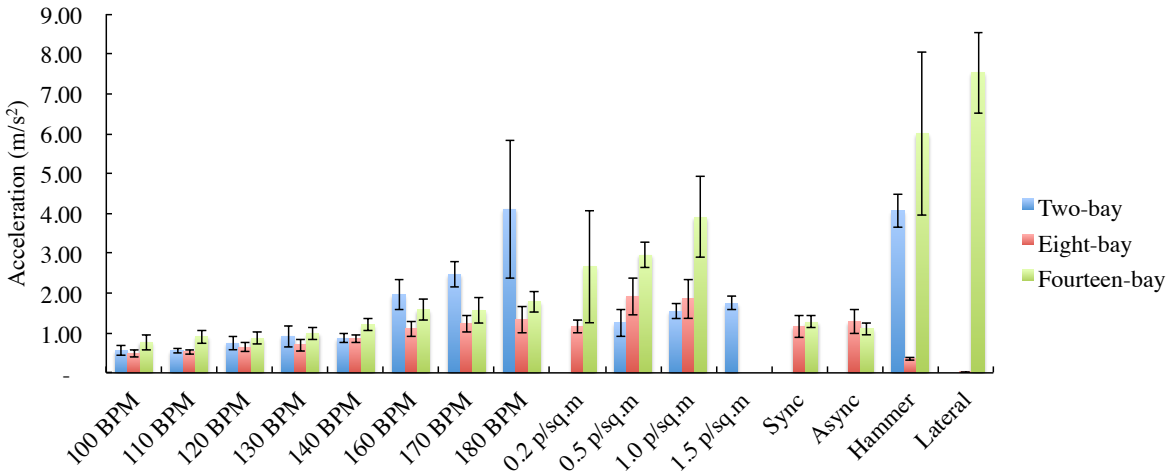

Figure 4.9: Peak acceleration for all bridge spans in lateral direction

imposed frequency will be constant but the amplitude of the vibration increased as the span increases, thus an increase in acceleration.

For the pedestrian crowds on the two-bay and eight-bay bridges, both the RMS and peak accelerations increased with an increase in crowd density. For the fourteen-bay bridge, the RMS accelerations increase with the crowd size but the peak accelerations do not. This could suggest that in the relationship between peak acceleration and the number of pedestrians, $\sqrt{n}$, there is little influence to an increase of crowd size. The energy content of the signal however, characterised by the RMS of the acceleration, continues to increase with increasing crowd size. Similarly to the single pedestrian, as the bridge span increased, the RMS and peak accelerations increased, with the maximum RMS accelerations being for the 1.0 p/m^2 crowd test and the 180 BPM running test. The increase in crowd density on the fourteen-bay bridge does not exhibit the typical relationship of the vertical acceleration being double of the lateral acceleration. This is likely due to the fact that the natural frequency of the structure with the weight of the pedestrians is within lateral resonance range of pedestrian walking paces.

4.2 Load cell results

Load cell data were typically recorded at 500 Hz sampling frequency with the exception of single pedestrian tests on the two-bay and eight-bay bridges. Walking the length of the bridge elapsed quickly for these specimens, thus the sampling frequency was increased to 1000 Hz to obtain a longer data set. Though not covered in the scope of this thesis, frequency analysis of the load cell data will be completed. For adequate resolution and frequency range, the sampling frequency was at least double of the maximum desired frequency attainable. This is due to the Nyquist value of 2, mentioned in the accelerometer

results section.

All load cell plots are the combination of all four units, thus showing the total load of the bridge and pedestrian(s). In the following sections, sample plots are given to illustrate the results of the load measurements, the remaining of which can be found in Appendix B. Sample plots are consistent with those from the acceleration results.

4.2.1 Single pedestrian results

Figure 4.10 shows the load results from a pedestrian walking at 120 BPM on the fourteen-bay bridge. Figure 4.11 shows the load from the same pedestrian running on the same bridge at 180 BPM.

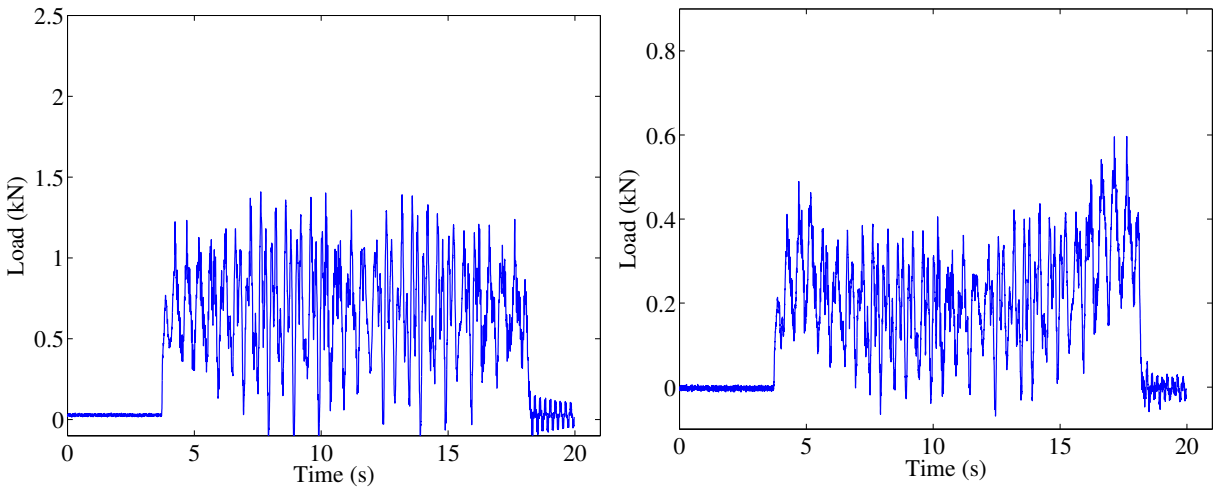

(a) Vertical

(b) Lateral

Figure 4.10: Sample load histories for single person walking at a pace of 120 BPM, weight: 0.65 kN, leg length: 0.95 m, fourteen-bay

As the pace of the pedestrian increases, the time interval between the peaks decreases.

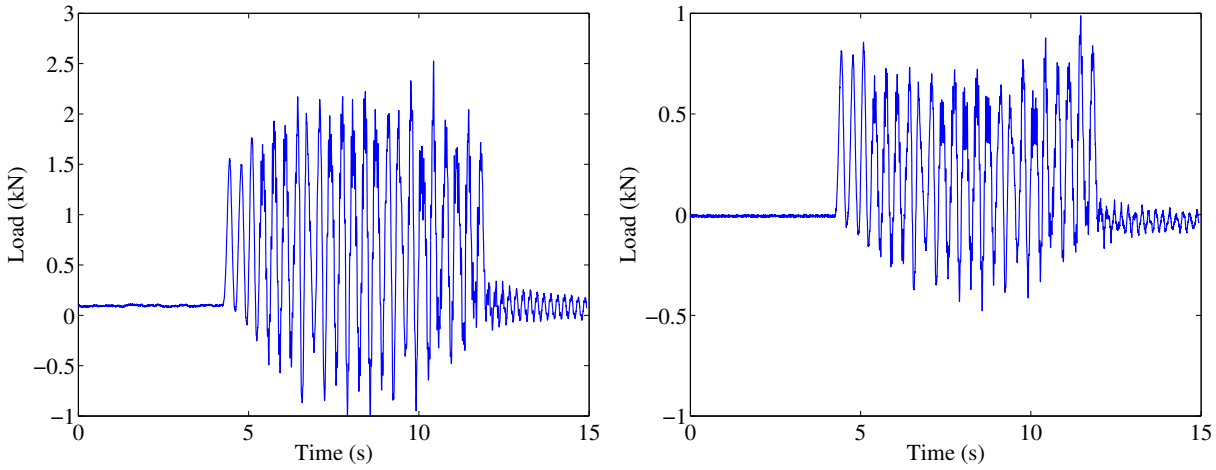

(a) Vertical (b) Lateral

Figure 4.11: Sample load histories for single person running at a pace of 180 BPM, weight: 0.65 kN, leg length: 0.95 m, fourteen-bay

The shape of the peaks changes with the increase in pace due to the biomechanical nature of walking compared to running. The individual impacts from the heel and toe are visible on the 120 BPM test, whereas the running tests show a single impact. The amplitude of oscillation increases greatly with the increase in pace where they oscillate about the mean weight of the bridge and the pedestrian. This is still observed in the running tests, but is categorically different since the pedestrian is airborne while transitioning between feet.

Additionally, Figures 4.10 and 4.11 show that the vertical load is greater than the lateral load. The plots were zeroed at the weight of the bridge, thus the negative load is the effect of the high amplitude from the walking load. From literature, a pedestrian will produce a lateral force 10% of their body weight (69). This was completed on a stiff structure, however, and thus more closely resembles the load results from the two-bay bridge in Appendix B. The eight-bay and fourteen-bay were more flexible structures, and

thus the lateral load was closer to 0.3 of the vertical load. The results from the two-bay bridge were expected to resemble that of the literature and were met. It was also expected that the longer spans would behave uniquely, though the lateral load contribution was not predicted, to the two-bay bridge since their first lateral frequencies are much closer to pedestrian walking paces.

As bridge span increased the peak load above the weight of the pedestrian and the bridge, given the same walking pace, also increased. The peak load, given a particular walking frequency, increased with longer bridge spans, as seen in Appendix B.

4.2.2 Pedestrian crowd results

For the purposes of discussion on load results of pedestrian crowds, the fourteen-bay specimens with crowd densities of 0.5 p/m^2 and 1.0 p/m^2. Figure 4.12 shows the load results for a crowd of 0.5 p/m^2. Figure 4.13 shows the load results for a crowd of 1.0 p/m^2.

Peak load remains approximately constant over the various crowd density tests. The spacing between the peaks is uneven due to the various walking paces of the pedestrians. The load data, however, follows an overall trend of ramping up and then ramping down of the load with the oscillations superimposed. With smaller pedestrian crowds, the presence of each individual can be observed. Again, a ratio of the lateral load to the vertical load of approximately 0.3 can be observed for the crowd loading tests.

4.2.3 Peak load results

All analyses were completed on all 30 trials of every test. The single pedestrian tests are those noted by the walking pace, the crowd tests by the pedestrian density, the two

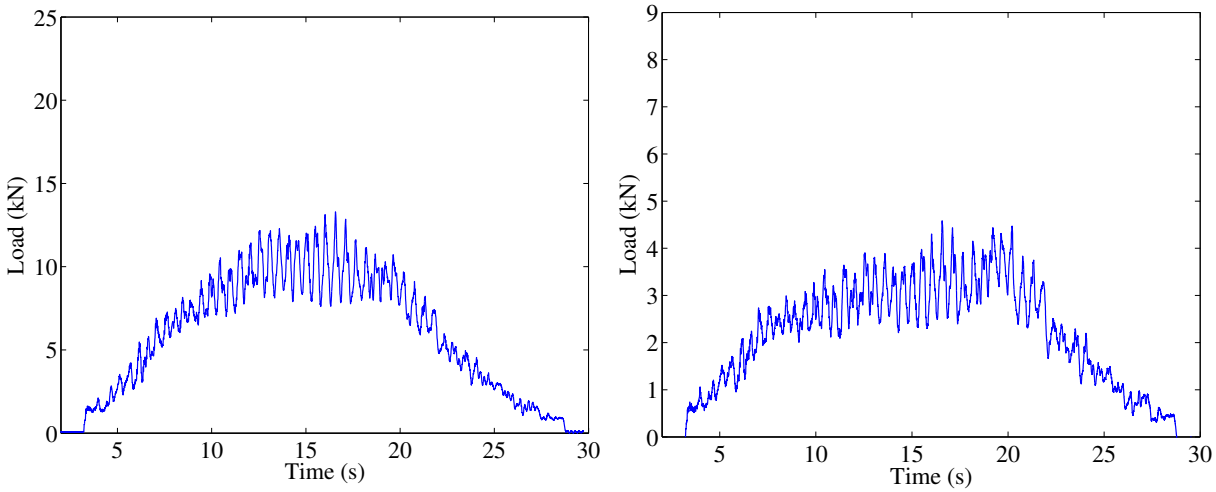

(a) Vertical

(b) Lateral

Figure 4.12: Sample load histories for 0.5 p/m^2 walking, total weight: 9.66 kN, fourteen-bay

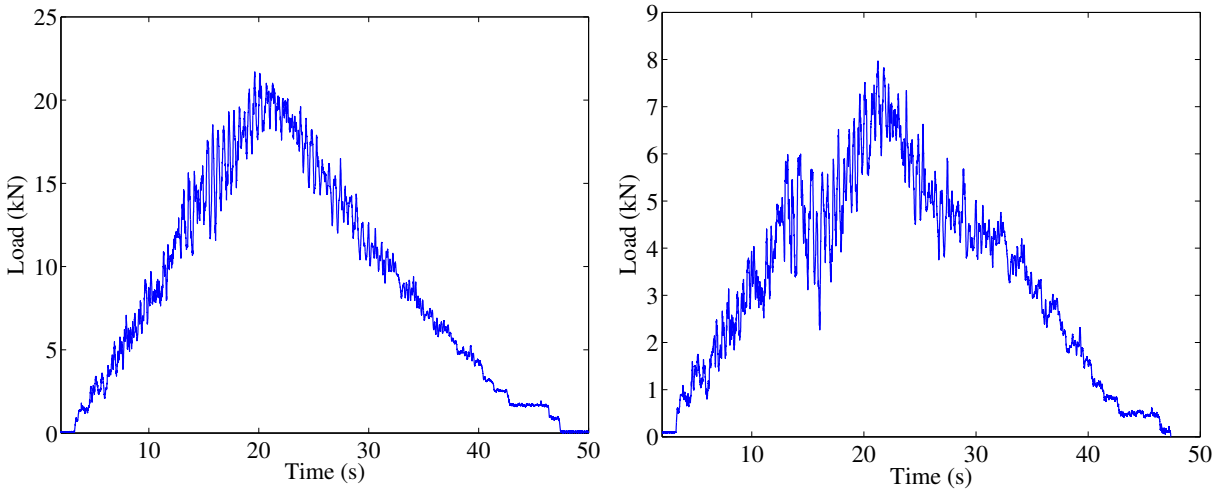

(a) Vertical

(b) Lateral

Figure 4.13: Sample load histories for 1.0 p/m^2 walking, total weight: 20.32 kN, fourteen-bay

pedestrian tests by "Sync" and "Async". Some tests were not completed for each bridge span (i.e., only the two-bay bridge tested 1.5 p/m^2). Figures 4.14 and 4.15 show the mean and standard deviation of the peak load.

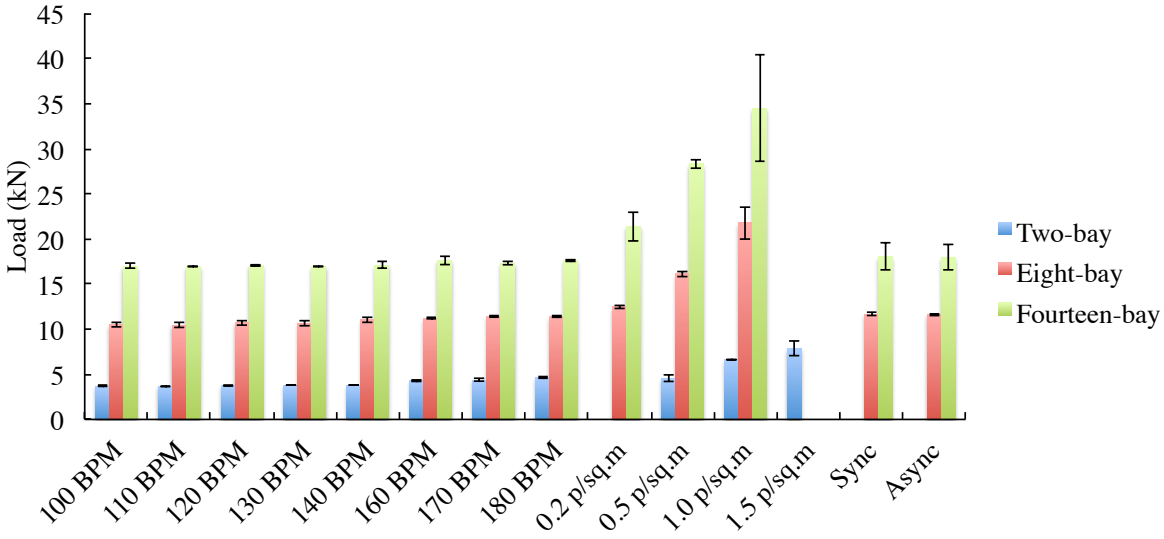

Figure 4.14: Peak load for all bridge spans in vertical direction

The lateral load for the two-bay and eight-bay bridges are very similar throughout the single pedestrian tests whereas the laterally-sensitive fourteen-bay bridge registers a greater load. This was expected given visual inspection during testing and that the fourteen-bay bridge with the largest crowd weighed enough to be in the lateral resonance range of pedestrian walking paces. As the walking pace increases, the vertical and lateral loads increase. The highest attained loads for every bridge is during the largest crowd test from that bridge (i.e., 1.5 p/m^2 for the two-bay bridge and 1.0 p/m^2 for the eight-bay and fourteen-bay bridges). The two pedestrian tests walking synchronously and asynchronously measure the same load. For the fourteen-bay bridge, the ratio between the peak load and the total load applied by the pedestrians decreased from 1.4 at 0.2 p/m^2 to 0.9 at 1.0 p/m^2.

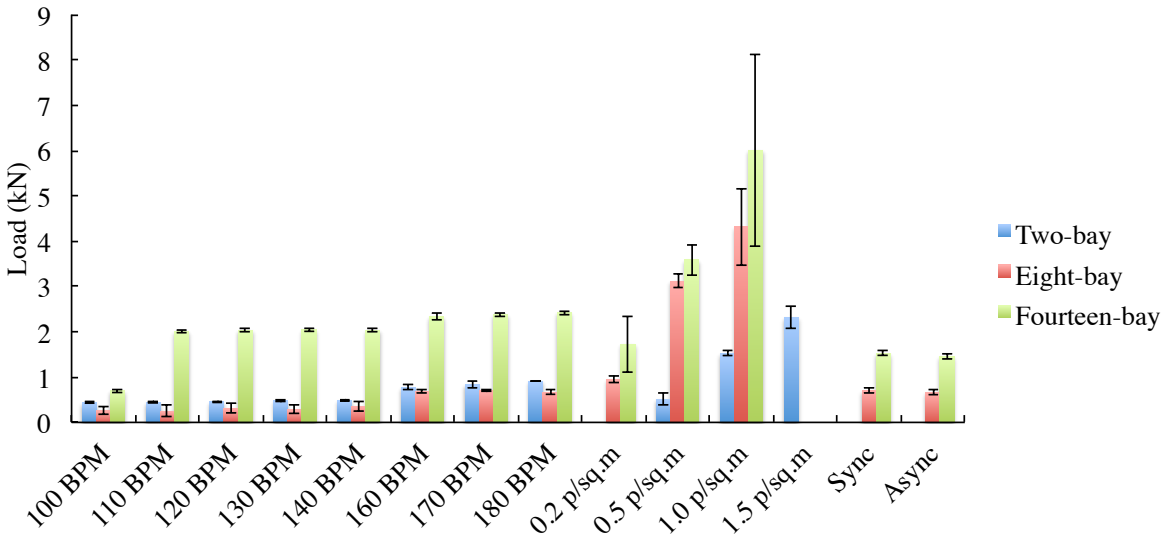

Figure 4.15: Peak load for all bridge spans in lateral direction

4.3 Strain gauge results

Strain gauges were only installed on the eight-bay and fourteen-bay bridges since the these two specimens demonstrated observable movement during testing. Only three strain gauges, two on the bottom chord and the top face of the diagonal, were active during the tests on the eight-bay bridge. Results were processed with a low-pass filter at 10 Hz, which is well above the walking frequencies and first natural frequencies of the bridge. The purpose of the strain data are for future fatigue work on aluminium structures.

In the following subsections, sample strain results were plotted for the eight-bay and fourteen-bay bridge configurations. Results are plotted as axial and bending strains for each member on each test. Axial strain is:

$$\epsilon_{axial} = \frac{\epsilon_{top} + \epsilon_{bottom}}{2} \tag{4.2}$$

and the bending strain is:

$$\epsilon_{bending} = \frac{\epsilon_{top} - \epsilon_{bottom}}{2} \tag{4.3}$$

It is important to note that the bottom chord is part of a truss, where the centre of gravity is above the bottom chord, putting both faces of the bottom chord in tension. The bending strain recorded here is the bending within the element, and the axial strain is a measure of the structure's overall bending strain.

In the following sections, sample plots are given to illustrate the results of the accelerometer measurements, the remaining of which can be found in Appendix C.

4.3.1 Single pedestrian results

For the purposes of discussion on strain results of a single pedestrian, the fourteen-bay specimens with pedestrians walking at 120 BPM and running at 180 BPM will be referenced. Figure 4.16 shows the strain results from a pedestrian walking at 120 BPM on the fourteen-bay bridge. Figure 4.17 shows the strain results from a pedestrian walking at 180 BPM on the fourteen-bay bridge.

For the single pedestrian walking frequencies, as seen for the 120 BPM and 180 BPM tests, there is negligible bending strain in the diagonal and minimal bending strain in the bottom chord. Axial strain is the predominant measurement, with the strain in the bottom chord consistently greater than the strain in the diagonal. These results were expected since the diagonals, top chords, and bottom chords form a truss and the bottom chord in a simply supported truss would be taking tension. Since the pedestrian walks from one end of the bridge to the other, the strain in the diagonal is greater when the pedestrian is closest to the strain gauge and decreases as the pedestrian walks away.

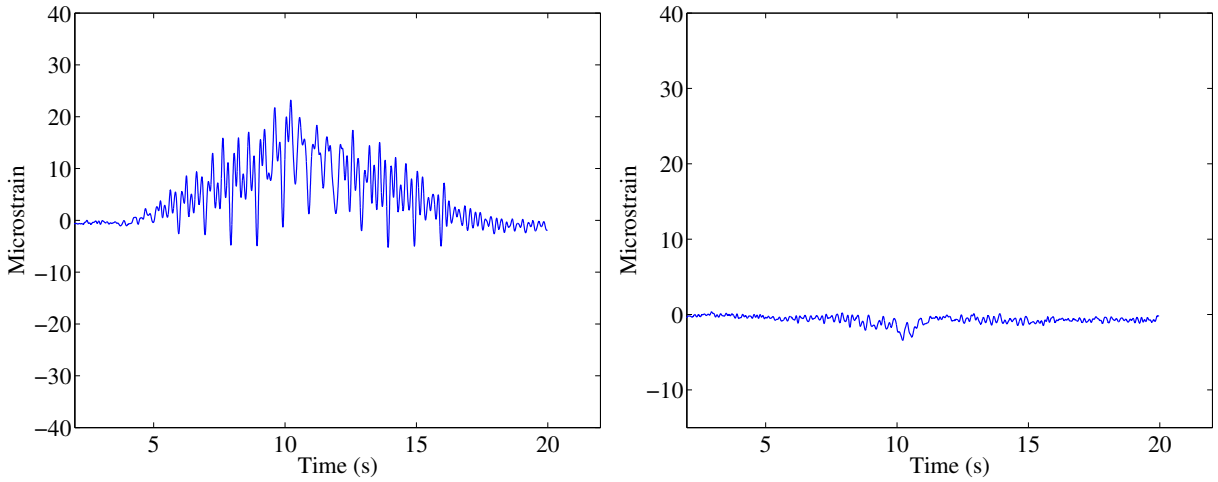

(a) Bottom chord axial

(b) Bottom chord bending

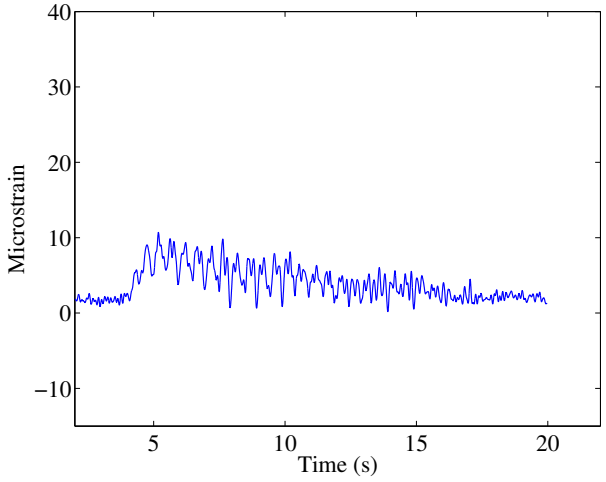

(c) Diagonal axial

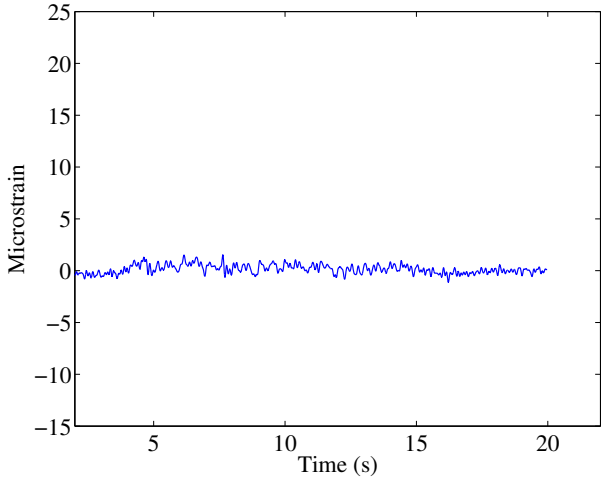

(d) Diagonal bending

Figure 4.16: Sample strain histories for single person walking at a pace of 120 BPM, weight: 0.65 kN, leg length: 0.95 m

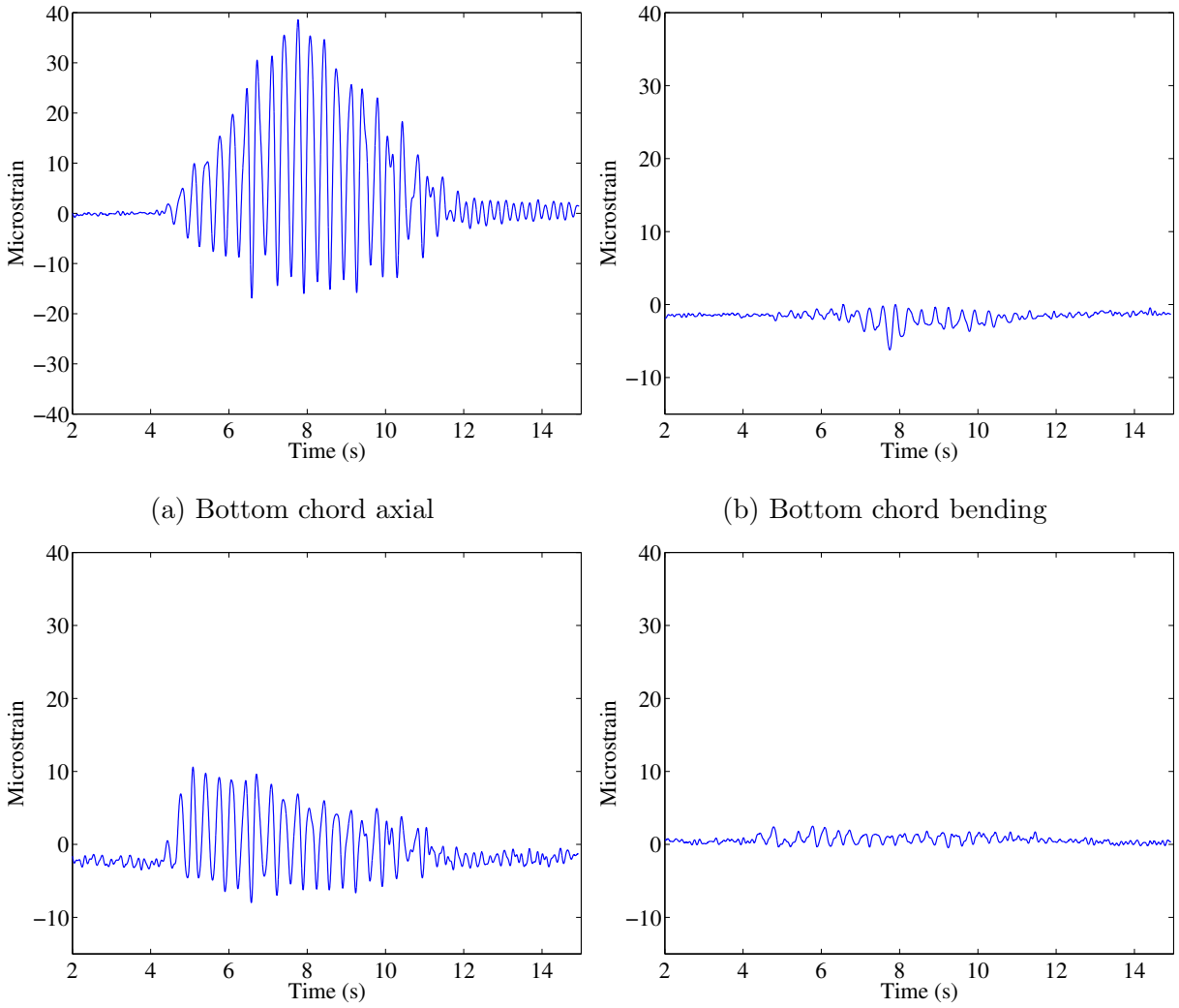

(a) Bottom chord axial

(b) Bottom chord bending

(c) Diagonal axial

(d) Diagonal bending

Figure 4.17: Sample strain histories for single person walking at a pace of 180 BPM, weight: 0.65 kN, leg length: 0.95 m

The same ramp up and ramp down trend that was noticed on the load cell plots can be seen on the 120 BPM strain data. However, strain data from the 180 BPM test oscillates about zero.

4.3.2 Pedestrian crowd results

Figure 4.18 shows the strain results for a crowd of 0.2 p/m^2. Of the fourteen-bay bridge pedestrian crowd tests, the 0.2 p/m^2 was the only set of tests that did not reach the voltage limits on the amplifier for the strain gauges on the diagonal. The plots of the other crowd densities are available in Appendix C, however future work on these specimens will require re-calibration of the voltage amplification.

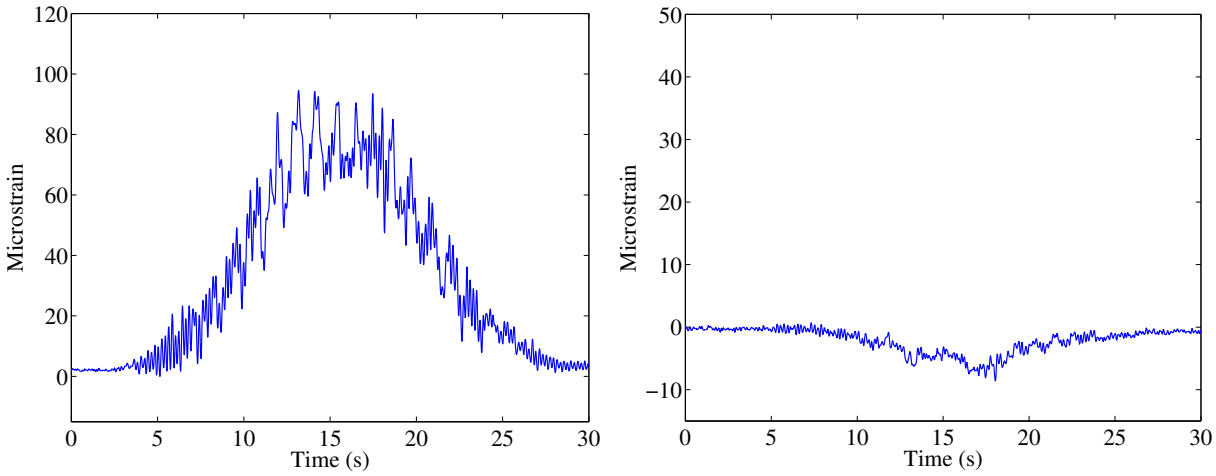

(a) Bottom chord axial

(b) Bottom chord bending

4.3.3 Peak strain results

Tables 4.1 and 4.2 summarise the peak strains for the eight-bay and fourteen-bay specimens. Since only the bottom-face strain gauge was active for the eight-bay bridge tests, neither

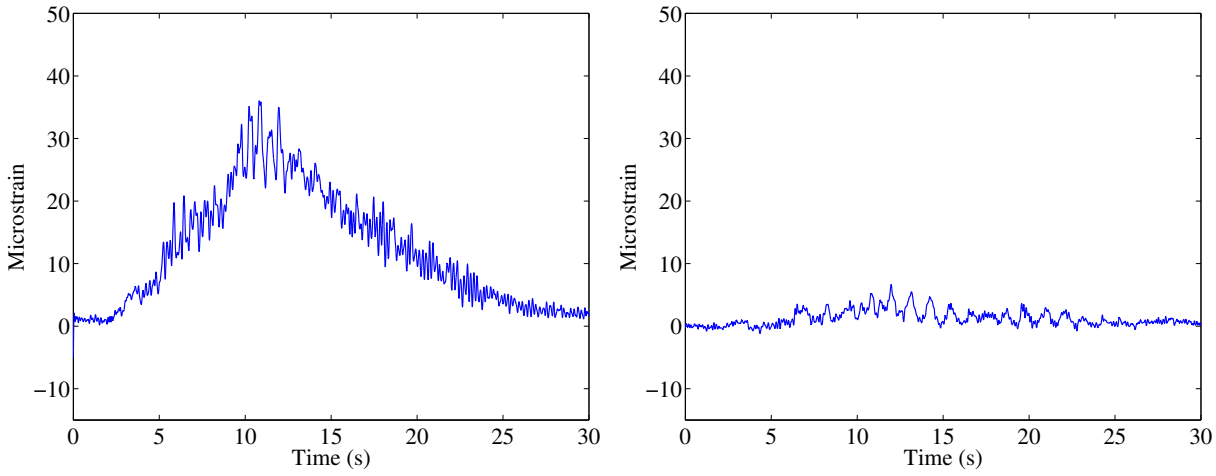

(c) Diagonal axial

(d) Diagonal bending

Figure 4.18: Sample strain histories for 0.2 p/m^2 walking, total weight: 4.27 kN

the axial nor bending strain could be calculated. Since the bending strain of the bottom chord is very low in comparison to its axial strain, the structure nearly behaves as an ideal truss.

Strains for the eight-bay bridge were greater than the fourteen-bay bridge for the single pedestrian tests, which was not expected. The two pedestrian tests walking synchronously and asynchronously yielded very similar peak strain results for the eight-bay and fourteen-bay bridges. Additionally, longer bridge spans result in larger member forces and thus larger strain values are possible for the crowd loading. As per the load and acceleration values for the eight-bay bridge, the strain values are greater for walking frequencies that coincide with the structure's natural frequencies.

The axial and bending strains in the diagonals of the fourteen-bay bridge, however, cannot be properly analysed for the 0.5 p/m^2 or 1.0 p/m^2 crowd densities since the strain gauges were not electrically calibrated on the amplifier to read such large strain values.

Table 4.1: Eight-bay bridge strain peak

Test	Bottom chord				Diagonal	
	Axial (10^{-6})		Bend (10^{-6})		Bottom (10^{-6})	
	μ	σ	μ	σ	μ	σ
100 BPM	31.14	12.31	3.93	1.05	13.70	5.04
110 BPM	30.54	11.15	3.66	0.89	13.78	4.60
120 BPM	33.83	9.54	3.87	1.24	14.61	3.91
130 BPM	33.06	9.68	4.28	1.11	14.30	3.98
140 BPM	30.01	10.46	4.23	1.18	12.81	4.26
160 BPM	41.09	11.44	6.86	1.99	20.15	5.47
170 BPM	38.86	9.66	7.56	1.67	16.92	3.65
180 BPM	37.23	12.42	6.96	1.86	17.37	5.12
0.2 p/m^2	35.96	9.83	6.54	1.62	17.55	4.76
0.5 p/m^2	64.56	16.87	10.41	0.89	33.20	7.72
1.0 p/m^2	89.58	20.12	19.61	5.12	47.35	10.59
Sync	33.86	10.29	5.15	1.40	14.97	4.24
Async	34.65	10.26	4.73	1.42	16.13	4.32

Other than these anomalies in the highest crowd density tests, in most cases the bottom chord exhibits higher strains in the faster walking paces and in the diagonal in the lower walking paces. Faster walking paces incur a higher intensity of impact, imposing a "bouncing" effect to the bridge. The bottom chord at midspan could be more sensitive to this movement since it is a longer element and not as well braced at the diagonal.

Since the yield stress of the T-6061 aluminium alloy is 241 MPa, Hooke's Law can be

Table 4.2: Fourteen-bay bridge strain peak

Test	Bottom chord				Diagonal			
	Axial (10^{-6})		Bend (10^{-6})		Axial (10^{-6})		Bend(10^{-6})	
	μ	σ	μ	σ	μ	σ	μ	σ
100 BPM	10.47	2.71	2.13	0.59	26.26	2.18	3.29	0.37
110 BPM	11.58	3.42	2.37	0.54	25.62	2.05	3.54	0.50
120 BPM	11.85	6.50	3.49	8.25	29.33	2.45	3.92	0.48
130 BPM	12.82	3.53	2.49	0.54	30.33	3.44	3.86	0.45
140 BPM	12.20	3.94	3.22	1.46	34.61	4.46	3.89	0.78
160 BPM	20.96	4.32	3.52	0.96	59.72	5.92	5.91	2.09
170 BPM	18.18	3.18	3.42	0.86	53.92	5.22	5.38	0.94
180 BPM	18.85	4.64	3.91	1.14	55.13	4.98	5.65	0.64
0.2 p/m2	90.97	26.03	33.18	1.19	25.08	5.44	12.29	9.02
0.5 p/m2	145.19	33.48	75.16	2.03	-	-	-	-
1.0 p/m2	282.91	95.70	80.78	12.31	-	-	-	-
Sync	30.73	2.61	31.08	0.44	35.48	2.19	9.40	0.73
Async	27.42	1.77	31.55	0.52	34.43	2.33	9.01	0.54

used to determine yield strain:

$$\epsilon = \frac{\sigma}{E} \tag{4.4}$$

where ϵ is strain and σ is axial stress. Equations 4.2 and 4.3 were used. The yield stress of aluminium is 3460 microstrain, 3.46x10^{-3} m/m. The axial and bending stresses in both bridge specimens for the single and two pedestrian tests were well within the elastic region of aluminium. The crowd tests induce larger stresses, most notably on the fourteen-bay bridge.

Bending strains on the fourteen-bay bridge reach a peak of approximately 81 microstrain on the bottom chord. Axial strains on the fourteen-bay bridge reach a peak of approximately 283 microstrain on the bottom chord.

4.4 Displacement results

Three types of displacements were calculated amongst the bridge specimens: self-weight deflection, lateral displacement from tests, and vertical deflection due to a 700 N person at midspan. Self-weight displacements were not measured for the two-bay bridge since little or no movement was perceived by pedestrians. Midspan self-weight deflection was noticed on the eight-bay and fourteen-bay bridges. Using high-precision digital civil surveying equipment, the midspan deflection was 8 mm for the eight-bay bridge, and 69 mm for the fourteen-bay bridge. The deflection of the fourteen-bay bridge was confirmed by stretching a piece of piano wire horizontally from each end of the bridge and measuring the deflection from the wire to the bridge at midspan.

Since lateral displacements on the fourteen-bay bridge were significant during the $1.0p/m^2$ density tests, a marker was held over a board clamped to the midspan of the bridge to mark the lateral deflection. The peak-to-peak displacement of the bridge was a maximum of 120 mm. This large lateral movement led to an investigation of how horizontal bracing under the deck would affect the amplitude of vibration. The lateral deflection was measured during the lateral pulley release test, 32 mm, as a repeatable and predictable source for later comparison.

The vertical deflections under a static 700 N pedestrian at midspan were 0.40 mm, 0.50 mm, and 1.27 mm for the two-bay, eight-bay, and the fourteen-bay bridge respectively.

The fourteen-bay bridge deflection had a standard deviation of 0.05 mm, the other two specimens had a standard deviation of zero over three trials.

4.5 Summary

The overall trends from these experiments on the three full-scale pedestrians bridges with regards to the acceleration, load, and strain data were; all increase with increasing walking pace; all increase with an increased crowd density, most increased as bridge span increased, and lateral data were most often less than the vertical (with the exception of the fourteen-bay bridge under large crowd loading). Strain data for single pedestrians walking did not increase with increased bridge span. These results were expected since eight-bay and fourteen-bay bridges compared to the two-bay bridge are significantly longer with higher member forces and thus be more responsive to pedestrian loading. Another trend is that the two-bay bridge and the eight-bay bridge behave more similarly than the eight-bay bridge and the fourteen-bay bridge. Given the results of the finite element analysis of these specimens, this was expected. The shortest bridge span does not exhibit typical bridge behaviour since the short chords were very rigid. Construction of more bridge specimens was not possible for the timeframe of this thesis, but a parametrisation of bridge span between the eight and fourteen bays would determine the point at which lateral-sensitivity develops. In the next chapter, these data are used to assess the results of the finite element models that were built, extract the natural frequencies and damping ratio from the acceleration data, and calculate DLFs from the load data. These analysis results are then used to evaluate the bridge specimen's performance using dynamic design codes and to propose a preliminary damper design for the fourteen-bay bridge.

Chapter 5

Analysis

5.1 Finite element analysis

5.1.1 Model setup

Overview

A finite element model of each bridge was constructed to fulfill three purposes:

- to ensure satisfactory static design,
- to predict the fundamental modes in a bridge for optimal sensor placement, and
- to validate the model using the measured data.

Even though similar checks were completed at the design stage of the Make-A-Bridge, simple element yielding and maximum deflection checks were made possible with the model

based on the design drawings. In addition to modelling the unloaded static structure, the design weight of 700 N for a single pedestrian was applied at the midspan along the deck. This was to check the model behaviour compared to dynamic design checks from CSA S6-06 (27). Using the highest crowd density from HIVOSS, the bridge was checked for strength and stiffness to ensure the structure remained elastic under service loads. The fourteen-bay bridge is compared to the Ultimate Limit State (ULS) of CSA S6-06.

Placement of the accelerometers determined which natural frequencies are captured based on their mode shapes. A vertical sensor at the midspan, for example, will experience little to no excitation from the second vertical mode since the midspan is stationary for this mode. However, a vertical sensor at the quarter span, $L/4$, of the bridge, will experience partial excitation from the first mode and the maximum amplitude of the second mode. The finite element model —through an eigenvalue analysis —identifies all modes of vibration, from which the optimal sensor arrangement can be designed to capture excitation from the fundamental modes. Pony truss bridges have an open cross section shape, which will permit localised modes.

Upon completion of signal processing of the measured data, the accelerometer results can be compared to the predicted values from the finite element model. Discrepancies between the measurement data and the model can be due to idealised model assumptions, connectivity of the members, or structural behaviour not present in the simplified model. Due to the symmetry and constant cross section of this pony-truss bridge, in conjunction with ideal symmetric and anti-symmetric mode shapes, it was determined that sensors should be placed at $L/4$ and $L/2$.

Despite only building full-scale structures for the two-bay, eight-bay and fourteen-bay bridges, finite element models were built of all possible lengths from two bays to fifteen bays, in increment lengths of one bay. The construction methodology was extrapolated to

bridge lengths of up to twenty bays. Breaks in the elements were inserted in the model where the splice joints occur on the full-scale bridges to allow for modification of the connectivity properties. The following sections outline the material, cross-section, and connection properties of the finite element models.

Model inputs

The finite element models were constructed using the structural analysis software, SOFiSTiK FEA 2013 (82), which includes structural design and modal analysis capabilities. The assumed properties of T6061 aluminium include a specific weight of 26.6 kN/m^3, and Young's modulus of 69637 MPa. All sections in the models were simulated as frame elements, capable of resisting axial and bending forces. No damping was explicitly entered into the computer model.

Definition of the cross sections, with exception to the bottom chord and the longitudinal deck stringers, had to be simplified due to the complexity of the cross-section shapes of the extruded aluminium members. The tubular extruded sections of the bridge, diagonal and transversal, were modelled as tube cross sections with a wall thickness to reflect the true cross-sectional area of these members. The top chord was modelled as a rectangular section of the same dimensions as the true section with an equivalent wall thickness. Since modal analysis of structures often leads to inaccurate estimate when connecting plate or shell elements to frame elements, the deck was not directly modelled. Instead, the weight of the deck was incorporated into the bottom chord, transversals, and stringers as an increase in material density. Since the deck was only attached to the transversals through a set of U-bolts, it was determined that the deck does not provide significant lateral stiffness to the structure.

In addition to these section property definitions, an additional fictitious member was created to model a stationary 700 N pedestrian at the midspan. The weight was modelled by modifying the material density of this member so that the overall weight of the structure increased by 700 N. Since the closest element to the midspan changes depending on whether the bridge has an even or odd number of bays, the pedestrian load was modelled on the midspan transveral for even-numbered bay bridges, and on the midspan stringer for odd-numbered bay bridges. This method was used instead of modelling a point load as to ensure that the mass of the pedestrian was included in the modal analysis, rather than just an excitation force.

Connectivity

The Make-A-Bridge product employs bolted rather than welded member connections. Welding around an entire joint can be considered a fully moment-restrained connection, however bolted connections can experience minor slip and rotation. Based on the construction of the bridge specimens, the following end releases in the global coordinate system were implemented for the model to more accurately predict the structural response:

1. moment about y and z axis released (lateral and vertical), allowing free rotation about the x axis for the connection of the ends of the top chord to the vertically-aligned diagonal members,

2. moment about y axis released (lateral), allowing free rotation in the vertical (x-z) plane, at the splice locations on the top chord,

3. moment about y axis released (lateral), allowing free rotation in the vertical (x-z) plane, for the connection of the diagonals into the top chord, and

4. moment about z axis released (vertical), allowing free rotation in the horizontal (x-y) plane, for the connection of the transversals to the stringers.

Figure 5.1 locates the joint releases in the finite element models.

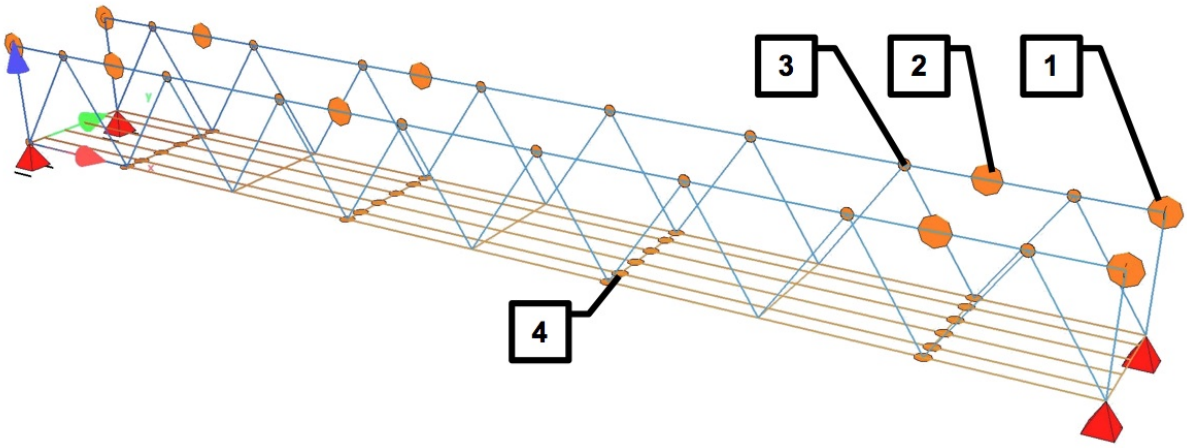

Figure 5.1: Joint releases of the finite element model to simulate bolted connections

The first type of release originates from the diagonals being connected inside the top chord with a single bolt, which is an ideal manifestation of a pin-connected joint. The second type of release accounts for the possible movement of the U-bolts along the transversal. Additionally, movement that was not modelled was the possible moment release of the diagonals and the transverse members within the cast joints due to the neoprene sleeves. Not only could this have allowed for movement but may have affected the damping ratio of the bridge specimens.

5.1.2 Modal analysis results

Eigenvalue, or modal, analysis is a mathematical method to solve for the natural frequencies, damping ratio, and mode shape for multi-degree of freedom system. The equations

that explain the motion of each mass are linearized and solved using linear algebra. The active participating mass is the percent mass of the structure that is contributing to a particular mode.

Modal analysis results from finite-element models provide all possible modes of vibration (number equal to the degrees-of-freedom). However, only a fraction of these modes can be measured using sensors, due in part to sensor placement and low energy associated with many higher modes. Tables 5.1 summarises the vibration modes predicted by the finite element models of the two-bay, eight-bay, and fourteen-bay bridges. Modal mass per mode is reported as a mass fraction of the bridge that is actively engaged in that mode.

Figures 5.2, 5.3, and 5.4 show the finite element analysis of the first mode for each bridge specimen. All remaining figures of the finite element modal analysis are provided in Appendix D. Note that the magnitude of the member forces are indicated by the colour gradient, where blue is the minimum and red is the maximum.

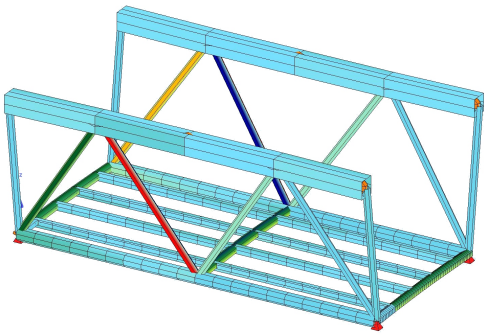

Figure 5.2: First mode from two-bay bridge FE model: 7.6 Hz

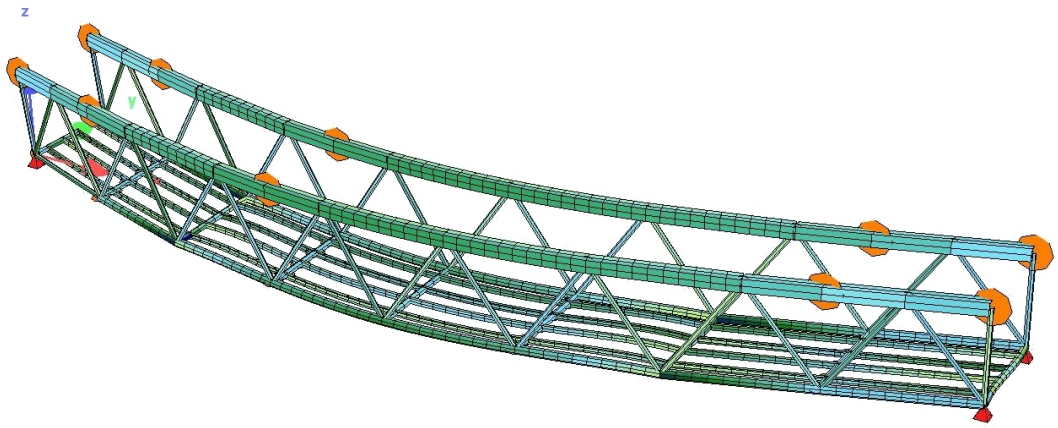

Figure 5.3: First mode from eight-bay bridge FE model: 2.3 Hz

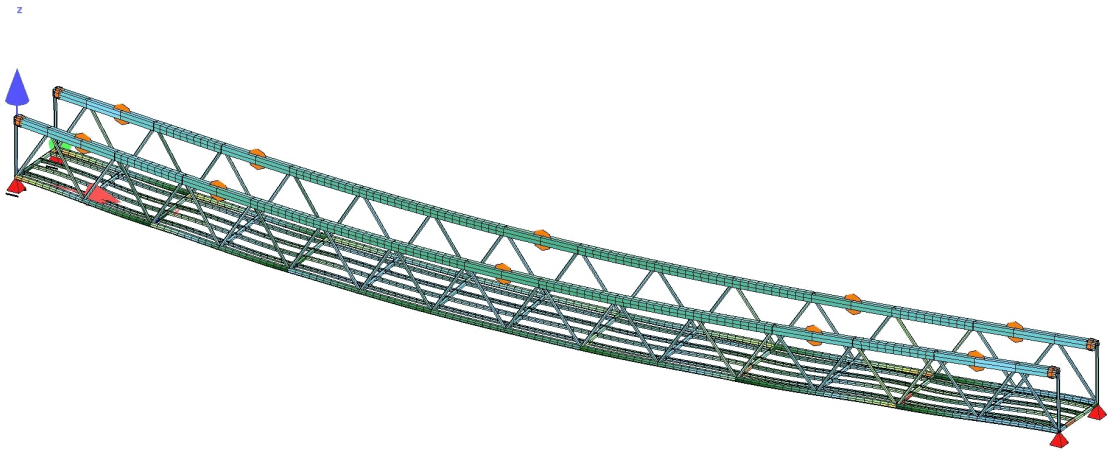

Figure 5.4: First mode from fourteen-bay bridge FE model: 0.9 Hz

Table 5.1: Finite element results for two-bay, eight-bay, and fourteen-bay bridges

Two-bay bridge		Eight-bay bridge		Fourteen-bay bridge	
f_n (Hz)	Modal mass (%)	f_n (Hz)	Modal mass(%)	f_n (Hz)	Modal mass (%)
7.6	18.1	2.3	48.7	0.9	46.6
8.1	19.7	6.1	42.3	2.2	49.6
15.4	38.7	8.1	19.5	3.9	43.6
17.9	11.4	9.8	24.6	5.1	43.7
18.6	10.4	11.0	41.6	5.8	12.9
31.7	30.1	11.8	9.5	5.8	40.7
34.1	8.9	14.3	9.2	7.8	34.1
37.9	8.2	15.8	7.0	7.9	12.0
40.5	23.1	16.9	31.8	9.4	9.4
44.1	10.7	18.0	7.2	9.8	27.6
44.1	10.2	19.9	27.7	11.2	10.6
50.1	16.2	23.3	27.9	12.0	5.1
59.9	28.4	24.0	6.1	12.2	13.9
88.1	29.9	24.7	32.1	12.4	7.9
109.5	10.3	26.5	6.3	14.5	13.6
119.3	6.0	31.3	41.3	14.7	4.4
138.5	16.5	32.1	24.8	15.3	16.1
138.5	9.7	37.2	37.3	15.6	8.3
161.4	21.5	38.6	9.3	17.3	6.4
180.9	19.4	38.9	24.4	17.4	3.9

Appendix D contains images of the resulting mode shapes from each of the natural

frequencies in Table 5.1. From these mode shapes, the first few modes of each direction of movement, vertical, lateral, and torsional, can be identified visually. Several of the modes solved by the finite element software will either be local modes or coupled modes introducing vibration in multiple planes. Table 5.2 summarises the significant mode shapes for each bridge specimen.

Table 5.2: Significant modes for two-bay, eight-bay, and fourteen-bay bridges

Two-bay bridge		Eight-bay bridge		Fourteen-bay bridge	
f_n (Hz)	Mode shape	f_n (Hz)	Mode shape	f_n (Hz)	Mode shape
15.4	1st lateral	2.3	1st lateral	0.9	1st lateral
40.5	1st vertical	6.1	2nd lateral	2.2	2nd lateral
109.5	1st torsional	16.9	1st vertical	3.9	3rd lateral
		23.3	1st torsional	5.0	1st vertical
		32.1	2nd vertical	5.8	1st torsional
		47.9	2nd torsional	7.8	4th lateral
				12.0	2nd vertical
				21.9	2nd torsional

The Make-A-Bridge product was specifically fabricated so that various spans from two bays to fifteen bays, in one bay increments, could be built. Due to timing of the project, not all of these spans were built, but all of the finite element models were created. Additionally, specimens with spans up to twenty bays were constructed in the finite element analysis software using the same segment lengths (Figure 5.5).

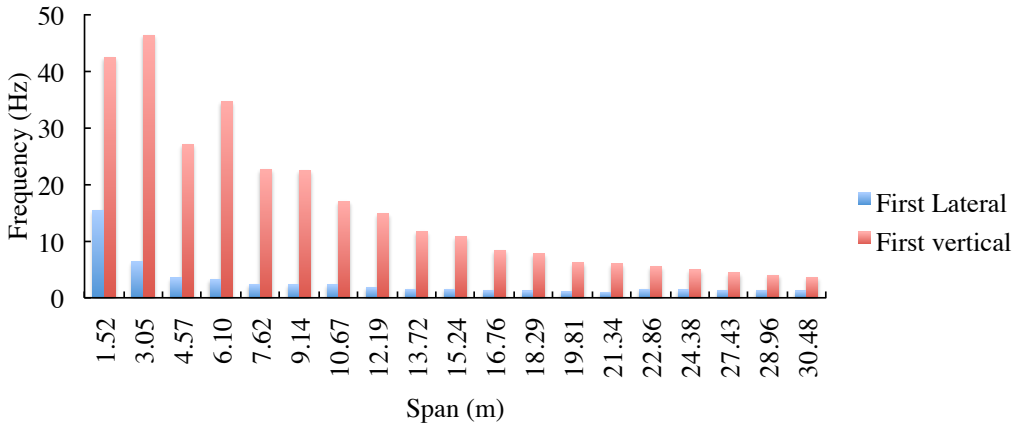

Figure 5.5: First vertical and first lateral natural frequencies from SOFiSTiK finite element model of all bridge spans

5.1.3 Connectivity-sensitivity analysis

Previously, an in-place aluminium bridge in Brossard, Québec, was subjected to dynamic testing and analysis of natural frequencies and modes shapes (87). This was a 44 m span welded aluminium pedestrian pony truss bridge. Due to the welded connections, the finite element model was such that all the members were fixed about each axis. The specimens under investigation were bolted, however, and thus experienced some degree of rotation. With this in mind, the models were assessed to study the effects of connectivity restraints. From this assessment, it was found that the degree of restraint greatly influenced the resulting natural frequencies.

The natural frequencies from the models cannot be compared directly, as the restraints alter the global dynamic behaviour (and hence the resulting modes) of the structure. Instead, the relative error in the fundamental frequency and the last frequency was recorded for each specimen. For each specimen, the global trends of the first few modes will be

discussed.

Table 5.3 shows the first 3 modes and the first vertical modes for the bolted and welded bridge models of the two-bay bridge. For the two-bay bridge, the first natural frequencies were 7.6 Hz and 9.0 Hz for the bolted and welded models respectively. Both of these modes were a combination of vertical and lateral vibrations. The second and third modes in both models are both lateral modes, and the third mode is a weak longitudinal movement within the deck.

Table 5.3: Bolted and welded FE models of two-bay bridge

Mode	Bolted (Hz)	Welded (Hz)
1	7.6	9.0
2	8.1	10.6
3	17.2	21.0
Vertical	40.5	42.0

Table 5.4 shows the first 3 modes and the first vertical mode for the bolted and welded bridge models of the eight-bay bridge. In both of the bolted and welded models, the first natural frequency was a strong lateral mode. The second and third modes resulting from the finite element model were weak lateral and torsional modes respectively.

Table 5.4: Bolted and welded FE models of eight-bay bridge

Mode	Bolted (Hz)	Welded (Hz)
1	2.3	3.5
2	6.1	8.4
3	8.1	9.2
Vertical	16.9	18.2

Table 5.5 shows the first 3 modes and the first vertical mode for the bolted and welded bridge models of the fourteen-bay bridge. Similar to the two-bay and eight-bay bridges, the mode types remain the same whether the bridge is simulated as a bolted or welded structure. The difference, however, is the increase in stiffness that occurs due to the fully moment-connected joints from welding.

Table 5.5: Bolted and welded FE models of fourteen-bay bridge

Mode	Bolted (Hz)	Welded (Hz)
1	0.9	1.7
2	2.2	3.8
3	3.9	6.3
Vertical	5.1	7.6

5.2 System identification

In this section, the signal processing tools investigated in this thesis are discussed, including Fast Fourier Transform (FFT), power spectral density, and second-order blind identification

(SOBI). The FFT allows for maximum extraction of natural frequencies, which is useful for comparison to the finite element model. The power spectral density is a rudementary form of a second order statistical analysis of the signal, which identifies the highest energy mode. Lastly, SOBI is a more complex statistical analysis which can separate multiple natural frequencies based on the quality of the signal and the number of measurements. In this thesis, the power spectral density and SOBI methods are only used for the first natural frequencies in the vertical and lateral directions, where SOBI is then used to extract the damping ratios of those modes.

5.2.1 Fast Fourier Transform

The simplest form of frequency domain analysis is to perform a Fast Fourier Transform on the time-series data collected by the instrumentation. Since the impact loading tests do not impose a forced frequency, peaks in the FFT from these data sets correspond to the natural frequencies of the structure. Figures 5.6, 5.7, and 5.8 show sample FFT plots of both vertical and lateral accelerometers at midspan. Since a direct lateral test was not performed for the two-bay bridge, the lateral data from the hammer test are shown instead.

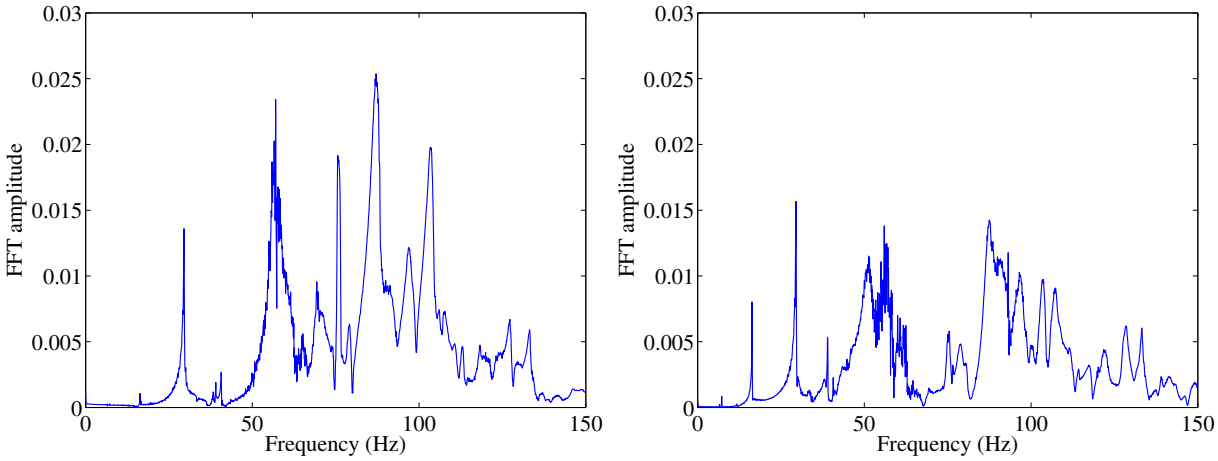

(a) Vertical, 04+Z

(b) Lateral, 05+Y

Figure 5.6: Two-bay bridge FFT from hammer impact test

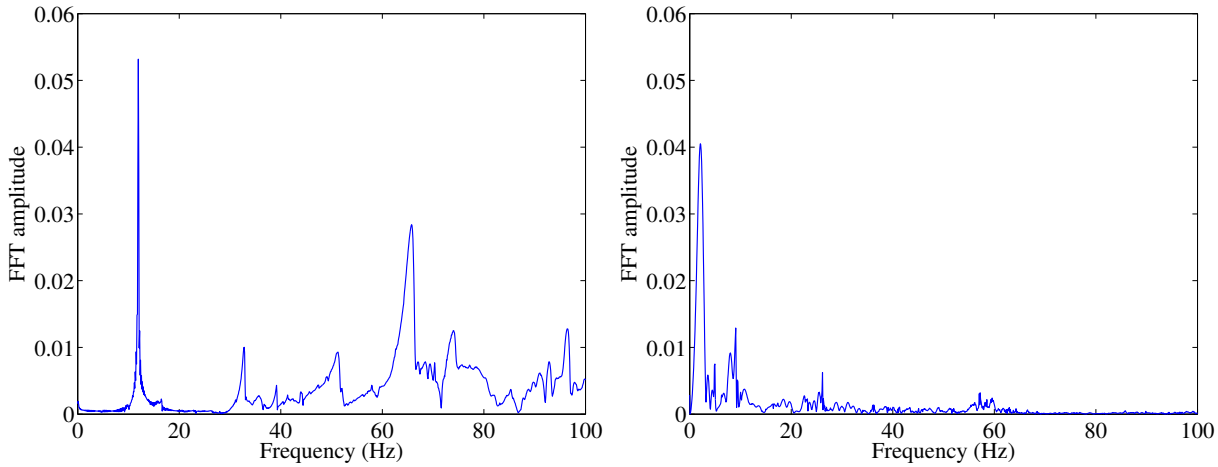

(a) Vertical, 04+Z

(b) Lateral, 05+Y

Figure 5.7: Eight-bay bridge FFT, vertical from hammer impact test and lateral from lateral pulley release test

Table 5.6 shows the mean and standard deviation of the FFT peaks over all of the

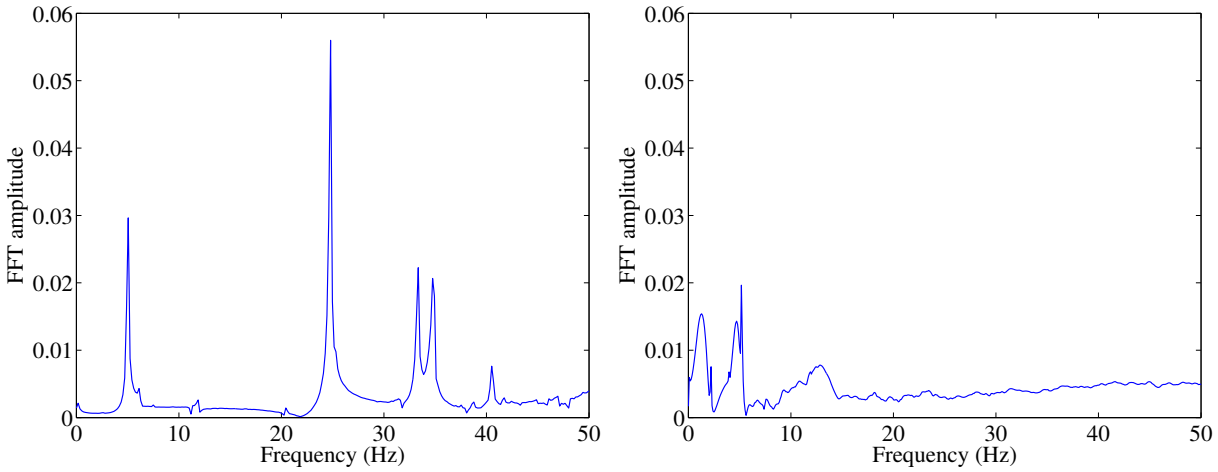

(a) Vertical, 04+Z

(b) Lateral, 05+Y

Figure 5.8: Fourteen-bay bridge FFT, vertical from hammer impact test and lateral from lateral pulley release test

impact tests. Results from both hammer impact and lateral pulley release tests are included in this table.

The FFT of the two-bay bridge contains many closely-spaced frequencies in the higher mode range. The presence of closely-spaced modes presents significant challenges to many signal-processing methods because these techniques rely on well-separated peaks. A trend that emerged in the eight-bay and fourteen-bay bridges in the lateral direction is that the first lateral frequency is a highly damped one (due to a very rounded peak), possibly caused due to slippage between the bridge supports and the underlying support structure. Furthermore, the spacing between the frequency peaks increases, making the process of modal identification (explained later) easier for the longer span.

Table 5.6: FFT natural frequencies from bridge specimens

Two-bay bridge		Eight-bay bridge		Fourteen-bay bridge	
μ	σ	μ	σ	μ	σ
7.2	0.03	2.3	0.12	1.4	0.00
17.4	0.12	4.9	0.10	2.5	0.07
28.5	0.15	6.8	0.15	4.9	0.11
34.4	0.25	7.8	0.51	6.1	0.08
40.4	0.33	9.1	0.11	8.1	0.48
45.3	0.35	10.0	0.09	8.3	0.50
49.5	0.58	11.9	0.07	9.1	0.00
60.4	0.68	15.6	0.91	11.3	0.29
90.4	1.20	16.4	0.16	12.0	0.00
109.0	2.52	23.0	0.24	13.4	0.13
121.0	1.83	25.7	0.56	14.7	0.22
137.2	0.28	29.9	1.38	16.2	0.00
		32.9	0.22	20.5	0.08
		35.5	0.40	21.4	0.00
		39.2	0.03	24.6	0.00
		41.5	0.21	24.6	0.00
		44.5	1.03	27.6	0.00
		48.7	0.07	31.0	0.77
		51.7	0.57	32.8	0.16
		56.5	0.90	34.9	0.08
		60.7	3.29		
		65.4	0.98		

5.2.2 Power spectral density

Another statistical signal processing tool to extract the frequencies of the highest energy is to calculate the power spectral density. Given an excitation, $F(t)$, using the convolution theorem, the response can be written as (100):

$$X(t) = \int_{-\infty}^{\infty} F(t)h(t-\tau)d\tau \tag{5.1}$$

where the mean response is the expectation (100):

$$E[X(t)] = \int_{-\infty}^{\infty} E[F(t)h(t-\tau)]d\tau \tag{5.2}$$

Taking the cross-correlation of the random signal and itself given a time lag, τ, called the autocorrelation $R_{XX}(\tau)$, allows for a further analysis of the signal properties as follows (100):

$$\begin{aligned} R_{XX}(\tau) &= E[X(t)X(t+\tau)] \\ &= E[\textstyle\int_{-\infty}^{\infty} h(\tau_1)F(t-\tau_1)d\tau_1 \int_{-\infty}^{\infty} h(\tau_2)F(t+\tau-\tau_2)d\tau_2] \\ &= \textstyle\int_{-\infty}^{\infty}\int_{-\infty}^{\infty} h(\tau_1)h(\tau_2)E[F(t-\tau_1)F(t+\tau-\tau_2)]d\tau_1 d\tau_2 \\ &= \textstyle\int_{-\infty}^{\infty}\int_{-\infty}^{\infty} h(\tau_1)h(\tau_2)R_{FF}(\tau+\tau_1-\tau_2)d\tau_1 d\tau_2 \end{aligned} \tag{5.3}$$

The Fourier transform of $R_{XX}(\tau)$ results in the power spectral density in the frequency domain:

$$S_{XX}(\omega) = \int_{-\infty}^{\infty} R_{XX}(\tau)e^{-i\omega\tau}d\tau \tag{5.4}$$

Table 5.7 summarises the results from the free vibration tests on the bridge specimens. For each hammer impact or lateral pulley release test, the lowest frequency peak —in most cases the only peak —was selected. The population mean and standard deviation was taken of these results. Results from the power spectral density confirm the results obtained from the FFT of the raw vibration signals with the exception of the fourteen-bay bridge vertical frequency.

Table 5.7: Power spectral density frequency analysis

	Two-bay bridge		Eight-bay bridge		Fourteen-bay bridge	
	μ	σ	μ	σ	μ	σ
First vertical	40.2	0.20	16.2	0.04	3.8	0.35
First lateral	17.5	0.04	2.3	0.04	1.4	0.02

5.2.3 Second-order blind identification

As detailed previously in Chapter 2, this second-order statistical analysis uses the autocorrelation of the signal to solve the inverse problem of separating the individual structural frequencies and the associated mode shapes. It was noted that these bridge specimens have very closely spaced natural frequencies in the frequency domain, making traditional modal estimation methods very difficult. While the method did not yield meaningful results for the short span, the first vertical and lateral modes for the eight-bay and fourteen-bay bridges were successfully determined using this method. A time lag of 500 was used for this purpose. Many of the SOBI results above the first vertical or first lateral mode contained mixed frequencies, and were thus not well-separated. Table 5.8 summarises the mean and standard deviation of damping, μ_ξ and σ_ξ respectively, for that given averaged natural frequency from the previous table, μ_f.

Table 5.8: Results from the second-order method

	Eight-bay bridge			Fourteen-bay bridge		
	μ_f (Hz)	μ_ξ	σ_ξ	μ_f (Hz)	μ_ξ	σ_ξ
Vertical	16.6	0.097	0.056	4.97	0.148	0.083
Lateral	2.34	0.320	0.172	1.33	0.361	0.16

Damping estimate using decaying exponential

The rate at which the energy decays in a signal after an impact test is a function of the structural damping. Using a simple exponential decay trend, the damping could be approximated for all bridge spans (Table 5.9). The table also references the frequency to which the decaying trend was applied. It is important to note that this method, while extensively used in the field, yields correct results only for simple systems where most of the structural response is contained in a single mode. Hence, not surprisingly, the results do not correspond well with the second-order method, as for the bridge spans considered here there is contribution from several modes which makes the results less reliable.

Table 5.9: Exponential decay approximation of damping

	Two-bay bridge			Eight-bay bridge			Fourteen-bay bridge		
	μ_f (Hz)	μ_ξ	σ_ξ	μ_f (Hz)	μ_ξ	σ_ξ	μ_f (Hz)	μ_ξ	σ_ξ
Vertical	17.5	0.009	0.002	16.6	0.03	0.002	4.97	0.06	0.02
Lateral	40.2	0.02	0.007	2.34	0.20	0.04	1.33	0.25	0.09

5.3 Design code comparison

In the following sections, the bridge specimens are evaluated on the dynamic criterion from the Canadian design standards and the European HIVOSS footbridge guide (27)(39). The goals are to:

- determine where the specimen bridges lie on the spectrum of dynamic performance for each code, and
- determine the accuracy of the empirical equations for maximum acceleration.

5.3.1 CSA S6-06

The Canadian Highway Bridge Code C3.4.4 (Commentary on CAN/CSA-S6- 06, Canadian Highway Bridge Design Code) recommends checking values for a single pedestrian (weighing 700 N) against the serviceability criteria prescribed in their commentary. If the first flexural frequency is above 4 Hz, it is reduced by up to 70% at greater than or equal to 5 Hz. This code only applies to bridges above 10 m, therefore the two-bay bridge is not included in the analysis but its measured results are provided for comparison to the other specimens. Table 5.10 summarises the dynamic code applied to the eight-bay and fourteen-bay bridges assuming a 0.8% damping.

Using the fourteen-bay bridge as an example calculation, the dynamic response factor, Ψ, for this bridge length is 7.5. The static midspan deflection due to the 700 N person was 1.27 mm. The first flexural frequency is 4.9 Hz, above 4 Hz, and is therefore scaled down by a portion the 70% reduction factor for an effective frequency of 1.8 Hz. Therefore, using

the calculation from Chapter 2:

$$\begin{aligned} a_{max} &= 4\pi^2 f_1^2 w_S K \Psi \\ &= 4\pi^2 (1.8Hz)^2 (0.00127m)(1)(7.5) \\ &= 1.22m/s^2 \end{aligned} \tag{5.5}$$

Table 5.10: CSA S6-06 single pedestrian acceleration

Pace (Hz)	Peak acceleration (m/s^2)		
	Two-bay	Eight-bay	Fourteen-bay
CSA S6-06	-	2.58	1.22
1.67	0.67	0.73	1.08
1.83	0.62	0.75	1.02
2.00	0.60	1.14	0.99
2.17	0.82	1.08	0.95
2.33	1.01	1.90	1.25
2.67	1.87	1.37	2.05
2.83	1.94	1.61	2.15
3.00	3.08	1.81	2.44

Of the specimens considered, the first flexural frequency for the two-bay bridge (7.2 Hz) is outside the range considered dynamically sensitive by CSA S6-06. The first flexural frequencies for the eight-bay and fourteen-bay bridge are 2.3 Hz and 1.4 Hz, respectively (5.6). Based on these values, the predicted peak accelerations using the simplified methods are listed in the first row in Table 5.9. Note that the directionality (whether the first flexural mode is a vertical, lateral, or coupled) is ignored in this simplified calculation. CSA S6-06

states that the first flexural frequency is to be used ignoring torsional contributions, without providing explanation as to what exactly this means. For this thesis, this is interpreted as the lowest frequency achieved from an eigenvalue analysis using the finite-element model. CSA S6-06 recommends a detailed dynamic analysis where the bridge dynamics contain multiple modes below pedestrian walking range of 4 Hz, but this is not pursued in this thesis.

Using the maximum acceleration due to a single pedestrian walking on each specimen span and the CSA predicted design acceleration, the maximum bridge span that does not exceed the design standards is 15.4 m (Figure 5.9). The consequence of exceeding the maximum acceleration is a violation of the serviceability limit states, therefore the movement will be great enough for pedestrians to feel unsafe.

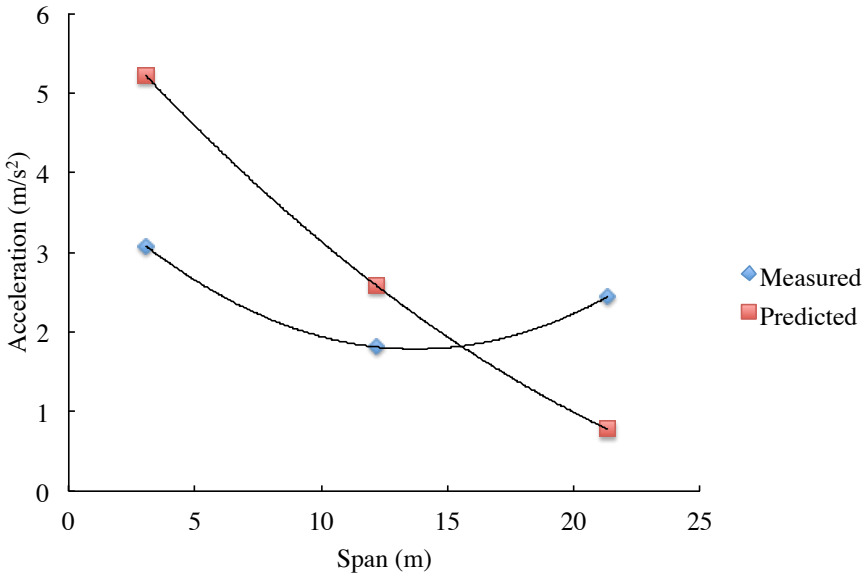

Figure 5.9: CSA S6-06 design compared to measured acceleration

For static strength and deflection requirements, CSA S6-06 clause 3.8.9 prescribes the

maximum of 4.0 kPa to all three bridge specimens for the Ultimate Limit State (ULS). This is a much greater distributed load than prescribed by HIVOSS. This thesis does not contain a full code design check of the bridge specimen, though maximum compressive and maximum tension stresses were extracted from the finite element model of the fourteen-bay bridge. Since the fourteen-bay bridge is the most flexible, its finite element model was subjected to the static load. With this load on the finite element model, the maximum tension stress located in the bottom chord and is 35 MPa. The maximum compressive stress is located in the top chord and is 55 MPa. The calculated stresses are moderate compared to the yield strength, but that a more rigorous check is needed to verify that all Code strength requirements are satisfied. Midspan deflection is $L/402$ which does not have a prescripted maximum, but AASHTO LRFD recommends $L/1000$ for pedestrian bridges (1).

5.3.2 HIVOSS

Unlike the CSA standard, HIVOSS guidelines 4.3.1 (39) focus on crowd loading, not on an individual pedestrian. The philosophy used here is that generally the governing loads are contributed from multiple pedestrians, not an individual pedestrian. This is also consistent with observed failures on footbridges. The crowd densities in this thesis were selected to match the boundary values between traffic classes according to the HIVOSS guidelines in Chapter 2. Table 5.11 lists the recorded peak accelerations for the three bridge configurations. These tests involved volunteers walking on the bridge, corresponding to various crowd densities. Crowd tests were repeated three times, thirty times, and ten times for the two-bay, eight-bay, and fourteen-bay bridges respectively. The mean of all peak accelerations were recorded and then classified according to the comfort class levels defined in

HIVOSS (Table 5.11).

Table 5.11: Measurements and HIVOSS crowd acceleration classification

Crowd density (p/m^2)	Peak acceleration (m/s^2)					
	Two-bay		Eight-bay		Fourteen-bay	
	Vertical	Lateral	Vertical	Lateral	Vertical	Lateral
0.2	N/A	N/A	1.79	1.16	4.20	2.67
0.5	1.50	1.25	3.72	1.92	4.05	2.96
1.0	1.93	1.54	2.90	1.85	4.26	3.90
1.5	2.44	1.74	N/A	N/A	N/A	N/A
Legend	CL 1	CL 2	CL 3	CL 4		

Results from tests show that none of the bridge specimens experienced less than 0.5 m/s^2 of acceleration, the HIVOSS prescribed limit of comfortable acceleration, but with the shortest specimen, the amplitude of vibrations were very small, therefore barely any movement could be noticed. The fourteen-bay bridge experienced significant oscillations, beyond the acceptable level of comfort prescribed by the codes. The resulting motion caused imbalance, where test subjects reported significant difficulty maintaining their balance while walking.

The design process in HIVOSS to calculate the maximum acceleration, detailed previously, is not applicable for these bridges. The scaling factor of resonance between pedestrians' walking pace and the bridge's natural frequency does not account for the frequencies of the bridge specimens. Additionally, the number of pedestrians present for the 0.2 p/m^2 crowd tests on all bridges is below the minimum threshold of the HIVOSS guidelines. The traffic class below 0.2 p/m^2, called very weak traffic, consists of 15 pedestrians.

5.4 Dynamic load factors

The work previously conducted by Rainer (71) used a very stiff simply supported structure with a fundamental frequency of 12.0 Hz, for the pedestrians to walk across. The two-bay bridge from this thesis is such that its first flexural frequency is well beyond the walking frequency range, which makes it ideal to validate the results from Rainer's work. DLFs are embedded in all design codes, including CSA S6-06 for dynamic design.

The DLFs were calculated by extracting each peak from ten trials of each test and taking the mean of these peaks. The weight of the bridge and the pedestrian were then subtracted from these peak values, leaving the amplified load. The DLF is then the ratio between this amplified load and the weight of the pedestrian. The mean and standard deviation was taken of the DLFs from all thirty trials, given one walking frequency. Figure 5.10 summarises the dynamic load factors for both walking and running cases.

Referring back to the conclusions from Rainer's work in Chapter 2, Figure 5.10 exhibits similar trends for the DLFs over the various frequencies for walking and running tests. The measured DLFs for walking are between 0.5 and 0.7 and for running are between 1.4 and 1.8. From Rainer's work, the DLFs for walking frequencies are between 0.3 and 0.6 and running frequencies around 1.4. In the tests conducted here, the peak walking DLF occurs at 2.17 Hz, rather than 2 Hz as noted by Rainer, and the DLF corresponding to running are also higher. These differences may be attributable in part to the rather short span of the bridge, which resulted in very short duration test data.

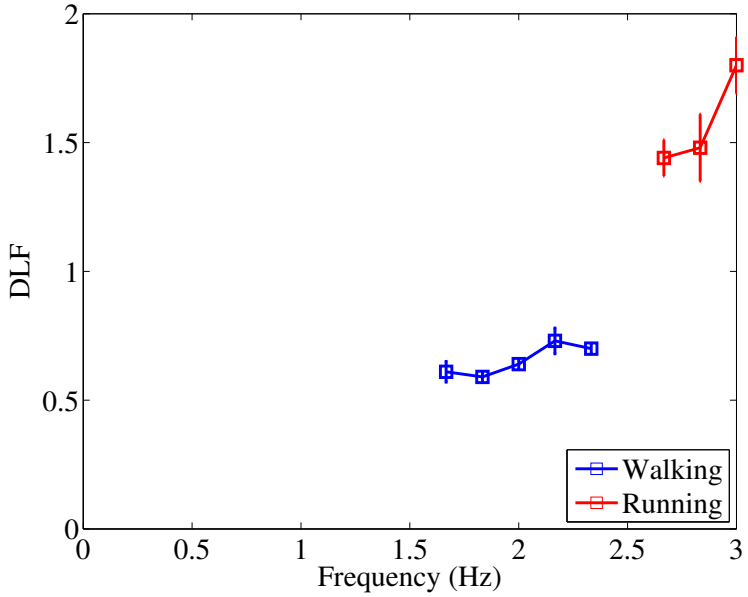

Figure 5.10: Two-bay bridge DLF

5.5 Tuned mass damper design

The following is a simple case study to illustrate a tuned mass damper design using the properties of the fourteen-bay bridge. With a total mass of approximately 1600 kg, the modal mass is $0.5m$, thus the active mass in the calculations is 800 kg. The first lateral of 1.4 Hz is highly damped with over 10% structural damping. However, assuming a 1% damping, a mass ratio of $0.02\bar{m}$ yields an amplitude ratio of approximately 5.5. Please note that a significantly higher value of lateral damping was obtained (10%) due to the slip between the bridge and the supports. This is to say that if the bridge experiences a maximum lateral amplitude of 25 mm, then the peak stroke of the damper, would be 275 mm. This will be limited using a damper attached in parallel to the elastic element in the tuned mass damper. At a mass ratio, $\bar{m}$, of 0.02 m and damping, ξ of 0.01, the following

properties result:

$$\begin{aligned} f_{opt} &= 0.972 \\ \xi_d|_{opt} &= 0.089 \\ \xi_e &= 0.059 \end{aligned} \tag{5.6}$$

Thus, the damper properties with relation to the main structure are:

$$\begin{aligned} m_d &= 0.02m = 0.02(800kg) = 16kg \\ \omega_d &= 0.972\omega = 0.972(1.4 * 2 * \pi) = 8.6rad \\ k_d = \bar{m} f_{opt}^2 k &= 0.0190k = 0.0190\omega^2 * m = 1170N/m \end{aligned} \tag{5.7}$$

Therefore, a tuned mass damper of 16 kg with a spring constant of 1170 N/m would allow for a maximum lateral bridge movement of 50 mm. The optimal damping ratio of the TMD would be 8.9% for a primary structure damping of 1.0 %. Since the first lateral mode is of primary concern, this damper will be located at the midspan of the bridge. For ease of construction, the TMD could be split into two separate masses, both located in proximity to each other near the midspan. This damper design is based on fundamental principles and these parameters will be used in future work for the design and testing of a TMD for this bridge specimen. Two proposed designs are: to install two static TMDs under the traverse members or to design a mobile TMD that can drive on the deck surface to optimise its location for maximum damping.

5.6 Lateral bracing

5.6.1 Modelling lateral bracing

Two types of lateral bracing were used: a single diagonal per bay, called "N-bracing", and two diagonals per bay, called "X-bracing". The lateral bracing consists of angle sections of

aluminium, bolted into the web of the cast joints between the transversal and the bottom chord. In the case of the X-bracing arrangement, the angles are secured together at their intersection.

The finite element model of the fourteen-bay bridge was modified to incorporate both N-bracing and X-bracing. Components were added as pin-jointed elements to the existing nodes. The modifications to the original structure changed the first natural mode from lateral at 1.1 Hz to torsional at 3.6 Hz for N-bracing and 3.8 Hz for X-bracing. There was a significant change in the natural frequency and the mode shape between the original structure and those with either form of bracing. In the finite element model, the modal displacement at the midspan between the original structure and that of the N-bracing is reduced by a factor of approximately 1.5.

5.6.2 Measuring the effect of lateral bracing

Lateral impact and crowd loading tests were performed with both the N-bracing and X-bracing. Crowds consisted of 10 pedestrians for the N-bracing tests and 20 pedestrians for the X-bracing tests. Crowd size was selected based on the maximum number of participants available for the test. The primary mode of vibration clearly changed from lateral in the case of no bracing to torsional for the braced cases. The FFT calculated from the accelerometer data shows the dominant modes (Table 5.12). These frequencies were present in the lateral impact and pedestrian crowd tests as well.

Table 5.12: Measured torsion and vertical modes from horizontally braced bridges

	N-bracing (Hz)	X-bracing (Hz)
1st torsion	2.5	2.6
1st vertical	4.9	4.8
2nd torsion	7.7	8.2

The average acceleration RMS from the set of N-bracing tests is 0.36 m/s^2 and of X-bracing tests is 0.43 m/s^2, sensors at midspan at locations 04+Z and 05+Y. Since these values are in the same range as those noted for the crowd tests without bracing, it can be inferred that the energy contained in the signal from braced and unbraced structures is very similar; however, the mode of dissipation is greatly different (lateral mode in the un-braced case to coupled modes in the braced cases). The unbraced mode moves laterally and dissipates energy through the friction contact between the deck plates and at the supports. The braced mode moves torsionally and is a much stiffer structure.

Using the finite element models, the first natural frequency of the bridge with a torsion mode 3.6 Hz and 3.7 Hz for N-bracing and X-bracing respectively. Measured results are subject of future work not in this thesis.

Since the lateral displacement of the structure without bracing was of interest, the lateral displacement due to the lateral load was measured for both types of bracing. This consisted of laterally loading the bridge with two 50 lb weights using a pulley system. When loaded with 100 lb, the N-bracing resulted in 6 mm peak displacement and the X-bracing resulted in 3 mm of displacement. In comparison, without any bracing, the same lateral load resulted in 32 mm displacement amplitude, greater by a factor of 5.3 compared to N-bracing. Thus, the presence of bracing greatly increases the lateral stiffness of the

structure.

5.6.3 Geometric sensitivity

So far in this thesis, the alternatives for reducing structural vibration amplitudes have been to install horizontal bracing or to design a tuned-mass damper. These measures focused on the fourteen-bay bridge due to its large lateral movements under crowd loading during the laboratory experiments. Another alternative when analyzing the design of aluminium pony truss bridges is to parametrise the height between the top and bottom chords or the width of the bridge, and observe the resulting changes to its dynamic properties.

A preliminary analysis of the fourteen-bay bridge was completed based on the finite element models without bracing, N-bracing, and X-bracing. From each model, two variations were created where only the width or the height were manipulated, but not simultaneously. The weight of the bridge is more sensitive to changes in the width of the bridge compared to changes in the height. In order to compare the effect of the changing either set of dimensions, the weight of the widened or heightened bridges were held constant. The natural frequency of the first lateral/torsional and the first vertical modes were checked for changes, as well as the modal displacement at the midspan. The displacements produced by the simulation were true to nature, but the relative changes between these displacements were useful for comparing the behaviour of different bridge spans.

Manipulating the width of the braceless bridge had no effect other than a small frequency change due to the added mass. Increasing the height, however, quickly increased the first vertical natural frequency to well out of the pedestrian walking frequency. The N-bracing and X-bracing models behaved nearly identically. Increasing the width also increased the natural frequency of the first torsion mode, but this had no effect on the natural

frequency of the first vertical mode. Increasing the height of the top chord increased the natural frequency of the first vertical mode, but had no effect on the torsional mode. Since the lateral or torsional mode on all three bridge models are within the range of pedestrian walking influence, the most effective design change would be to increase the deck width. For the braced models, a width increase of 200 mm, 500 mm, and 1000 mm results in a torsional frequency increase of 0.4 Hz and 0.6 Hz, and 0.7 Hz respectively. If the bridge was widened by 1000 mm and held a live load of 4 kPa as per CSA S6-06 clause 3.8.9, the maximum tension stress is 50 MPa in the bottom chord and the maximum compressive stress in the top chord is 75 MPa. The midspan deflection would be 73 mm, thus $L/292$, which is well above the AASHTO LRFD suggested $L/1000$ deflection recommendation. In varying the height between the top and bottom chords, a height of 2.5 m would ensure that the AASHTO deflection recommendation is satisfied. Though this increases the vertical natural frequency, deepening the truss is independent of the lateral frequencies, which are of concern on the fourteen-bay bridge.

Chapter 6

Conclusions & recommendation

6.1 Conclusions

The dynamic behaviour of aluminium pedestrians bridges was assessed; experimentally with full-scale specimens, theoretically with finite element models, and empirically using design codes. Conclusions are based on an extensive set of experimental trials on bolted aluminium pony-truss bridges of two-bay, eight-bay, and fourteen-bay spans.

The finite element models of the bridge specimens yielded the same natural frequencies and mode shapes as the measured data from the accelerometers. Connections in the finite element model included releases of degrees of freedom to emulate the allowable movement from the bolted connections and splice locations. This shows that the modelling methods, assumptions, and measurement techniques are reliable and can be used for further research on pedestrian bridges.

The load cell data from individual pedestrian walking tests permitted the calculation of the DLFs associated with a range of walking speeds on all three bridge specimens.

Results for DLF obtained from the short-span specimen largely agreed with previous tests published in the literature. The eight-bay and fourteen-bay bridges had lateral natural frequencies within the range of walking frequencies and thus could not be used to calculate the DLFs.

The Canadian Highway Bridge Design Code S6-06 and the European HIVOSS footbridges guideline were used to assess the serviceability of bridge specimens for single pedestrian and crowd loading, respectively. According to studies referenced by S6-06, structures with flexural frequencies above 4 Hz will not be governed by dynamic design, but should still be verified if the natural frequency is below 6 Hz. The calculated maximum acceleration due to a single pedestrian for the long span bridge (fourteen-bay bridge) was exceeded by the measured acceleration. The eight-bay bridge maximum prescribed accelerations are greater than the measured data by a factor of 1.3. The HIVOSS footbridge design code does not adequately prescribe a maximum acceleration for the bridge specimens so that it exceeds the measured values.

The CSA S6-06 calculation for maximum acceleration is limited to bridge spans above 10 m, therefore the two-bay bridge does not fall under the jurisdiction of this code. In terms of loading, the CSA S6-06 only accounts for the effect of one pedestrian, and does not contain any prescriptive measures for crowd loading. HIVOSS guidelines mainly focus on crowd loading, and propos modified models for single pedestrians. Using CSA S6-06 for static design, the maximum stresses in the members of the fourteen-bay bridge do not indicate a concern, the deflection does not meet the AASHTO recommended $L/1000$. A full-scale design check was not completed so adequacy of the fourteen-bay bridge cannot be determined. Both codes, however, make the assumption that major vibrations only occur when the bridge's first natural frequency aligns with the walking frequency of the pedestrians. This is particularly seen in the HIVOSS guidelines where the amplification factor

would discount all of the bridge specimens from this thesis since their natural frequencies are above the limits of interest.

The maximum measured strain was in the bottom chord was moderate in comparison to the factored yield strain of aluminium. This does not indicate any concerns though a full Code check was not completed to determine if this was acceptable. In most cases, the strain in the bottom chord is greater than the strain in the diagonal. Strain values on the diagonal member were not obtainable for the two larger crowd tests on the fourteen-bay bridge due to instrumentation error. The strain for the single

The presence of either N-bracing or X-bracing greatly reduced the lateral movement of the bridge, by a minimum factor of 5.3. The primary mode of vibration changed from lateral when unbraced, to torsion when braced. There was little to no change in the vertical mode and no major difference in terms of natural frequency, RMS accelerations, or mode shape between the N-bracing and the X-bracing.

6.2 Recommendations

The topic that leaves the most room for development is the re-assessment of the CSA S6-06 and HIVOSS guidelines in order to better define their criteria for dynamically-sensitive bridges. Even though the specimens of this thesis were not within the preferred regions of either of the codes, the longest span exceeded or nearly exceeded the code provisions. More work should be done on bridges with natural frequencies that are not in resonance with pedestrian walking pace, yet produce high amplitude vibrations under loading.

In order to better understand the human-structure interaction of aluminium pedestrian bridges, new load models should be developed. Key factors in these models should include:

a biomechanically accurate loading mechanism of the pedestrian's footfall and a response that can be explained by the data collected in this thesis. Having a model that explains the measured results well joins the experimental and theoretical components of this research, where the models can then be used to predict responses on future bridges.

It is recommended that the bridge be lengthened to achieve a lateral frequency closer to 1.0 Hz so that it becomes lively even for a single pedestrian walking case.

In order to mitigate vibration on a structure like the fourteen-bay bridge with light traffic, lateral bracing would be an acceptable choice. The lateral bracing still allows for bridge movement in larger crowds, which becomes a serviceability concern. For this type of bridge in dense traffic, a TMD is recommended.

References

[1] AASHTO. Load Resistance and Factor Design. Bridge Design Specifications America Association of State Highway and Transportation Official, Washington, D.C. USA, 2008.

[2] Giuseppe Abbiati, Anil Kumar, Rosario Ceravolo, and Nicola Tondini. Dynamic characterization of complex bridge structures with passive control systems. Structural Control and Health Monitoring, 32(19):511–534, February 2012.

[3] Parviz Ahadi, Mohtasham Mohebbi, and Kazem Shakeri. Using optimal multiple tuned liquid column dampers for mitigating the seismic response of structures. Civil Engineering, (592181):6, 2012.

[4] D.E. Allen and J.H. Rainer. Guidelines for the seismic evaluation of existing buildings. Canadian Journal of Civil Engineering, 22(3):500–505, June 1995.

[5] H. Bachmann. Case studies of structures with man-induced vibrations. Journal of Structural Engineering, 118(3):631–647, March 1992.

[6] H. Bachmann and W. Ammann. Vibrations in structures induced by man and machines. International Association of Bridge and Structural Engineering, 1987.

[7] Gebrail Bekdaü and Sinan Melih Nigdeli. Mass ratio factor for optimum tuned mass damper strategies. International Journal of Mechanical Sciences, 71:68–84, June 2013.

[8] A. Belouchrani, K. Abed-Meraim, J.F. Cardoso, and E. Moulines. A blind source separation technique using second-order statistics. IEEE Transactions on signal processing, 45(2):434–444, 1997.

[9] Amadeo Benavent-Climent. An energy-based method for seismic retrofit of existing frames using hysteretic dampers. Soil Dynamics and Earthquake Engineering, 31(10):1385–1396, October 2011.

[10] G.S. Bhuyan, E. Zhai, H. Ghalibafian, C. Ventura, D. Borthwick, R.P.B. Stewart, and J.H. Rainer. Seismic behavior of flexible conductors connecting substation equipment part i: Static and dynamic properties of individual components. IEEE Transactions on Power Delivery, 19(4):1673–1679, October 2004.

[11] J.R. Billing. Dynamic loading and testing of bridges in ontario. Canadian Journal of Civil Engineering, 11(4):833–843, December 1984.

[12] J Blanchard, B Davies, and J.W. Smith. Design criteria and analysis behaviour of bridges. Department of Transport, Crowthorne England, (SR275):90–106, 1977.

[13] R Blickhan. The spring-mass model for running and hopping. Journal of biomechanics, 22(11):1217–1227, 1989.

[14] Luca Bruno, Fiammetta Venuti, and Vittorio Nascé. Pedestrian-induced torsional vibrations of suspended footbridges: Proposal and evaluation of vibration countermeasures. Engineering Structures, 36:228–238, March 2012.

[15] Radlbeck C., Dienes E., and Kosteas D. Sustainability of aluminium in buildings. Structural Engineering International, (4):221–224, 2006.

[16] Juan M Caicedo and Johannio Marulanda. Fast mode identification technique for online monitoring. Structural Control and Health Monitoring, (March 2010):416–429, 2011.

[17] A Carotti. A tuning criterion for the inertial tuned damper: Design using phasors in the argand gauss plane. Applied Mathematical Modelling, 23:199–217, 1999.

[18] N. Carpineto, W. Lacarbonara, and F. Vestroni. Mitigation of pedestrian-induced vibrations in suspension footbridges via multiple tuned mass dampers. Journal of Vibration and Control, 16(5):749–776, April 2010.

[19] S.P. Carroll, J.S. Owen, and M.F.M. Hussein. Modelling crowd bridge dynamic interaction with a discretely defined crowd. Journal of Sound and Vibration, 331(11):2685–2709, May 2012.

[20] Carlos M Casado, Iván M Díaz, Jesús De Sebastián, Alfonso V Poncela, and Antolín Lorenzana. Implementation of passive and active vibration control on an in-service footbridge. Structural Control and Health Monitoring, (June 2011):70–87, 2013.

[21] R. Ceravolo. Use of instantaneous estimators for the evaluation of structural damping. Journal of Sound and Vibration, 274(1-2):385–401, July 2004.

[22] Rosario Ceravolo, Nicola Tondini, Giuseppe Abbiati, and Anil Kumar. Dynamic characterization of complex bridge structures with passive control systems. Structural Control and Health Monitoring, (March 2011):511–534, 2012.

[23] Shaohong Cheng, Neda Darivandi, and Faouzi Ghrib. The design of an optimal viscous damper for a bridge stay cable using energy-based approach. Journal of Sound and Vibration, 329(22):4689–4704, October 2010.

[24] Hyunhoon Choi and Jinkoo Kim. New installation scheme for viscoelastic dampers using cables. Canadian Journal of Civil Engineering, 37(9):1201–1211, September 2010.

[25] L.L. Chung, L.Y. Wu, K.H. Lien, H.H. Chen, and H.H. Huang. Optimal design of friction pendulum tuned mass damper with varying friction coefficient. Structural Control and Health Monitoring, (February 2012):544–559, 2013.

[26] Jerome J. Connor. Introduction to Structural Motion Control. Pearson Education Inc., Upper Saddle River, New Jersey, US, 2003.

[27] CSA. Commentary on CAN / CSA-S6-06 , Canadian Highway Bridge Design Code. 2011.

[28] Caricato da Arpingstone. London millennium bridge with st paul's.

[29] P Dallard, Tony Fitzpatrick, and Anthony Flint. London millennium bridge: Pedestrian induced lateral vibration. Journal of Bridge Engineering, 1(December):412–417, 2001.

[30] S.K. Das and J.G. Kaufman. Aluminium alloys for bridges and bridge decks. The Minerals, Metals and Materials Society, 1:61–72, 2007.

[31] Alex de la Chevrotiere. Structural assembly for constructing bridges and other structures. Patent CA 2688813, Canadian Intellectural Property Office, April 2010.

[32] Homayoon E. Estekanchi and Mohammad Ch. Basim. Optimal damper placement in steel frames by the endurance time method. 630(January):612–630, 2011.

[33] S Fryer and A Allergi. Helical design for footbridge. The Structural Engineer, 87(March):5–6, 2009.

[34] H. Ghalibafian, G.S. Bhuyan, C. Ventura, J.H. Rainer, D. Borthwick, R.P.B. Stewart, and E. Zhai. Seismic behavior of flexible conductors connecting substation equipmentäîpart ii: Shake tabletests. IEEE Transactions on Power Delivery, 19(4):1680–1687, October 2004.

[35] Rita Greco and Giuseppe Carlo Marano. Optimum design of tuned mass dampers by displacement and energy perspectives. Soil Dynamics and Earthquake Engineering, 49:243–253, June 2013.

[36] C.E. Grigorian, T.S. Yang, and E.P. Popov. Slotted bolted connection energy dissipators. Earthquake Spectra, 9(3), 1993.

[37] Gregg Haskell and David Lee. Fluid viscous damping as an alternative to base isolation.

[38] Fjalar Hauksson. Dynamic behaviour of footbridges subjected to pedestrian-induced vibrations. PhD thesis, Lund University, 2005.

[39] Christoph Heinemeyer, Christiane Butz, and Andreas Keil. Hivoss: Design of lightweight footbridges for human induced vibrations. JRC scientific and Technical Reports, 3(May), 2009.

[40] Kohju Ikago, Kenji Saito, and Norio Inoue. Seismic control of single degree of freedom

structure using tuned viscous mass. Proceedings of the 8th International Conference on Structural Dynamics, EURODYN 2011, (May 2011):453–474, 2012.

[41] E.T. Ingólfsson and C.T. Georgakis. A stochastic load model for pedestrian-induced lateral forces on footbridges. Engineering Structures, 33(12):3454–3470, December 2011.

[42] E.T. Ingólfsson, C.T. Georgakis, and J. Jönsson. Pedestrian-induced lateral vibrations of footbridges: A literature review. Engineering Structures, 45:21–52, December 2012.

[43] J. Kala, M. Bajer, J. Barnat, and J. Smutný. Experimental approach of the single pedestrian-induced excitation. Slovak Journal of Civil Engineering, XVIII(4):1–7, January 2010.

[44] Hiroshi Katsuura, Kaoru Yokoyama, Shunichi Nakamura, and Toshitsugu Kawasaki. Experimental studies on lateral forces induced by pedestrians. Journal of Constructional Steel Research, (64):347–252, May 2008.

[45] O Kratochvíl and J Križan. Bridge analysis structure under human induced dynamic load. World Academy of Science, Engineering and Technology, pages 852–857, 2012.

[46] J.A. Laman, J.S. Pechar, and T.E. Boothby. Dynamic load allowance for through-truss bridge. Journal of Bridge Engineering, (November):231–241, 1999.

[47] S.S. Law, Z.M. Wu, and S.L. Chan. Vibration control study of a suspension footbridge using hybrid slotted bolted connection elements. Engineering Structures, 26(1):107–116, January 2004.

[48] Stefano Lenci and Laura Marcheggiani. On the dynamics of pedestrians-induced lateral vibrations of footbridges. Nonlinear Dynamic Phenomena in Mechanics, pages 63–114, 2012.

[49] Z. Li and C.C. Chang. Adaptive quantification of noise variance using subspace technique. Journal of Engineering Mechanics, (April):469–478, 2012.

[50] S. Luo, Q.S. Yan, and H.J. Liu. Design of mitigation damper with support flexibility for stay cable under bridge deck excitation. Applied Mechanics and Materials, 2012.

[51] J.H.G. Macdonald. Pedestrian-induced vibrations of the clifton suspension bridge, uk. Proceedings of the ICE - Bridge Engineering, 161(2):69–77, January 2008.

[52] Tomasso Massai. Risk analysis of the wind-induced response of high-rise buildings.

[53] Y. Matsumoto, T. Nishioka, H. Shiojiri, and K. Matsuzaki. Dynamic design of footbridges. IABSE Proceedings, pages 1–15, 1987.

[54] F.M. Mazzolani. Structural applications of aluminium in civil engineering. Structural Engineering International, (4):1–4, 2006.

[55] Kyung-Won Min, Ji-Young Seong, and Jinkoo Kim. Simple design procedure of a friction damper for reducing seismic responses of a single-story structure. Engineering Structures, 32(11):3539–3547, November 2010.

[56] M. Mohebbi, K. Shakeri, Y. Ghanbarpour, and H. Majzoub. Designing optimal multiple tuned mass dampers using genetic algorithms (gas) for mitigating the seismic response of structures. Journal of Vibration and Control, 19(4):605–625, February 2012.

[57] Thomas M. Murray and David E. Allen. Floor vibrations floor vibrations due to human activity.

[58] Shun-ichi Nakamura and Toshitsugu Kawasaki. Lateral vibration of footbridges by synchronous walking. Journal of Constructional Steel Research, 62(11):1148–1160, November 2006.

[59] Shun-ichi Nakamura, Toshitsugu Kawasaki, Hiroshi Katsuura, and Kaoru Yokoyama. Experimental studies on lateral forces induced by pedestrians. Journal of Constructional Steel Research, 64(2):247–252, February 2008.

[60] Shunichi Nakamura and Toshitsugu Kawasaki. A method for predicting the lateral girder response of footbridges induced by pedestrians. Journal of Constructional Steel Research, 65(8-9):1705–1711, August 2009.

[61] French Association of Civil Engineering (SETRA). Technical guide: Footbridges: Assessment of vibration behaviour of footbridges under pedestrian loading. 2006.

[62] I Okura. Application of aluminum alloys to bridges and joining technologies. Welding International, (17):781–785, 2003.

[63] Aleksandar Pavic. Key results of modal testing of the millennium bridge, london. Proceedings of Footbridge 2002 conference, pages 1–10, 2002.

[64] J. Piechna. Analysis of dynamic loads on lightweight footbridge caused by lorry passing underneath. Bulletin of the Polish Academy of Science, Technical Science, 54(1), 2006.

[65] A.D. Pizzimenti and Ricciardelli F. The lessons of the wind engineering and their

application to the crowd–structure interaction. 8th Italian conference on wind engineering, 2004.

[66] F. Poncelet. Experimental modal analysis using blind source separation techniques. PhD thesis, 2010.

[67] F. Poncelet, G. Kerschen, J.-C. Golinval, and D. Verhelst. Output-only modal analysis using blind source separation techniques. Mechanical Systems and Signal Processing, 21(6):2335–2358, August 2007.

[68] J.W. Qin, S.S. Law, Q.S. Yang, and N. Yang. Pedestrian-bridge dynamic interaction, including human participation. Journal of Sound and Vibration, 332(4):1107–1124, February 2013.

[69] V. Racic, A. Pavic, and J.M.W. Brownjohn. Experimental identification and analytical modelling of human walking forces: Literature review. Journal of Sound and Vibration, 326(1-2):1–49, September 2009.

[70] J. H. Rainer. Force reduction factors for the seismic provisions of the national building code of canada. Canadian Journal of Civil Engineering, 14(4):447–454, August 1987.

[71] JH Rainer, G Pernica, and DE Allen. Dynamic loading and response of footbridges. Canadian Journal of Civil Engineering, pages 0–7, 1988.

[72] R. Rana and T.T. Soong. Parametric study and simplified design of tuned mass dampers. Engineering structures, pages 193–204, 1998.

[73] Kim J.R. Rasmussen and Jacques Rondal. Strength curves for aluminium alloy columns. Engineering Structures, 23(2000):1505–1517, 2006.

[74] M. Reiterer and F. Ziegler. Control of pedestrian-induced vibrations of long-span bridges. Structural Control and Health Monitoring, 13(6):1003–1027, November 2006.

[75] P. Reynolds, J. Wright, a. Pavic, and T. Armitage. Methodology for modal testing of the millennium bridge, london. Proceedings of the ICE - Structures and Buildings, 152(2):111–121, January 2002.

[76] A. Rezaiguia and D.F. Laefer. Semi-analytical determination of natural frequencies and mode shapes of multi-span bridge decks. Journal of Sound and Vibration, 328(3):291–300, December 2009.

[77] P.O. Riley, G. Paolini, U Della Croce, K.W. Paylo, and D.C. Kerrigan. A kinematic and kinetic comparison of overground and treadmill walking in healthy subjects. Gait and posture, (26):17–4, 2007.

[78] A. Rönnquist. Pedestrian induced vibrations of slender footbrifdges. PhD thesis, Norwegian University of Science and Technology, 2005.

[79] J.Y. Seong and K.W. Min. An analytical approach for design of a structure equipped with friction dampers. Procedia Engineering, 14:1245–1251, January 2011.

[80] Ayman A. Shama, John B. Mander, Stuart S. Chen, and Amjad J. Aref. Ambient vibration and seismic evaluation of a cantilever truss bridge. Engineering Structures, 23(2001):1281–1292, 2009.

[81] T. Siwowski. Aluminium bridges - past, present and future. Structural Engineering International, 4:286–293, 2006.

[82] SOFiSTiK. Sofistik ag. 2014.

[83] Stefano Sorace and Gloria Terenzi. Non-linear dynamic modelling and design procedure of fv spring- dampers for base isolation. 23:1556–1567, 2001.

[84] National Standard. CAN / CSA-S6-06 National Standard of Canada Canadian Highway Bridge Design Code. 2011.

[85] C. Sun, R.P. Eason, S. Nagarajaiah, and a.J. Dick. Hardening düffing oscillator attenuation using a nonlinear tmd, a semi-active tmd and multiple tmd. Journal of Sound and Vibration, 332(4):674–686, February 2013.

[86] A. Sychterz, S. Narasimhan, and S. Walbridge. A study on modal characterization and dynamic analysis of two aluminium pedestrian bridges in quebec. INALCO 2013 proceedings, pages 1–9, 2013.

[87] A. Sychterz, A. Sadhu, S. Narasimhan, and S. Walbridge. Results from modal testing of the daigneault creek bridge. CSCE 2012 conference proceedings, pages 1–11, 2013.

[88] Alexandros A. Taflanidis. Optimal probabilistic design of seismic dampers for the protection of isolated bridges against near-fault seismic excitations. Engineering Structures, 33(12):3496–3508, December 2011.

[89] I. Takewaki, K. Fujita, K. Yamamoto, and H. Takabatake. Smart passive damper control for greater building earthquake resilience in sustainable cities. Sustainable Cities and Society, 1(1):3–15, February 2011.

[90] P. Tindall. Aluminium in bridges. ICE Manual of Bridge Engineering, pages 345–355, 2008.

[91] Peter Van Overschee and Bart De Moor. Subspace identification for linear systems. Kluwer Academic Publishers, Dordrecht, Netherlands, 1996.

[92] Ilaria Venanzi, Filippo Ubertini, and Annibale Luigi Materazzi. Optimal design of an array of active tuned mass dampers for wind-exposed high-rise buildings. Structural Control and Health Monitoring, (May 2012):903–917, 2013.

[93] Fiammetta Venuti and Luca Bruno. Mitigation of human-induced lateral vibrations on footbridges through walkway shaping. Engineering Structures, 56:95–104, November 2013.

[94] X.Y. Wang, Y.Q. Ni, J.M. Ko, and Z.Q. Chen. Optimal design of viscous dampers for multi-mode vibration control of bridge cables. Engineering Structures, 27(5):792–800, April 2005.

[95] F. Weber, G. Feltrin, M. Maślanka, W. Fobo, and H. Distl. Design of viscous dampers targeting multiple cable modes. Engineering Structures, 31(11):2797–2800, November 2009.

[96] Jack Wen, Wei Guo, and Constantin Christopoulos. Performance spectra based method for the seismic design of structures equipped with passive supplemental damping systems. Earthquake Engineering and Structural Dynamics, (October 2012):935–952, 2013.

[97] Horst Werkle, Christiane Butz, and Roxana Tatar. Effectiveness of "detuned" tmd's for beam-like footbridges. Advances in Structural Engineering, 16(1):21–32, January 2013.

[98] M.B. Wilkinson and M. Outram. Principles of pressure transducers, resonance, damping and frequency response. Anaesthesia & Intensive Care Medicine, 10(2):102–105, February 2009.

[99] P. Xiang and A. Nishitani. Optimum design for more effective tuned mass damper system and its application to base-isolated buildings. Structural Control and Health Monitoring, 2013.

[100] W. Xie. Dynamics of structures and random vibrations course notes. CivE701, pages 29–31, 2013.

[101] Fujino Y, Pacheco B.M., Nakamura S.I., and Warnitchai P. Synchronization of human walking observed during lateral vibration of a congested pedestrian bridge. Earthquake Engineering Structural Dynamics, 9(22):41–58, 1993.

[102] R. Yang, X. Zhou, and X. Liu. Seismic structural control using semi-active tuned mass dampers. Earthquake Engineering and Engineering Vibration, 1(1):111–118, July 2002.

[103] P. Young. Improved floor vibration prediction methodologies. Proceedings of Arup Vibration Seminar on Engineering for Structural VibrationCurrent Developments in Research and Practice, 2001.

[104] H. Yu, F. Gillot, and M. Ichchou. Reliability based robust design optimization for tuned mass damper in passive vibration control of deterministic/uncertain structures. Journal of Sound and Vibration, 332(9):2222–2238, April 2013.

[105] L.I. Zhengying, M.U. Dejian, and Dang Pengpeng. Influence of traveling wave effect on passive seismic control of long-span bridge. Procedia Engineering, 14:2307–2314, January 2011.

[106] Delong Zuo, Jieying Hua, and Dean Van Landuyt. A model of pedestrian-induced bridge vibration based on full-scale measurement. Engineering Structures, 45:117–126, December 2012.

APPENDICES

Appendix A

Acceleration results

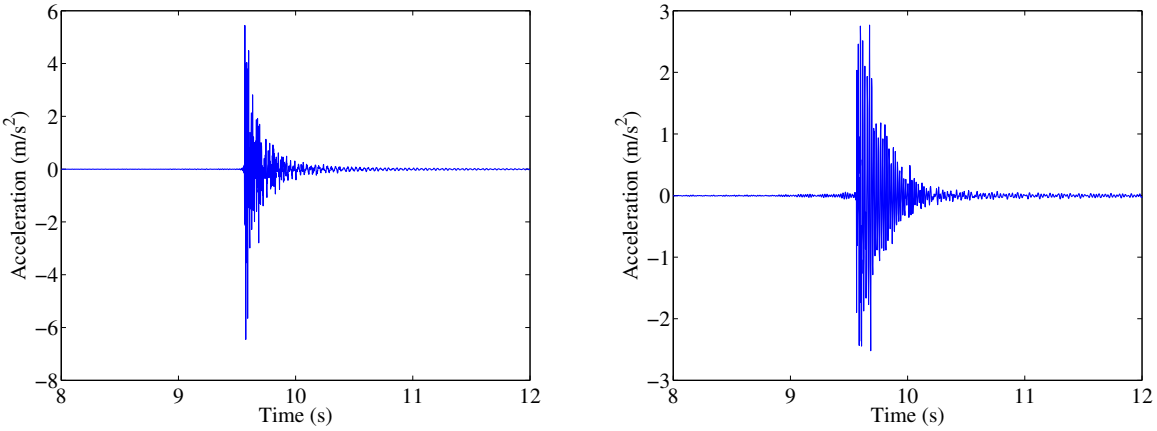

(a) Vertical, 04+Z

(b) Lateral, 05+Y

Figure A.1: Sample acceleration histories from impact test

Figure A.2 shows sample acceleration plots for a single person walking at a pace of 100 steps per minute, BPM.

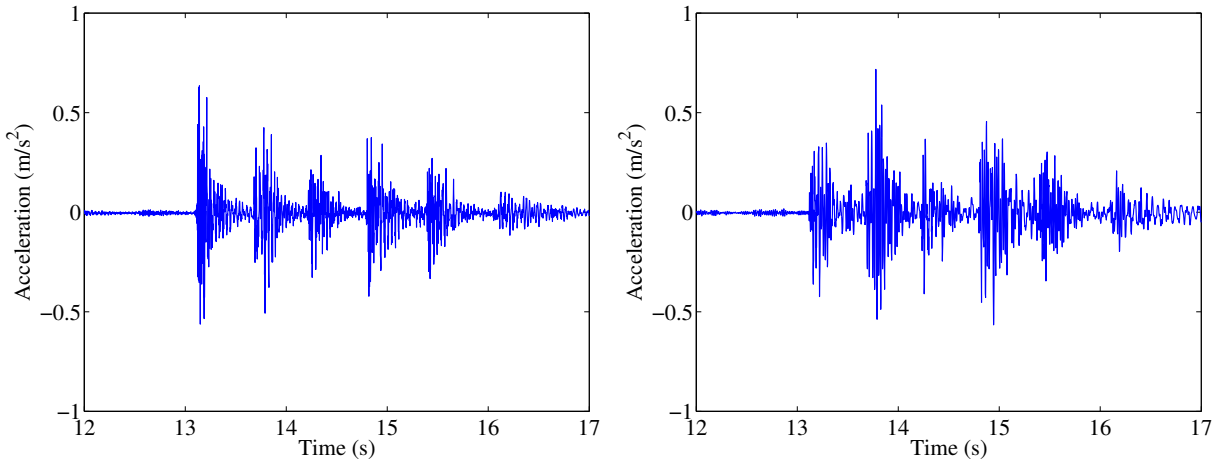

(a) Vertical, 04+Z

(b) Lateral, 05+Y

Figure A.2: Sample acceleration histories for single person walking at a pace of 100 BPM, weight: 0.61 kN, leg length: 0.89 m

Figures A.3, A.4, A.5, A.6, A.7, A.8, and A.9, show similar results for the same person running or walking at different speeds.

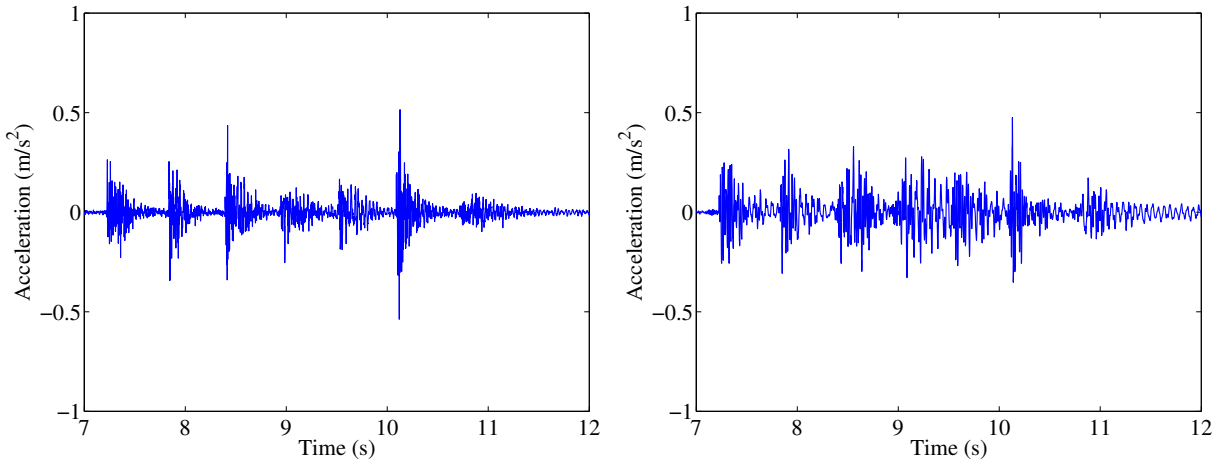

(a) Vertical, 04+Z

(b) Lateral, 05+Y

Figure A.3: Sample acceleration histories for single person walking at a pace of 110 BPM, weight: 0.61 kN, leg length: 0.89 m

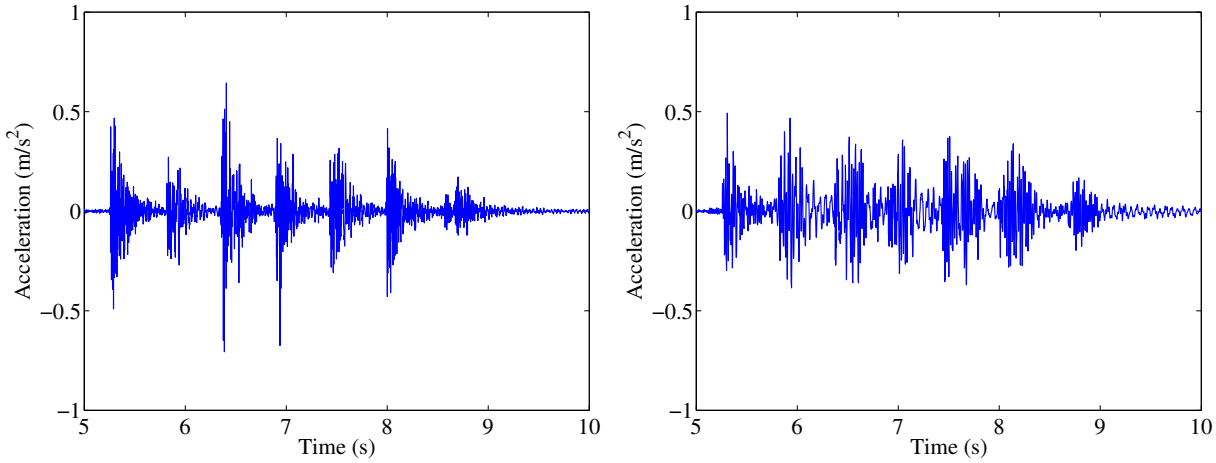

(a) Vertical, 04+Z

(b) Lateral, 05+Y

Figure A.4: Sample acceleration histories for single person walking at a pace of 120 BPM, weight: 0.61 kN, leg length: 0.89 m

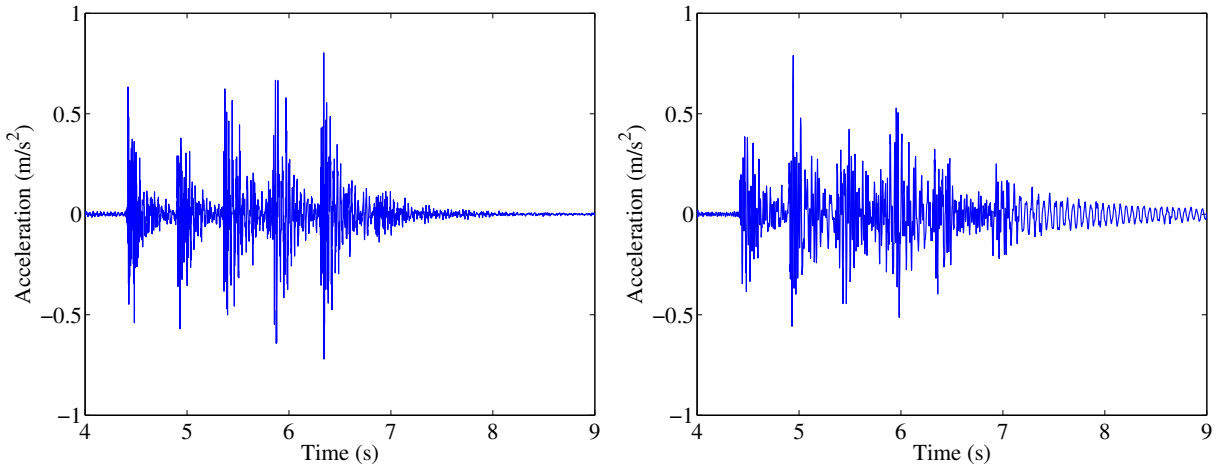

(a) Vertical, 04+Z

(b) Lateral, 05+Y

Figure A.5: Sample acceleration histories for single person walking at a pace of 130 BPM, weight: 0.61 kN, leg length: 0.89 m

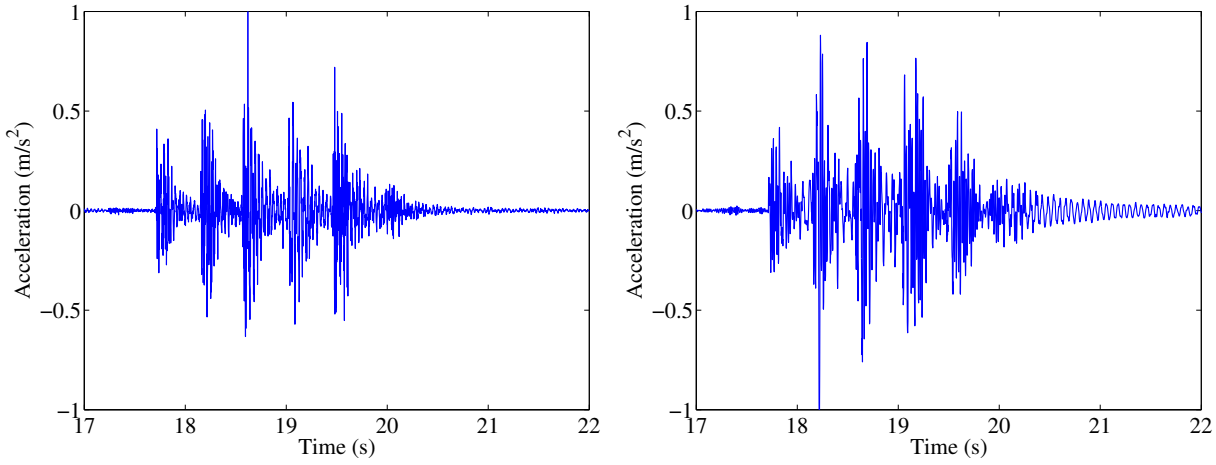

(a) Vertical, 04+Z

(b) Lateral 05+Y

Figure A.6: Sample acceleration histories for single person walking at a pace of 140 BPM, weight: 0.61 kN, leg length: 0.89 m

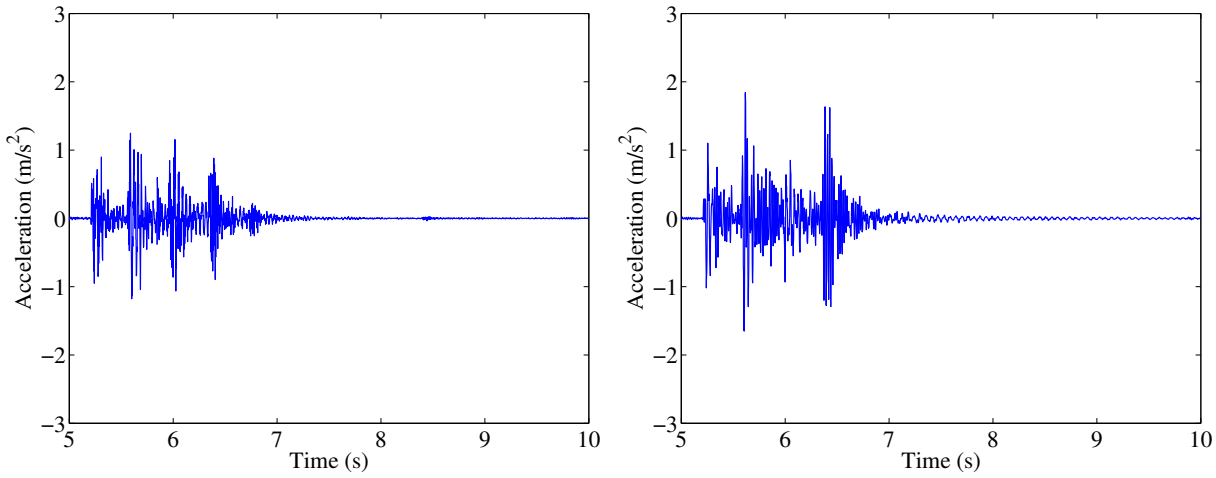

(a) Vertical, 04+Z

(b) Lateral, 05+Y

Figure A.7: Sample acceleration histories for single person running at a pace of 160 BPM, weight: 0.61 kN, leg length: 0.89 m

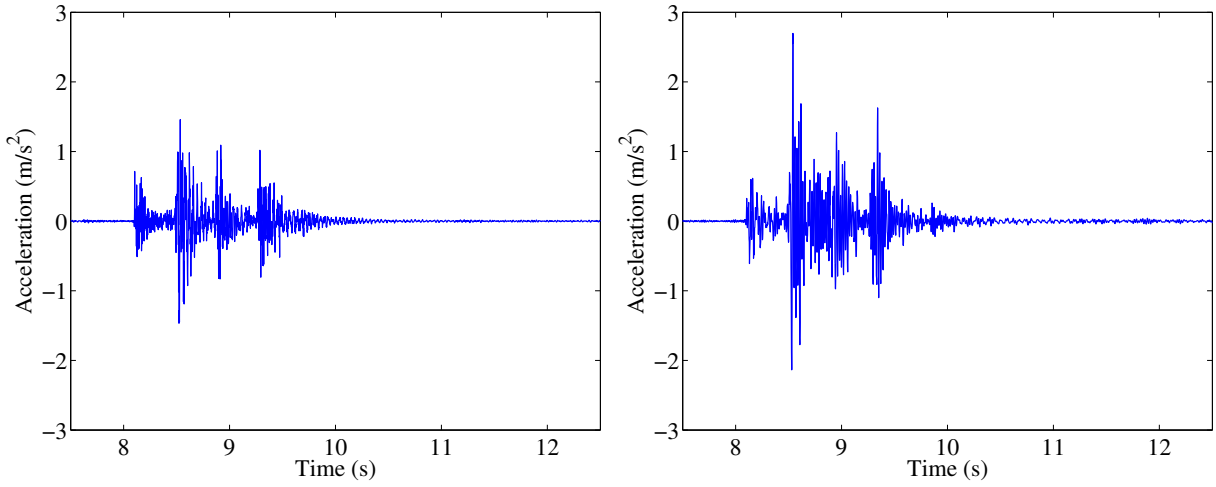

(a) Vertical, 04+Z

(b) Lateral, 05+Y

Figure A.8: Sample acceleration histories for single person running at a pace of 170 BPM, weight: 0.61 kN, leg length: 0.89 m

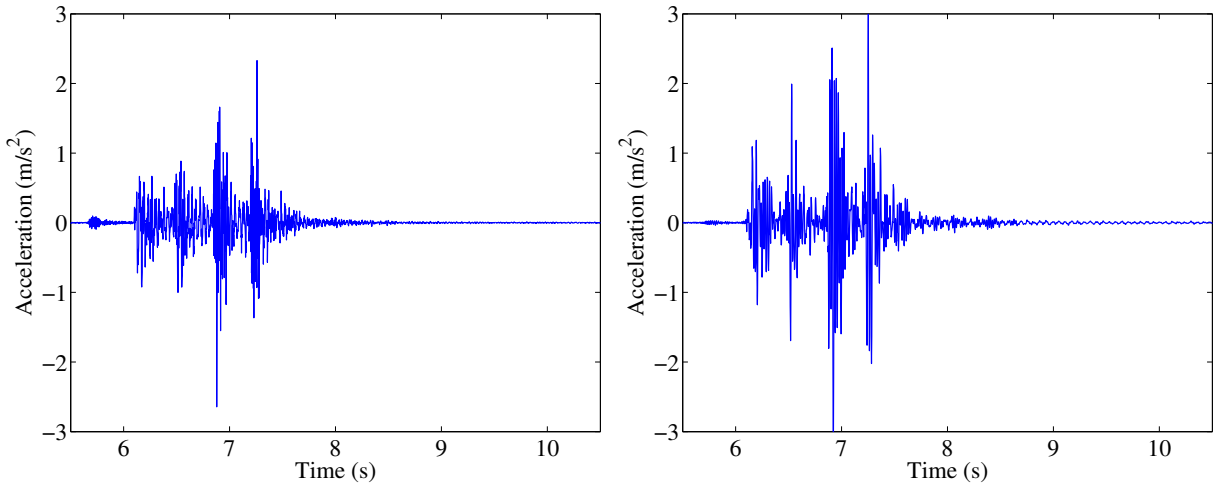

(a) Vertical, 04+Z

(b) Lateral, 05+Y

Figure A.9: Sample acceleration histories for single person running at a pace of 180 BPM, weight: 0.61 kN, leg length: 0.89 m

Figure A.10 shows sample results for two people (0.5 p/m^2) passing over the bridge at a time in the same direction.

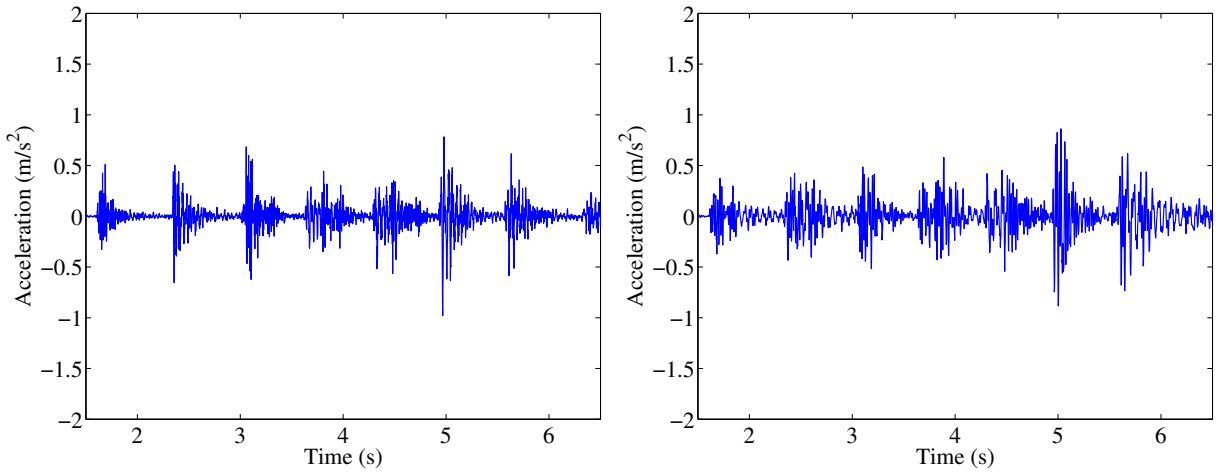

(a) Vertical, 04+Z

(b) Lateral, 05+Y

Figure A.10: Sample acceleration histories for 0.5 p/m^2 walking, total weight: 1.37 kN

Figures A.11 and A.12 show similar results for crowds of 1.0 p/m^2 and 1.5 p/m^2.

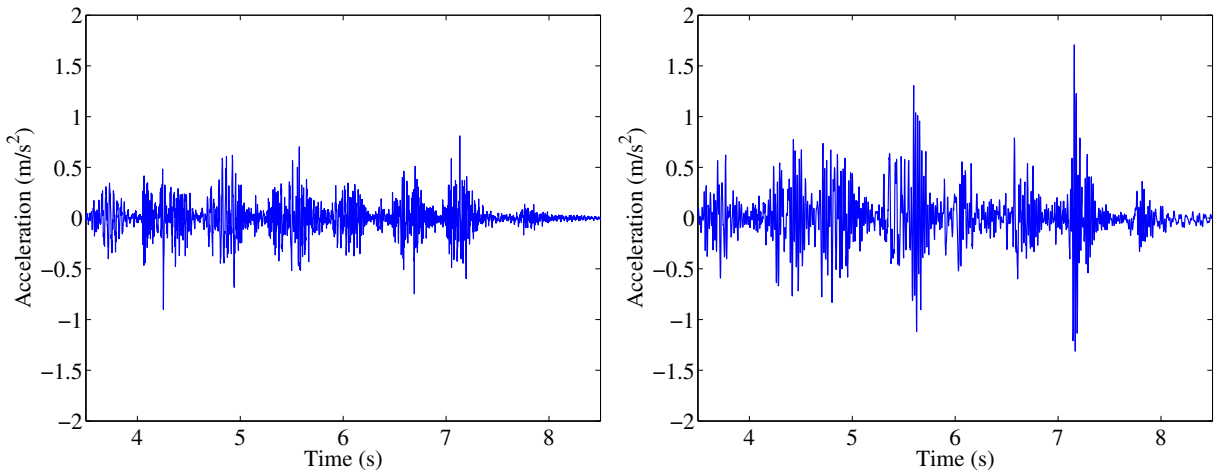

(a) Vertical, 04+Z

(b) Lateral, 05+Y

Figure A.11: Sample acceleration histories for 1.0 p/m^2 walking, total weight: 3.22 kN

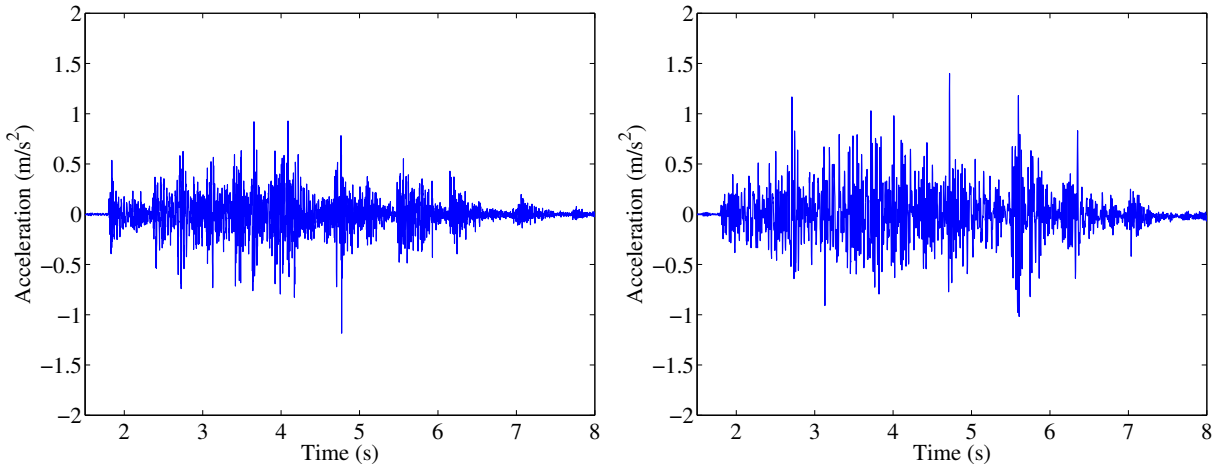

(a) Vertical, 04+Z

(b) Lateral, 04+Y

Figure A.12: Sample acceleration histories for 1.5 p/m^2 walking, total weight: 4.75 kN

A.0.1 Eight-bay bridge

Figure A.13 shows sample acceleration plots for the vertical hammer impact test.

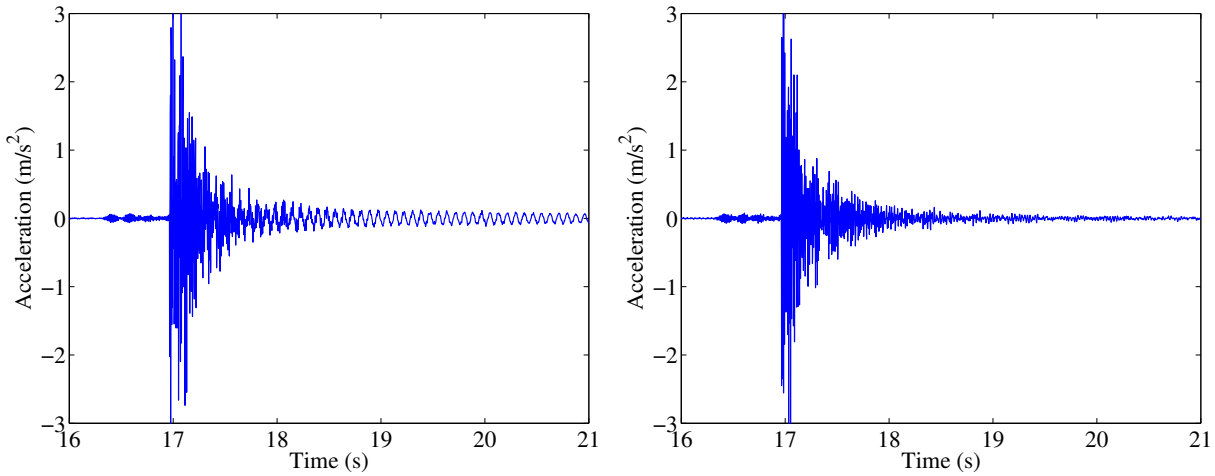

(a) Vertical, 04+Z

(b) Lateral, 05+Y

Figure A.13: Sample acceleration histories from impact test

Figure A.14 shows sample acceleration plots for the lateral pulley release test.

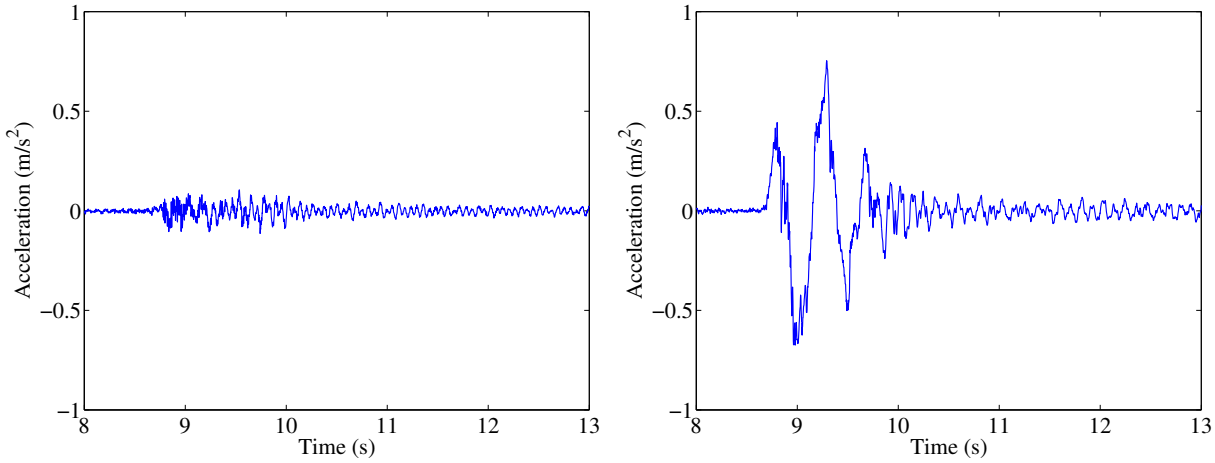

(a) Vertical, 04+Z

(b) Lateral, 05+Y

Figure A.14: Sample acceleration histories from lateral pulley release test

Figure A.15 shows sample acceleration plots for a single person walking at a pace of 100 BPM.

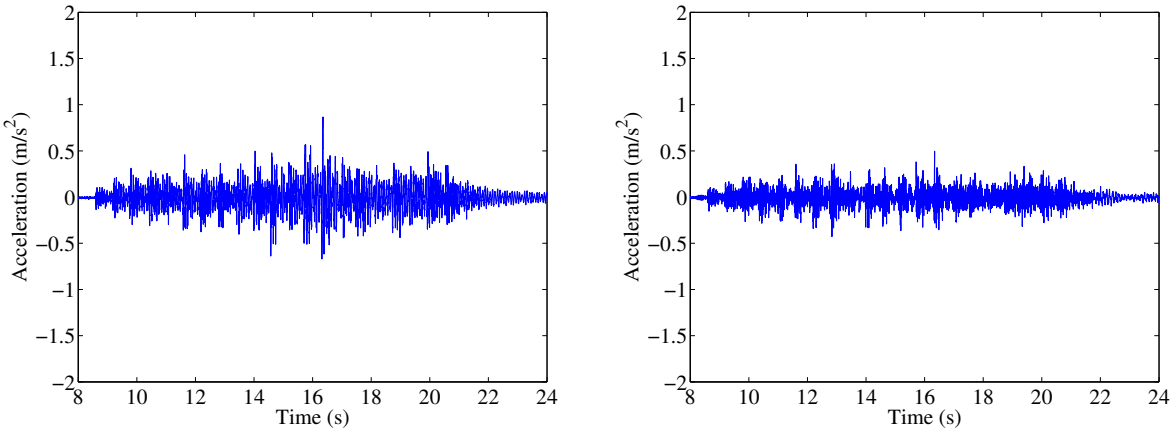

(a) Vertical, 04+Z

(b) Lateral, 05+Y

Figure A.15: Sample acceleration histories for single person walking at a pace of 100 BPM, weight: 0.65 kN, leg length: 0.95 m

Figures A.16, A.17, A.18, A.19, A.20, A.21, and A.22, show similar results for the same person running or walking at different speeds.

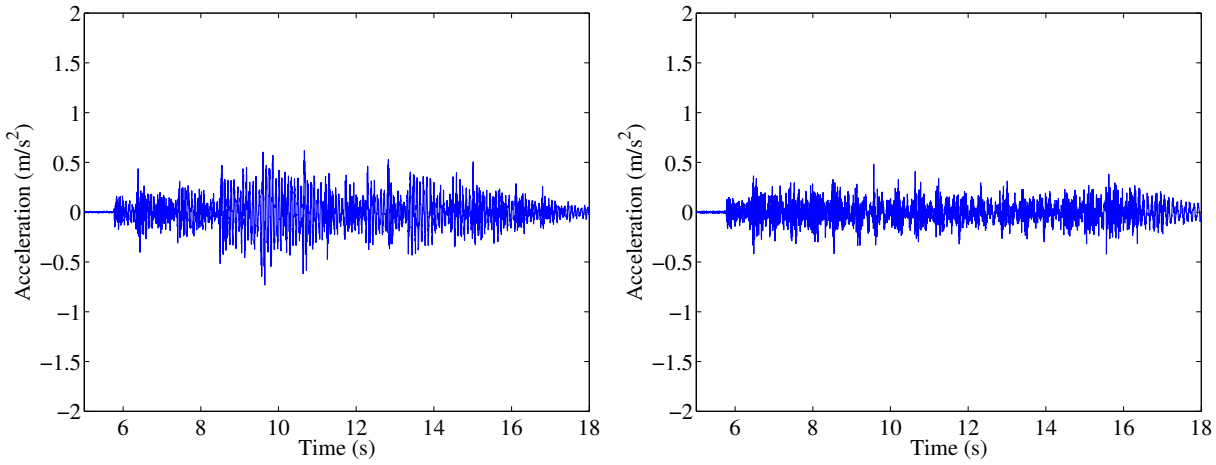

(a) Vertical, 04+Z

(b) Lateral, 05+Y

Figure A.16: Sample acceleration histories for single person walking at a pace of 110 BPM, weight: 0.65 kN, leg length: 0.95 m

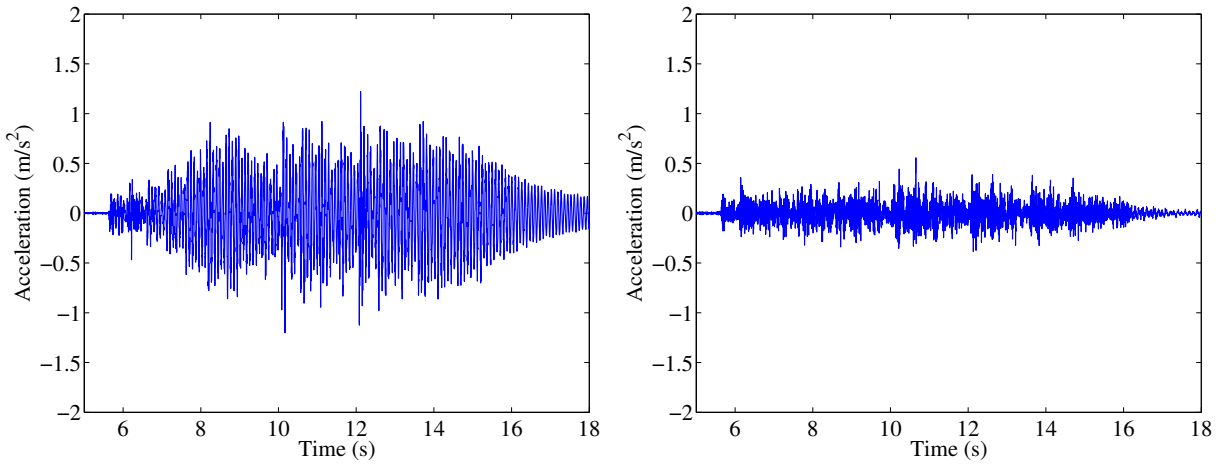

(a) Vertical, 04+Z

(b) Lateral, 05+Y

Figure A.17: Sample acceleration histories for single person walking at a pace of 120 BPM, weight: 0.65 kN, leg length: 0.95 m

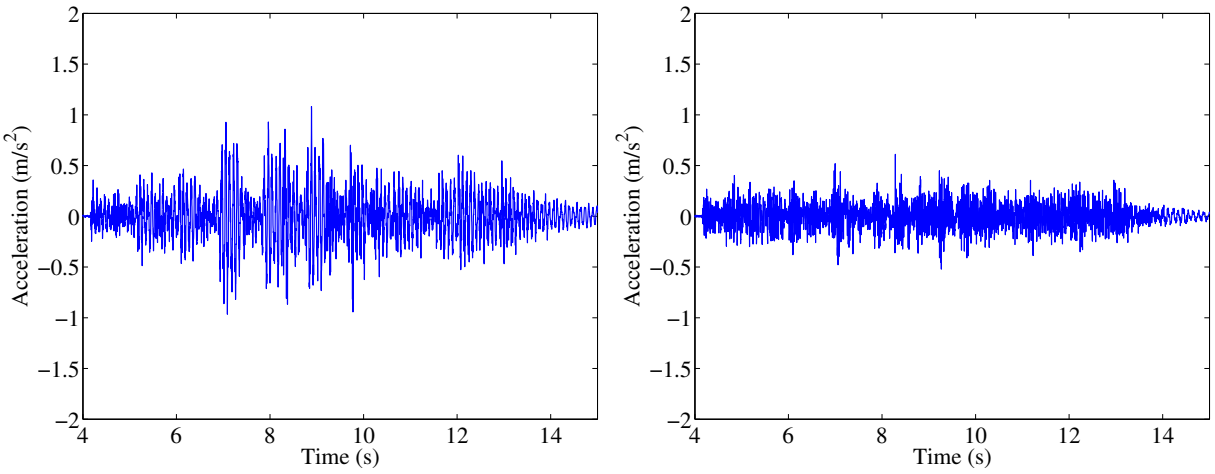

(a) Vertical, 04+Z

(b) Lateral, 05+Y

Figure A.18: Sample acceleration histories for single person walking at a pace of 130 BPM, weight: 0.65 kN, leg length: 0.95 m

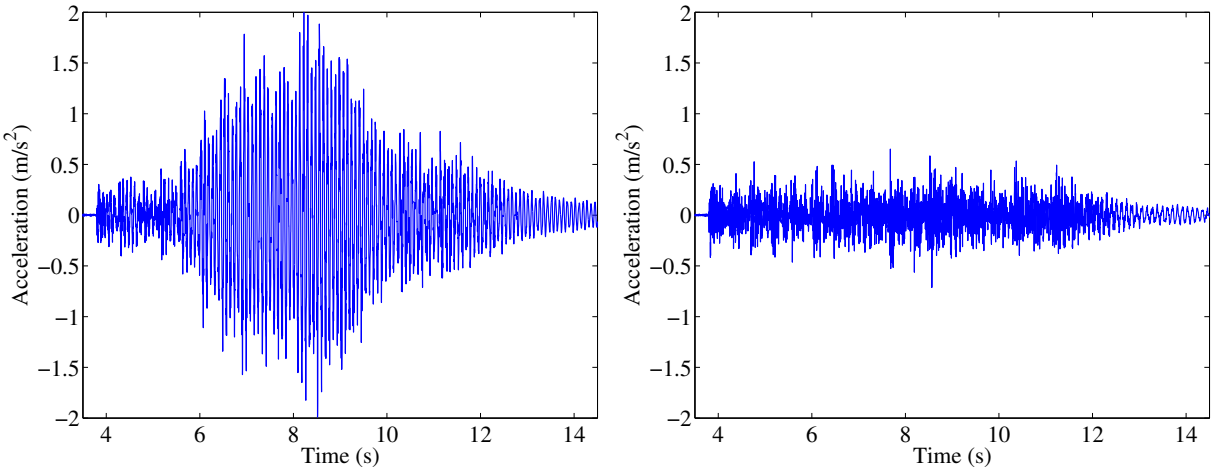

(a) Vertical, 04+Z

(b) Lateral, 05+Y

Figure A.19: Sample acceleration histories for single person walking at a pace of 140 BPM, weight: 0.65 kN, leg length: 0.95 m

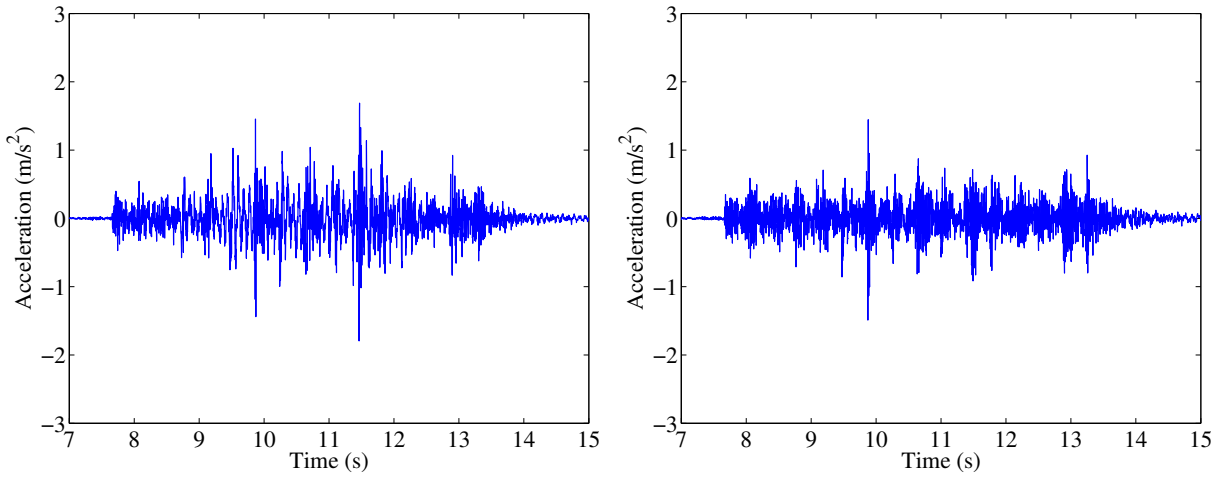

(a) Vertical, 04+Z

(b) Lateral, 05+Y

Figure A.20: Sample acceleration histories for single person running at a pace of 160 BPM, weight: 0.65 kN, leg length: 0.95 m

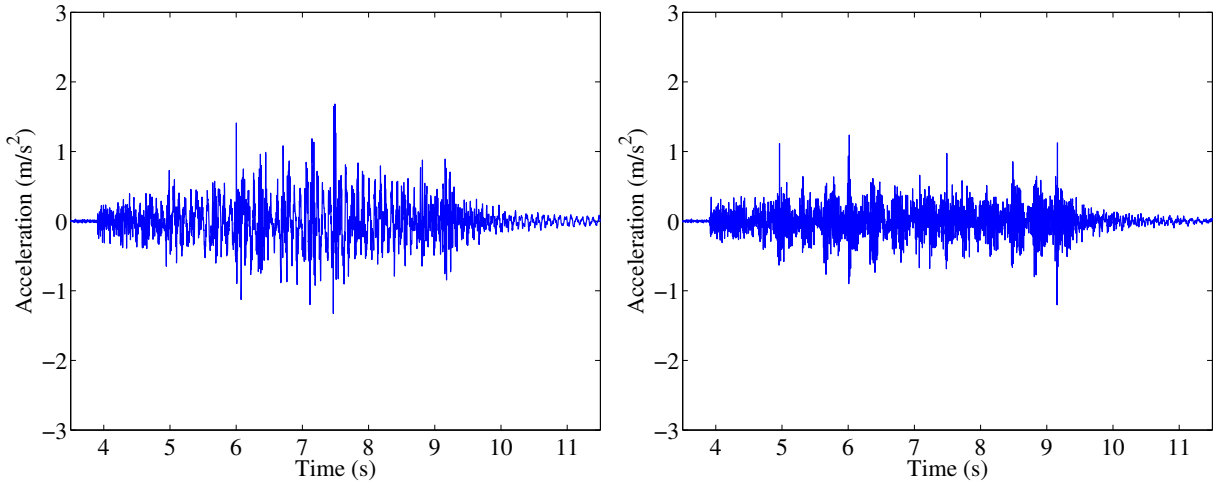

(a) Vertical, 04+Z

(b) Lateral, 05+Y

Figure A.21: Sample acceleration histories for single person running at a pace of 170 BPM, weight: 0.65 kN, leg length: 0.95 m

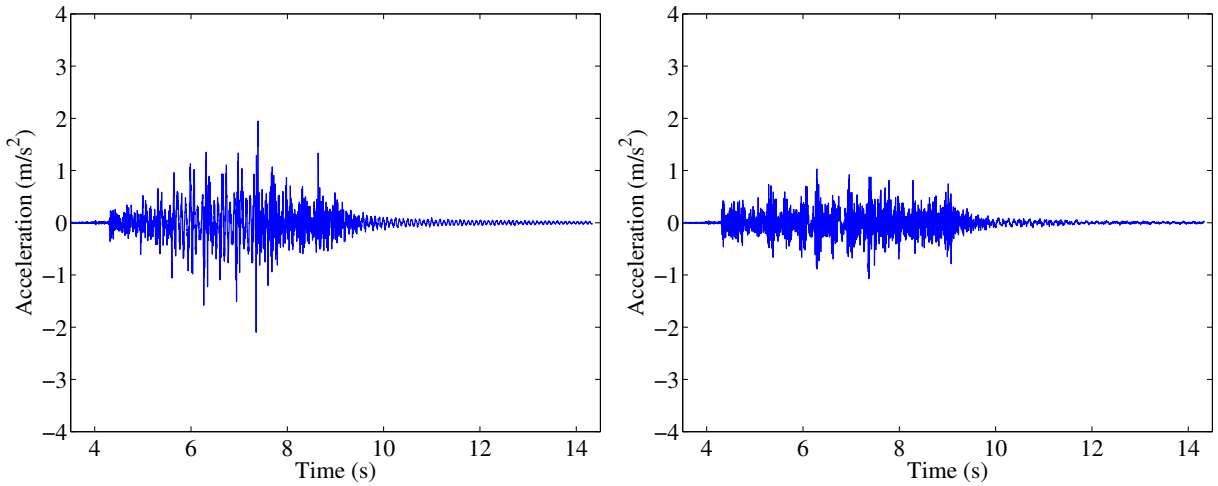

(a) Vertical, 04+Z

(b) Lateral, 05+Y

Figure A.22: Sample acceleration histories for single person running at a pace of 180 BPM, weight: 0.65 kN, leg length: 0.95 m

Figure A.23 shows sample results for the smallest crowd (0.2 p/m^2) passing over the bridge at a time in the same direction.

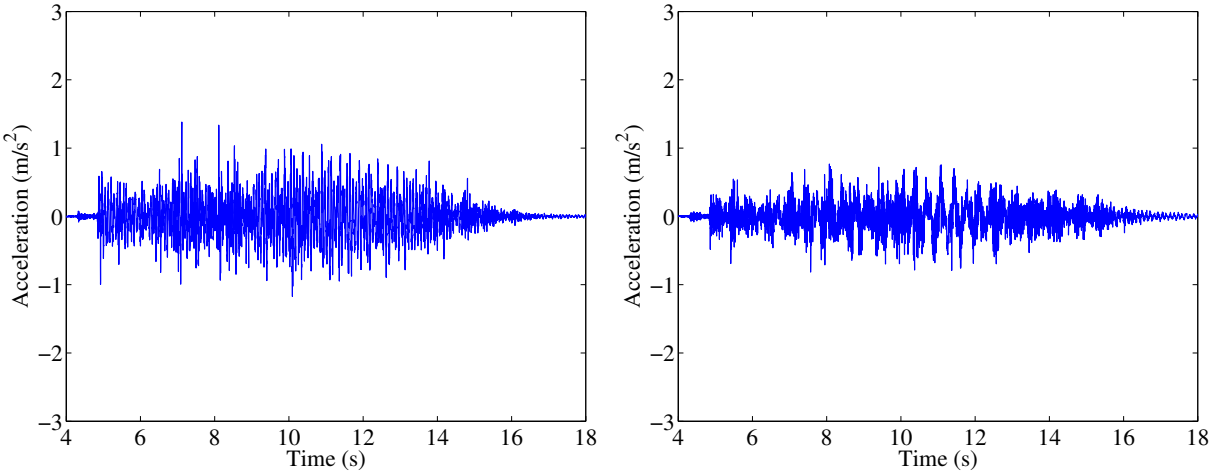

(a) Vertical, 04+Z (b) Lateral, 05+Y

Figure A.23: Sample acceleration histories for 0.2 p/m^2 walking, total weight: 2.18 kN

Figures A.24 and A.25 show similar results for crowds of 0.5 p/m^2 and 1.0 p/m^2.

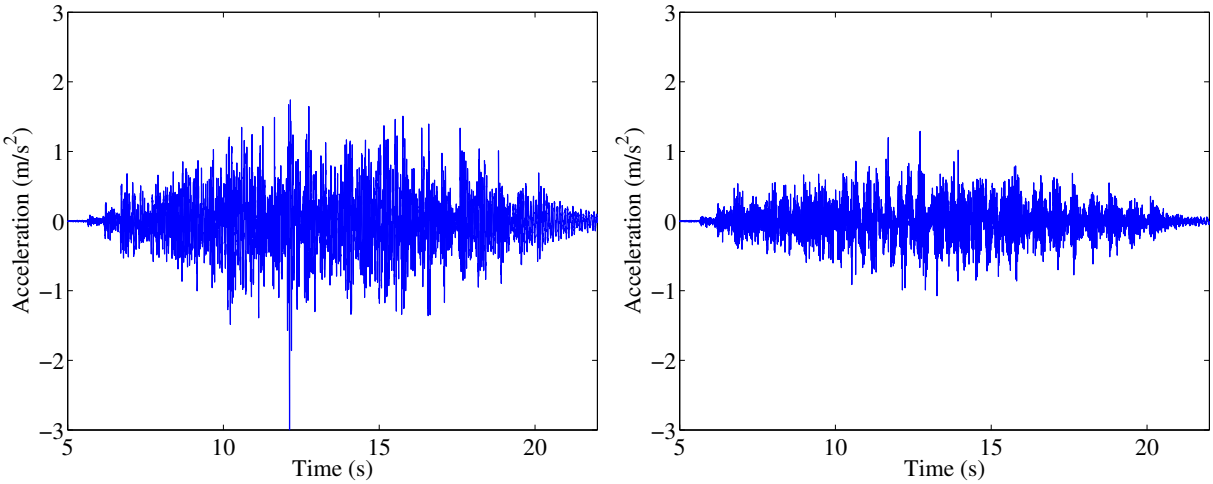

(a) Vertical, 04+Z (b) Lateral, 05+Y

Figure A.24: Sample acceleration histories for 0.5 p/m^2 walking, total weight: 5.41 kN

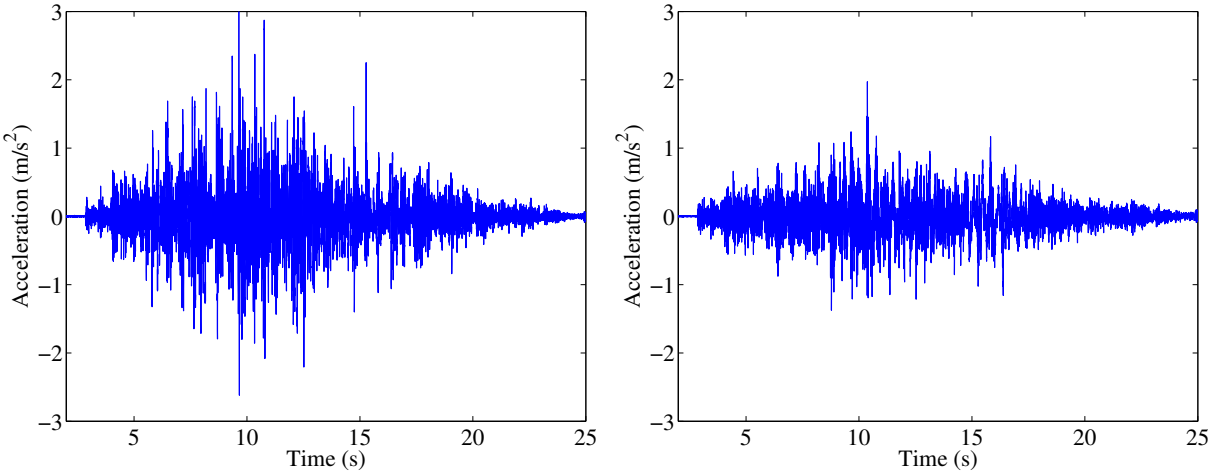

(a) Vertical, 04+Z

(b) Lateral, 05+Y

Figure A.25: Sample acceleration histories for 1.0 p/m^2 walking, total weight: 11.30 kN

Figures A.26 and A.27 show the acceleration histories for two people walking in sync and out of sync (one at 115 BPM and one at 130 BPM).

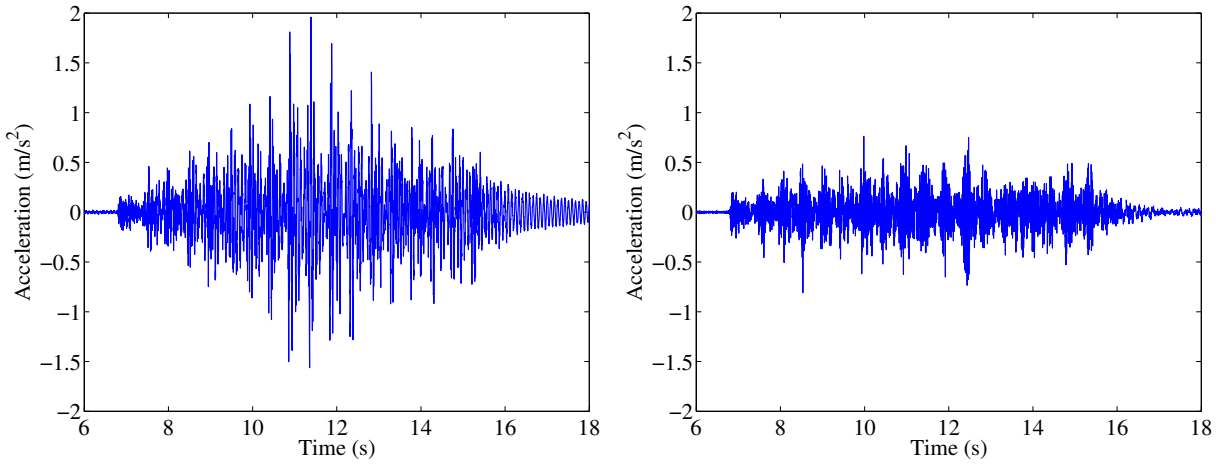

(a) Vertical, 04+Z

(b) Lateral, 05+Y

Figure A.26: Sample acceleration histories for two people walking synchronously, total weight: 1.25 kN

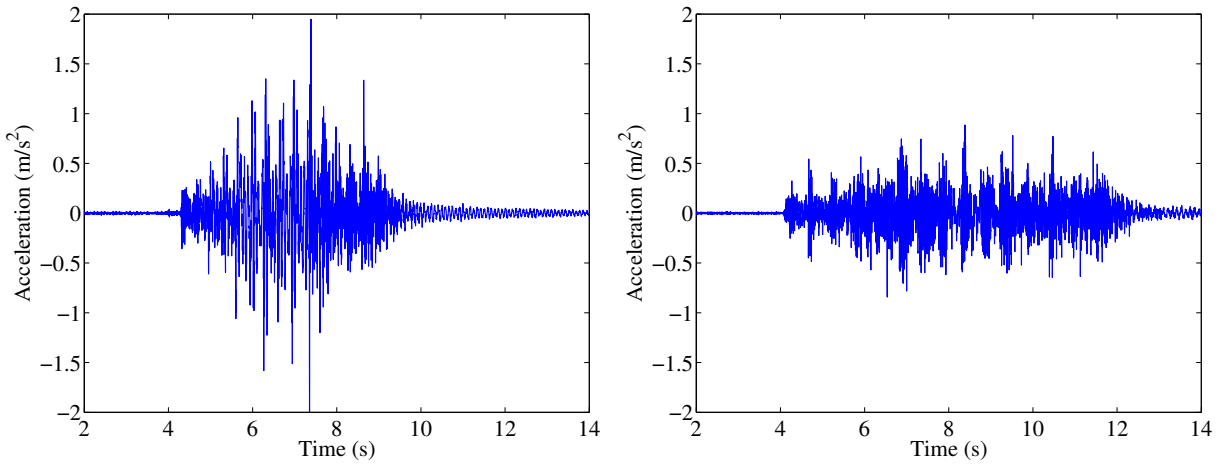

(a) Vertical, 04+Z

(b) Lateral, 05+Y

Figure A.27: Sample acceleration histories for two people walking asynchronously, total weight: 1.25 kN

A.0.2 Fourteen-bay bridge

Figure A.28 shows sample acceleration plots for the vertical hammer impact test.

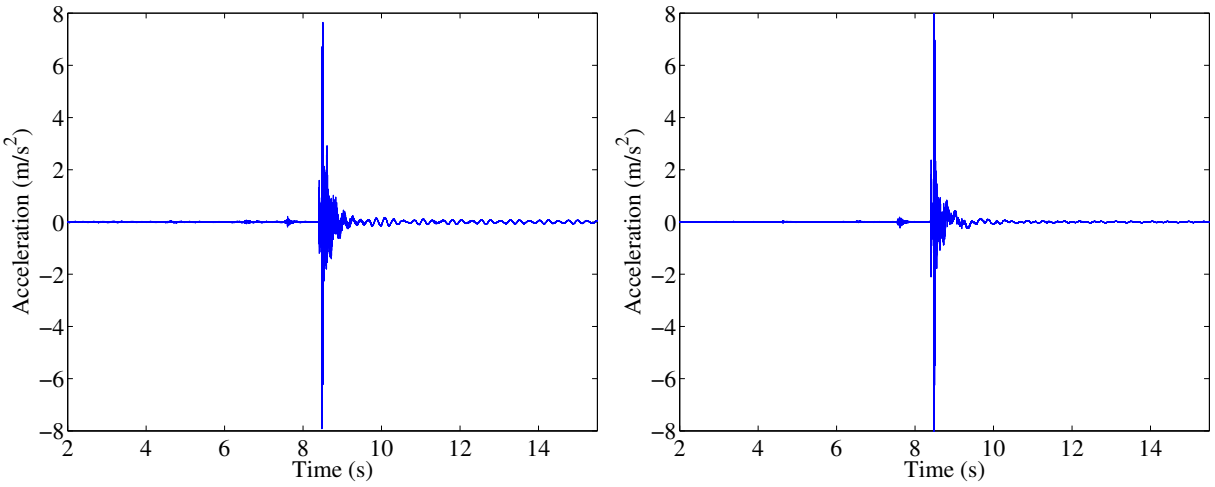

(a) Vertical, 04+Z

(b) Lateral, 05+Y

Figure A.28: Sample acceleration histories from impact test

Figure A.29 shows sample acceleration plots for the lateral pulley release test.

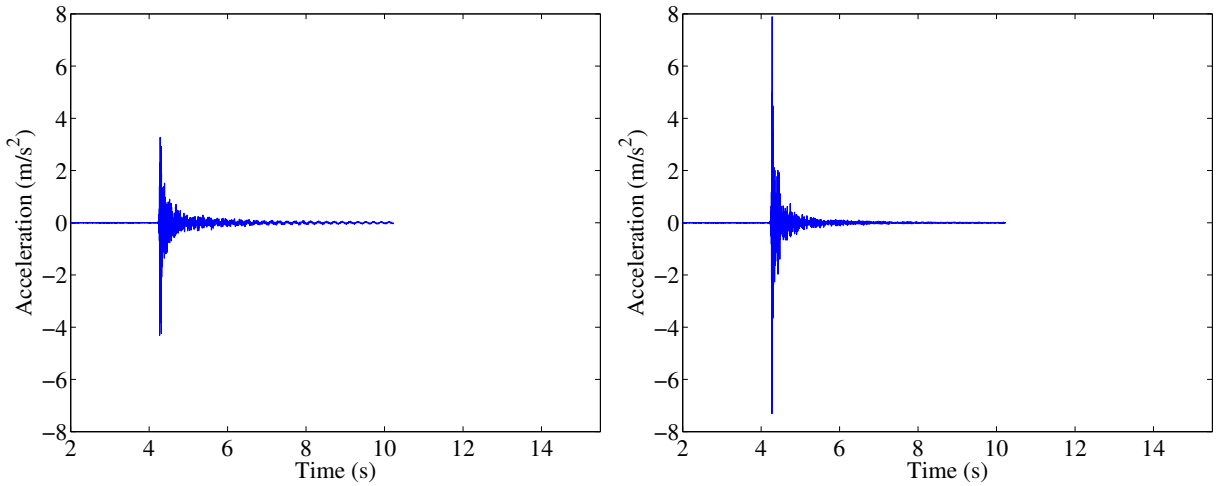

(a) Vertical, 04+Z

(b) Lateral, 05+Y

Figure A.29: Sample acceleration histories from lateral pulley release test

Figure A.30 shows sample acceleration plots for a single person walking at a pace of 100 BPM.

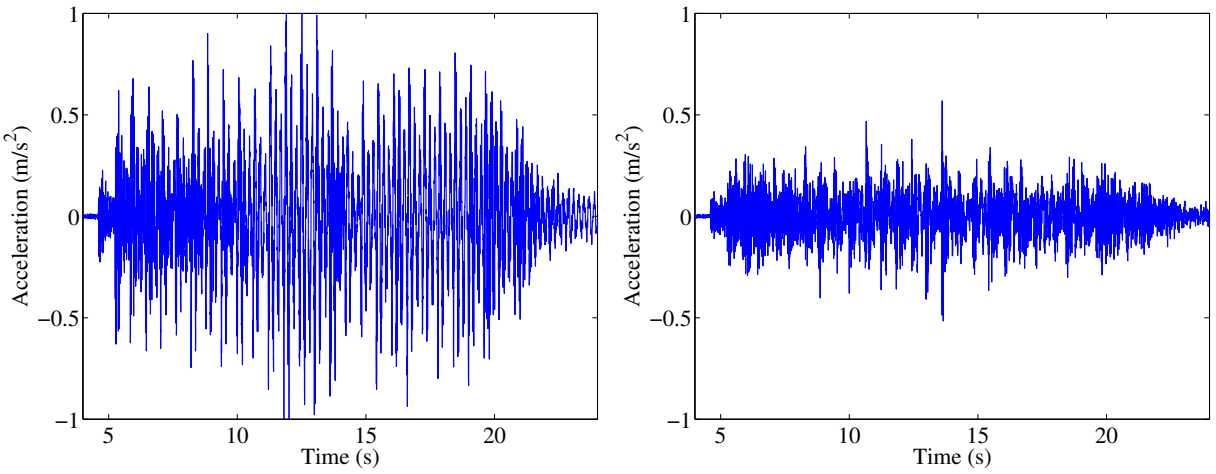

(a) Vertical, 04+Z

(b) Lateral, 05+Y

Figure A.30: Sample acceleration histories for single person walking at a pace of 100 BPM, weight: 0.65 kN, leg length: 0.95 m

Figures A.31, A.32, A.33, A.34, A.35, A.36, and A.37, show similar results for the same person running or walking at different speeds.

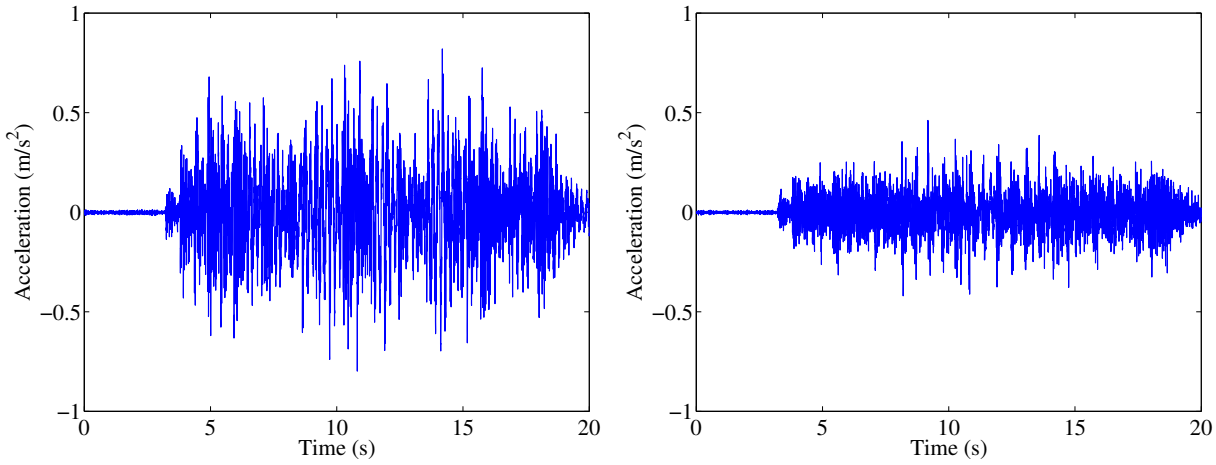

(a) Vertical, 04+Z

(b) Lateral, 05+Y

Figure A.31: Sample acceleration histories for single person walking at a pace of 110 BPM, weight: 0.65 kN, leg length: 0.95 m

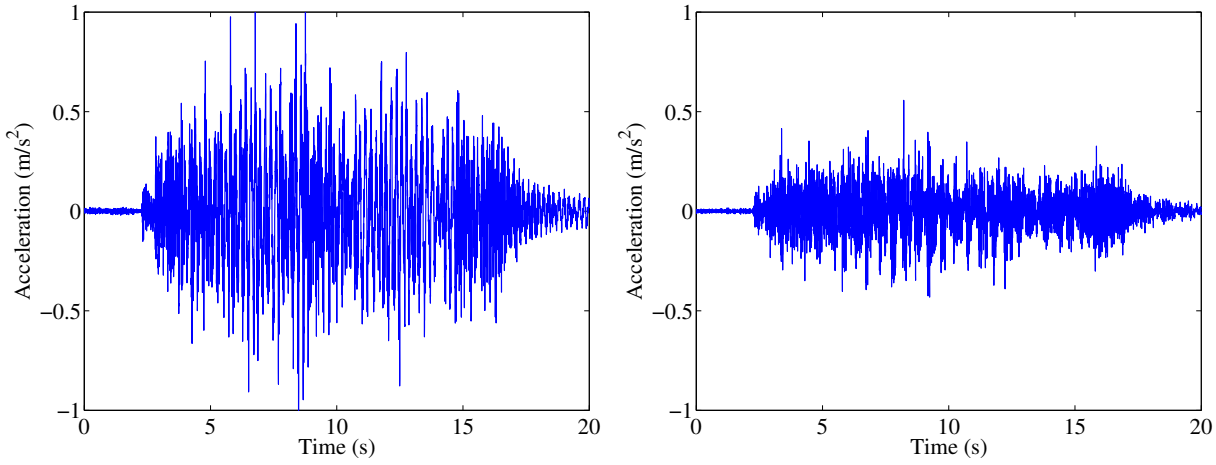

(a) Vertical, 04+Z

(b) Lateral, 05+Y

Figure A.32: Sample acceleration histories for single person walking at a pace of 120 BPM, weight: 0.65 kN, leg length: 0.95 m

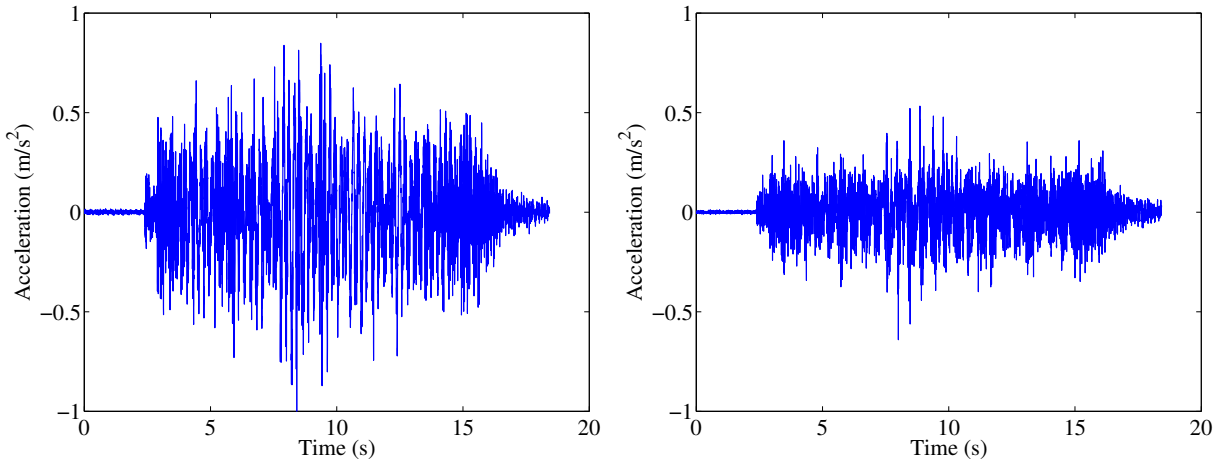

(a) Vertical, 04+Z

(b) Lateral, 05+Y

Figure A.33: Sample acceleration histories for single person walking at a pace of 130 BPM, weight: 0.65 kN, leg length: 0.95 m

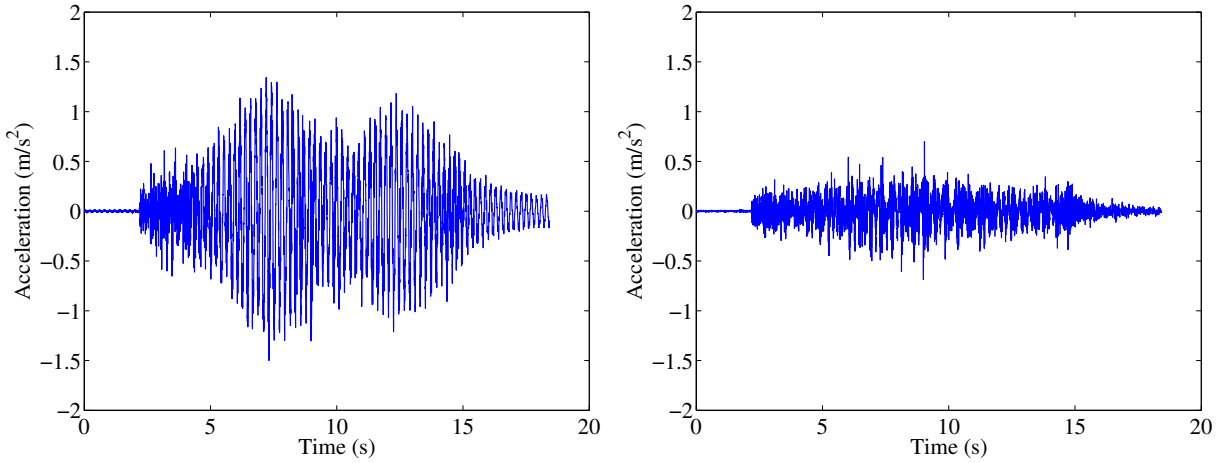

(a) Vertical, 04+Z

(b) Lateral, 05+Y

Figure A.34: Sample acceleration histories for single person walking at a pace of 140 BPM, weight: 0.65 kN, leg length: 0.95 m

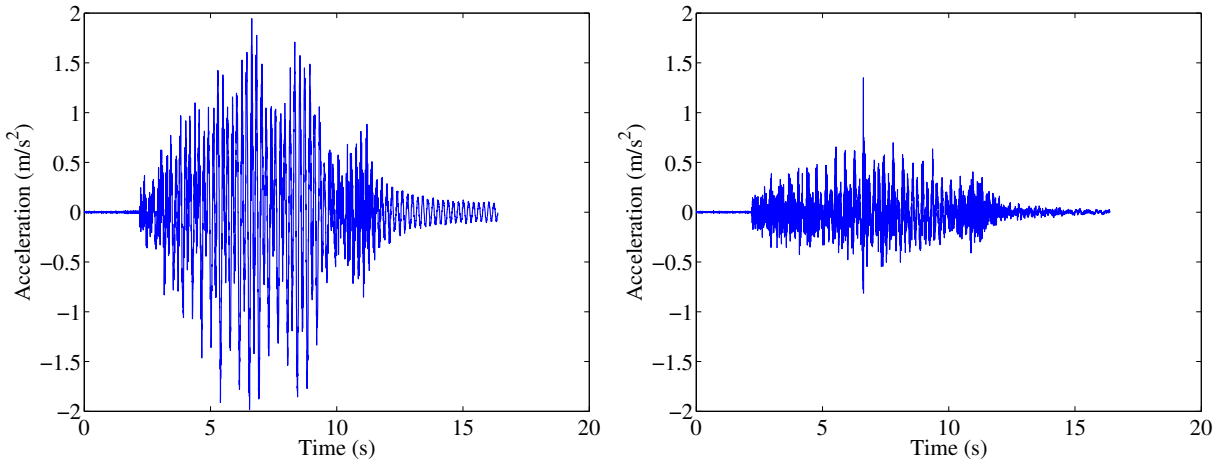

(a) Vertical, 04+Z

(b) Lateral, 05+Y

Figure A.35: Sample acceleration histories for single person running at a pace of 160 BPM, weight: 0.65 kN, leg length: 0.95 m

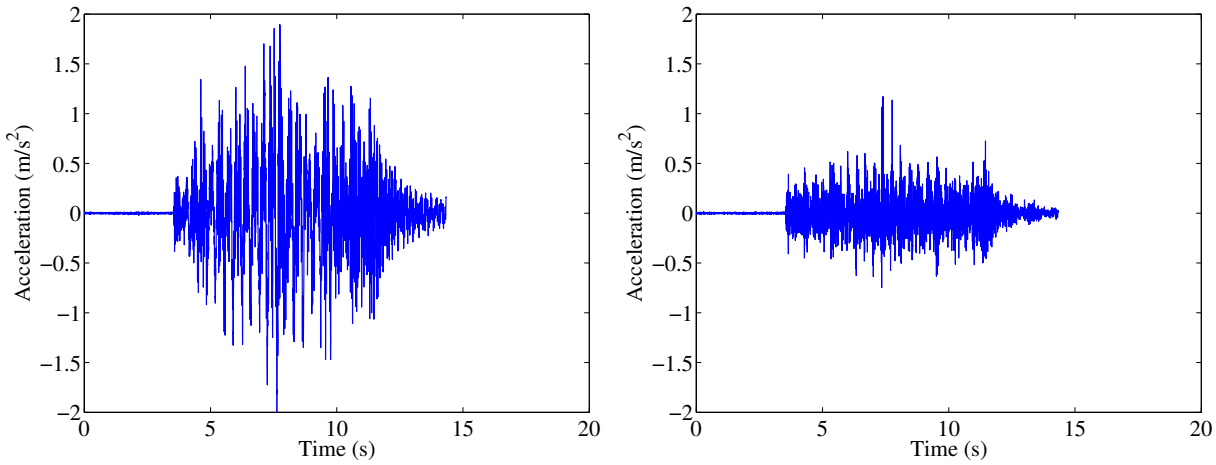

(a) Vertical, 04+Z

(b) Lateral, 05+Y

Figure A.36: Sample acceleration histories for single person running at a pace of 170 BPM, weight: 0.65 kN, leg length: 0.95 m

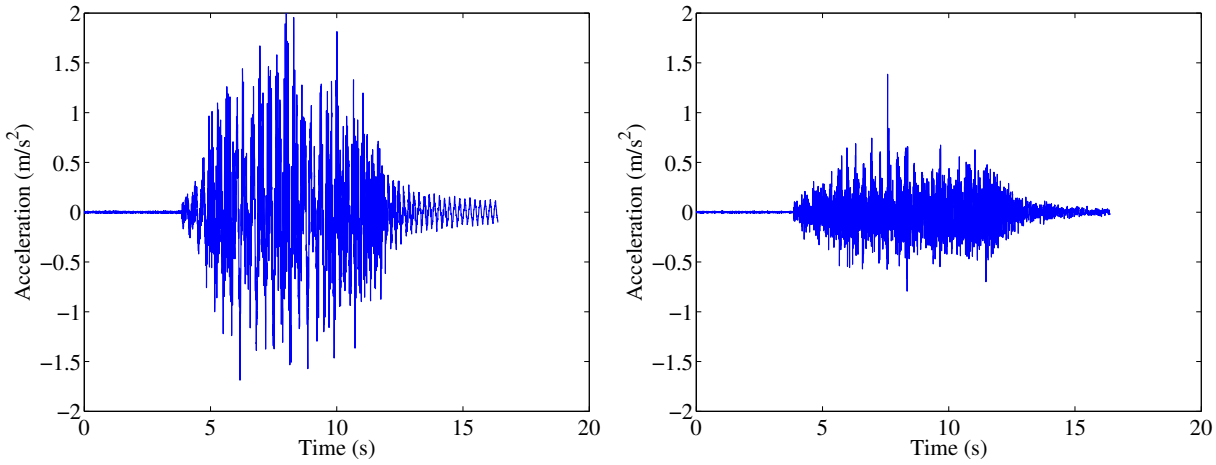

(a) Vertical, 04+Z

(b) Lateral, 05+Y

Figure A.37: Sample acceleration histories for single person running at a pace of 180 BPM, weight: 0.65 kN, leg length: 0.95 m

Figure A.38 shows sample results for the smallest crowd (0.2 p/m^2) passing over the bridge at a time in the same direction.

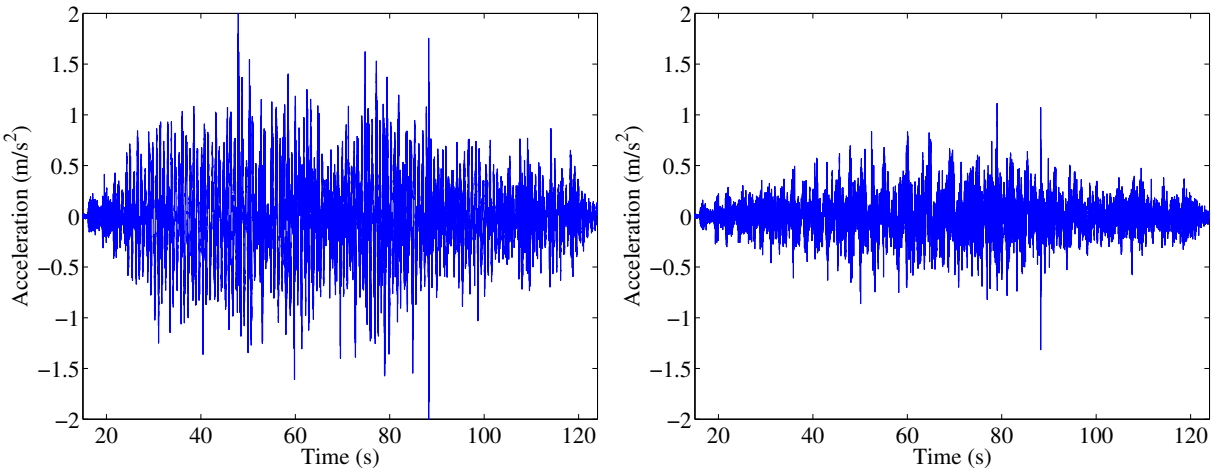

(a) Vertical, 04+Z (b) Lateral, 05+Y

Figure A.38: Sample acceleration histories for 0.2 p/m^2 walking, total weight: 4.27 kN

Figures A.39 and A.40 show similar results for crowds of 0.5 p/m^2 and 1.0 p/m^2.

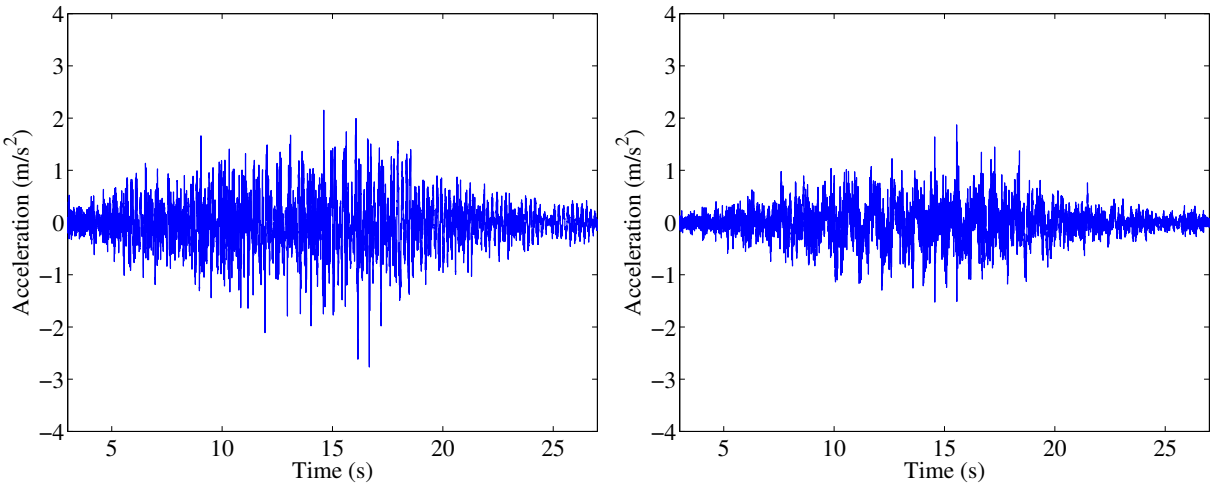

(a) Vertical, 04+Z (b) Lateral, 05+Y

Figure A.39: Sample acceleration histories for 0.5 p/m^2 walking, total weight: 9.66 kN

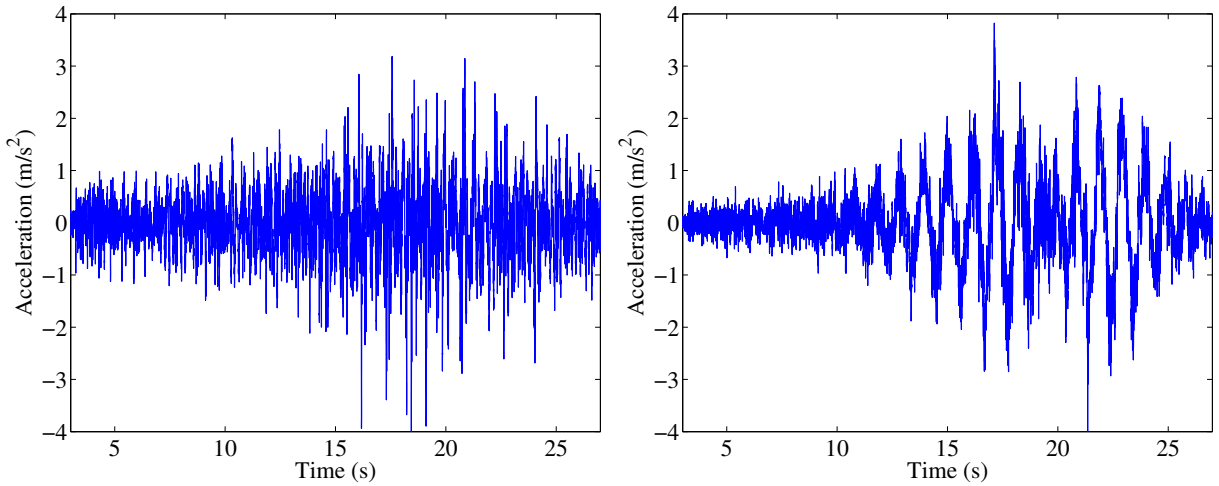

(a) Vertical, 04+Z

(b) Lateral, 05+Y

Figure A.40: Sample acceleration histories for 1.0 p/m^2 walking, total weight: 20.32 kN

Figures A.41 and A.42 show the acceleration histories for two people walking in sync and out of sync (one at 115 BPM and one at 130 BPM).

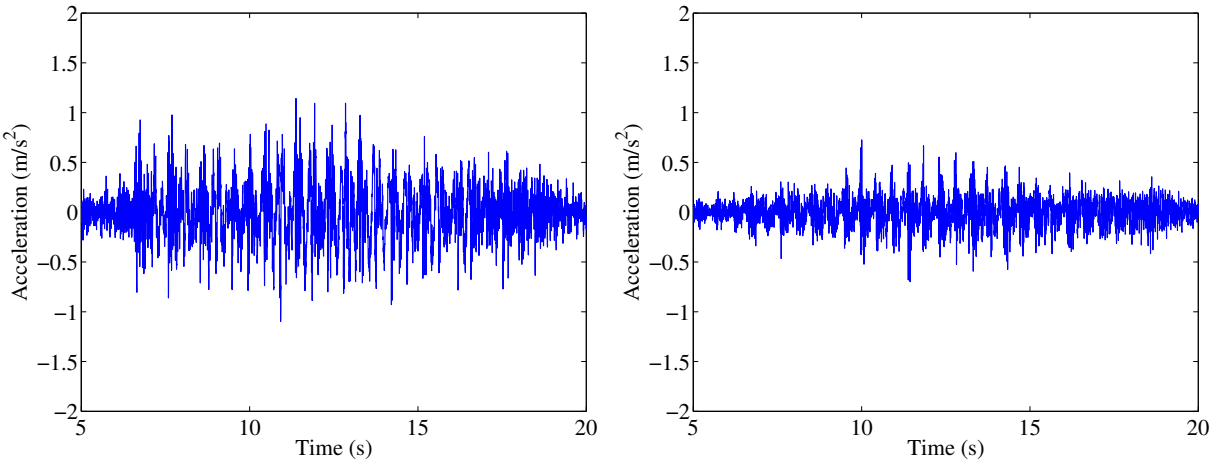

(a) Vertical, 04+Z

(b) Lateral, 05+Y

Figure A.41: Sample acceleration histories for two people walking synchronously, total weight: 1.25 kN

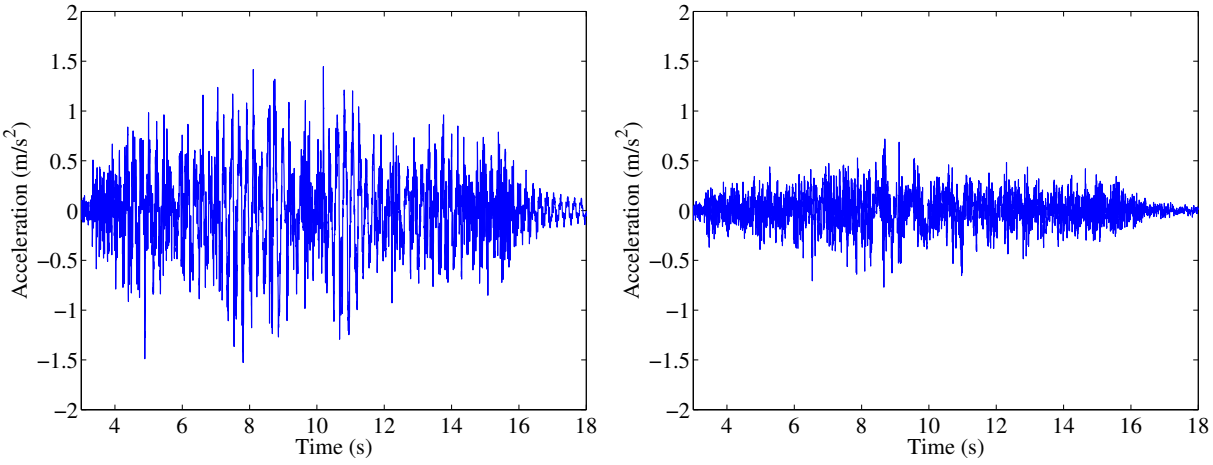

(a) Vertical, 04+Z

(b) Lateral, 05+Y

Figure A.42: Sample acceleration histories for two people walking asynchronously, total weight: 1.25 kN

Appendix B

Load cell results

B.0.3 Two-bay bridge

Figure B.1 shows sample load plots for a single person walking at a pace of 100 BPM.

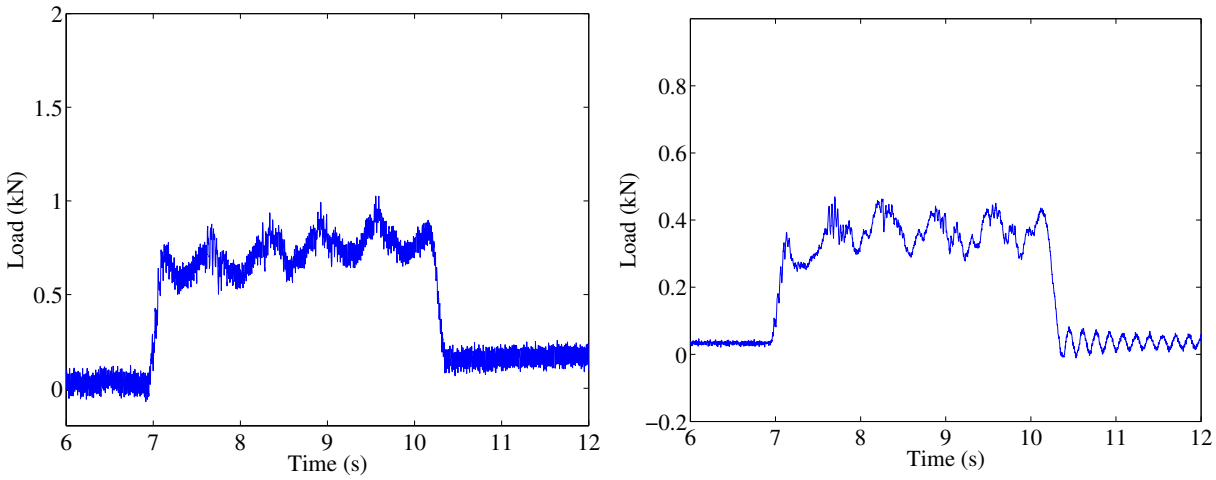

(a) Vertical

(b) Lateral

Figure B.1: Sample load histories for single person walking at a pace of 100 BPM, weight: 0.65 kN, leg length: 0.95 m

Figures B.2, B.3, B.4, B.5, B.6, B.7, and B.8, show similar results for the same person running or walking at different speeds.

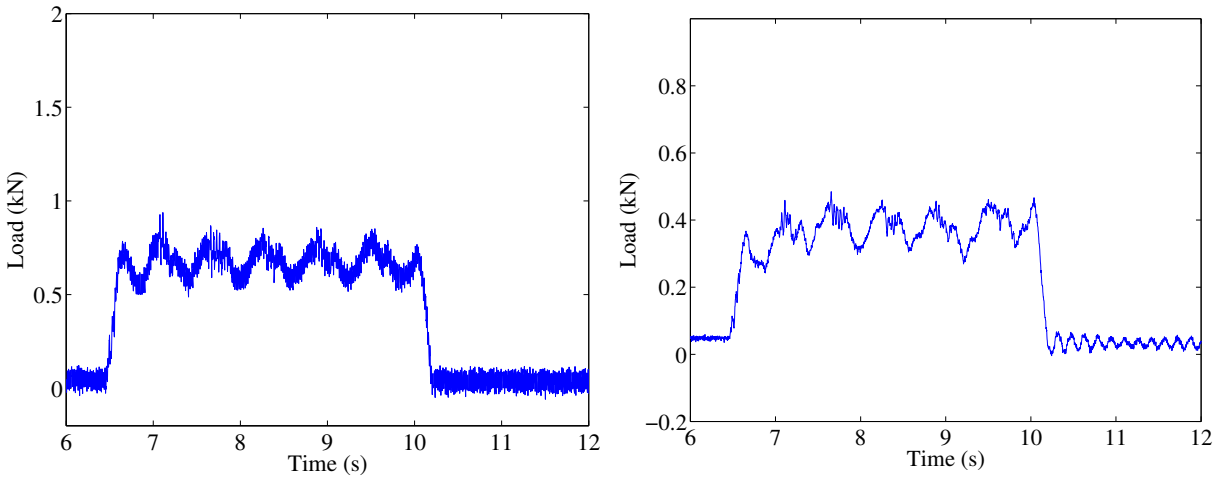

(a) Vertical (b) Lateral

Figure B.2: Sample load histories for single person walking at a pace of 110 BPM, weight: 0.65 kN, leg length: 0.95 m

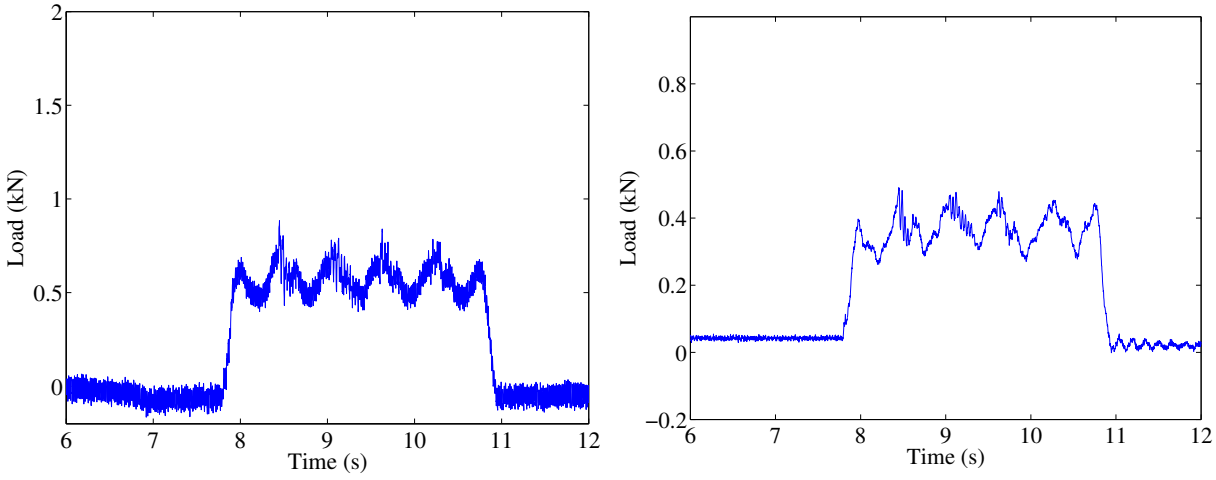

(a) Vertical (b) Lateral

Figure B.3: Sample load histories for single person walking at a pace of 120 BPM, weight: 0.65 kN, leg length: 0.95 m

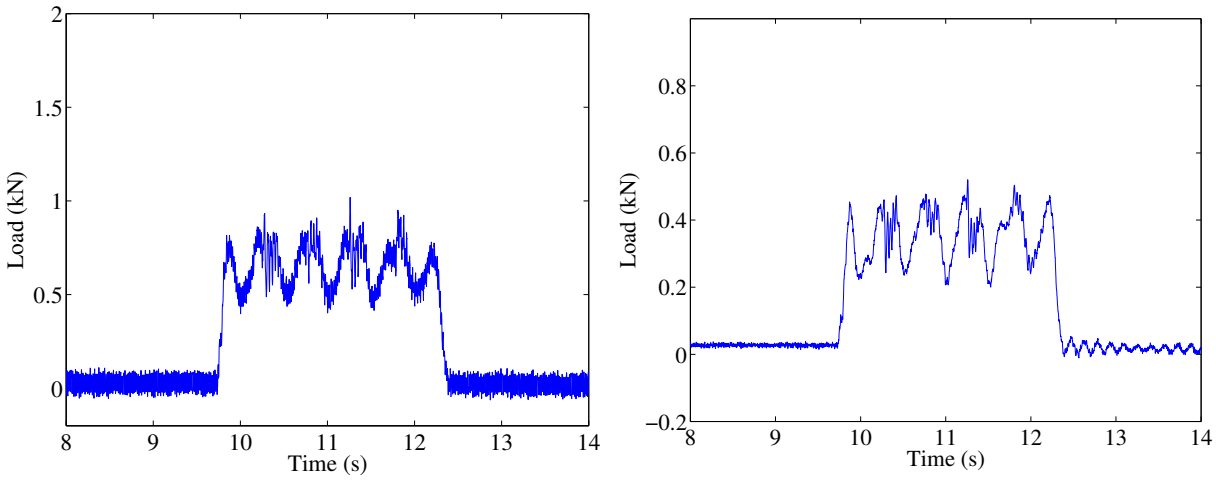

(a) Vertical

(b) Lateral

Figure B.4: Sample load histories for single person walking at a pace of 130 BPM, weight: 0.65 kN, leg length: 0.95 m

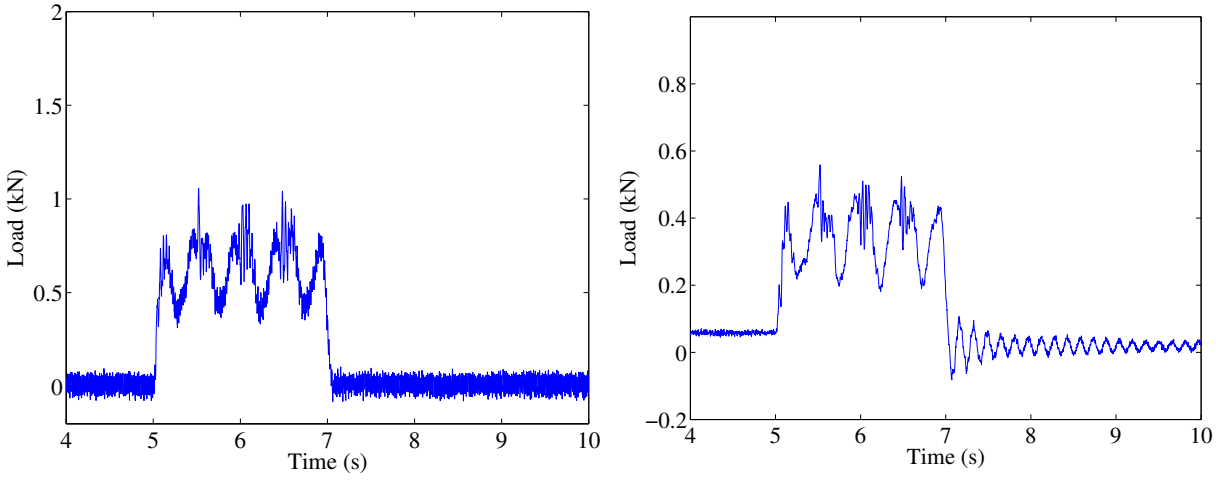

(a) Vertical

(b) Lateral

Figure B.5: Sample load histories for single person walking at a pace of 140 BPM, weight: 0.65 kN, leg length: 0.95 m

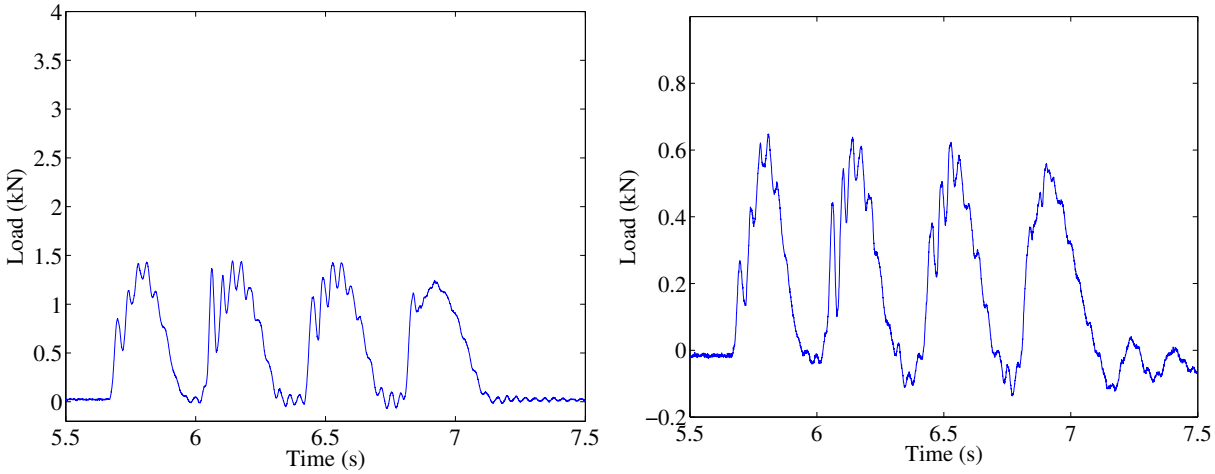

(a) Vertical

(b) Lateral

Figure B.6: Sample load histories for single person running at a pace of 160 BPM, weight: 0.65 kN, leg length: 0.95 m

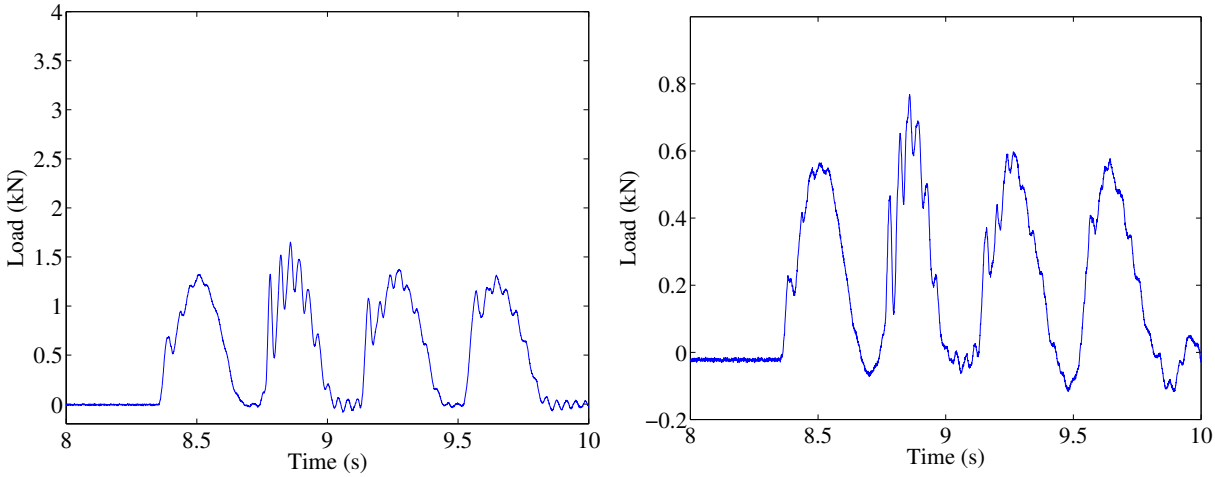

(a) Vertical

(b) Lateral

Figure B.7: Sample load histories for single person running at a pace of 170 BPM, weight: 0.65 kN, leg length: 0.95 m

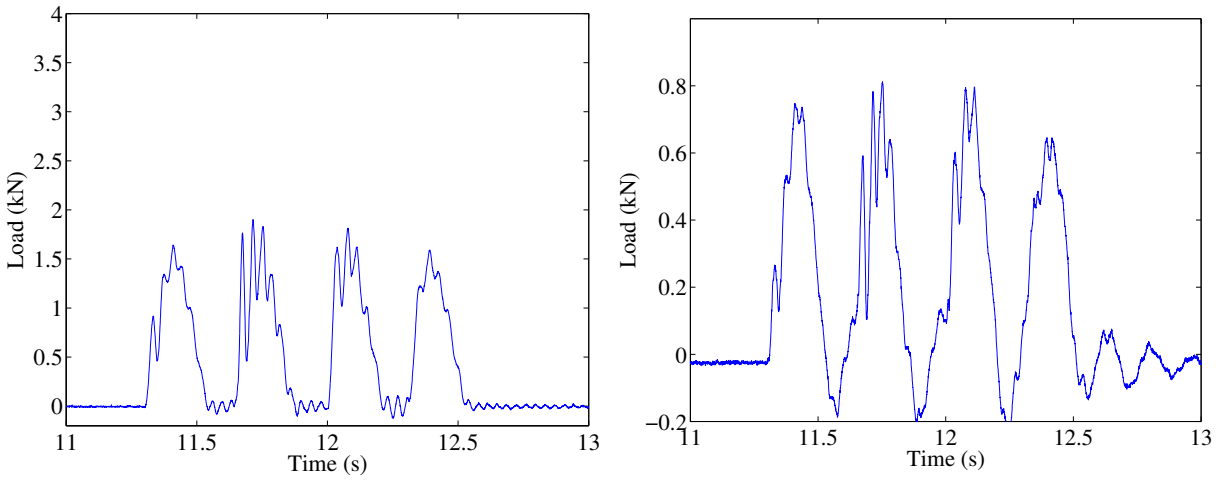

(a) Vertical

(b) Lateral

Figure B.8: Sample load histories for single person running at a pace of 180 BPM, weight: 0.65 kN, leg length: 0.95 m

Figure B.9 shows sample load results for the smallest crowd for the two-bay bridge (0.5 p/m^2) passing over the bridge at a time in the same direction.

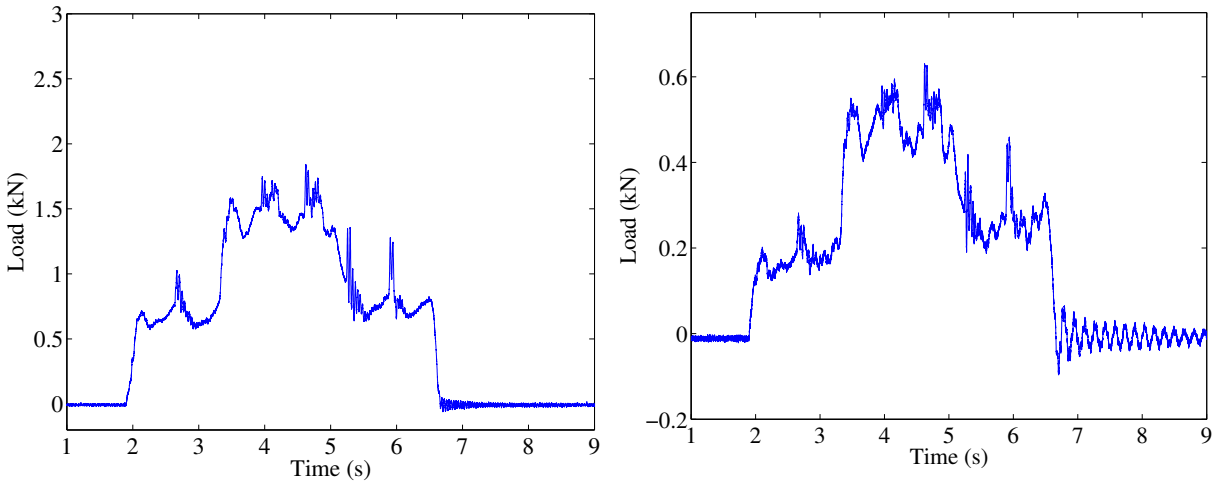

(a) Vertical

(b) Lateral

Figure B.9: Sample load histories for 0.5 p/m^2 walking, total weight: 1.37 kN

Similarly, figures B.10 and B.11 show similar load results for crowds of 1.0 p/m^2 and 1.5 p/m^2.

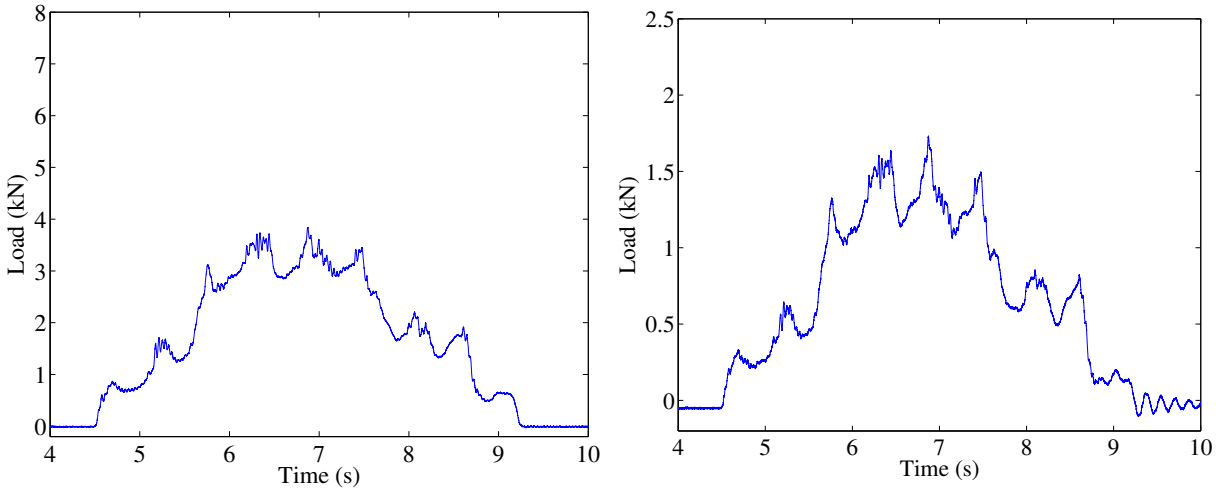

(a) Vertical

(b) Lateral

Figure B.10: Sample load histories for 1.0 p/m^2 walking, total weight: 3.22 kN

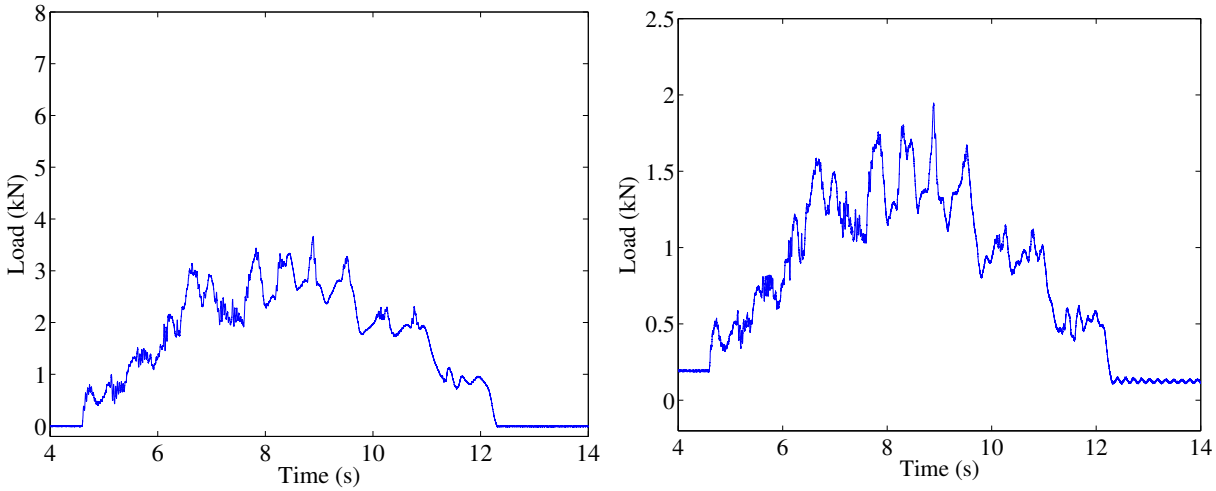

(a) Vertical

(b) Lateral

Figure B.11: Sample load histories for 1.5 p/m^2 walking, total weight: 4.75 kN

B.0.4 Eight-bay bridge

Figure B.12 shows sample load plots for a single person walking at a pace of 100 BPM.

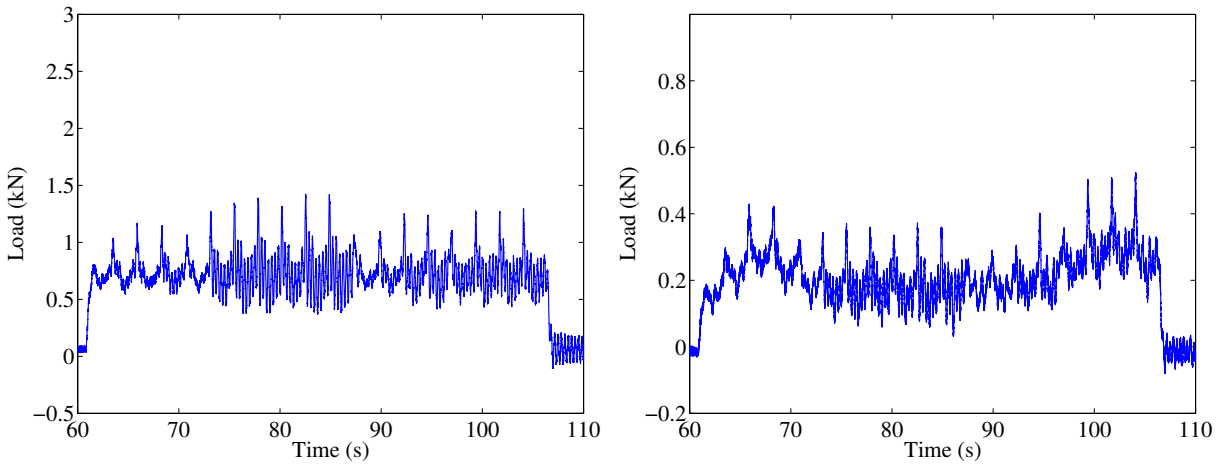

(a) Vertical (b) Lateral

Figure B.12: Sample load histories for single person walking at a pace of 100 BPM, weight: 0.65 kN, leg length: 0.95 m

Figures B.26, B.27, B.28, B.29, B.30, B.31, and B.32, show similar results for the same person running or walking at different speeds.

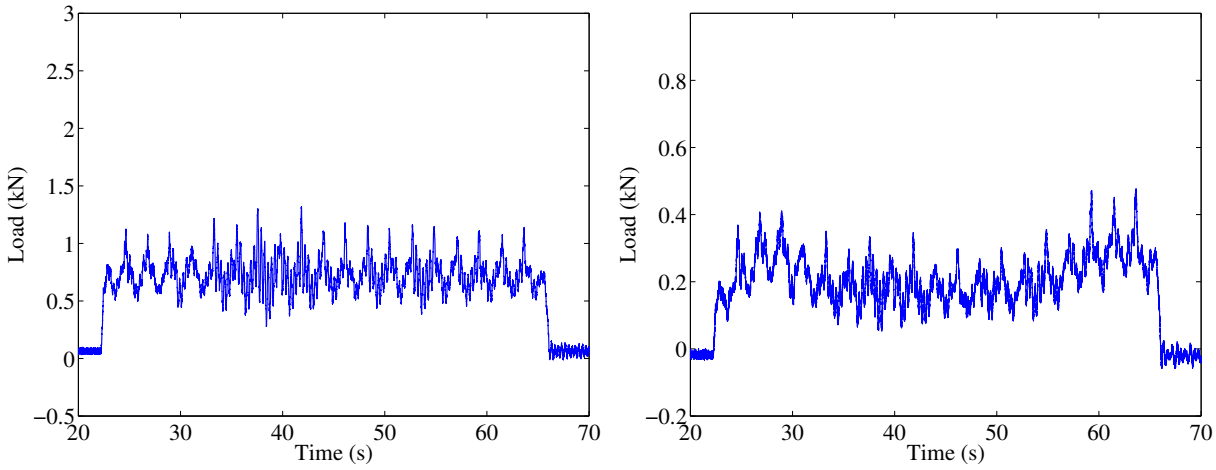

(a) Vertical (b) Lateral

Figure B.13: Sample load histories for single person walking at a pace of 110 BPM, weight: 0.65 kN, leg length: 0.95 m

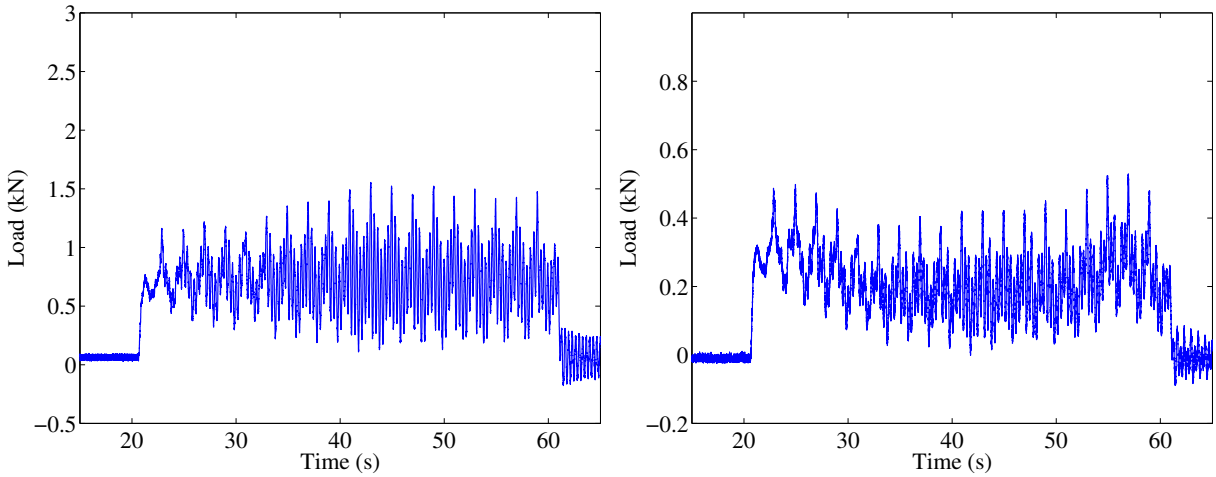

(a) Vertical (b) Lateral

Figure B.14: Sample load histories for single person walking at a pace of 120 BPM, weight: 0.65 kN, leg length: 0.95 m

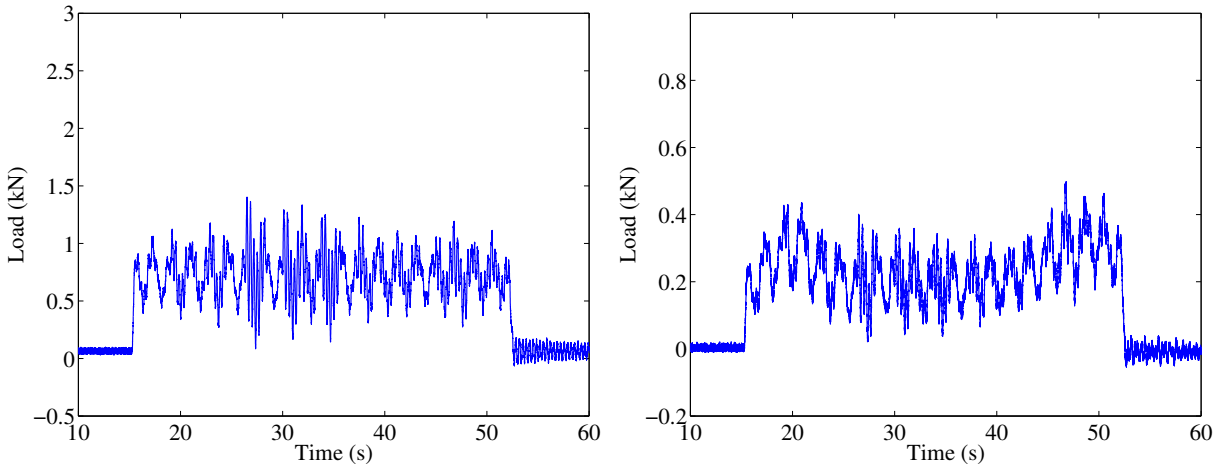

(a) Vertical (b) Lateral

Figure B.15: Sample load histories for single person walking at a pace of 130 BPM, weight: 0.65 kN, leg length: 0.95 m

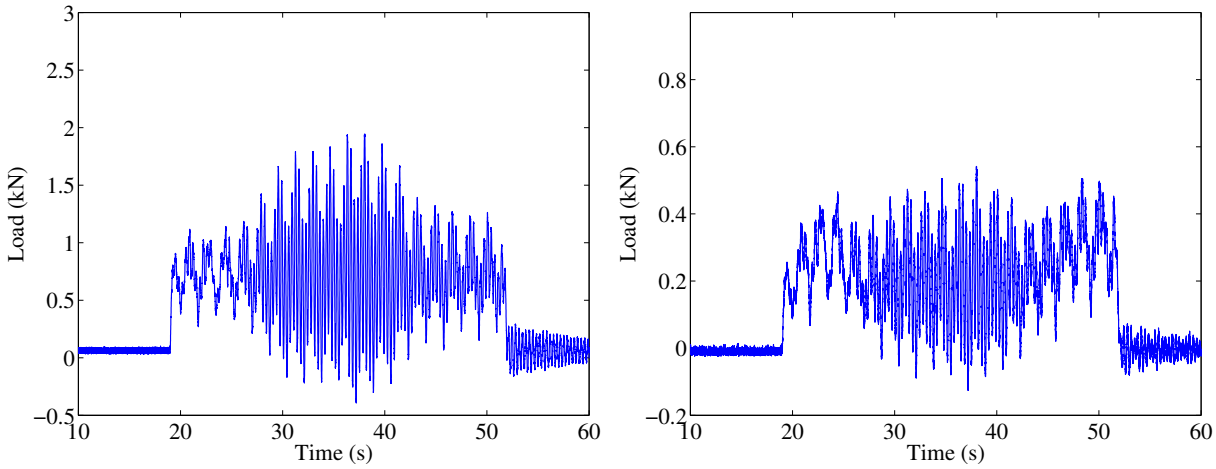

(a) Vertical (b) Lateral

Figure B.16: Sample load histories for single person walking at a pace of 140 BPM, weight: 0.65 kN, leg length: 0.95 m

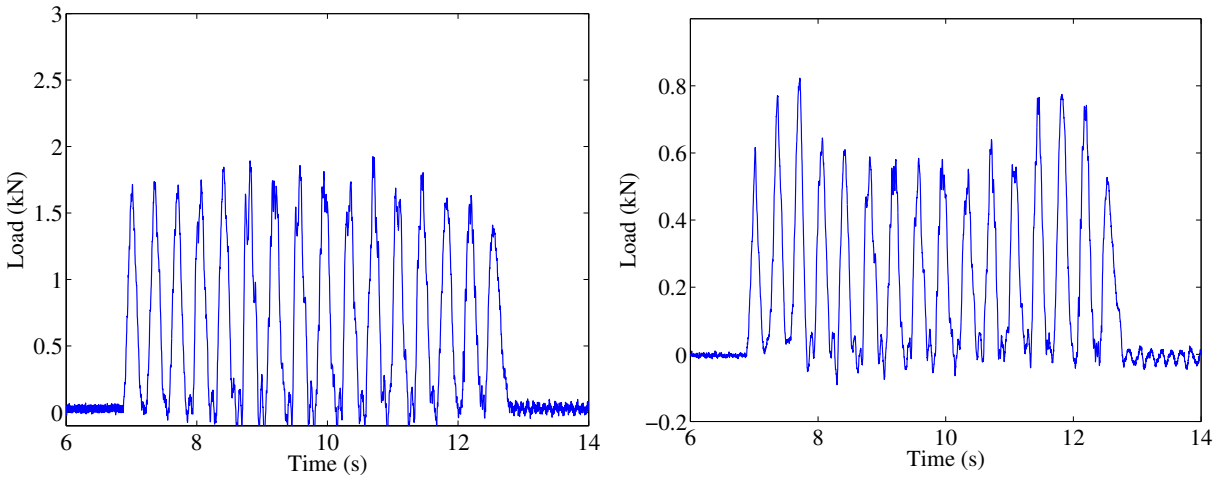

(a) Vertical

(b) Lateral

Figure B.17: Sample load histories for single person running at a pace of 160 BPM, weight: 0.65 kN, leg length: 0.95 m

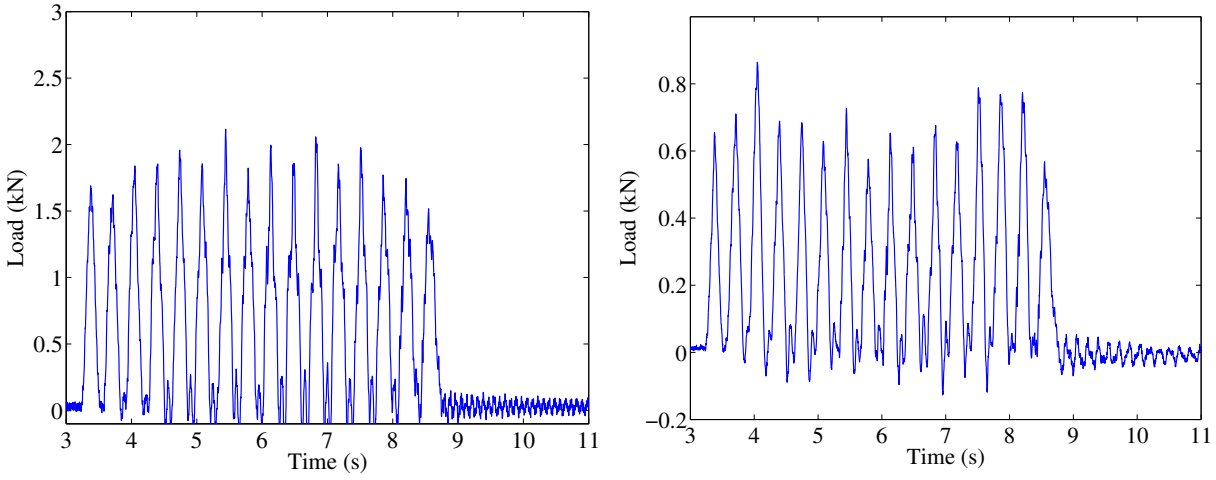

(a) Vertical

(b) Lateral

Figure B.18: Sample load histories for single person running at a pace of 170 BPM, weight: 0.65 kN, leg length: 0.95 m

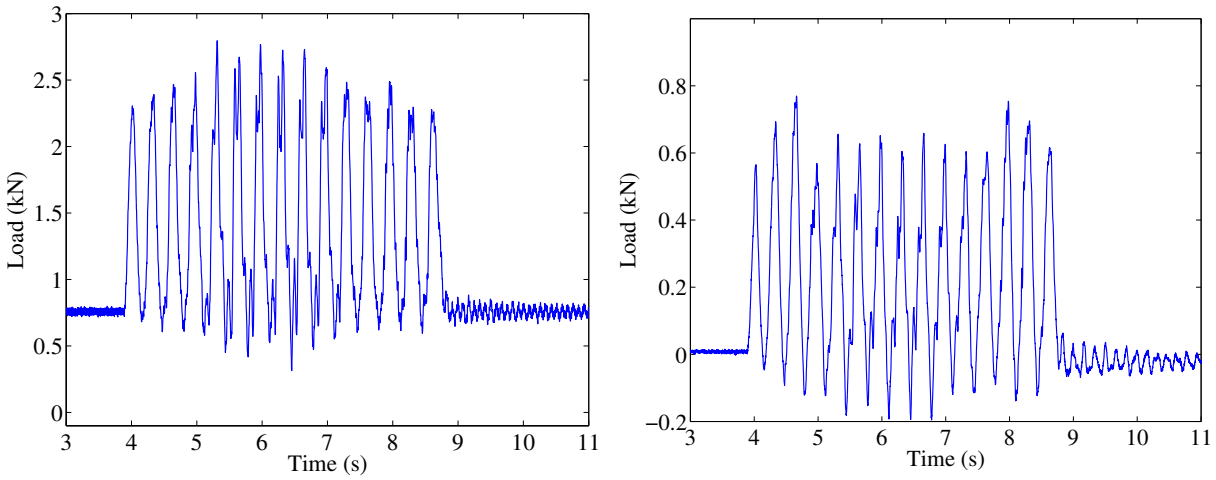

(a) Vertical

(b) Lateral

Figure B.19: Sample load histories for single person running at a pace of 180 BPM, weight: 0.65 kN, leg length: 0.95 m

Figure B.20 shows sample load results for the smallest crowd for the eight-bay bridge (0.2 p/m^2) passing over the bridge at a time in the same direction.

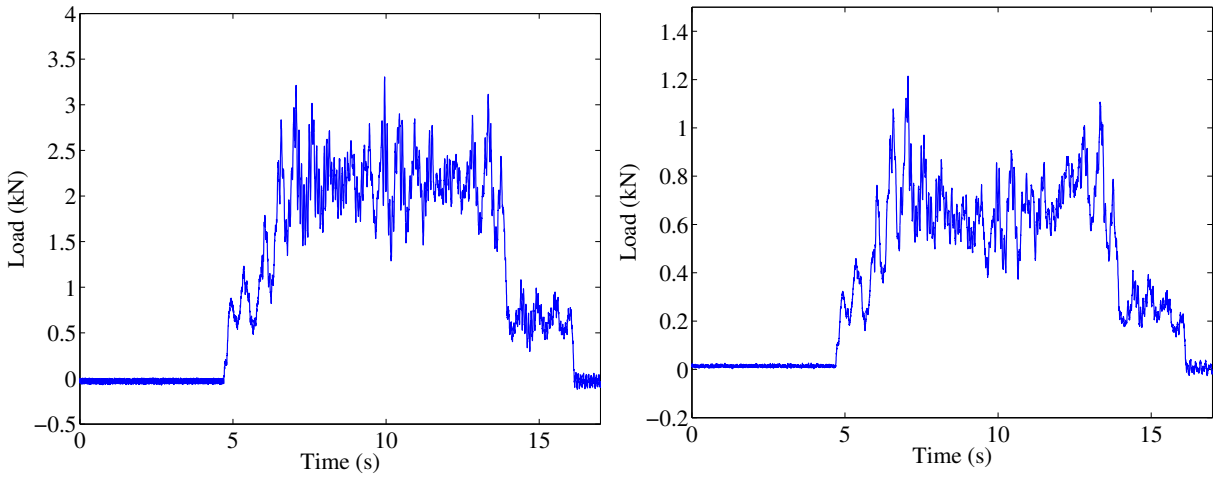

(a) Vertical

(b) Lateral

Figure B.20: Sample load histories for 0.2 p/m^2 walking, total weight: 2.18 kN

Similarly, figures B.21 and B.22 show similar load results for crowds of 0.5 p/m^2 and 1.0 p/m^2.

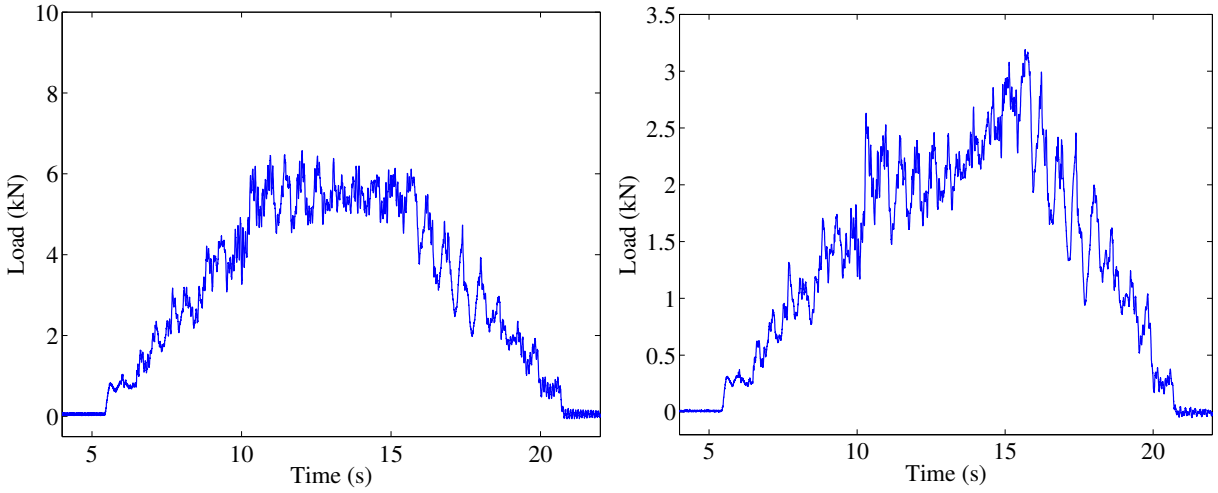

(a) Vertical (b) Lateral

Figure B.21: Sample load histories for 0.5 p/m^2 walking, total weight: 5.41 kN

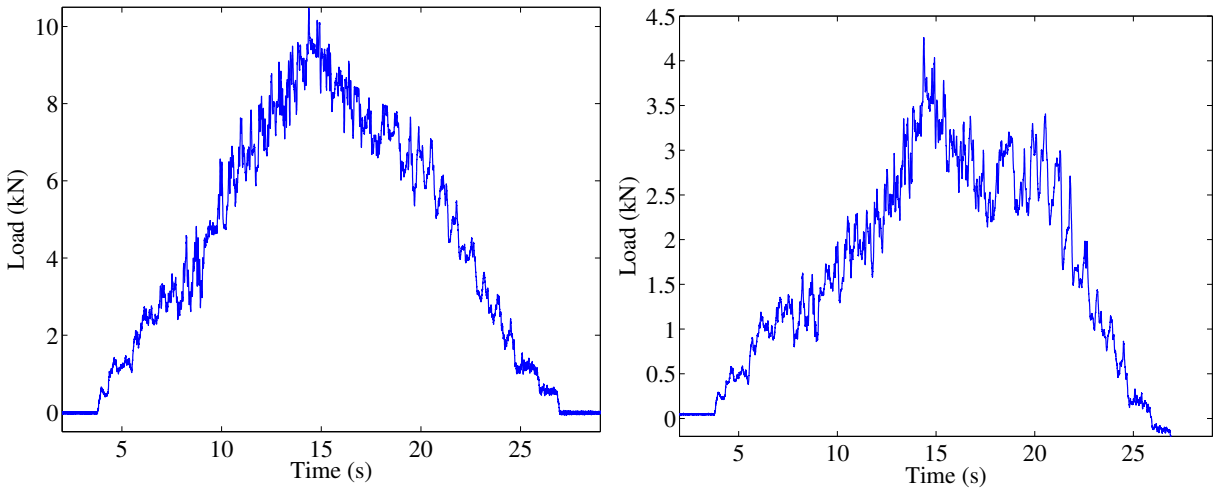

(a) Vertical (b) Lateral

Figure B.22: Sample load histories for 1.0 p/m^2 walking, total weight: 11.30 kN

Figures B.23 and B.24 show the load histories for two people walking in sync and out

of sync (one at 115 BPM and one at 130 BPM).

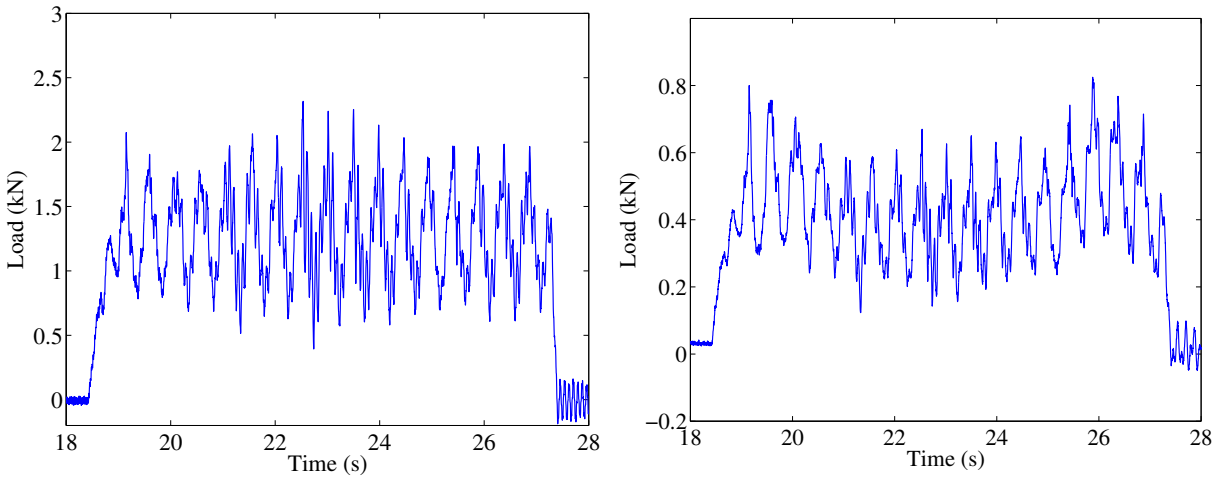

(a) Vertical

(b) Lateral

Figure B.23: Sample load histories for two people walking synchronously, total weight: 1.25 kN

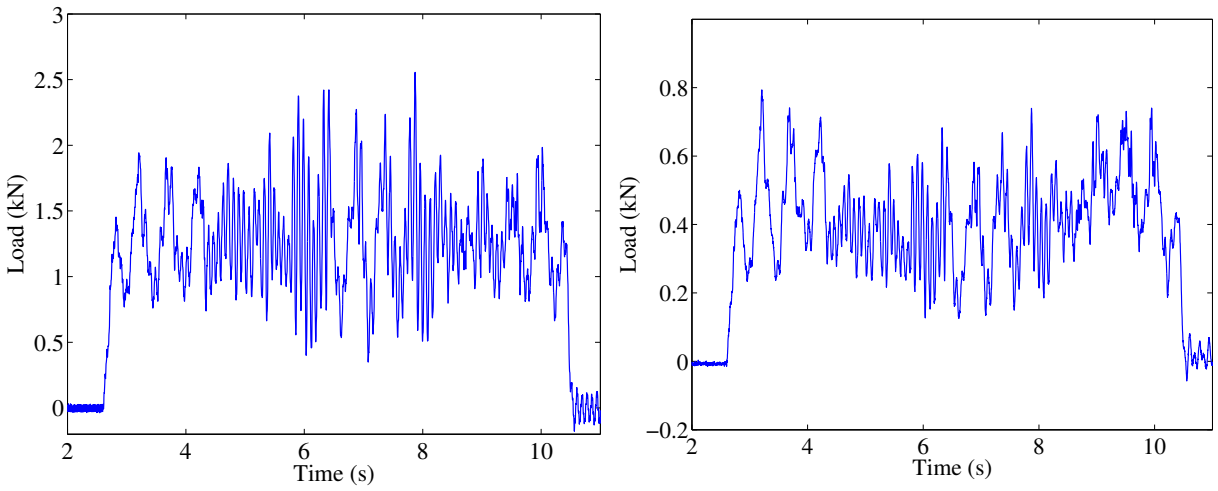

(a) Vertical

(b) Lateral

Figure B.24: Sample load histories for two people walking asynchronously, total weight: 1.25 kN

B.0.5 Fourteen-bay bridge

Figure B.12 shows sample load plots for a single person walking at a pace of 100 BPM.

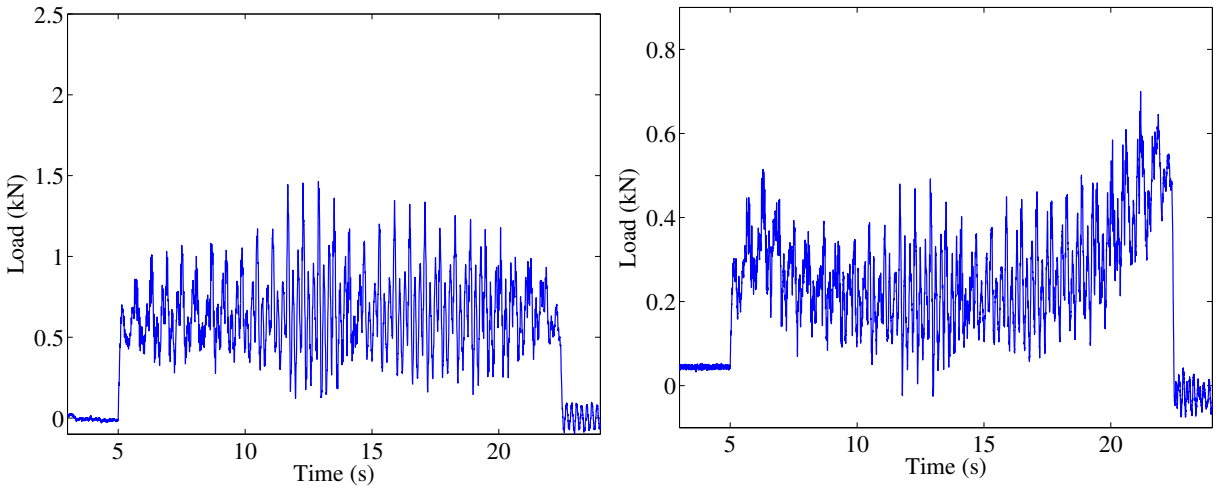

(a) Vertical

(b) Lateral

Figure B.25: Sample load histories for single person walking at a pace of 100 BPM, weight: 0.65 kN, leg length: 0.95 m

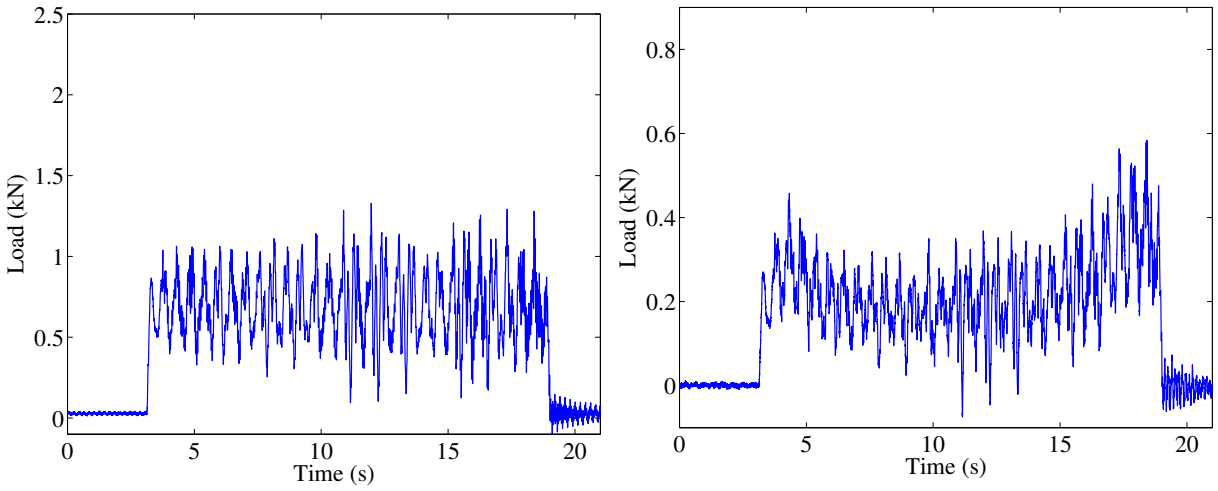

(a) Vertical

(b) Lateral

Figure B.26: Sample load histories for single person walking at a pace of 110 BPM, weight: 0.65 kN, leg length: 0.95 m

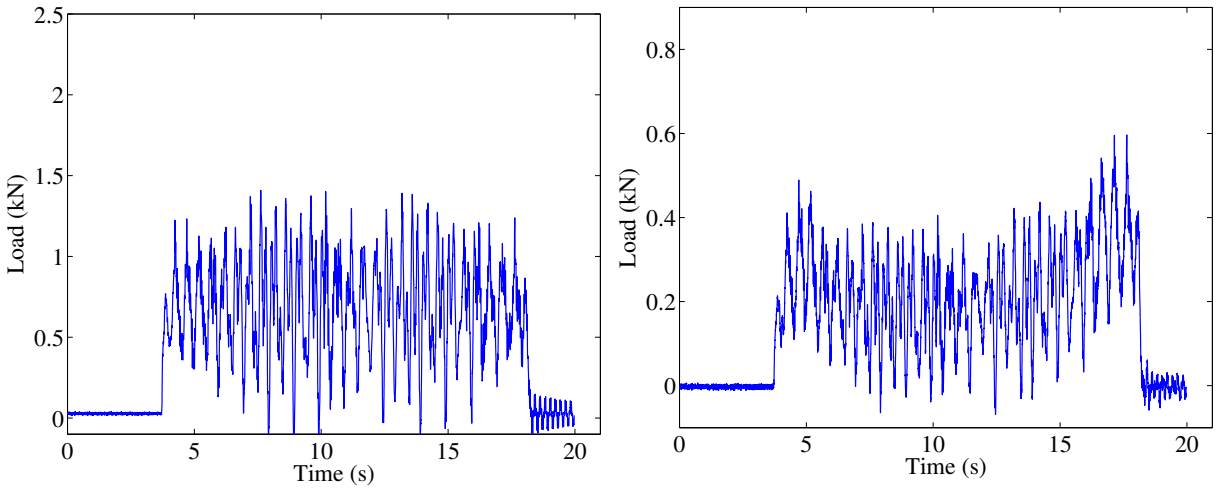

(a) Vertical

(b) Lateral

Figure B.27: Sample load histories for single person walking at a pace of 120 BPM, weight: 0.65 kN, leg length: 0.95 m

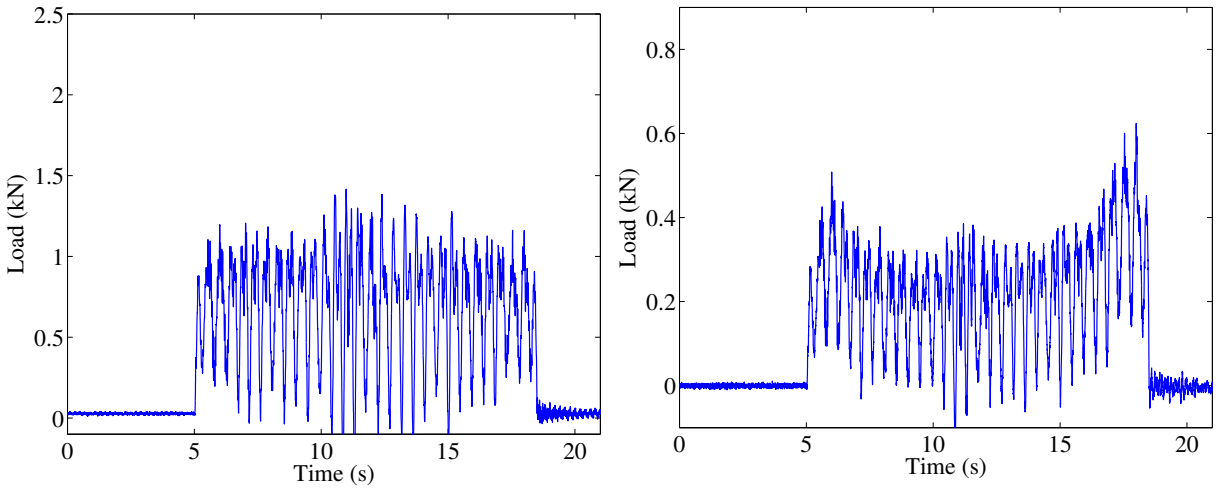

(a) Vertical

(b) Lateral

Figure B.28: Sample load histories for single person walking at a pace of 130 BPM, weight: 0.65 kN, leg length: 0.95 m

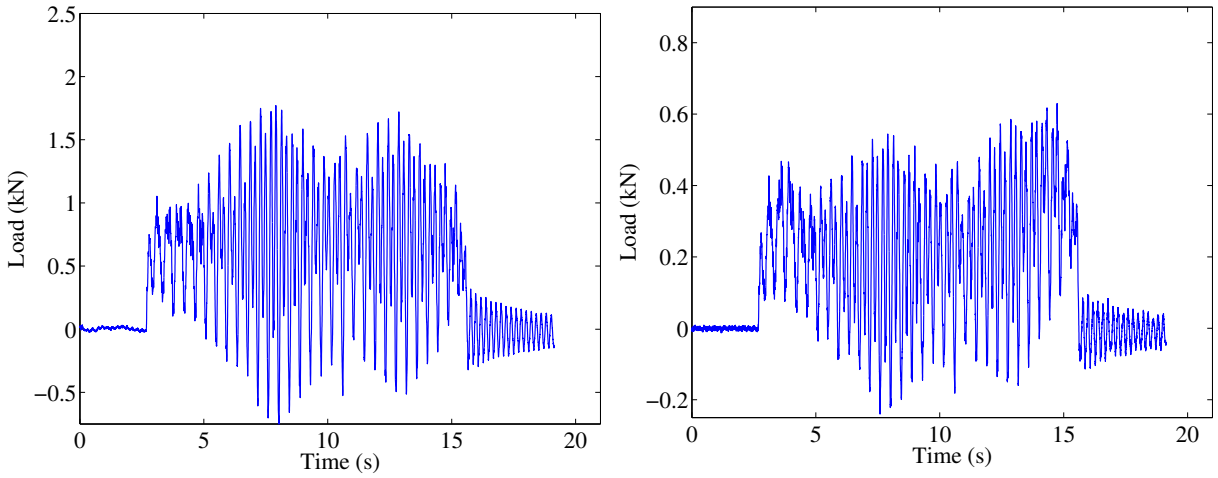

(a) Vertical

(b) Lateral

Figure B.29: Sample load histories for single person walking at a pace of 140 BPM, weight: 0.65 kN, leg length: 0.95 m

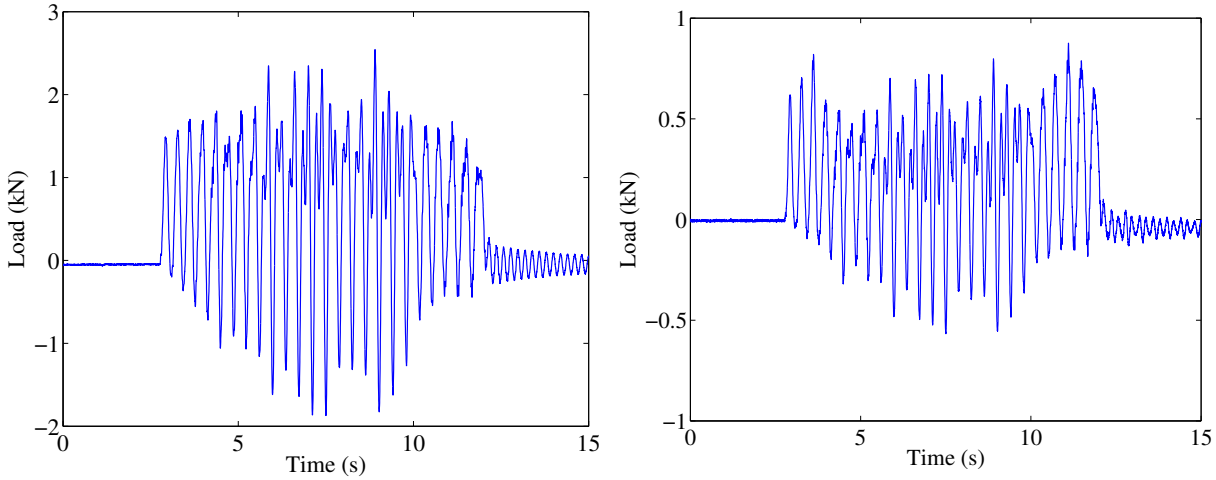

(a) Vertical (b) Lateral

Figure B.30: Sample load histories for single person running at a pace of 160 BPM, weight: 0.65 kN, leg length: 0.95 m

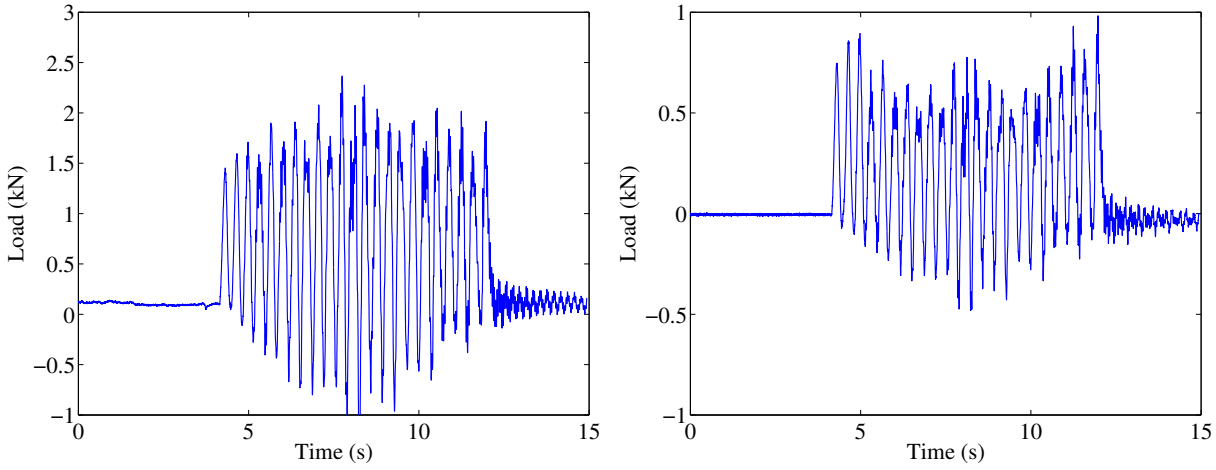

(a) Vertical (b) Lateral

Figure B.31: Sample load histories for single person running at a pace of 170 BPM, weight: 0.65 kN, leg length: 0.95 m

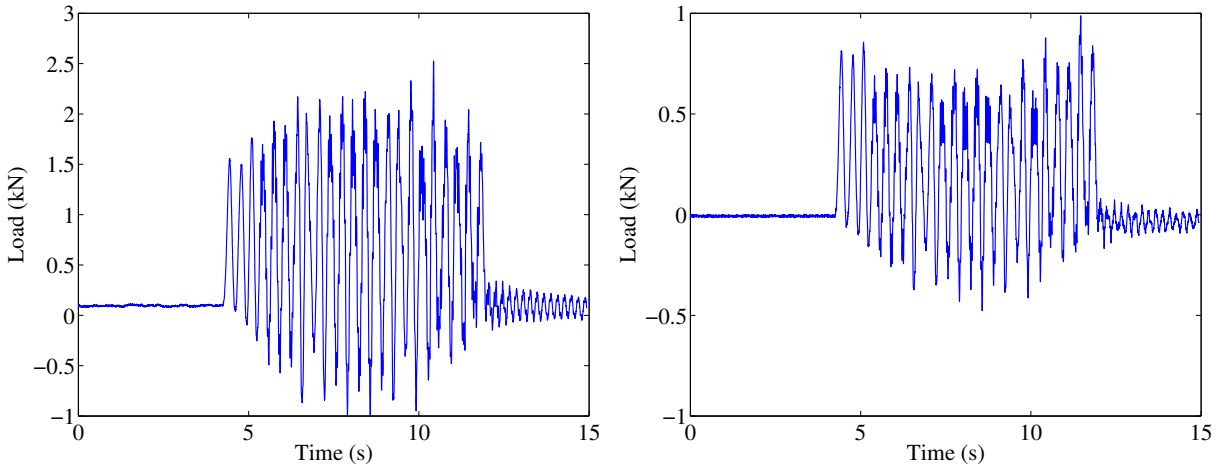

(a) Vertical (b) Lateral

Figure B.32: Sample load histories for single person running at a pace of 180 BPM, weight: 0.65 kN, leg length: 0.95 m

Figure B.33 shows sample load results for the smallest crowd for the fourteen-bay bridge (0.2 p/m^2) passing over the bridge at a time in the same direction.

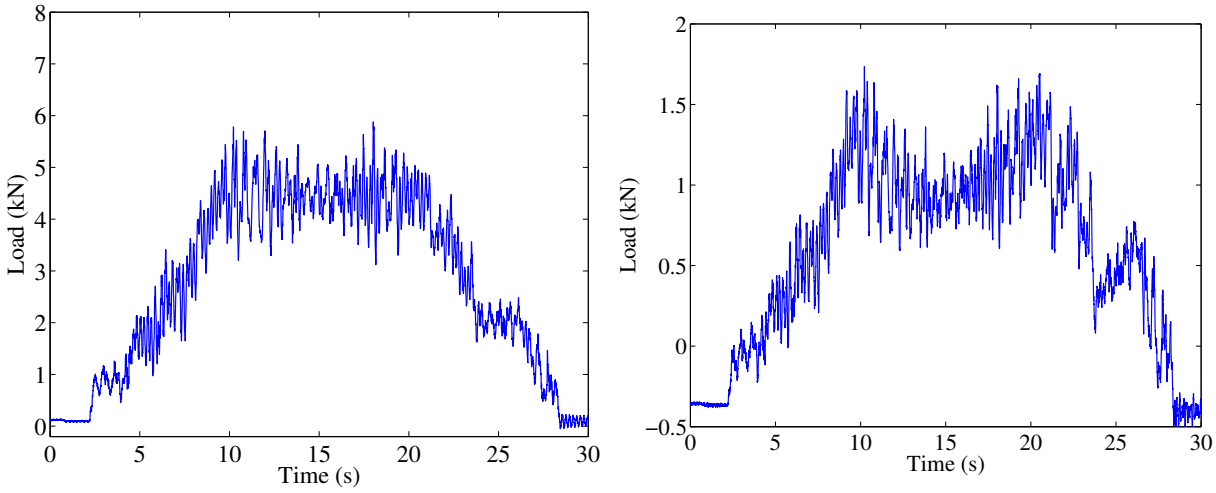

(a) Vertical

(b) Lateral

Figure B.33: Sample load histories for 0.2 p/m^2 walking, total weight: 4.27 kN

Similarly, figures B.34 and B.35 show similar load results for crowds of 0.5 p/m^2 and 1.0 p/m^2.

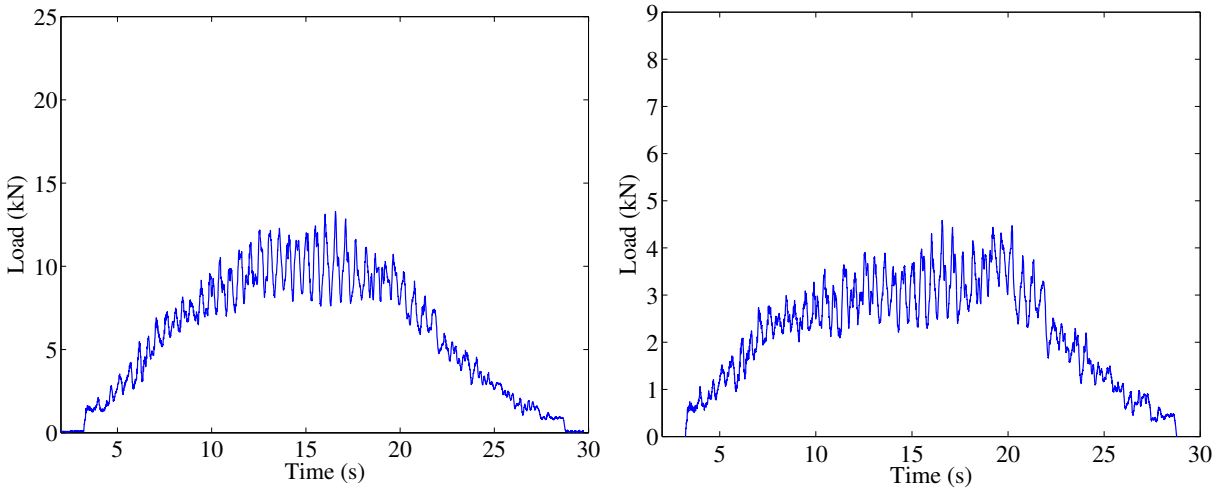

(a) Vertical

(b) Lateral

Figure B.34: Sample load histories for 0.5 p/m^2 walking, total weight: 9.66 kN

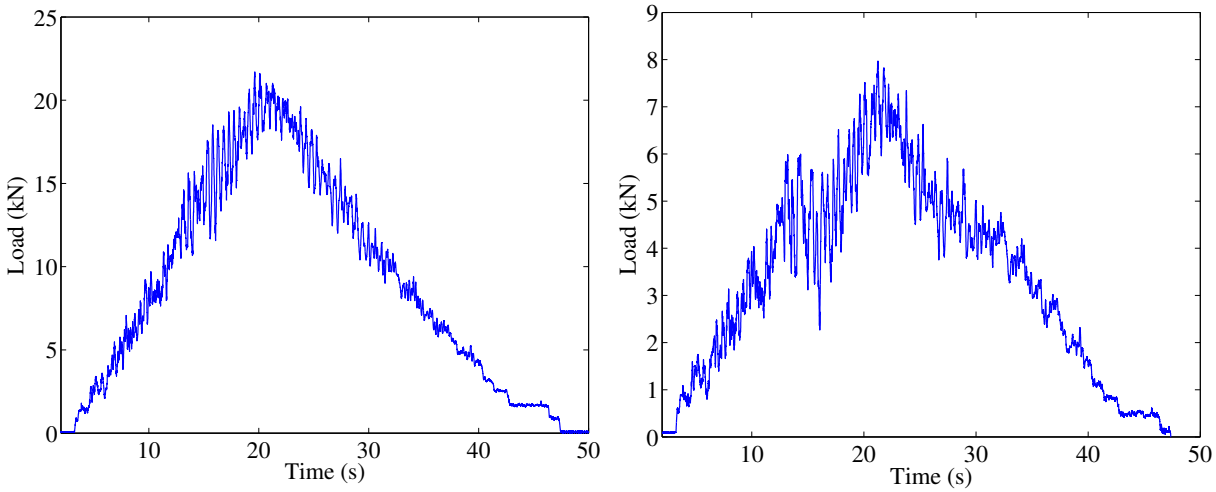

(a) Vertical

(b) Lateral

Figure B.35: Sample load histories for 1.0 p/m^2 walking, total weight: 20.32 kN

Figures B.36 and B.37 show the load histories for two people walking in sync and out

of sync (one at 115 BPM and one at 130 BPM).

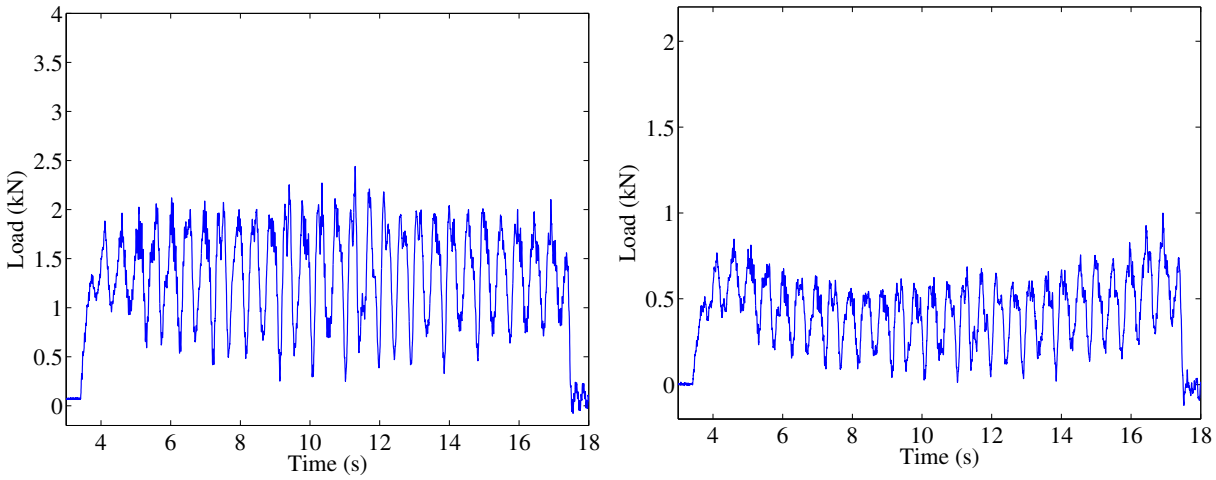

(a) Vertical

(b) Lateral

Figure B.36: Sample load histories for two people walking synchronously, total weight: 1.25 kN

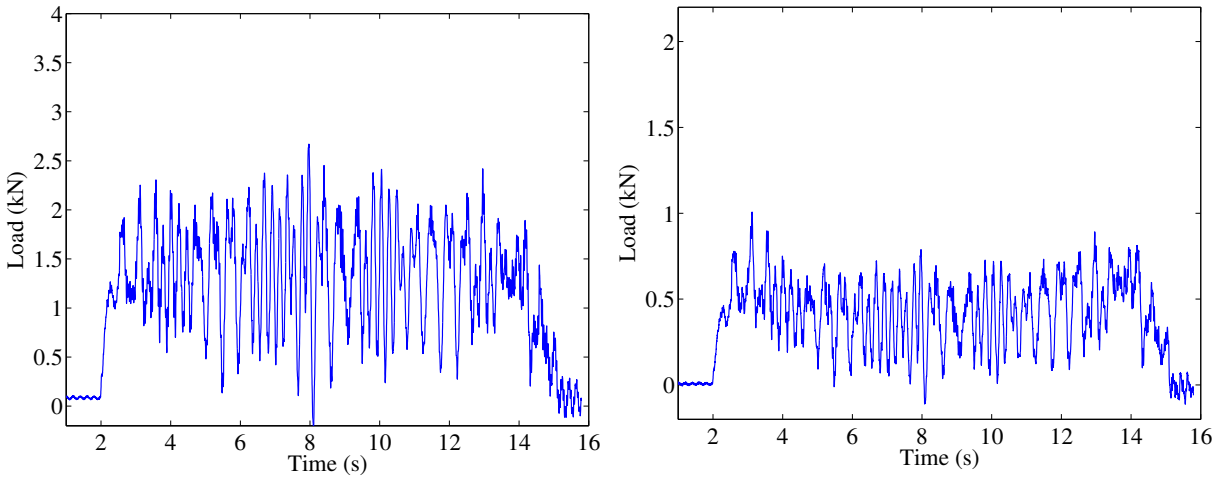

(a) Vertical

(b) Lateral

Figure B.37: Sample load histories for two people walking asynchronously, total weight: 1.25 kN

Appendix C

Strain gauge results

C.0.6 Eight-bay bridge

Figure C.1 shows sample strain plots for a single person walking at a pace of 100 BPM.

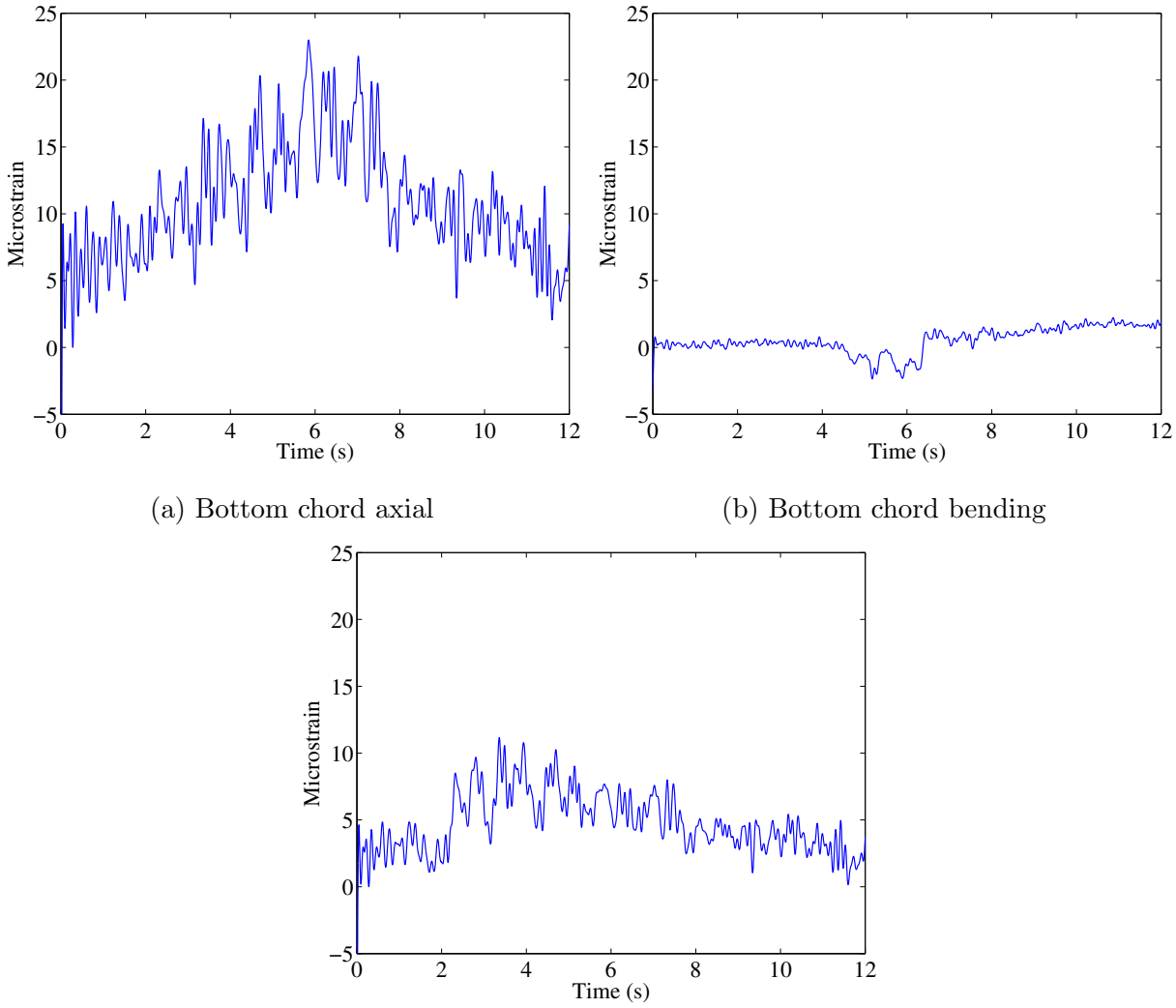

(a) Bottom chord axial

(b) Bottom chord bending

(c) Diagonal axial

Figure C.1: Sample strain histories for single person walking at a pace of 100 BPM, weight: 0.87 kN, leg length: 1.07 m

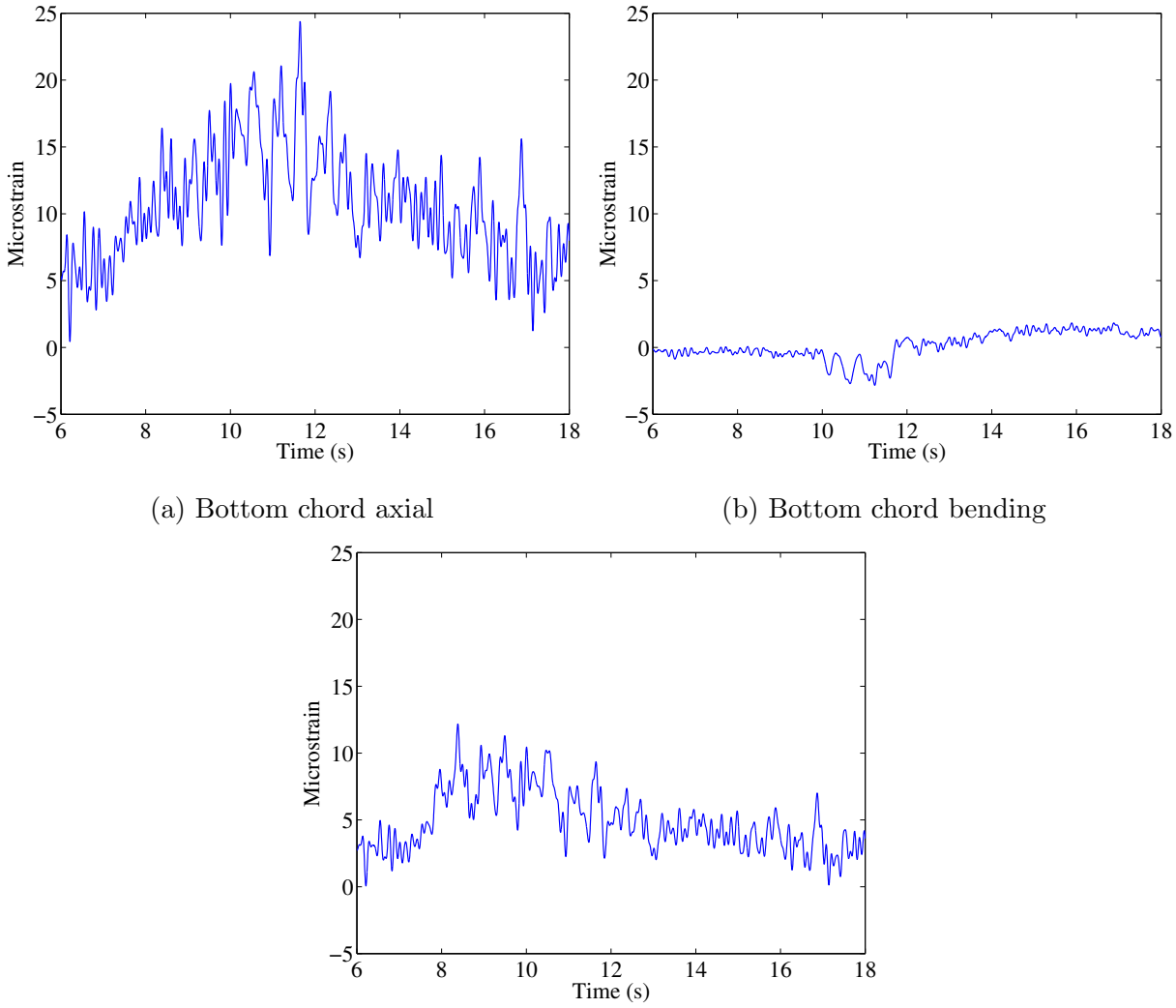

(a) Bottom chord axial

(b) Bottom chord bending

(c) Diagonal axial

Figure C.2: Sample strain histories for single person walking at a pace of 110 BPM, weight: 0.87 kN, leg length: 1.07 m

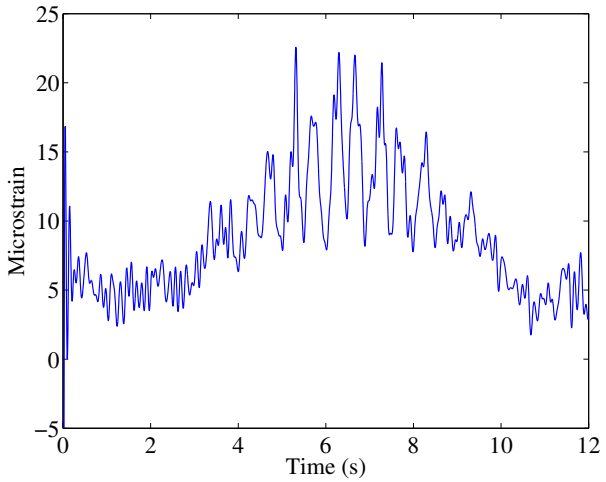

(a) Bottom chord axial

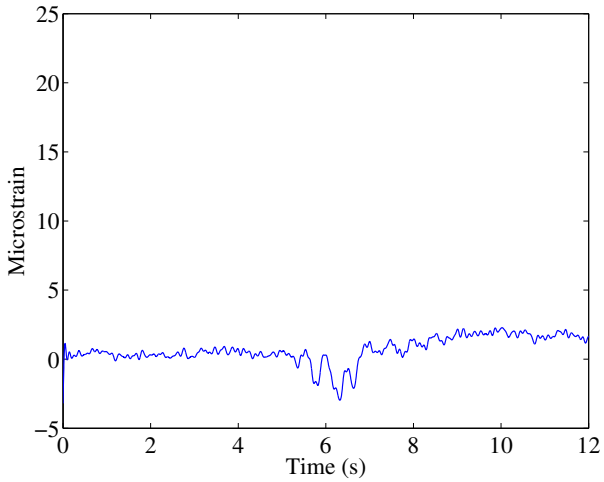

(b) Bottom chord bending

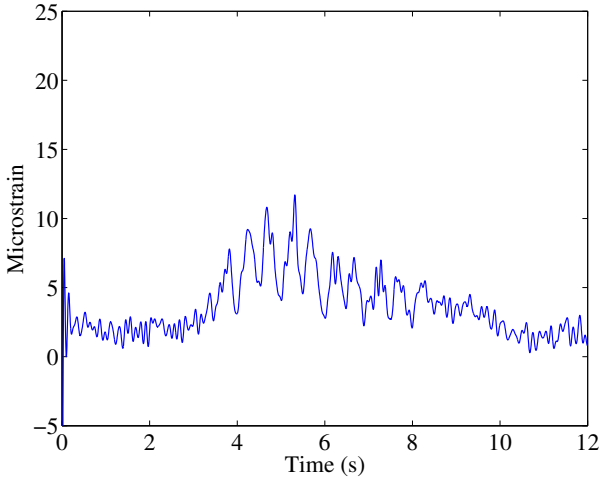

(c) Diagonal bottom-face strain

Figure C.3: Sample strain histories for single person walking at a pace of 120 BPM, weight: 0.87 kN, leg length: 1.07 m

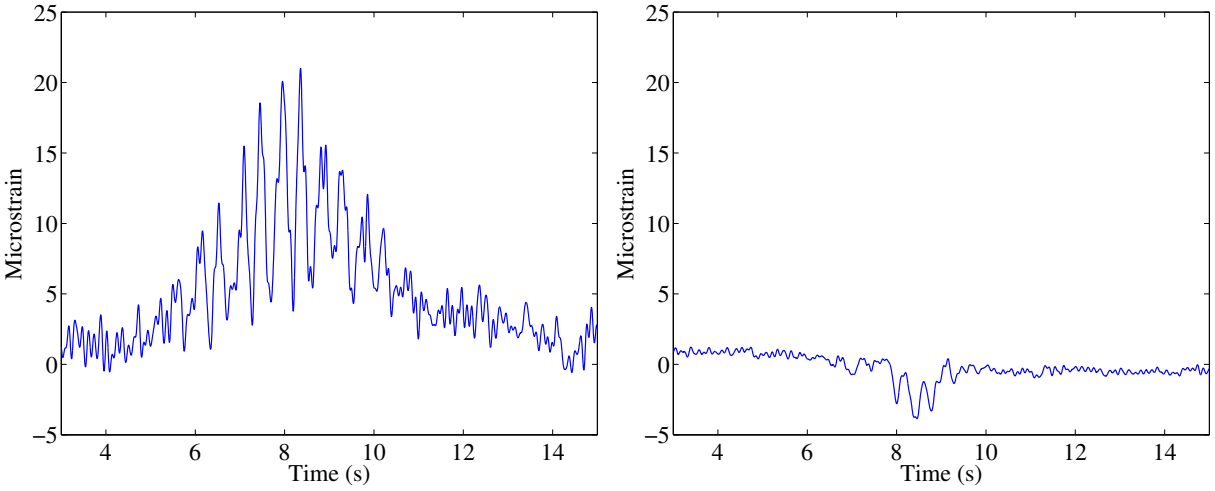

(a) Bottom chord axial

(b) Bottom chord bending

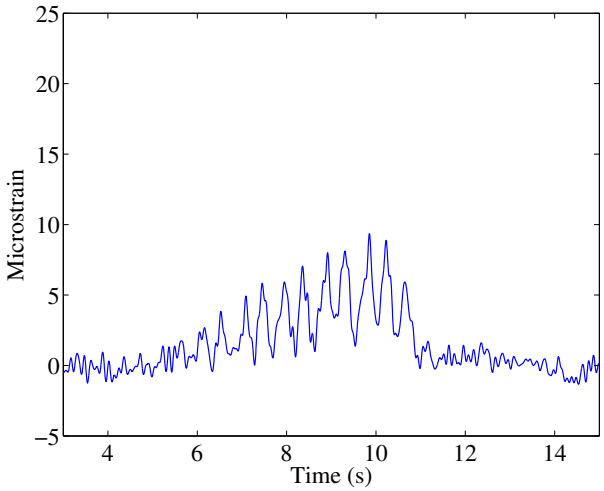

(c) Diagonal bottom-face strain

Figure C.4: Sample strain histories for single person walking at a pace of 130 BPM, weight: 0.87 kN, leg length: 1.07 m

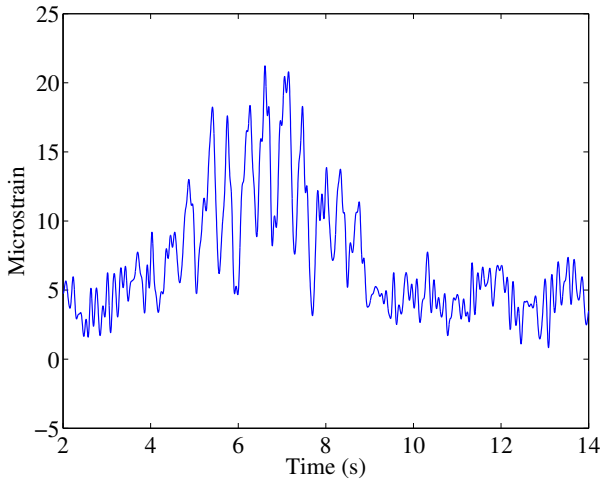

(a) Bottom chord axial

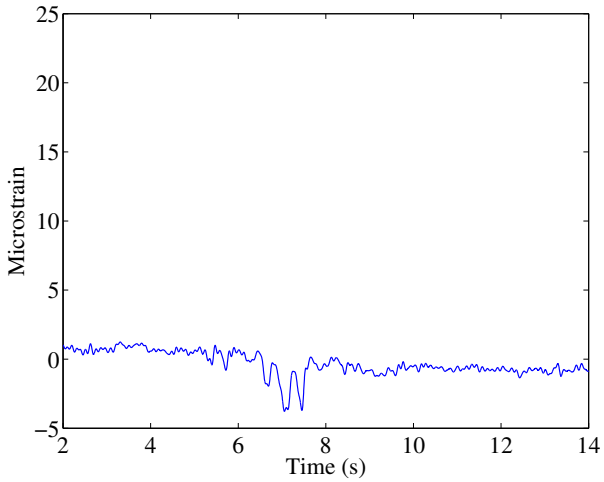

(b) Bottom chord bending

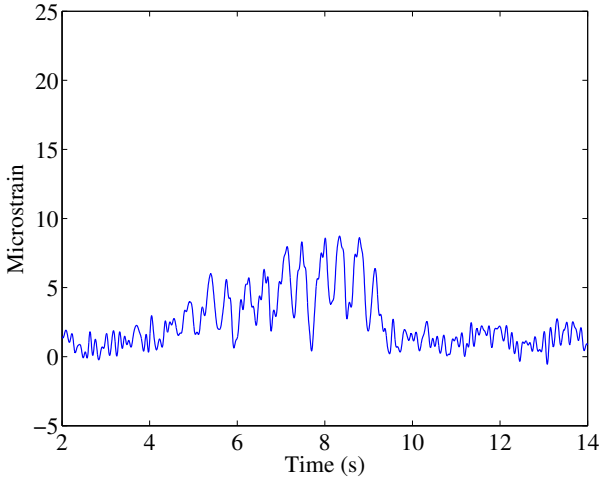

(c) Diagonal bottom-face strain

Figure C.5: Sample strain histories for single person walking at a pace of 140 BPM, weight: 0.87 kN, leg length: 1.07 m

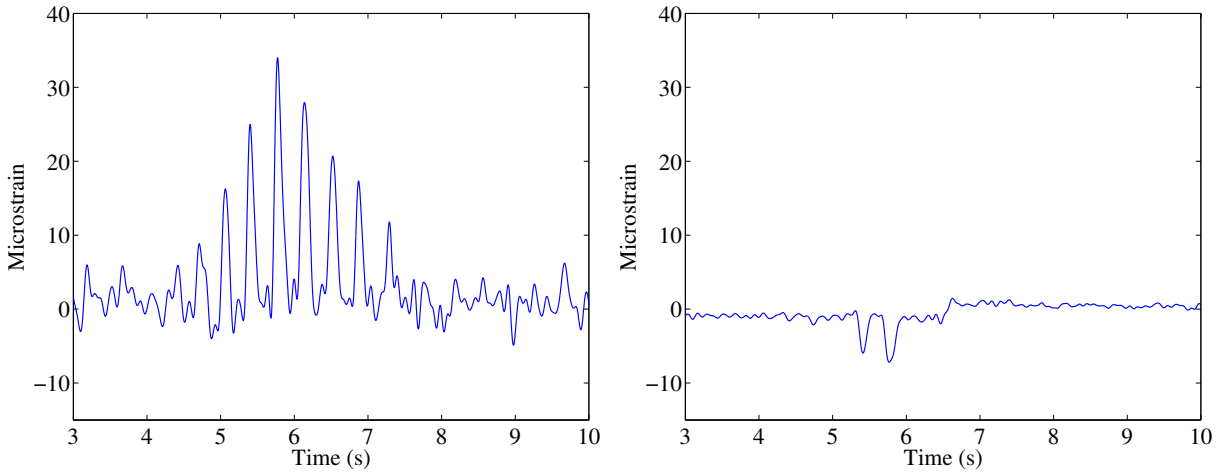

(a) Bottom chord axial

(b) Bottom chord bending

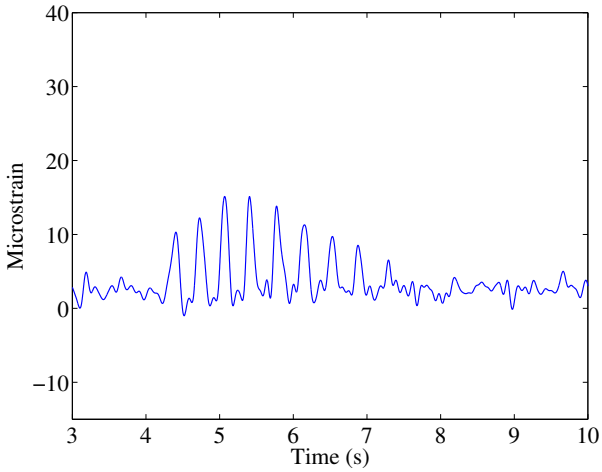

(c) Diagonal bottom-face strain

Figure C.6: Sample strain histories for single person walking at a pace of 160 BPM, weight: 0.87 kN, leg length: 1.07 m

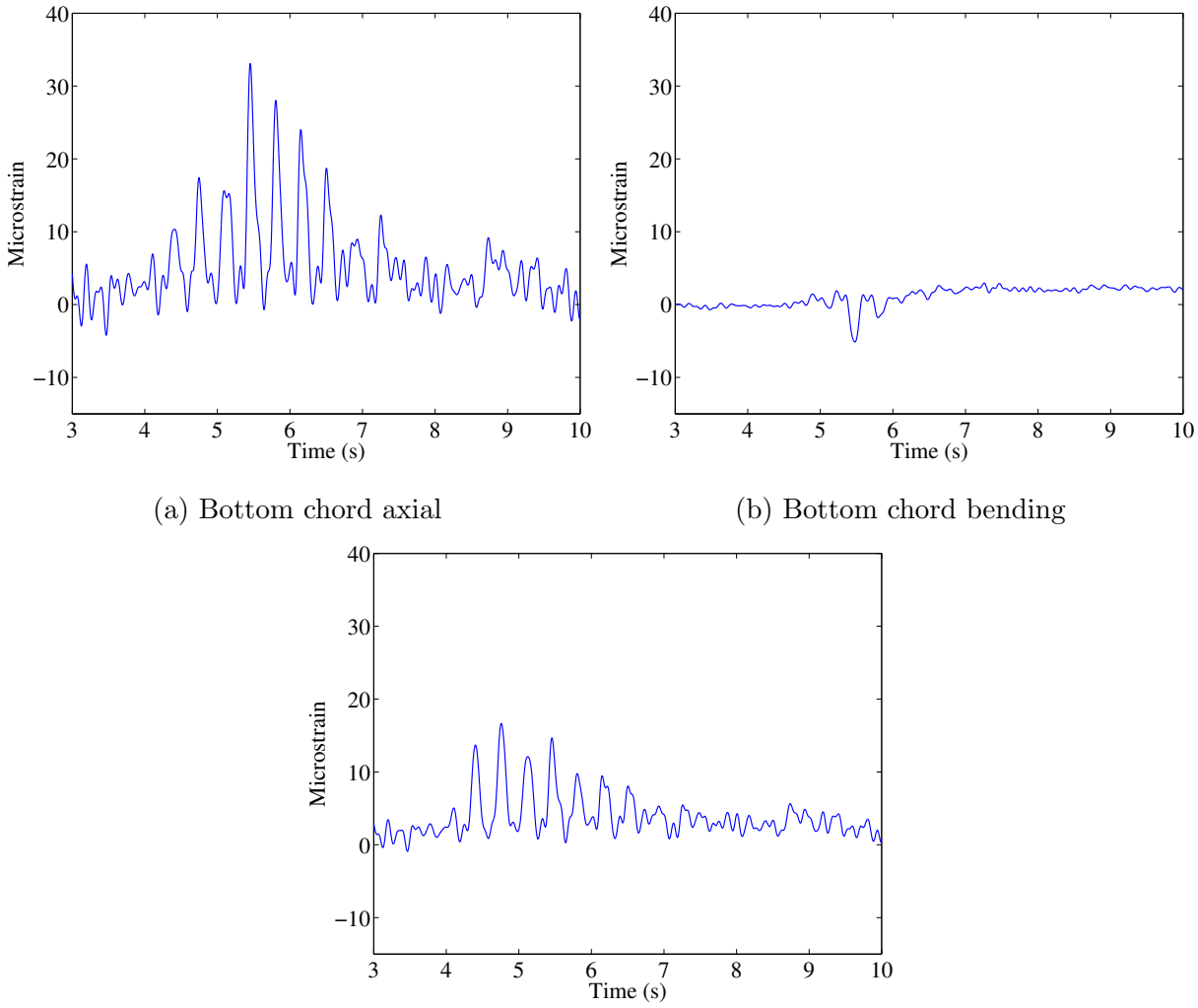

(a) Bottom chord axial

(b) Bottom chord bending

(c) Diagonal bottom-face strain

Figure C.7: Sample strain histories for single person walking at a pace of 170 BPM, weight: 0.87 kN, leg length: 1.07 m

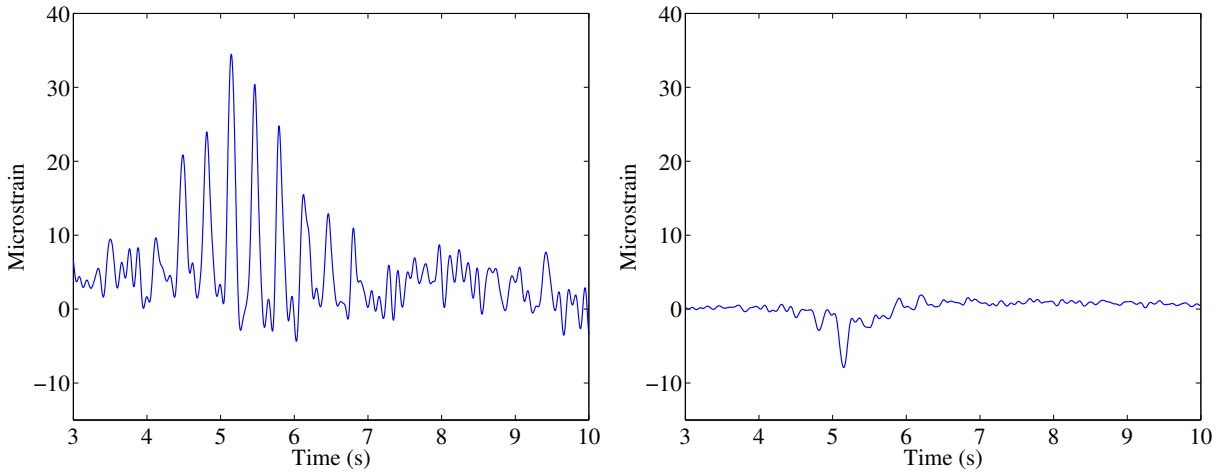

(a) Bottom chord axial

(b) Bottom chord bending

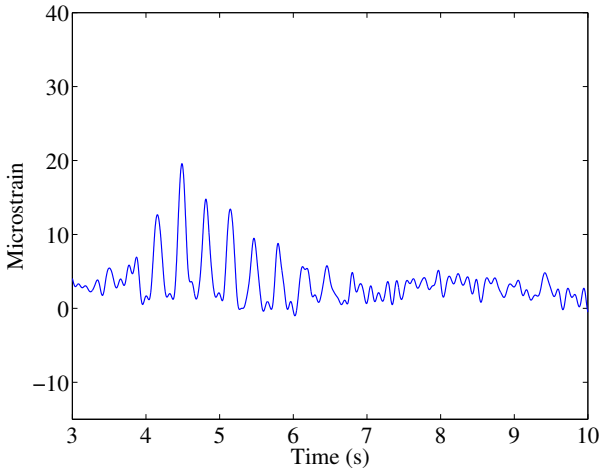

(c) Diagonal bottom-face strain

Figure C.8: Sample strain histories for single person walking at a pace of 180 BPM, weight: 0.87 kN, leg length: 1.07 m

Figure C.9 shows sample load results for the smallest crowd for the eight-bay bridge (0.2 p/m^2) passing over the bridge at a time in the same direction.

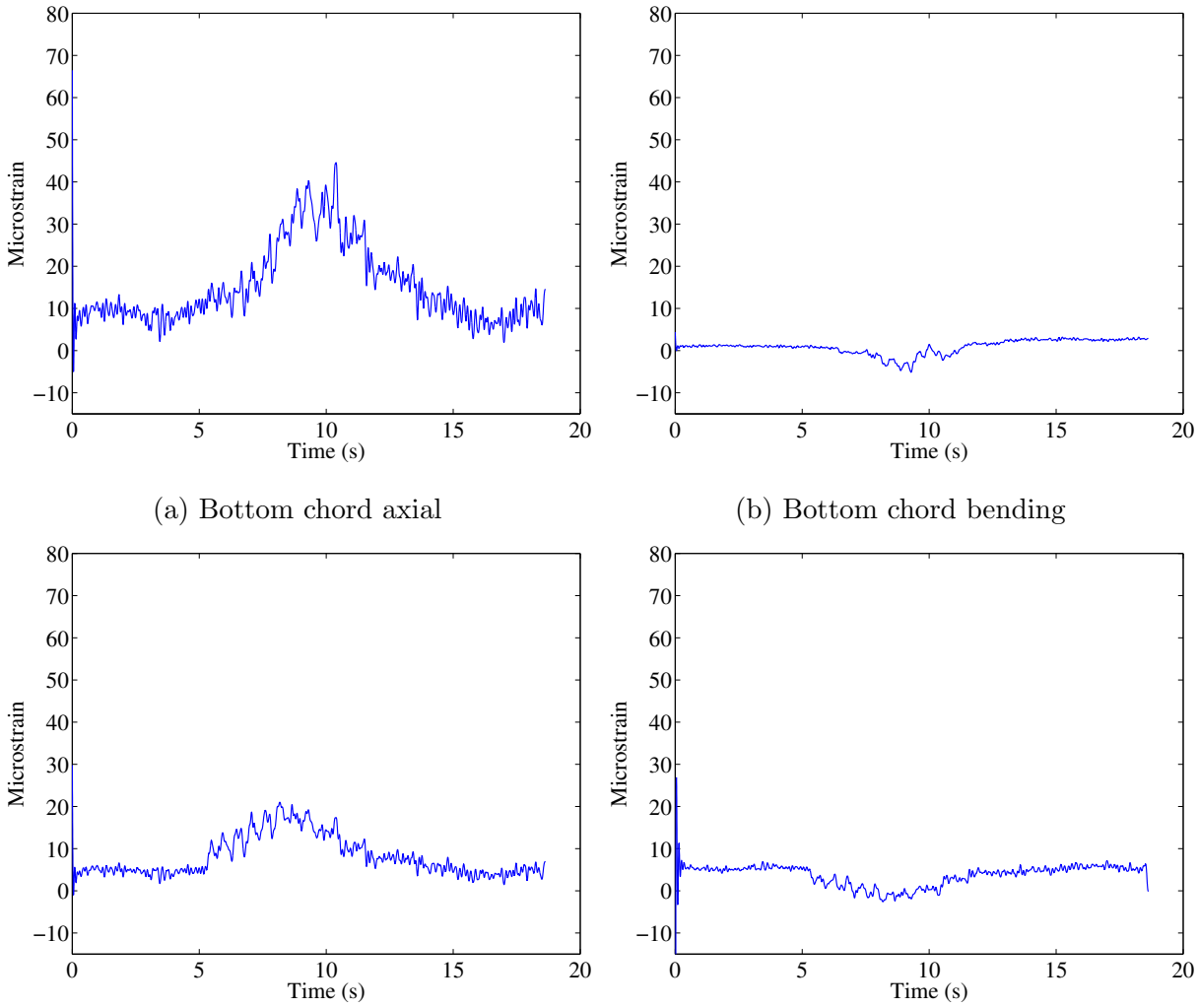

(a) Bottom chord axial

(b) Bottom chord bending

(c) Diagonal axial

(d) Diagonal bending

Figure C.9: Sample strain histories for 0.2 p/m^2 walking, total weight: 2.18 kN

Similarly, figures C.10 and C.11 show similar strain results for crowds of 0.5 p/m^2 and 1.0 p/m^2.

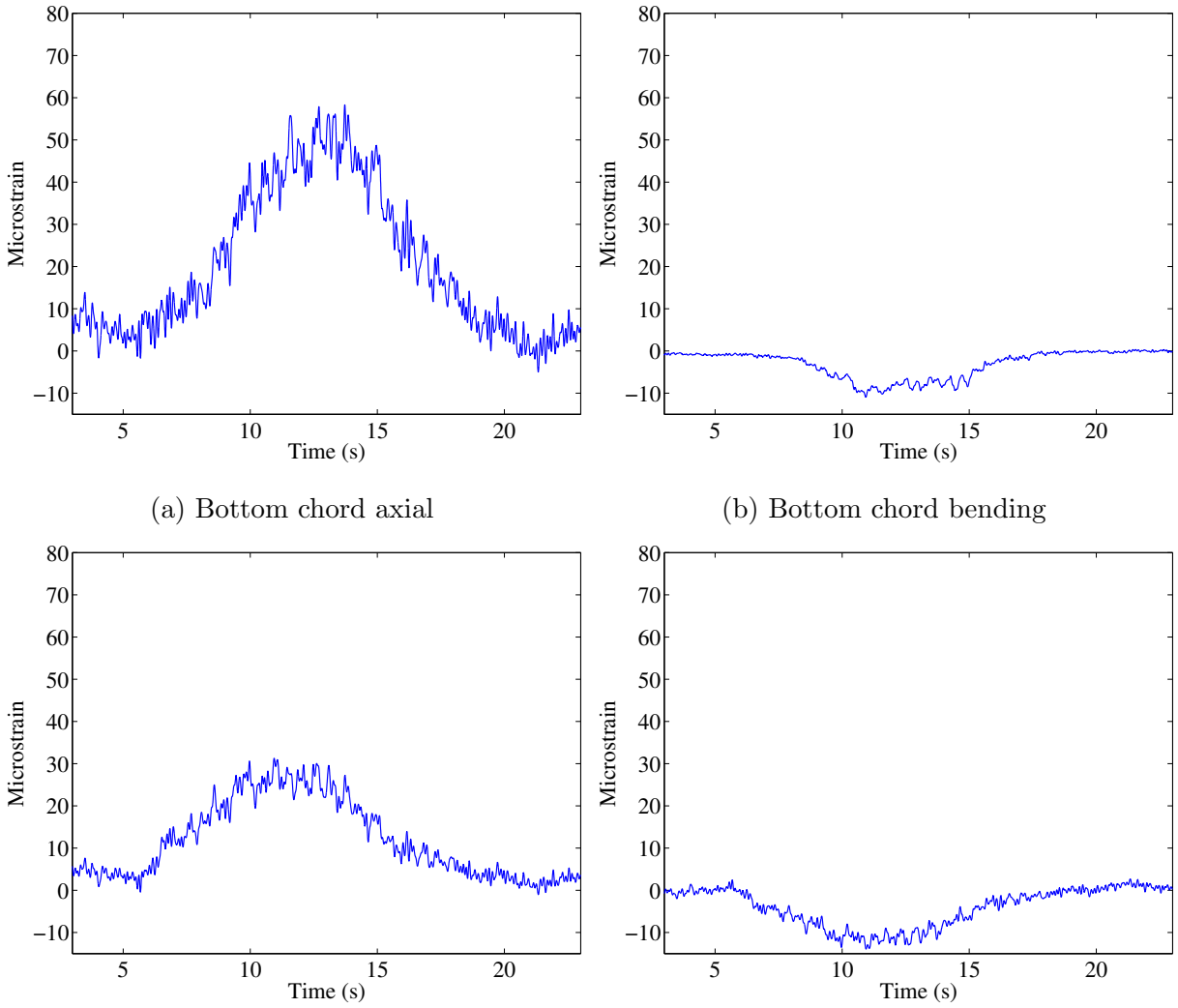

(a) Bottom chord axial

(b) Bottom chord bending

(c) Diagonal axial

(d) Diagonal bending

Figure C.10: Sample strain histories for 0.5 p/m^2 walking, total weight: 5.41 kN

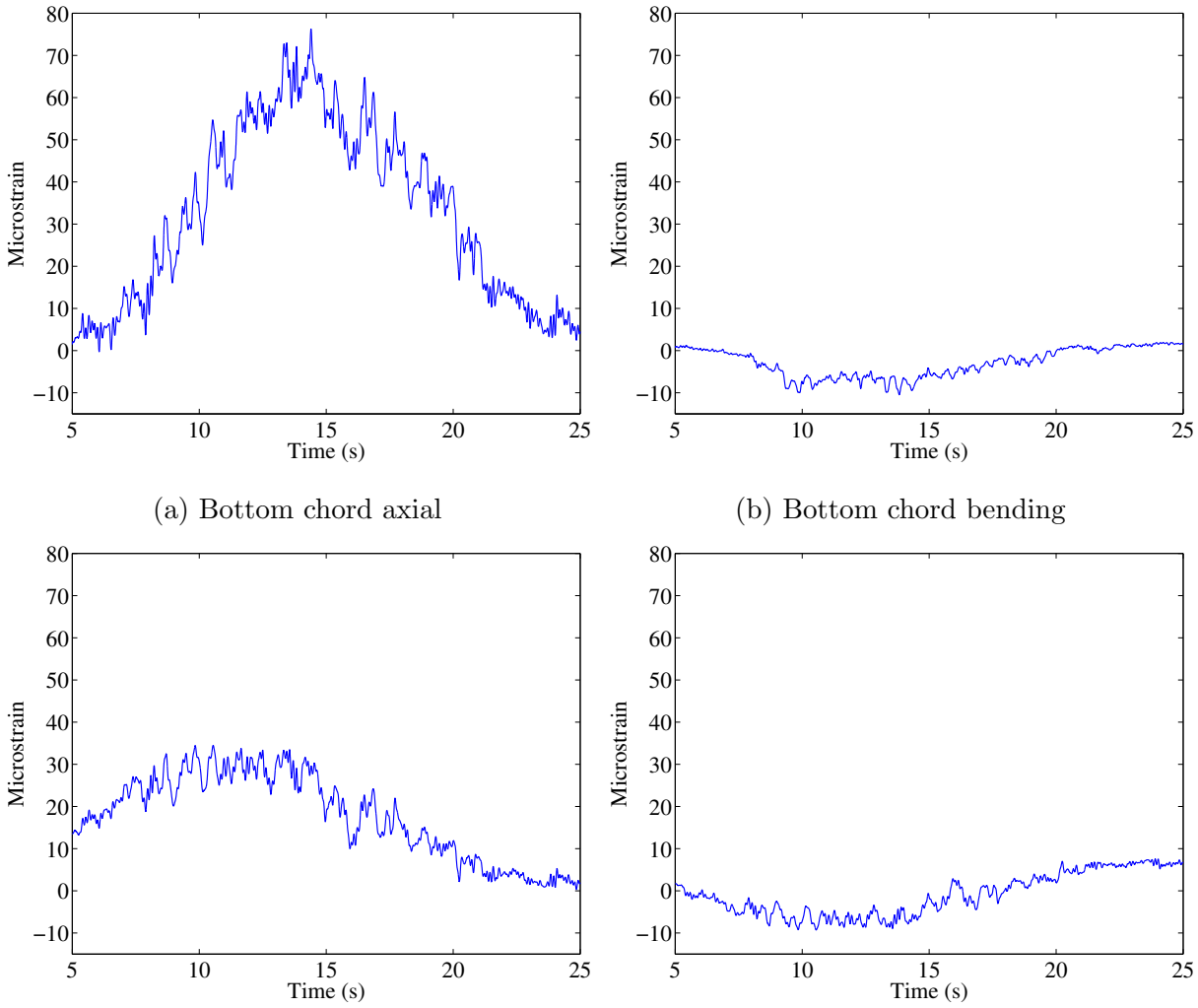

(a) Bottom chord axial

(b) Bottom chord bending

(c) Diagonal axial

(d) Diagonal bending

Figure C.11: Sample strain histories for 1.0 p/m^2 walking, total weight: 11.30 kN

Figures C.12 and C.13 show the strain histories for two people walking in sync and out of sync (one at 115 BPM and one at 130 BPM).

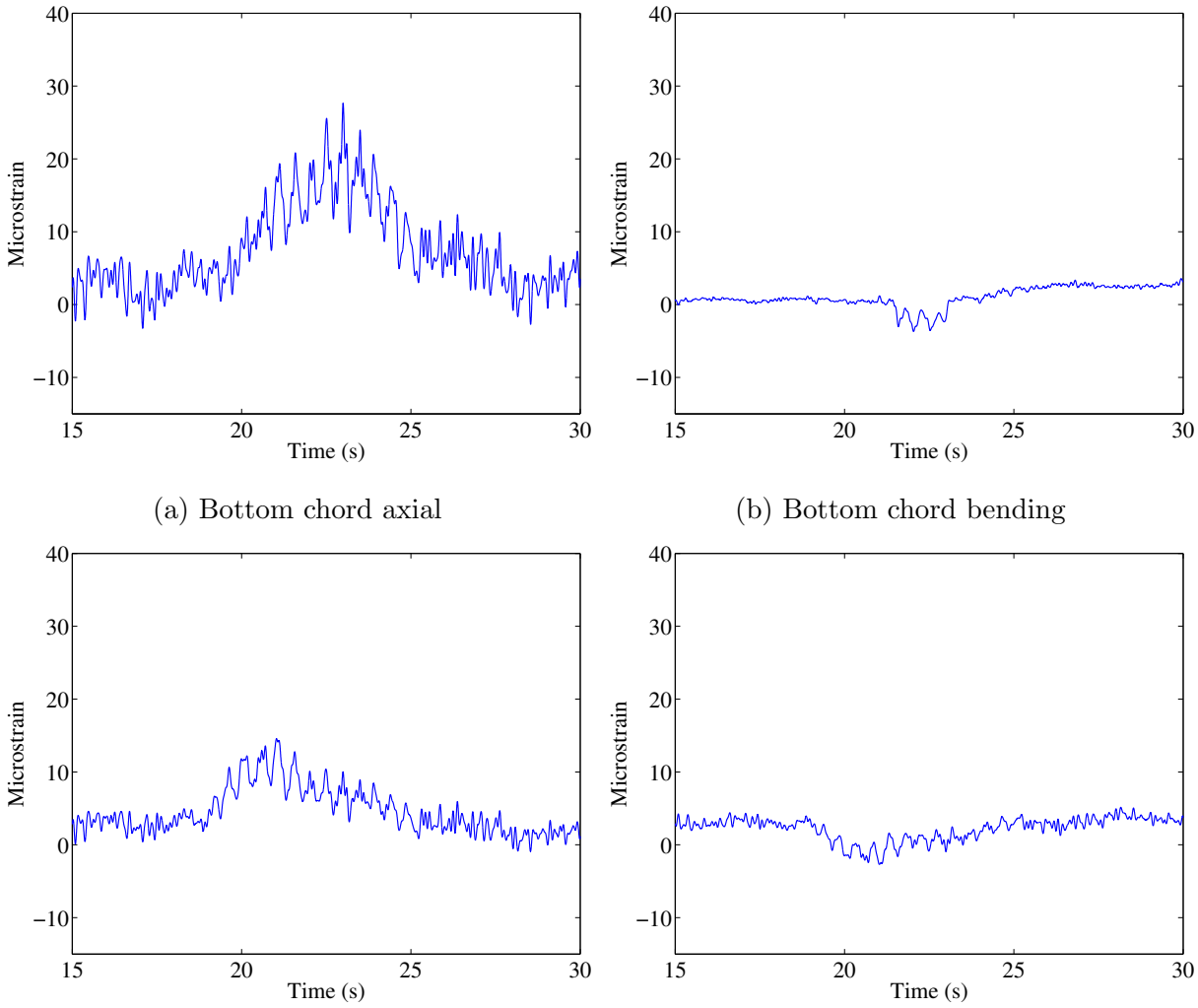

(a) Bottom chord axial

(b) Bottom chord bending

(c) Diagonal axial

(d) Diagonal bending

Figure C.12: Sample load histories for two people walking synchronously, total weight: 1.25 kN

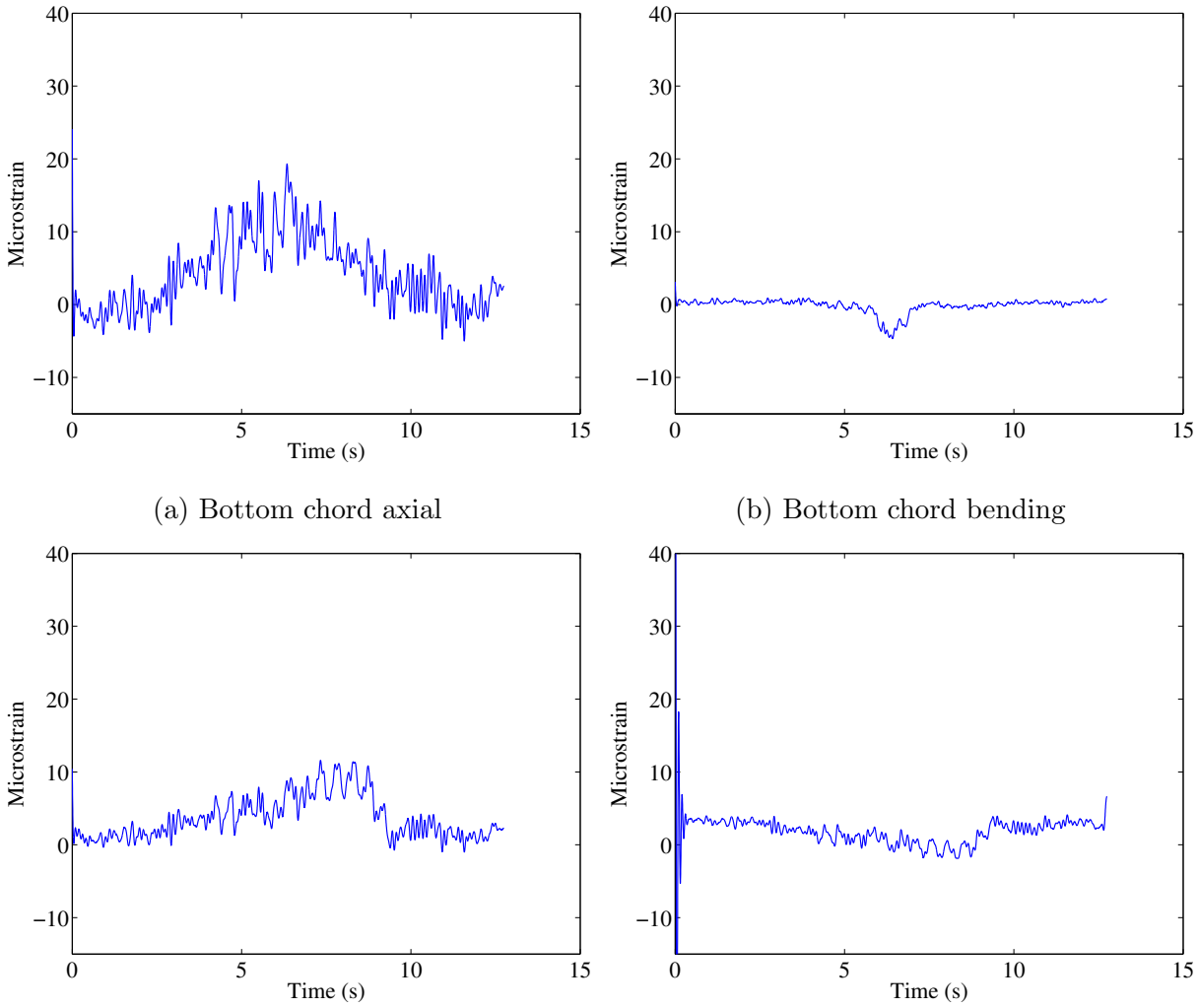

(a) Bottom chord axial

(b) Bottom chord bending

(c) Diagonal axial

(d) Diagonal bending

Figure C.13: Sample load histories for two people walking asynchronously, total weight: 1.25 kN

C.0.7 Fourteen-bay bridge

Figure C.14 shows sample strain plots for a single person walking at a pace of 100 BPM.

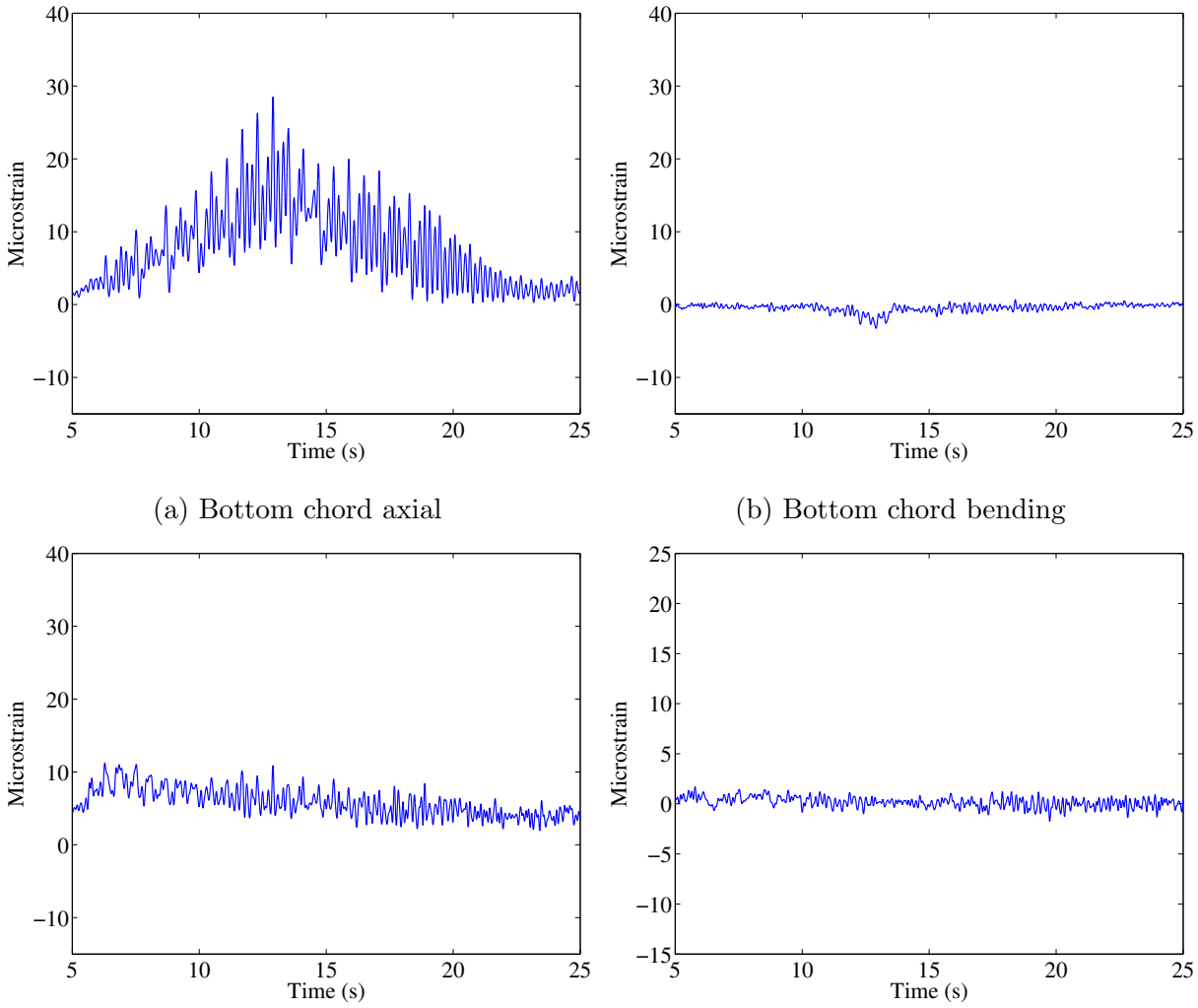

(a) Bottom chord axial

(b) Bottom chord bending

(c) Diagonal axial

(d) Diagonal bending

Figure C.14: Sample strain histories for single person walking at a pace of 100 BPM, weight: 0.65 kN, leg length: 0.95 m

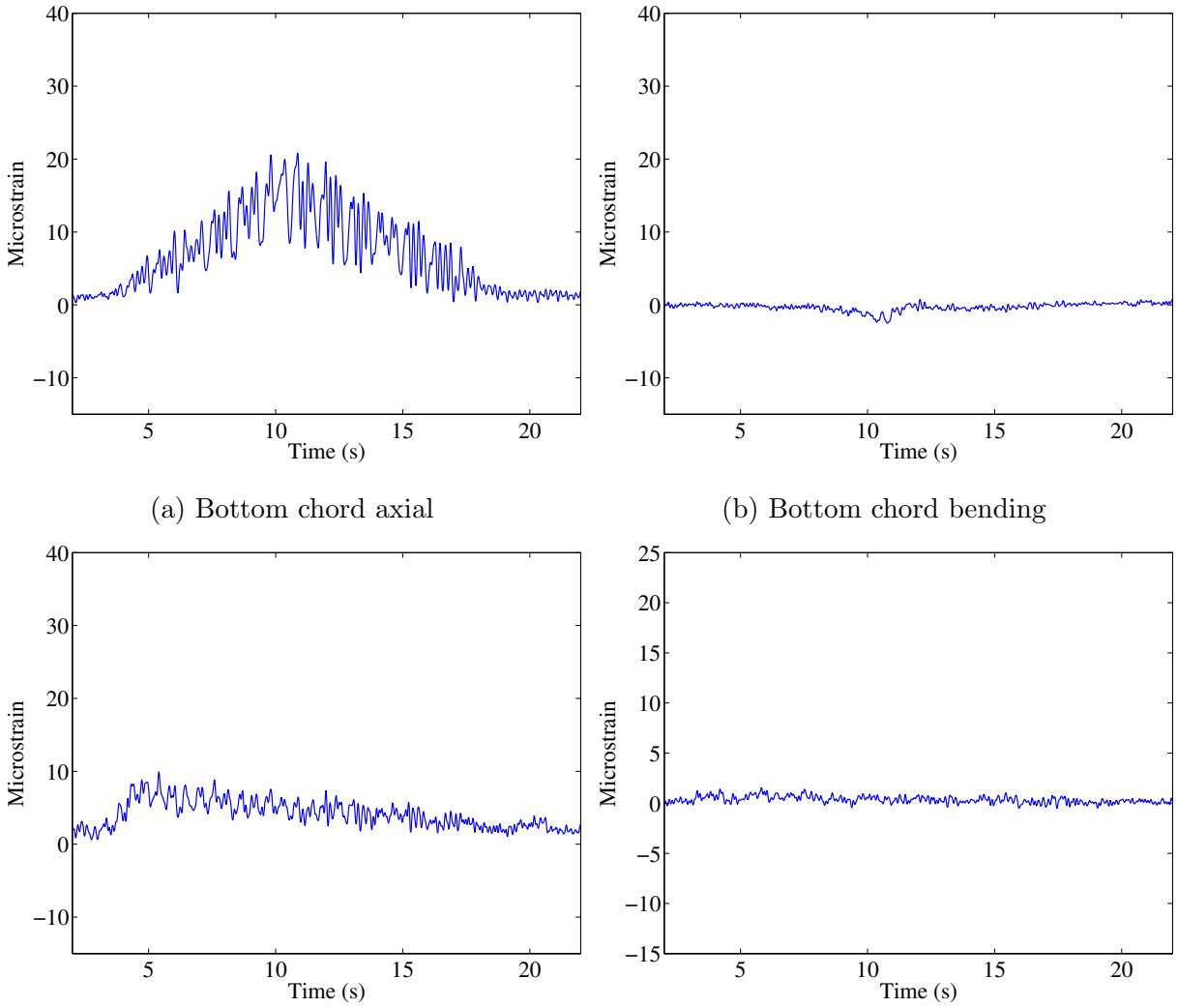

(a) Bottom chord axial

(b) Bottom chord bending

(c) Diagonal axial

(d) Diagonal bending

Figure C.15: Sample strain histories for single person walking at a pace of 110 BPM, weight: 0.65 kN, leg length: 0.95 m

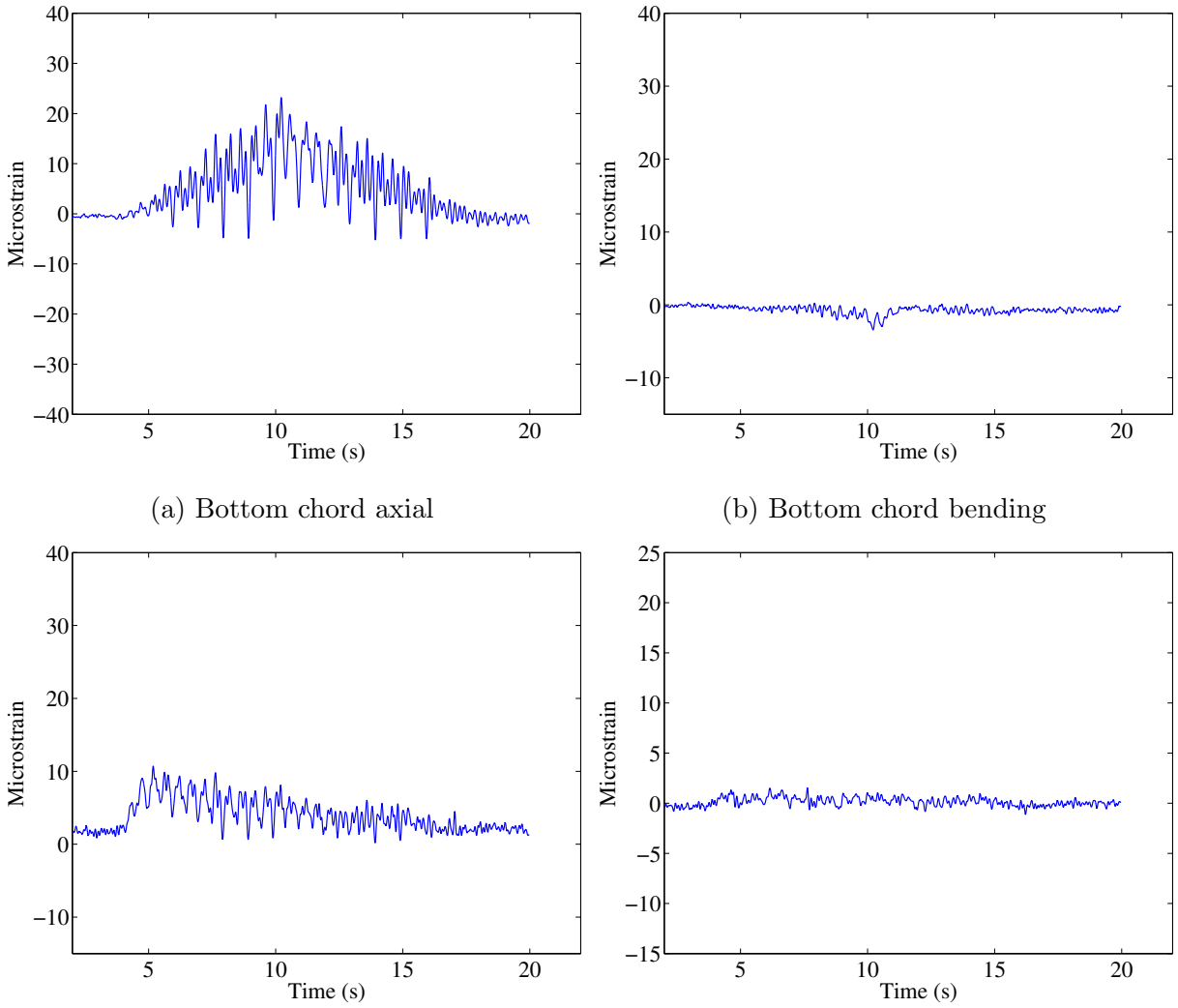

(a) Bottom chord axial

(b) Bottom chord bending

(c) Diagonal axial

(d) Diagonal bending

Figure C.16: Sample strain histories for single person walking at a pace of 120 BPM, weight: 0.65 kN, leg length: 0.95 m

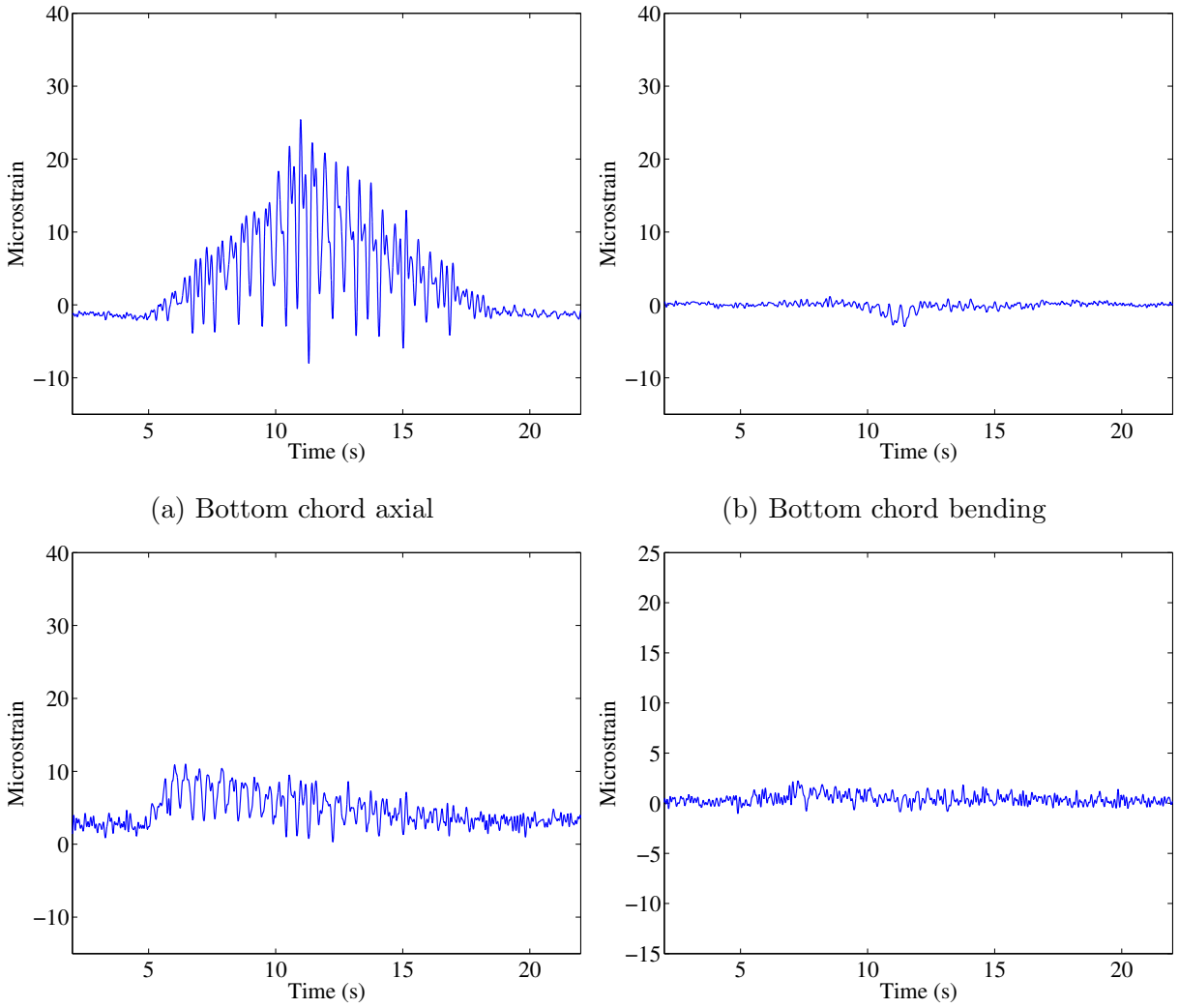

(a) Bottom chord axial

(b) Bottom chord bending

(c) Diagonal axial

(d) Diagonal bending

Figure C.17: Sample strain histories for single person walking at a pace of 130 BPM, weight: 0.65 kN, leg length: 0.95 m

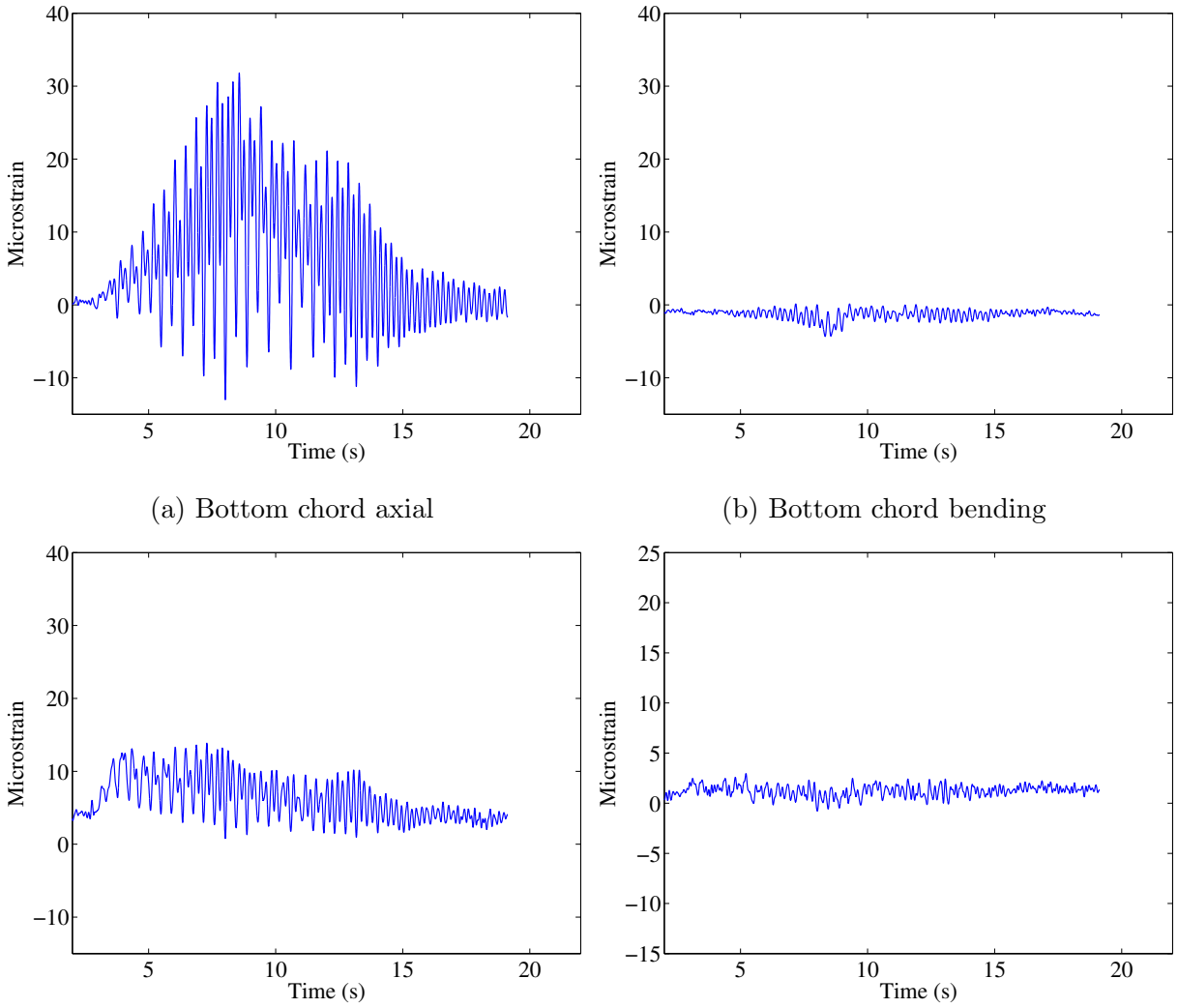

(a) Bottom chord axial

(b) Bottom chord bending

(c) Diagonal axial

(d) Diagonal bending

Figure C.18: Sample strain histories for single person walking at a pace of 140 BPM, weight: 0.65 kN, leg length: 0.95 m

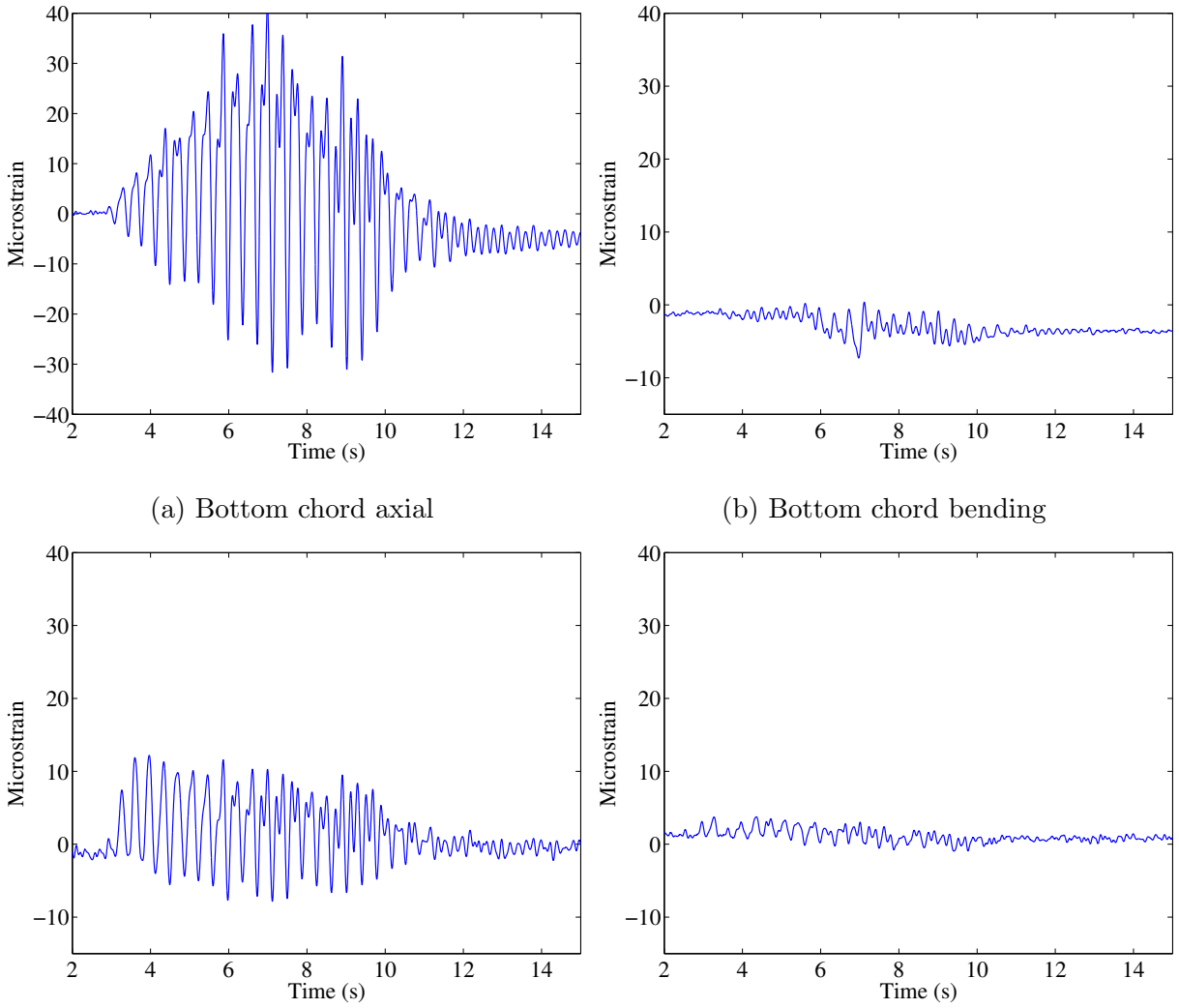

(a) Bottom chord axial

(b) Bottom chord bending

(c) Diagonal axial

(d) Diagonal bending

Figure C.19: Sample strain histories for single person walking at a pace of 160 BPM, weight: 0.65 kN, leg length: 0.95 m

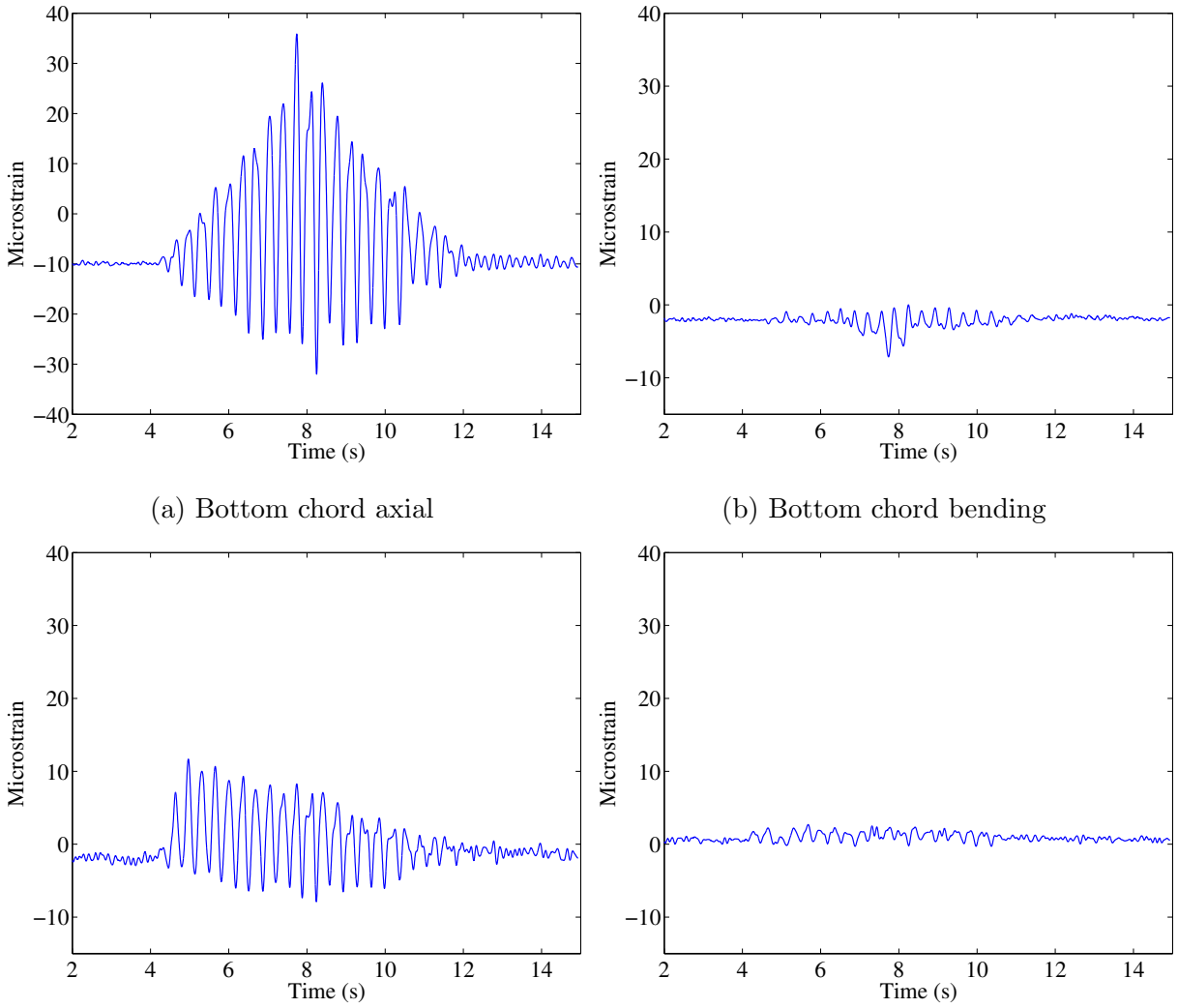

(a) Bottom chord axial

(b) Bottom chord bending

(c) Diagonal axial

(d) Diagonal bending

Figure C.20: Sample strain histories for single person walking at a pace of 170 BPM, weight: 0.65 kN, leg length: 0.95 m

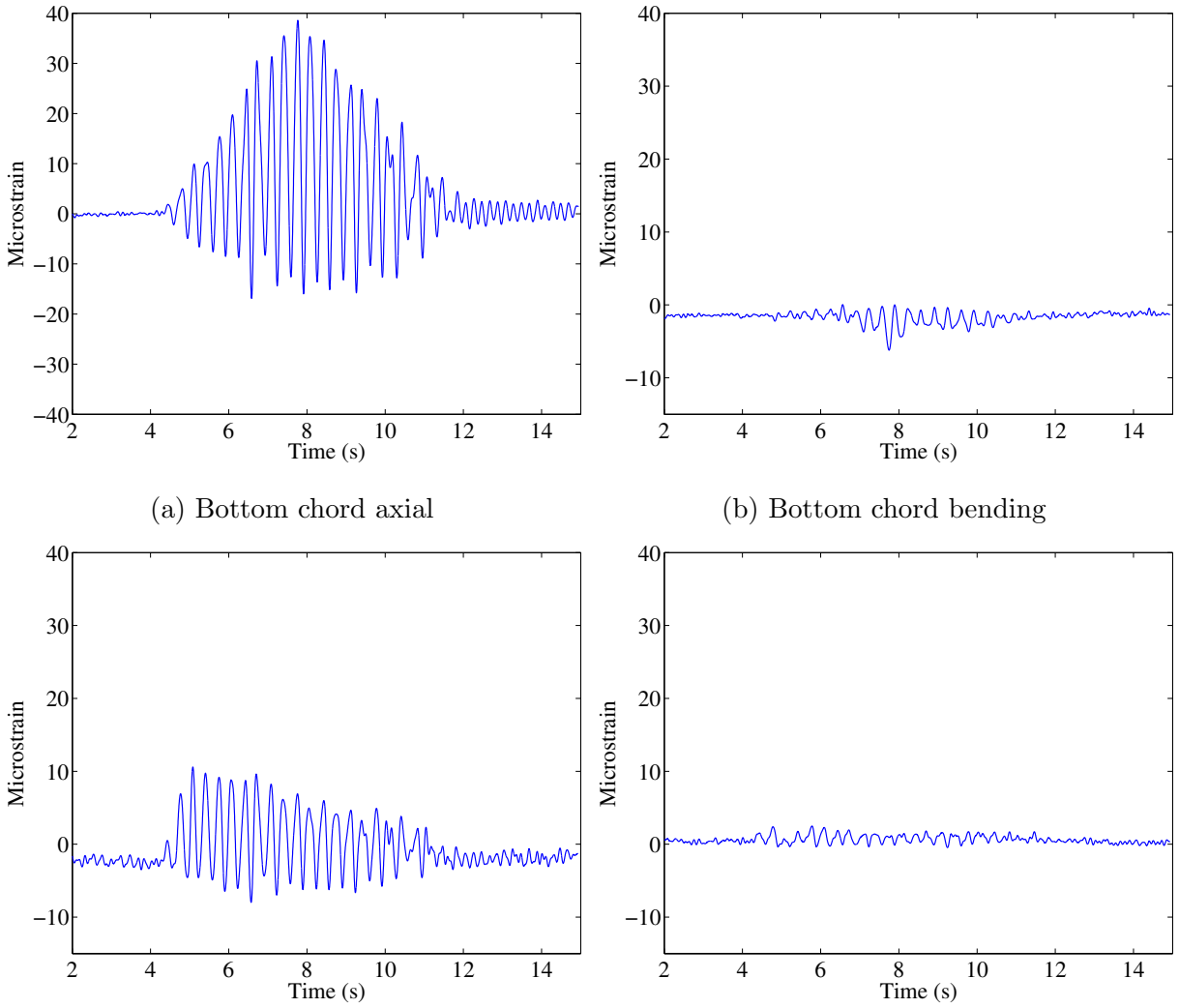

(a) Bottom chord axial

(b) Bottom chord bending

(c) Diagonal axial

(d) Diagonal bending

Figure C.21: Sample strain histories for single person walking at a pace of 180 BPM, weight: 0.65 kN, leg length: 0.95 m

Figure C.22 shows sample load results for the smallest crowd for the fourteen-bay bridge (0.2 p/m^2) passing over the bridge at a time in the same direction.

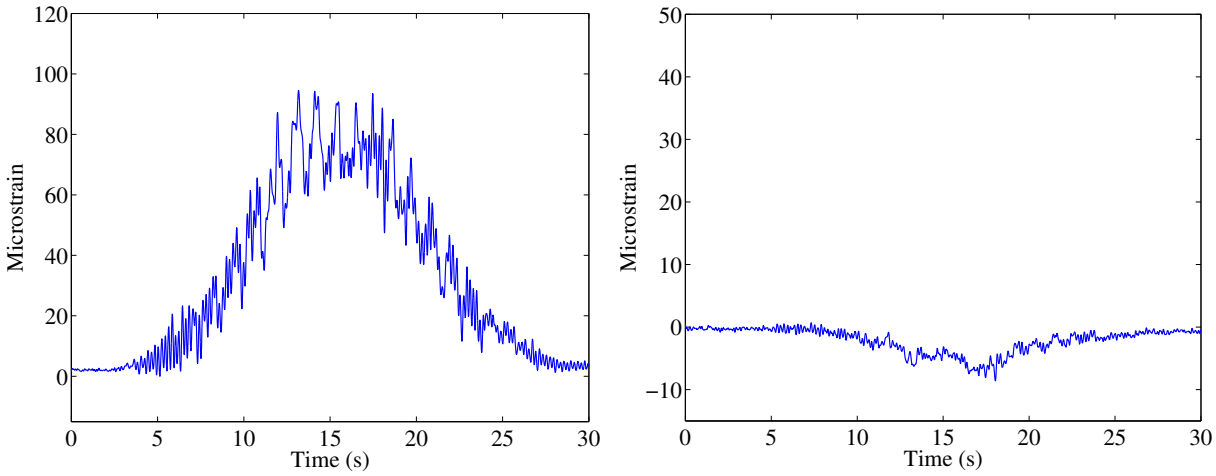

(a) Bottom chord axial

(b) Bottom chord bending

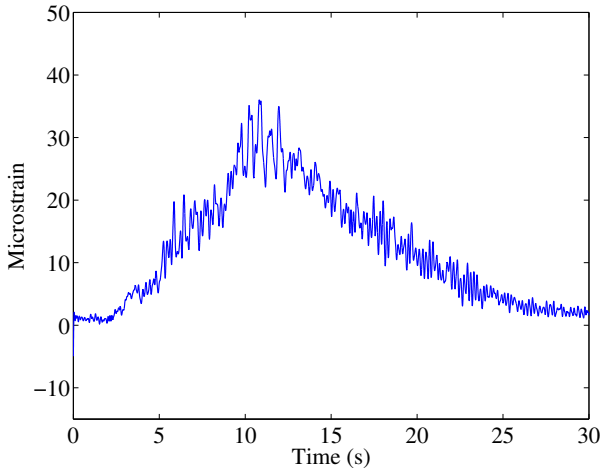

(c) Diagonal axial

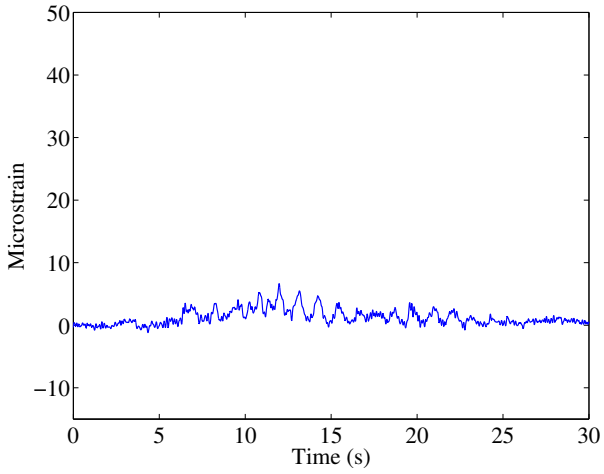

(d) Diagonal bending

Figure C.22: Sample strain histories for 0.2 p/m^2 walking, total weight: 4.27 kN

Similarly, figures C.23 and C.24 show similar strain results for crowds of 0.5 p/m^2 and 1.0 p/m^2.

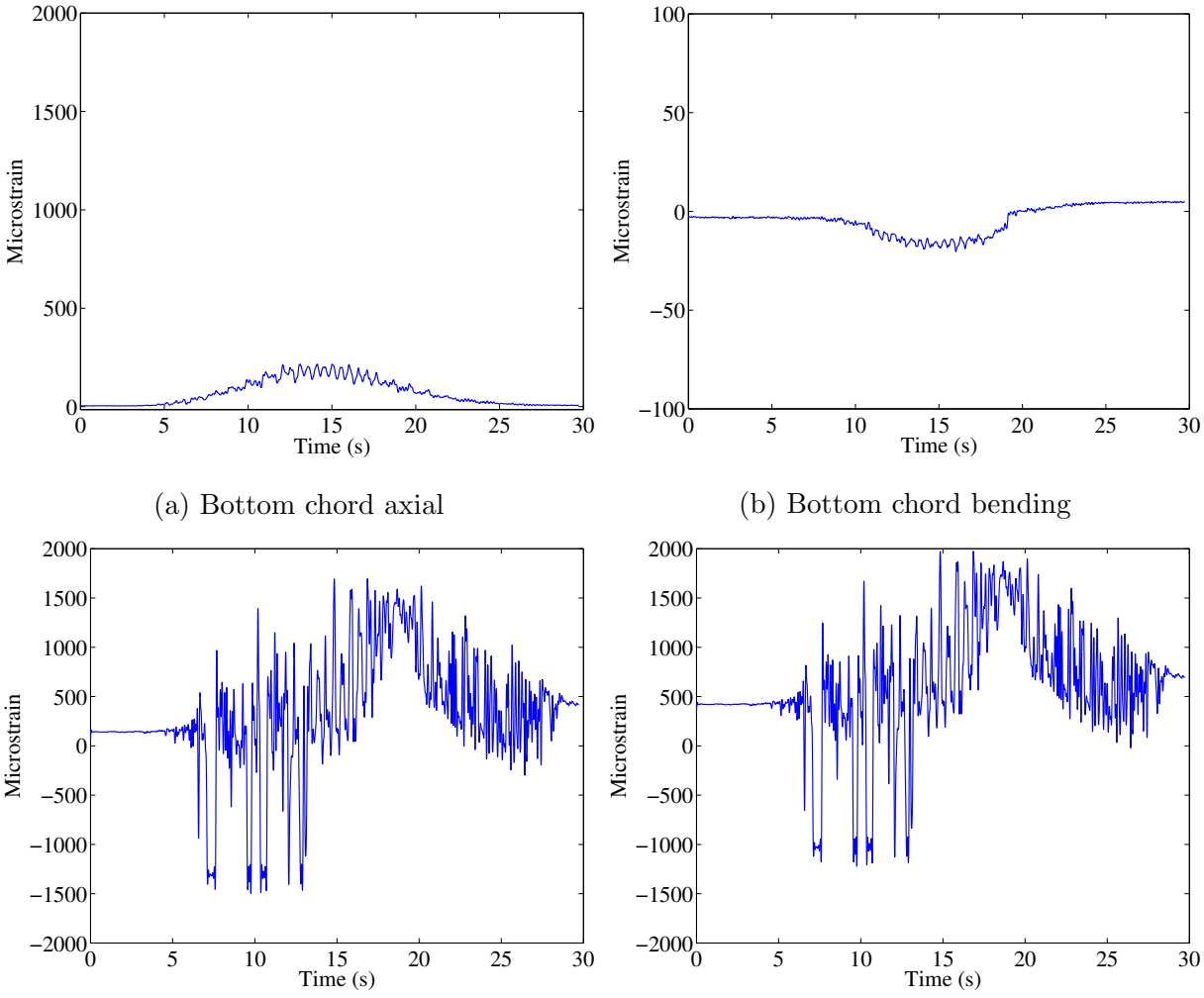

(a) Bottom chord axial

(b) Bottom chord bending

(c) Diagonal axial

(d) Diagonal bending

Figure C.23: Sample strain histories for 0.5 p/m^2 walking, total weight: 9.66 kN, suspected voltage overload on diagonal strain gauges

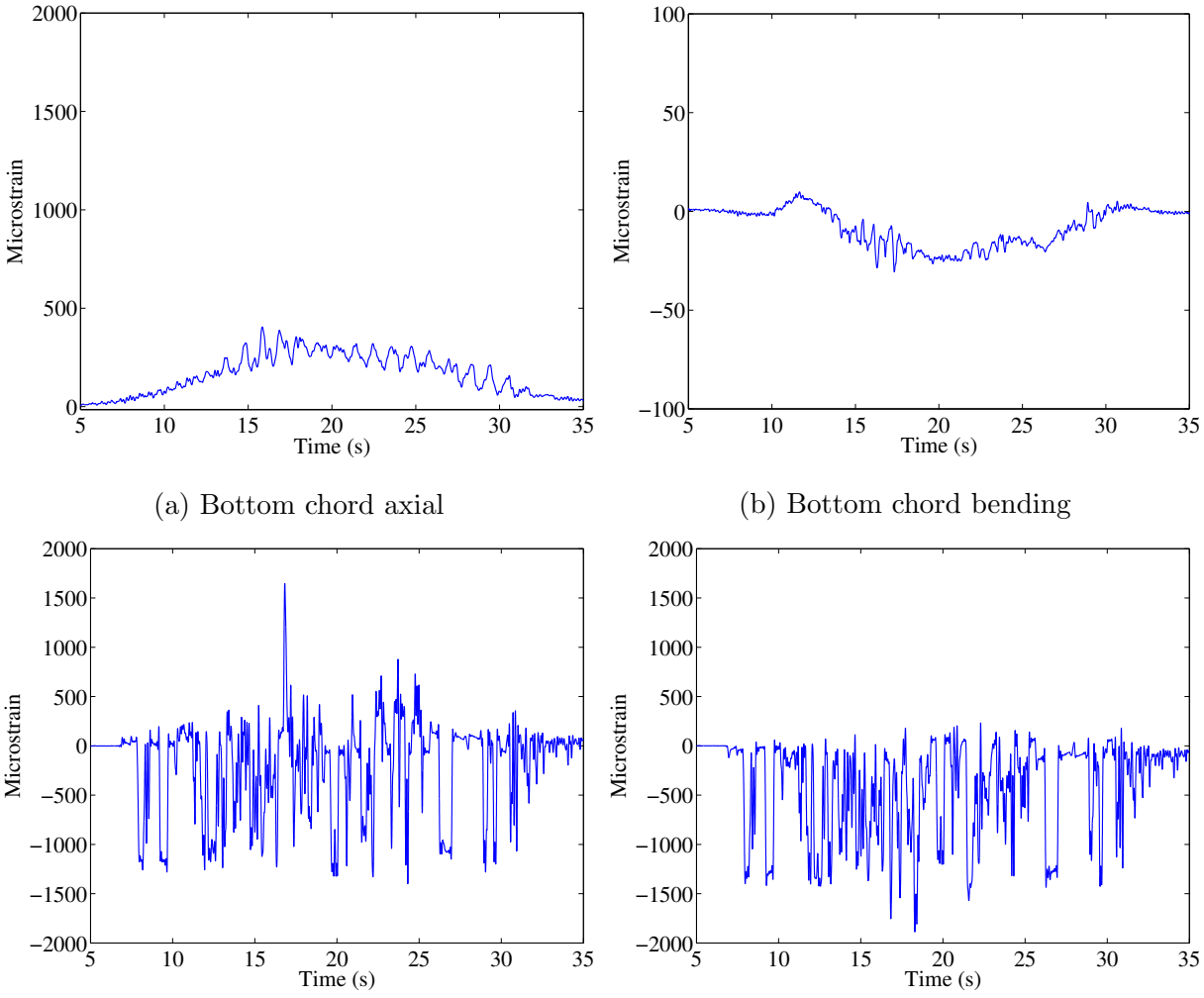

(a) Bottom chord axial

(b) Bottom chord bending

(c) Diagonal axial

(d) Diagonal bending

Figure C.24: Sample strain histories for 1.0 p/m^2 walking, total weight: 20.32 kN, suspected voltage overload on diagonal strain gauges

Figures C.25 and C.26 show the strain histories for two people walking in sync and out of sync (one at 115 BPM and one at 130 BPM).

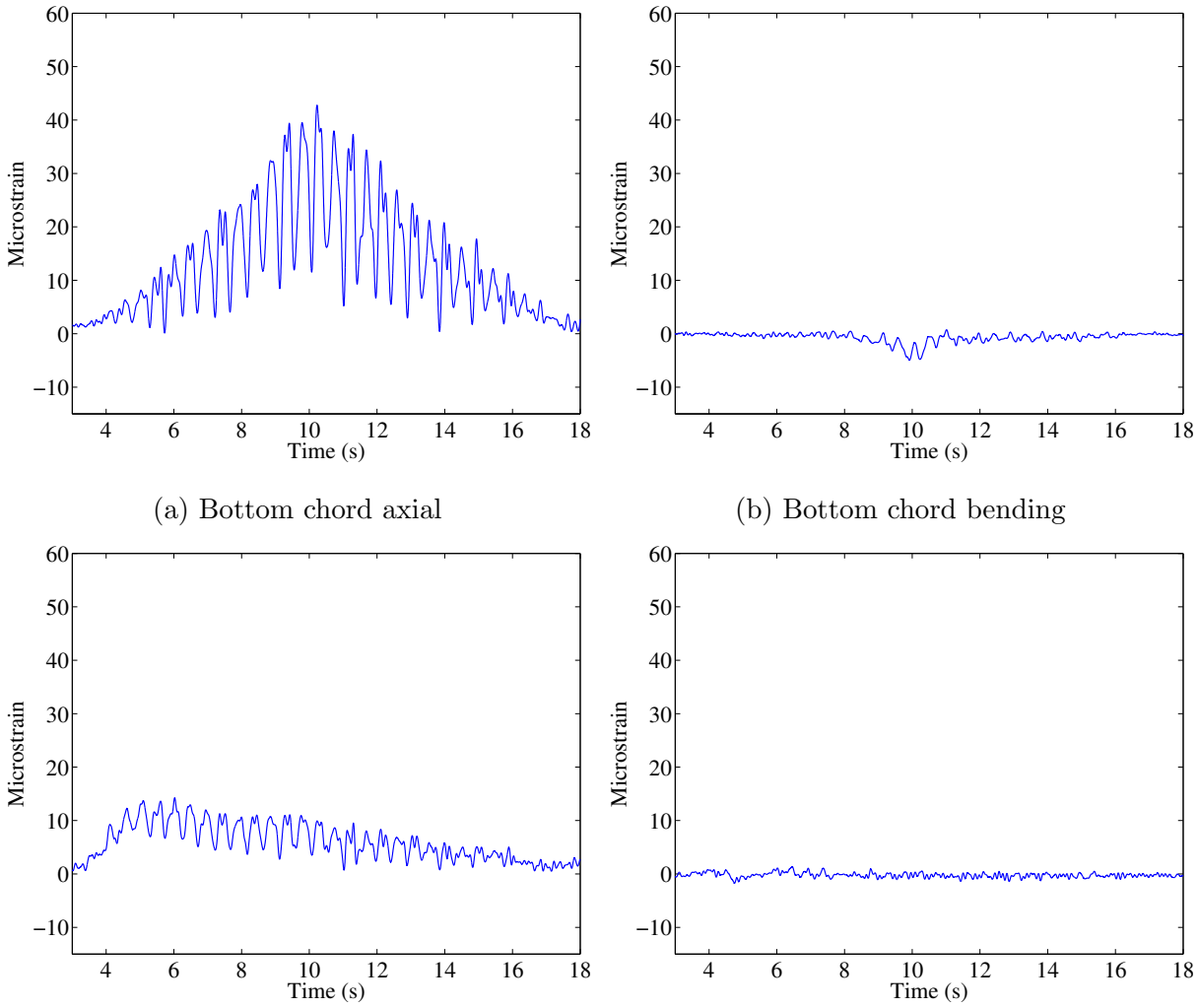

(a) Bottom chord axial

(b) Bottom chord bending

(c) Diagonal axial

(d) Diagonal bending

Figure C.25: Sample load histories for two people walking synchronously, total weight: 1.25 kN

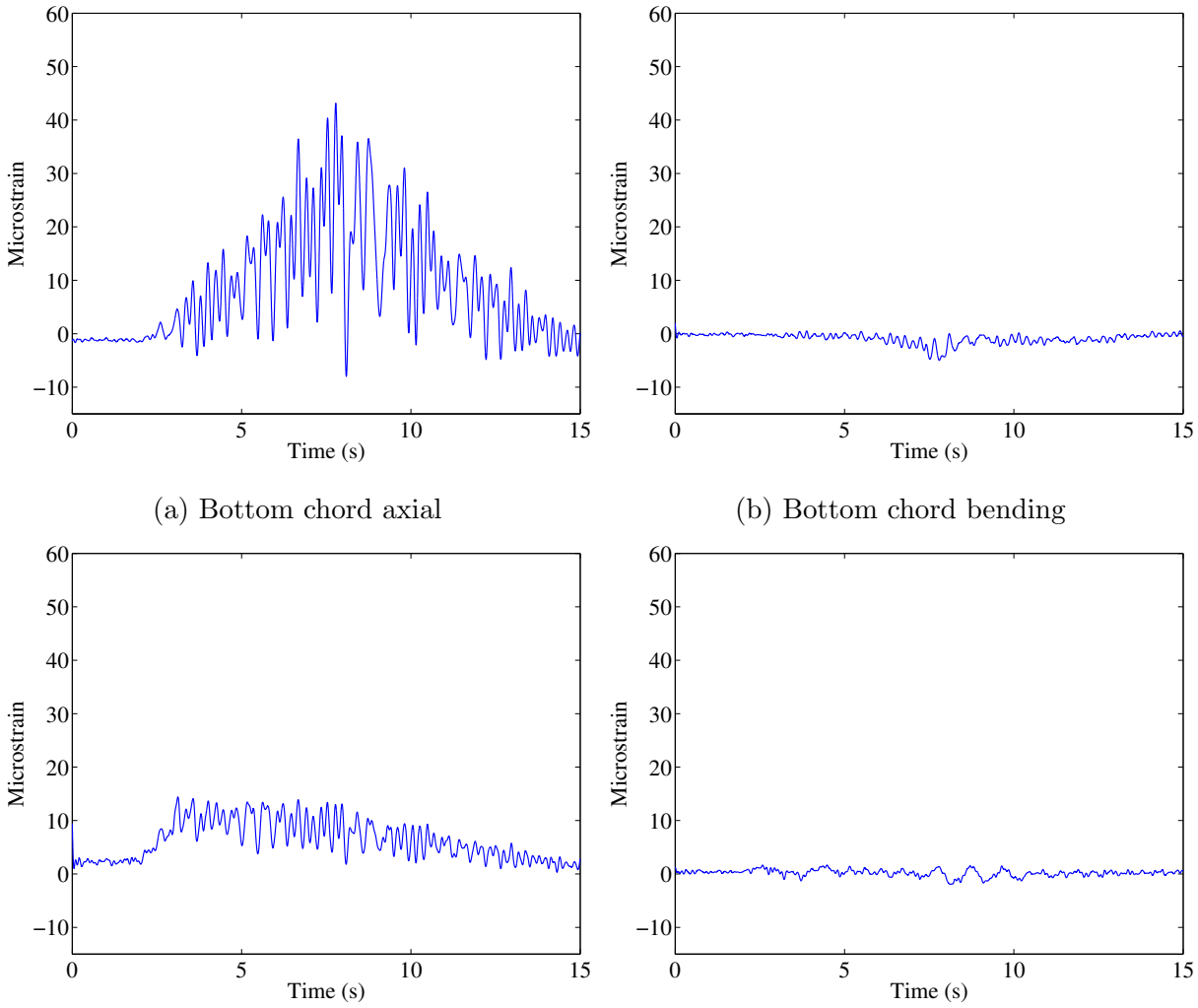

(a) Bottom chord axial

(b) Bottom chord bending

(c) Diagonal axial

(d) Diagonal bending

Figure C.26: Sample load histories for two people walking asynchronously, total weight: 1.25 kN

Appendix D

Finite element model results

Results from the SOFiSTiK finite element models of the two-bay, eight-bay, and fourteen-bay bridges are provided below. Note that the magnitude of the member forces are indicated by the colour gradient, where blue is the minimum and red is the maximum.

D.1 Two-bay bridge

Two-bay bridge

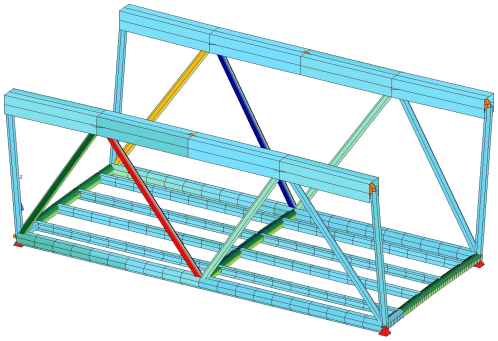

Figure D.1: Two-bay bridge: 7.55 Hz

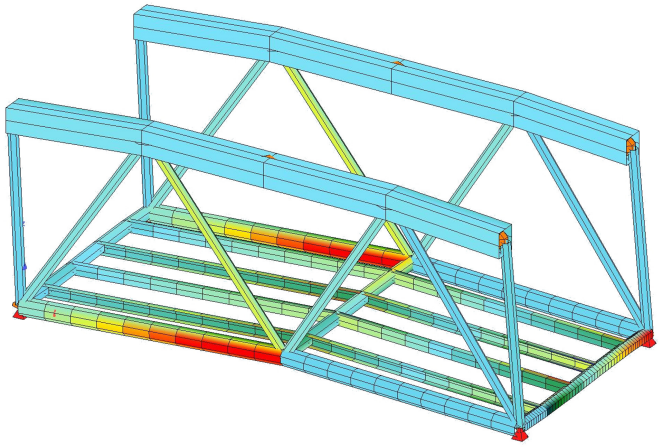

Figure D.2: Two-bay bridge: 15.38 Hz

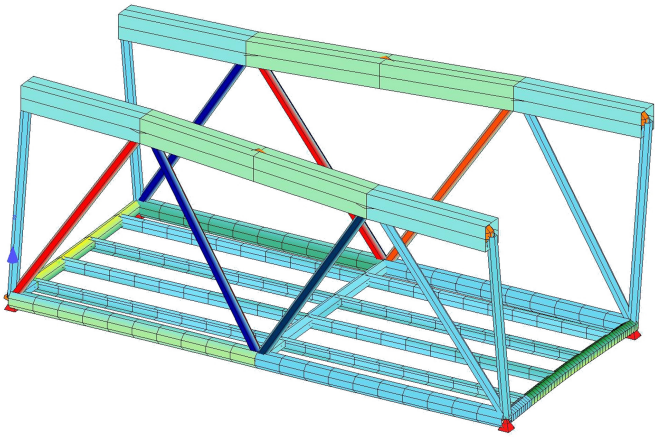

Figure D.3: Two-bay bridge: 17.90 Hz

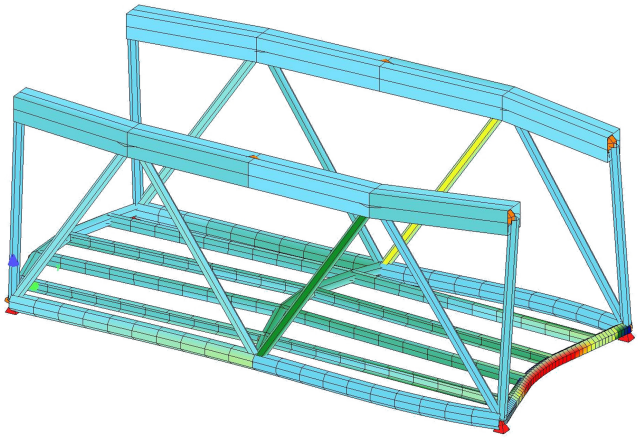

Figure D.4: Two-bay bridge: 31.66 Hz

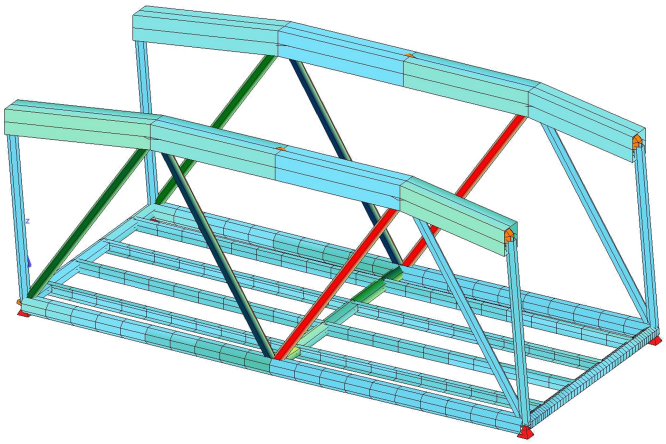

Figure D.5: Two-bay bridge: 37.88 Hz

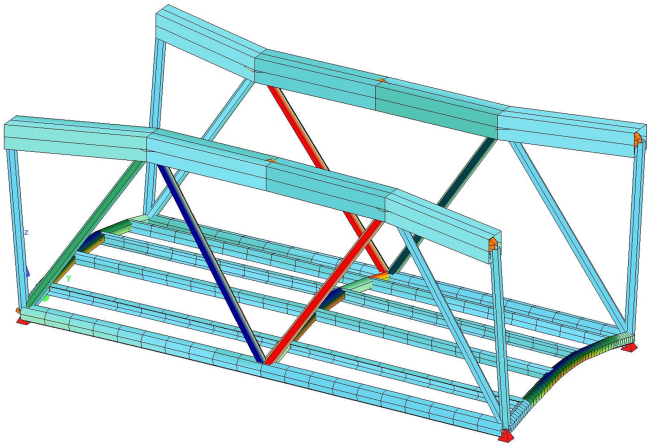

Figure D.6: Two-bay bridge: 42.37 Hz

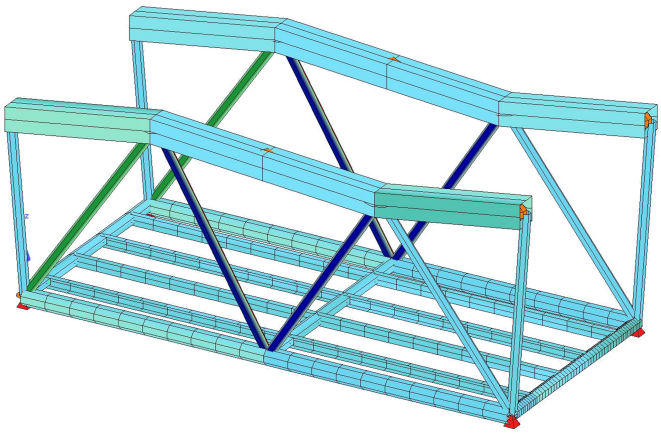

Figure D.7: Two-bay bridge: 44.08 Hz

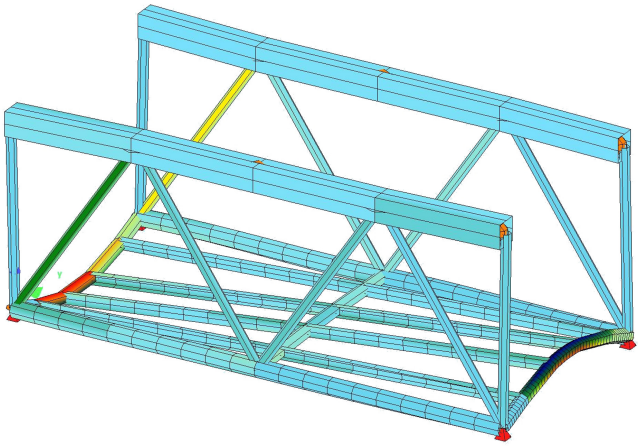

Figure D.8: Two-bay bridge: 50.11 Hz

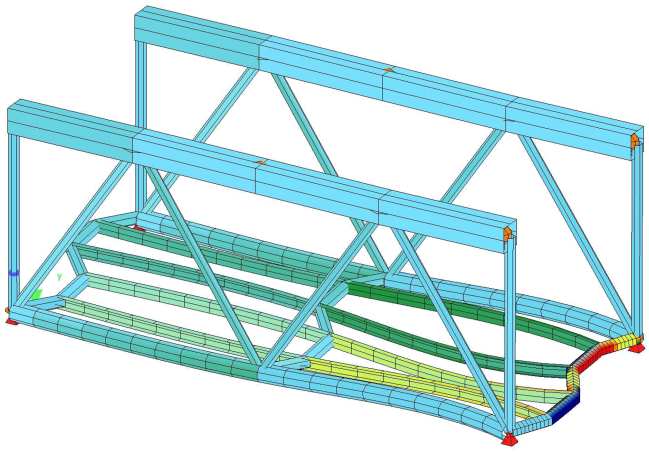

Figure D.9: Two-bay bridge: 88.13 Hz

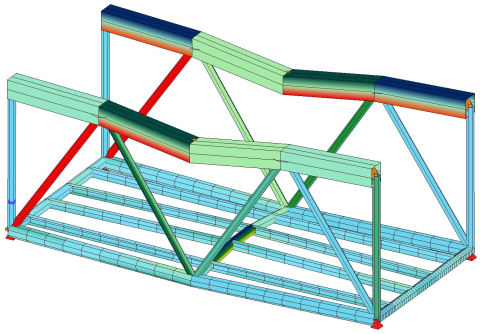

Figure D.10: Two-bay bridge: 119.29 Hz

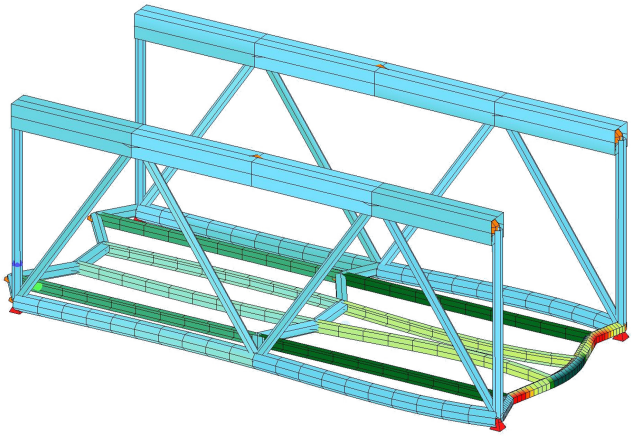

Figure D.11: Two-bay bridge: 138.47 Hz

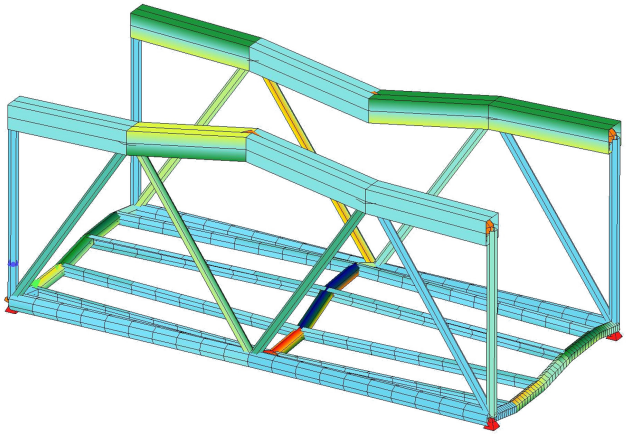

Figure D.12: Two-bay bridge: 142.32 Hz

D.2 Eight-bay bridge

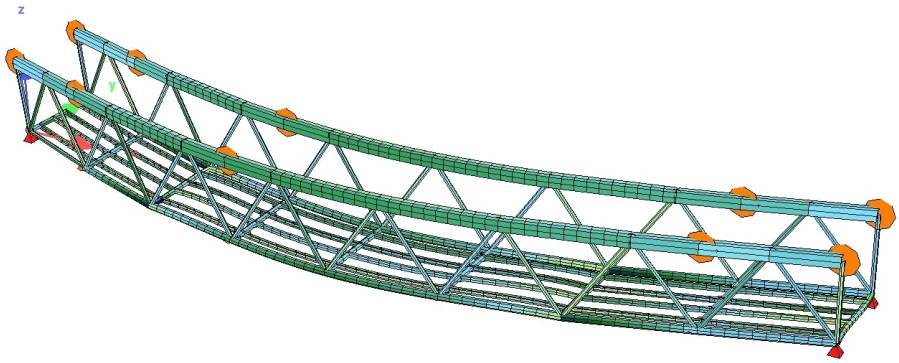

Figure D.13: Eight-bay bridge: 2.32 Hz

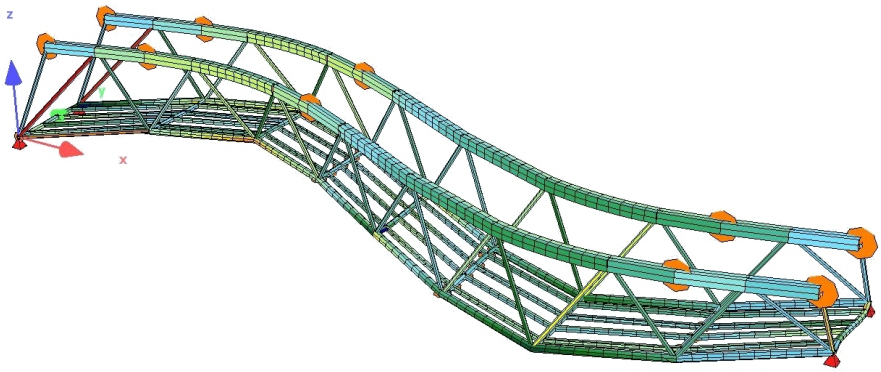

Figure D.14: Eight-bay bridge: 6.10 Hz

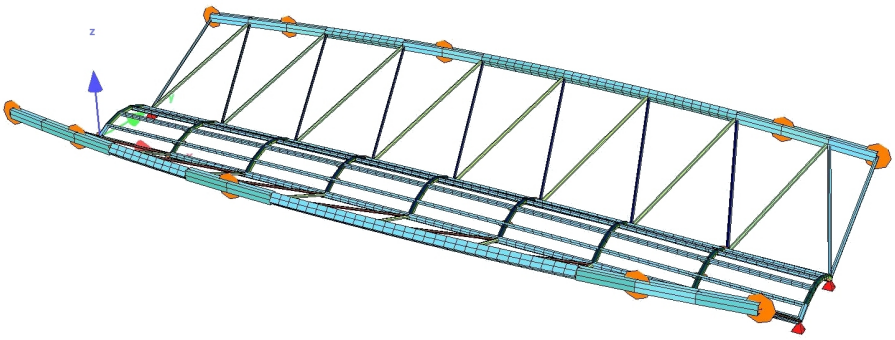

Figure D.15: Eight-bay bridge: 8.01 Hz

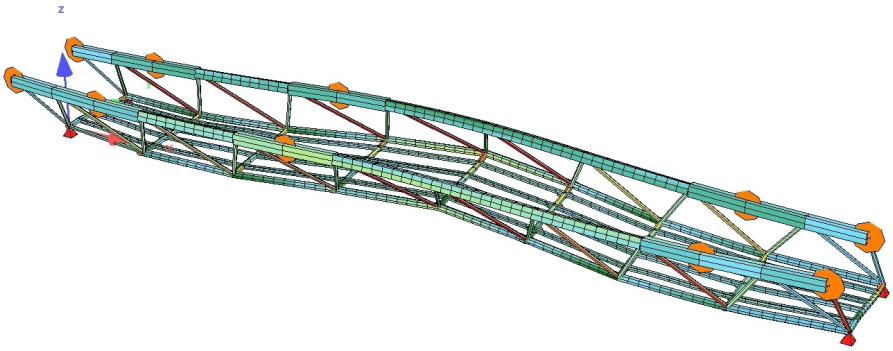

Figure D.16: Eight-bay bridge: 9.85 Hz

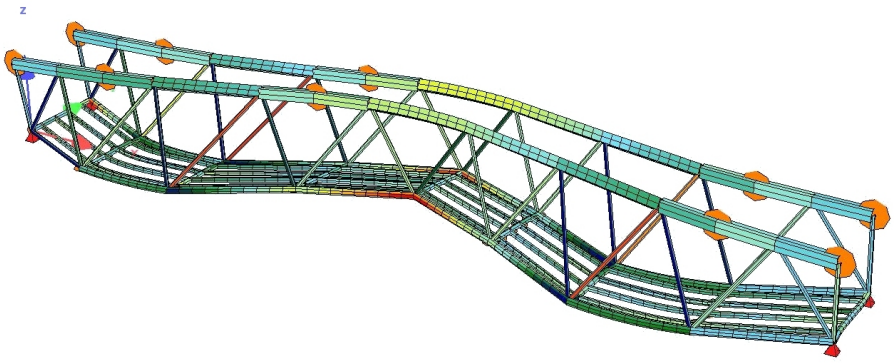

Figure D.17: Eight-bay bridge: 10.95 Hz

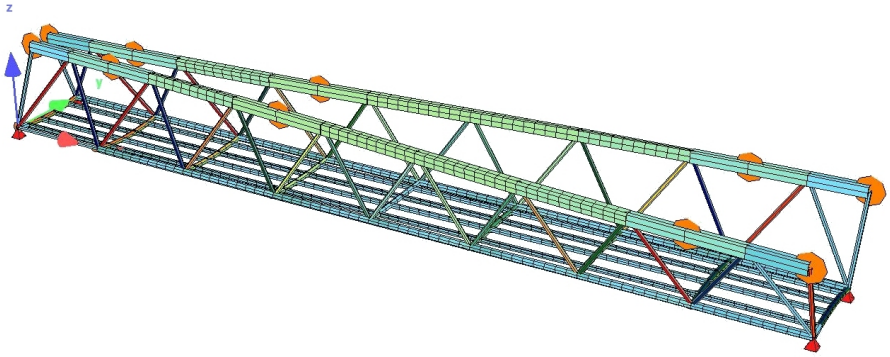

Figure D.18: Eight-bay bridge: 11.75 Hz

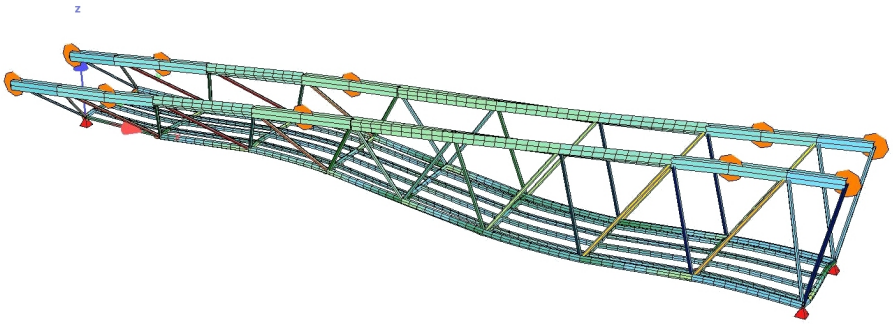

Figure D.19: Eight-bay bridge: 14.31 Hz

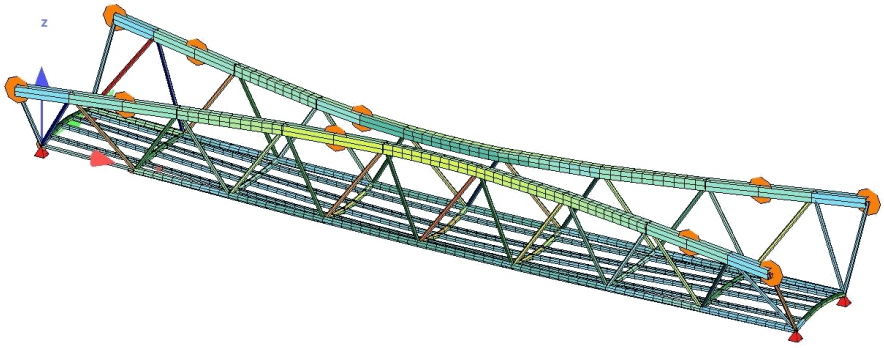

Figure D.20: Eight-bay bridge: 15.77 Hz

Figure D.21: Eight-bay bridge: 16.86 Hz

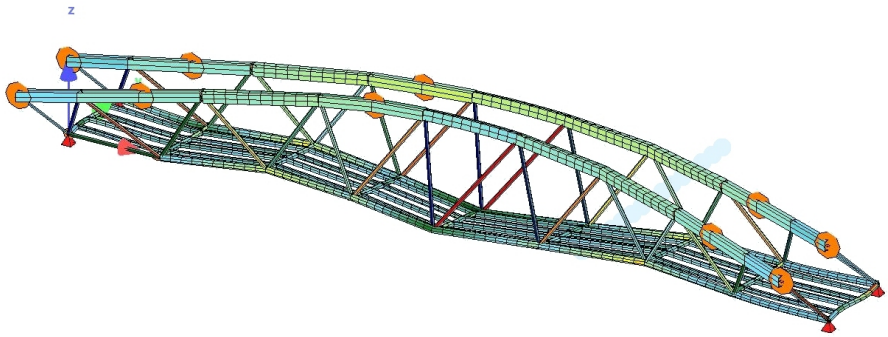

Figure D.22: Eight-bay bridge: 18.04 Hz

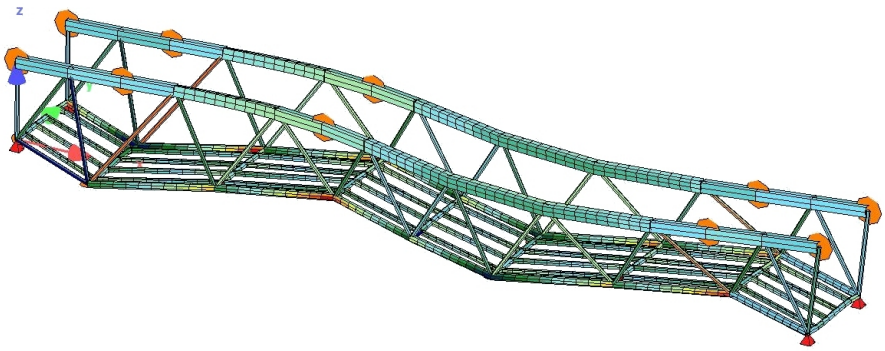

Figure D.23: Eight-bay bridge: 19.87 Hz

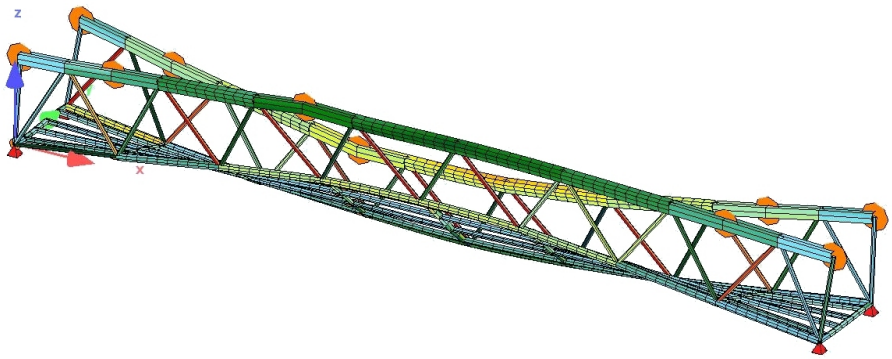

Figure D.24: Eight-bay bridge: 23.28 Hz

Figure D.25: Eight-bay bridge: 24.04 Hz

Figure D.26: Eight-bay bridge: 24.69 Hz

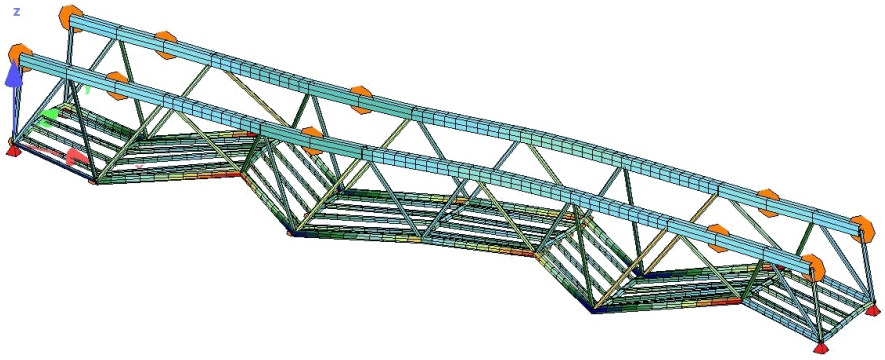

Figure D.27: Eight-bay bridge: 31.26 Hz

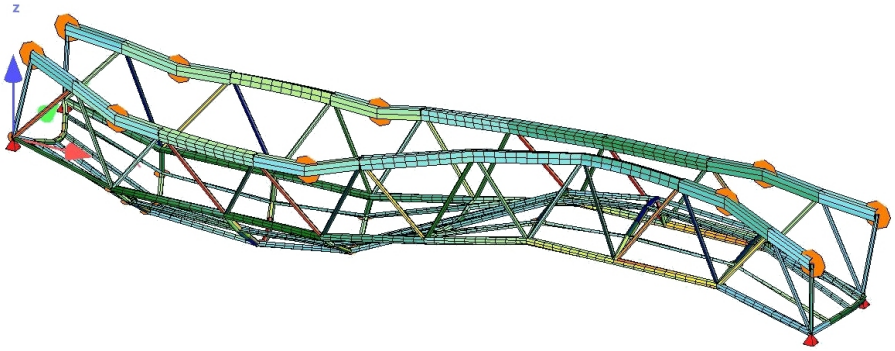

Figure D.28: Eight-bay bridge: 32.06 Hz

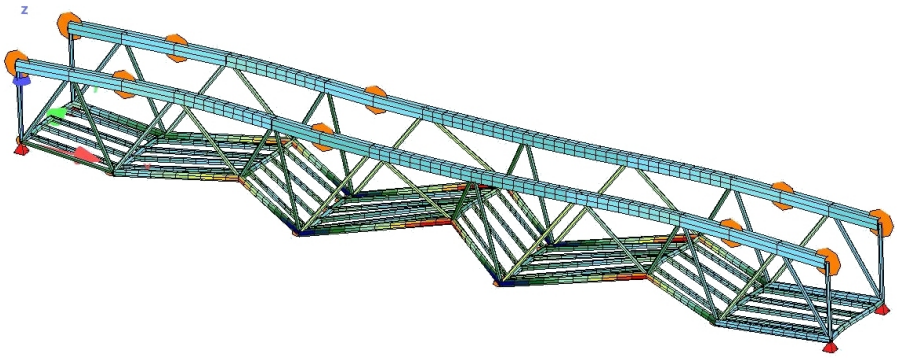

Figure D.29: Eight-bay bridge: 37.19 Hz

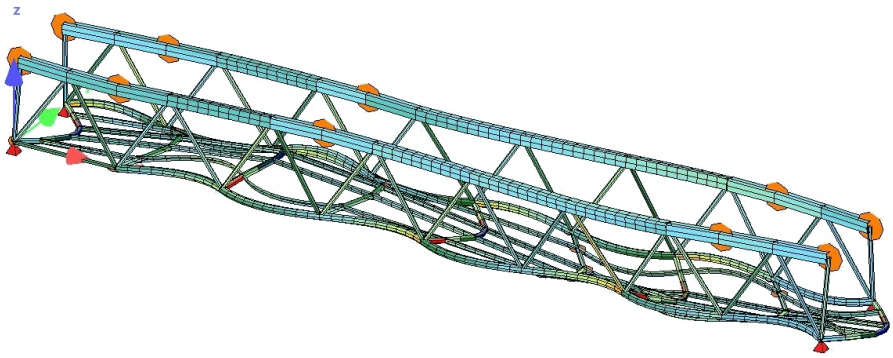

Figure D.30: Eight-bay bridge: 38.92 Hz

Figure D.31: Eight-bay bridge: 42.18 Hz

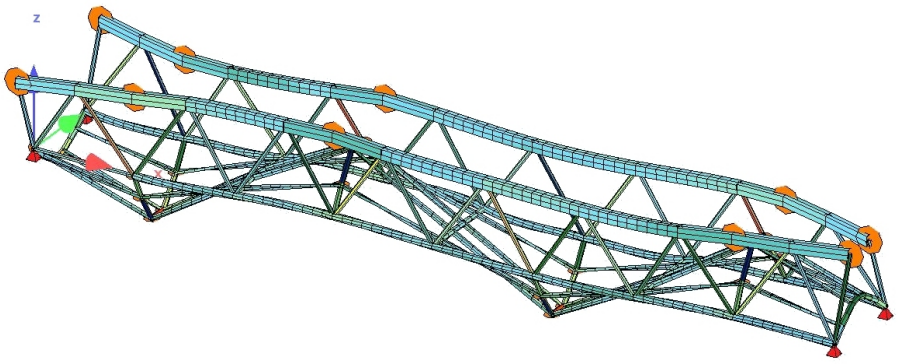

Figure D.32: Eight-bay bridge: 45.55 Hz

Figure D.33: Eight-bay bridge: 47.86 Hz

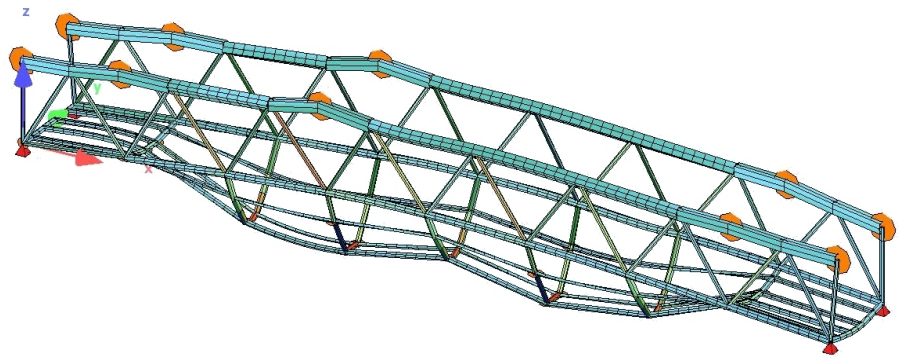

Figure D.35: Eight-bay bridge: 53.55 Hz

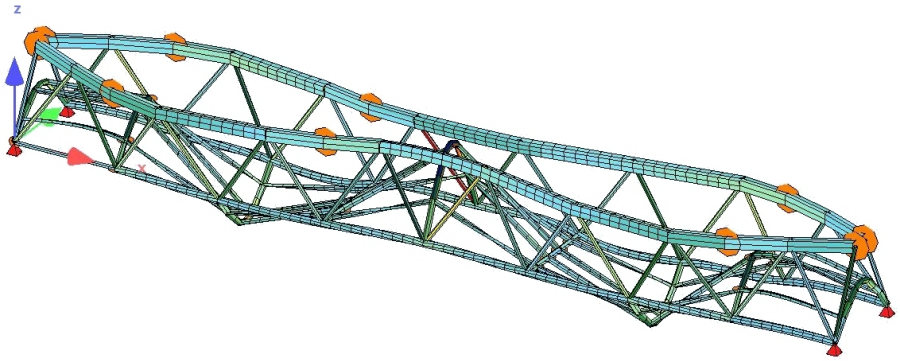

Figure D.34: Eight-bay bridge: 50.94 Hz

Figure D.36: Eight-bay bridge: 54.43 Hz

Figure D.37: Eight-bay bridge: 60.55 Hz

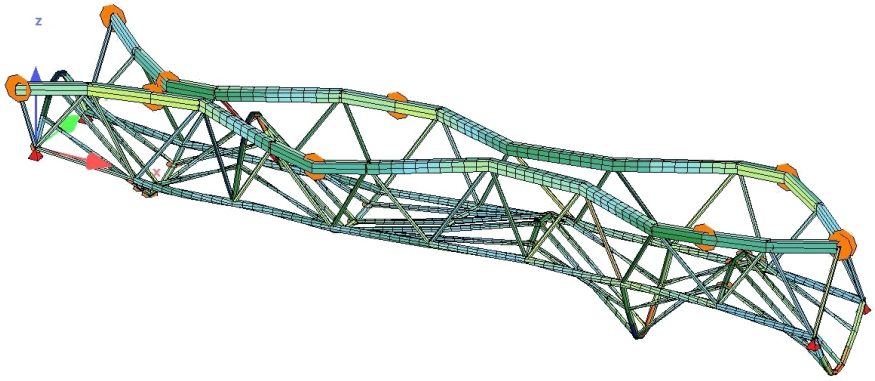

Figure D.38: Eight-bay bridge: 62.31 Hz

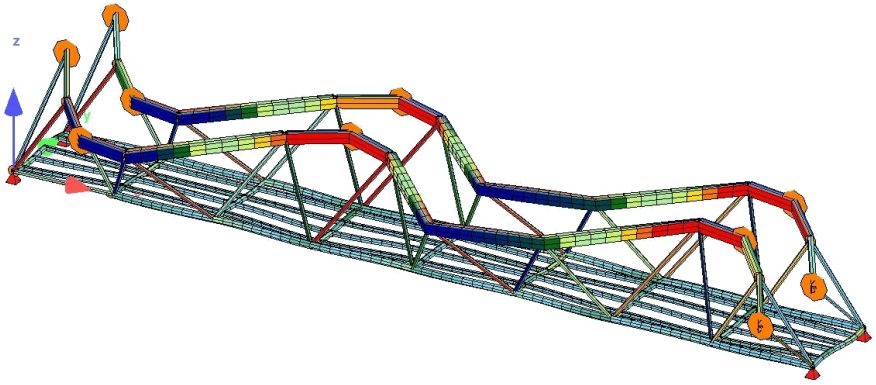

Figure D.39: Eight-bay bridge: 63.77 Hz

Figure D.40: Eight-bay bridge: 64.36 Hz

Figure D.41: Eight-bay bridge: 66.07 Hz

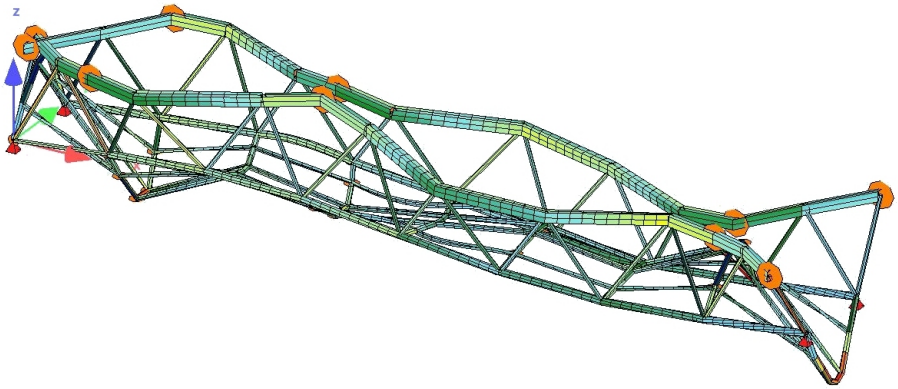

Figure D.42: Eight-bay bridge: 67.06 Hz

D.3 Fourteen-bay bridge

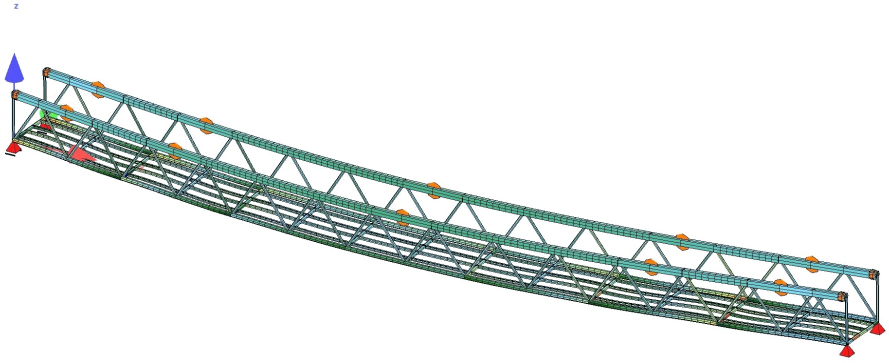

Figure D.43: Eight-bay bridge: 0.91 Hz

Figure D.44: Fourteen-bay bridge: 2.85 Hz

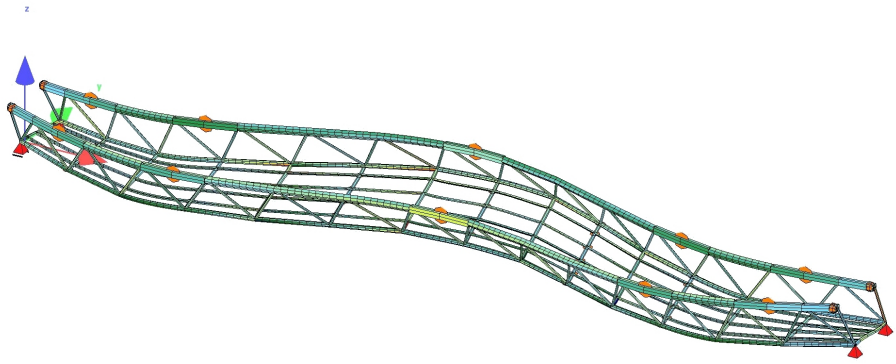

Figure D.45: Fourteen-bay bridge: 5.08 Hz

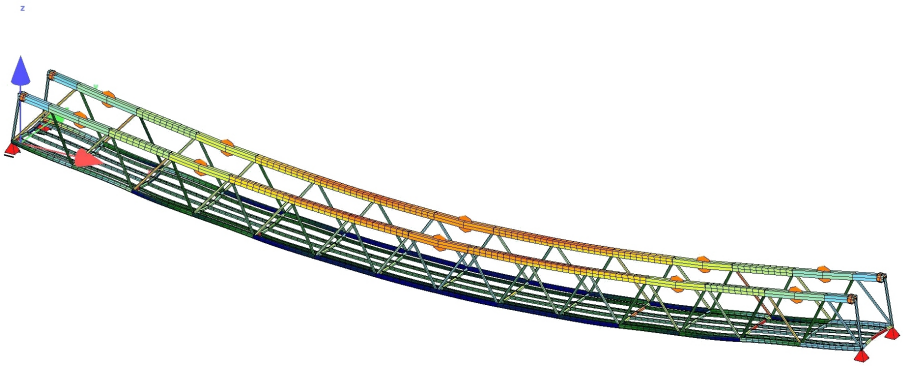

Figure D.46: Fourteen-bay bridge: 5.11 Hz

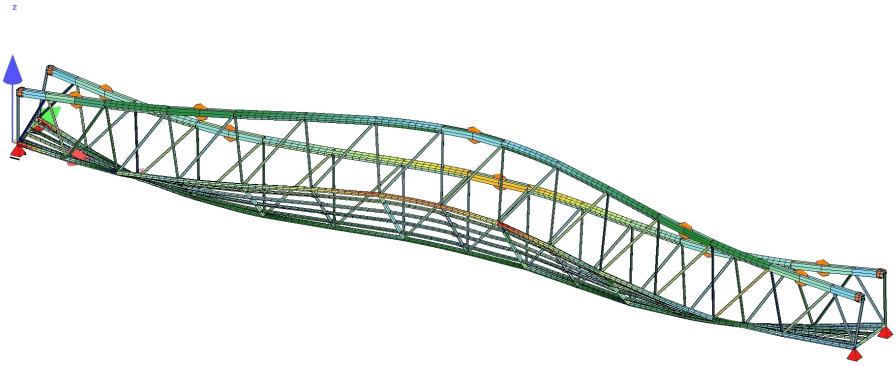

Figure D.47: Fourteen-bay bridge: 5.38 Hz

Figure D.48: Fourteen-bay bridge: 7.85 Hz

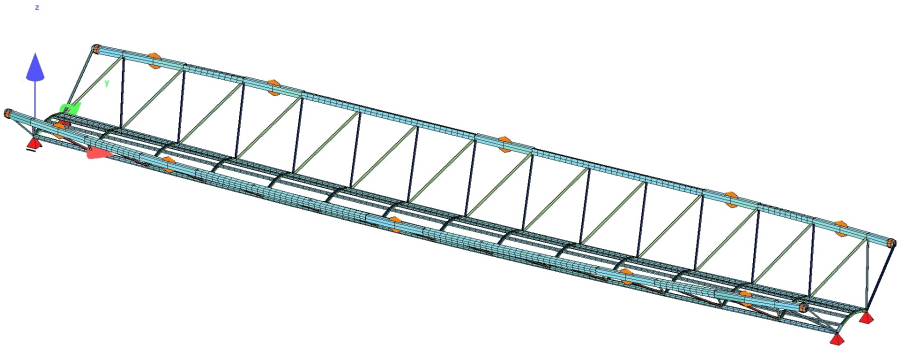

Figure D.49: Fourteen-bay bridge: 7.94 Hz

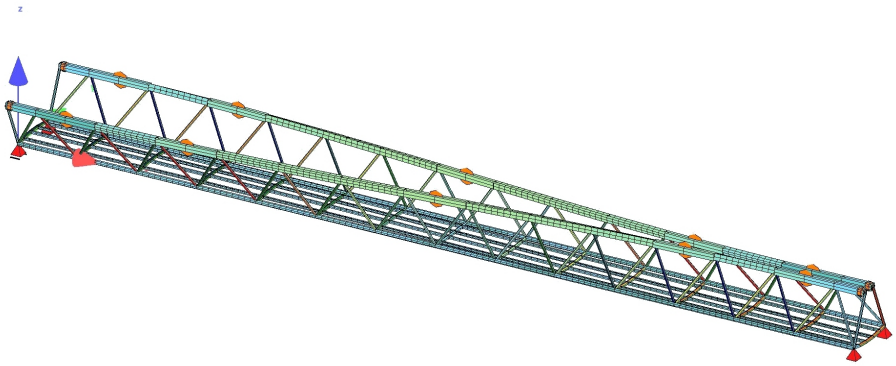

Figure D.50: Fourteen-bay bridge: 9.67 Hz

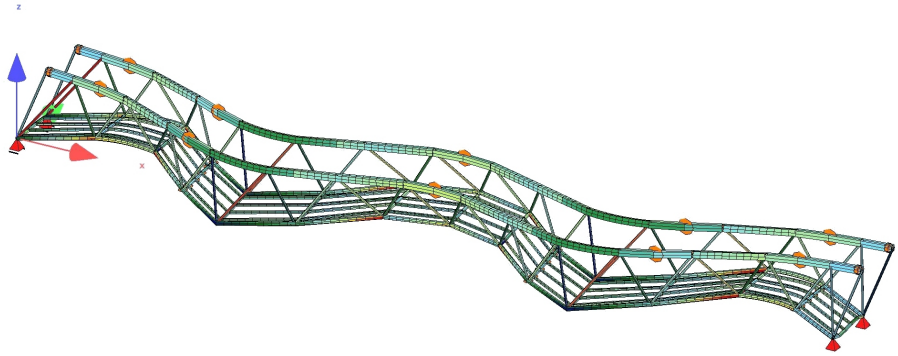

Figure D.51: Fourteen-bay bridge: 10.65 Hz

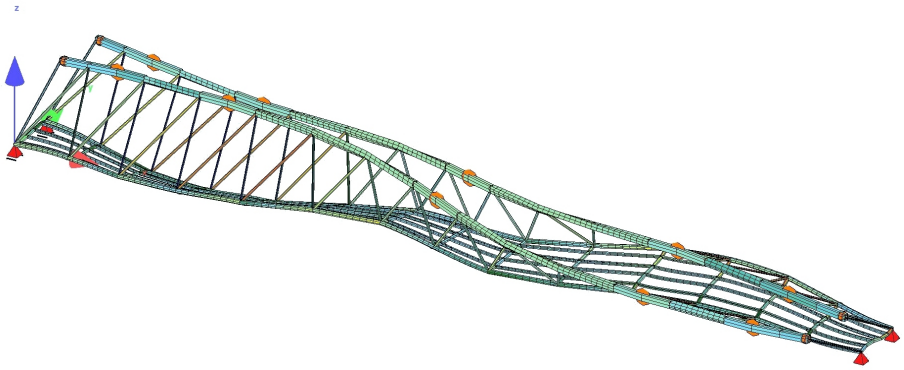

Figure D.52: Fourteen-bay bridge: 11.84 Hz

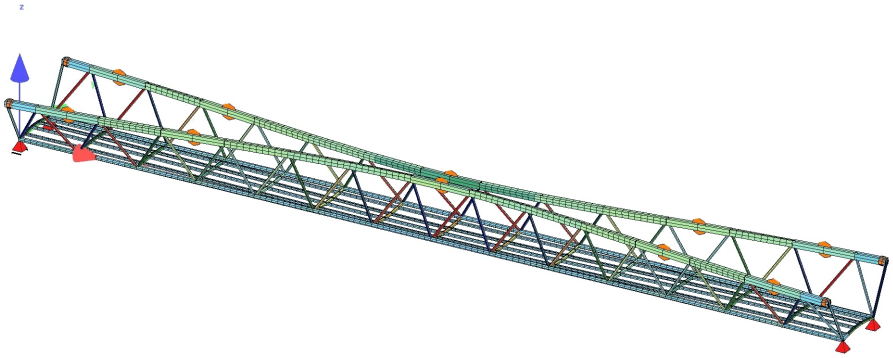

Figure D.53: Fourteen-bay bridge: 12.25 Hz

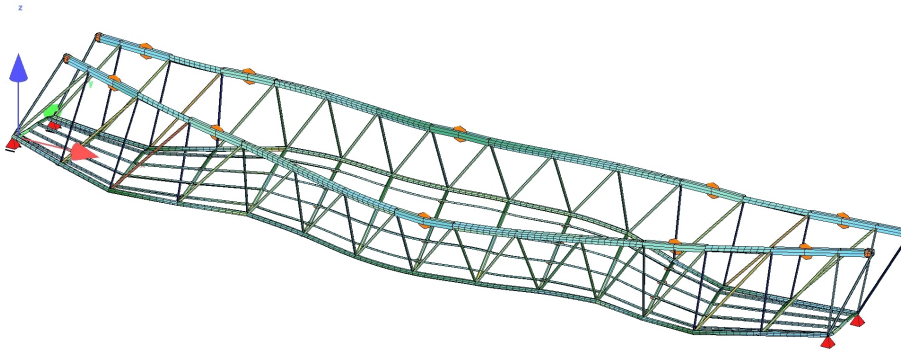

Figure D.54: Fourteen-bay bridge: 13.37 Hz

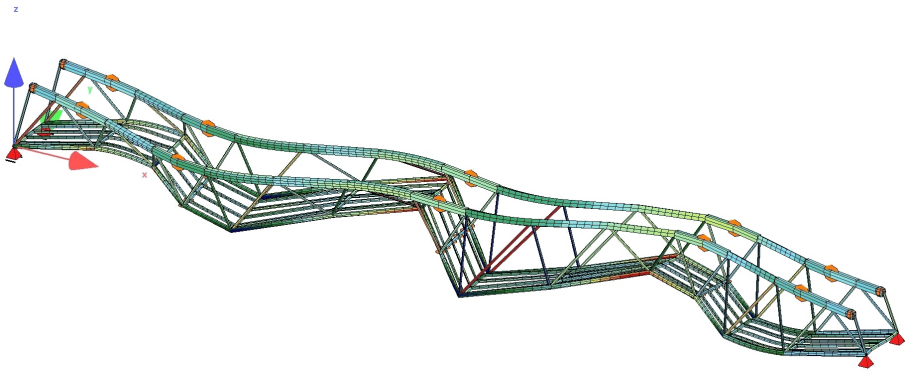

Figure D.55: Fourteen-bay bridge: 13.66 Hz

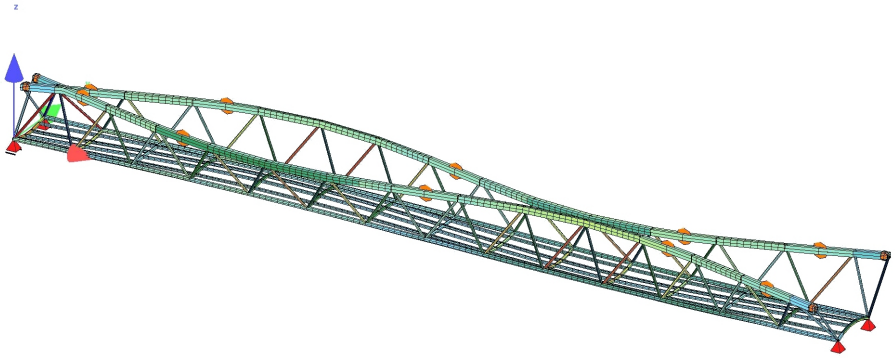

Figure D.56: Fourteen-bay bridge: 14.80 Hz

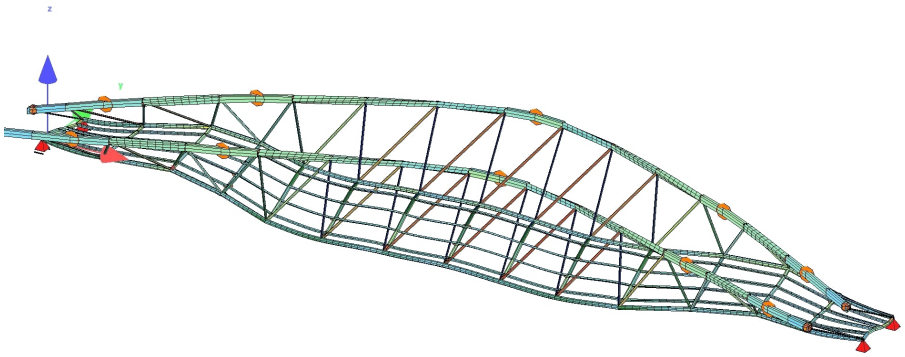

Figure D.57: Fourteen-bay bridge: 15.75 Hz

Figure D.58: Fourteen-bay bridge: 16.49 Hz

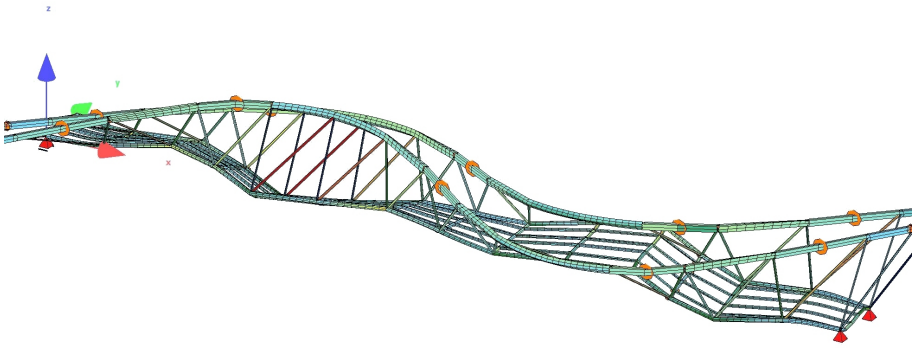

Figure D.59: Fourteen-bay bridge: 17.31 Hz

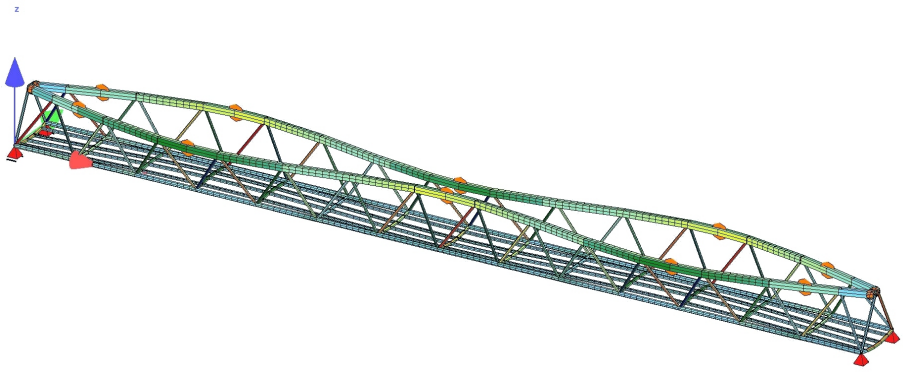

Figure D.60: Fourteen-bay bridge: 18.54 Hz

Figure D.61: Fourteen-bay bridge: 20.10 Hz

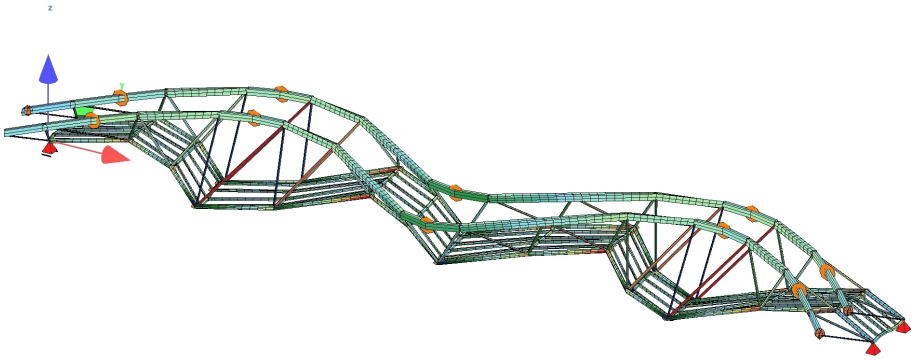

Figure D.62: Fourteen-bay bridge: 22.01 Hz

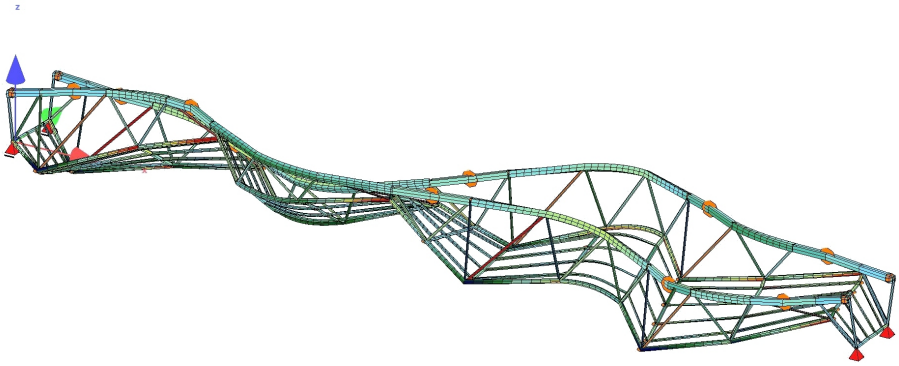

Figure D.63: Fourteen-bay bridge: 23.18 Hz

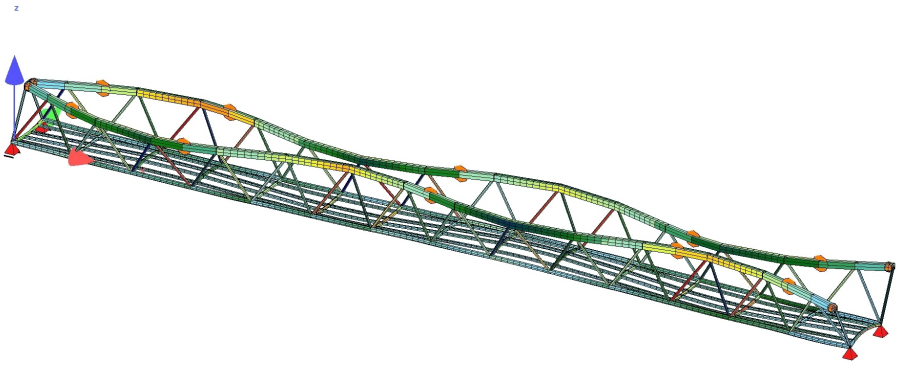

Figure D.64: Fourteen-bay bridge: 24.63 Hz

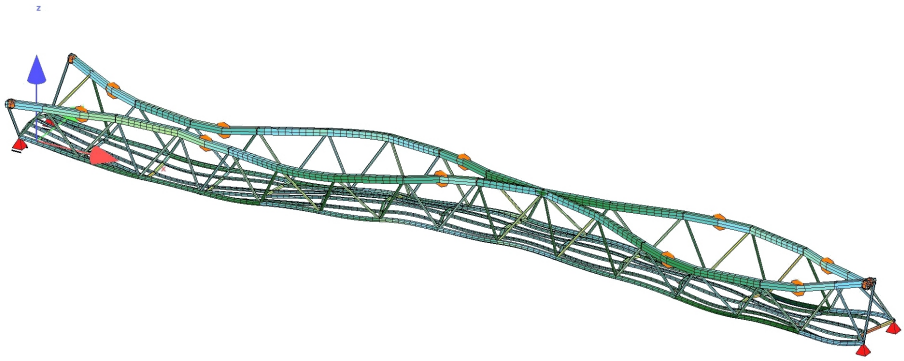

Figure D.65: Fourteen-bay bridge: 24.93 Hz

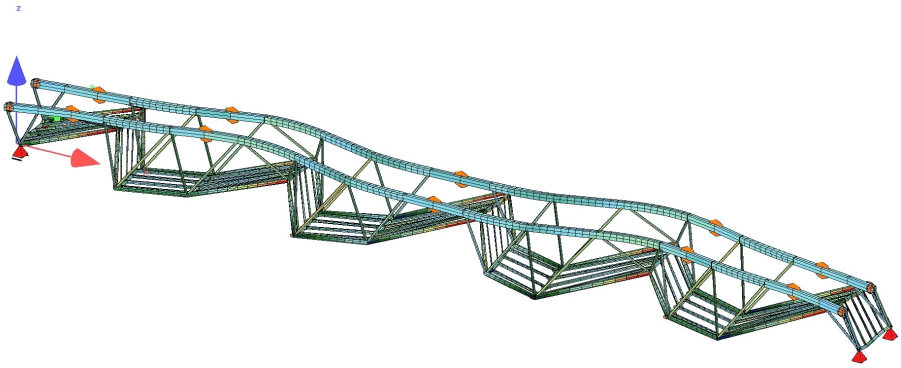

Figure D.66: Fourteen-bay bridge: 26.88 Hz

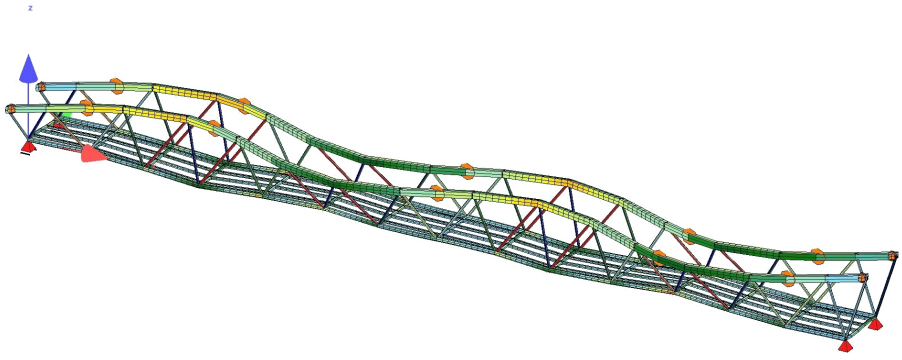

Figure D.67: Fourteen-bay bridge: 27.17 Hz

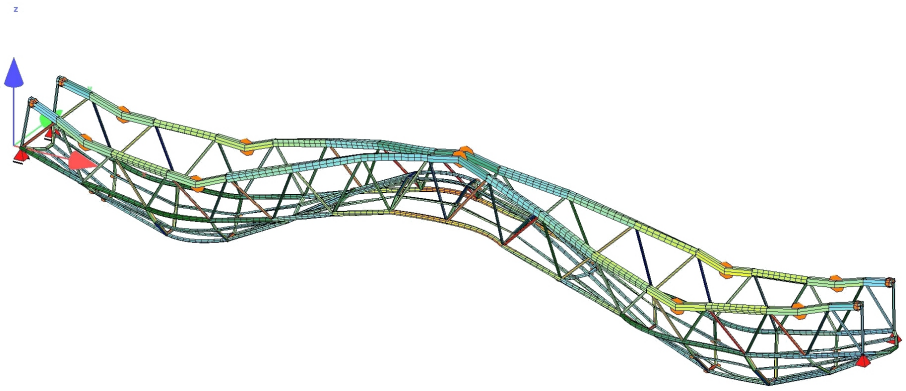

Figure D.68: Fourteen-bay bridge: 30.36 Hz

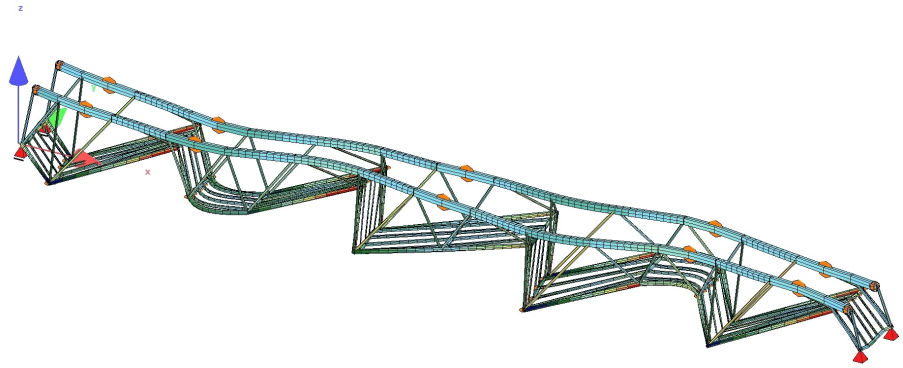

Figure D.69: Fourteen-bay bridge: 30.74 Hz

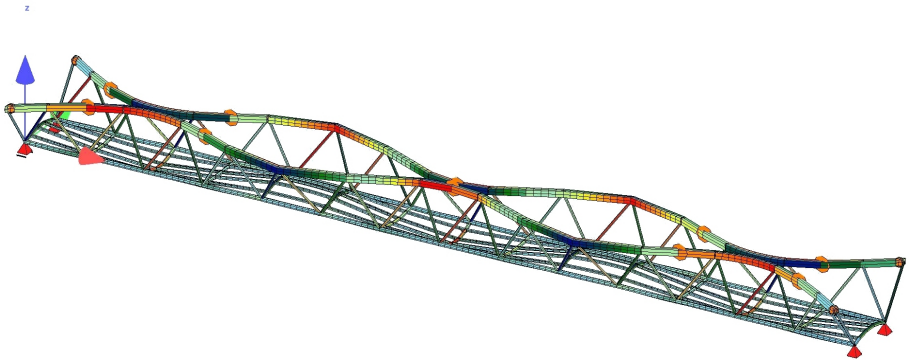

Figure D.70: Fourteen-bay bridge: 33.10 Hz

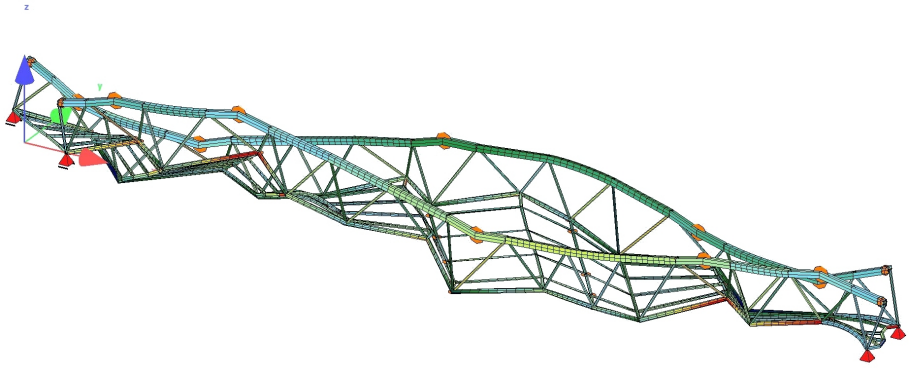

Figure D.71: Fourteen-bay bridge: 33.26 Hz

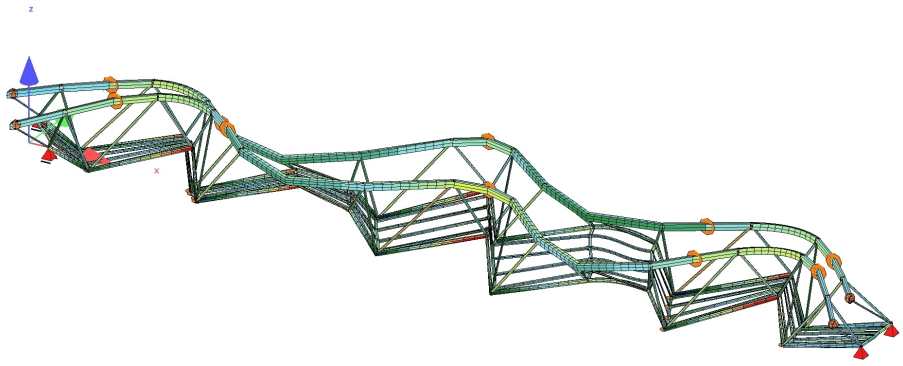

Figure D.72: Fourteen-bay bridge: 34.70 Hz

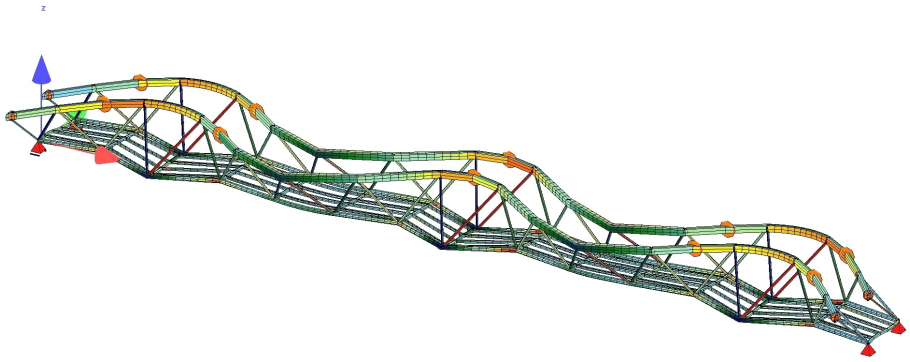

Figure D.73: Fourteen-bay bridge: 35.60 Hz

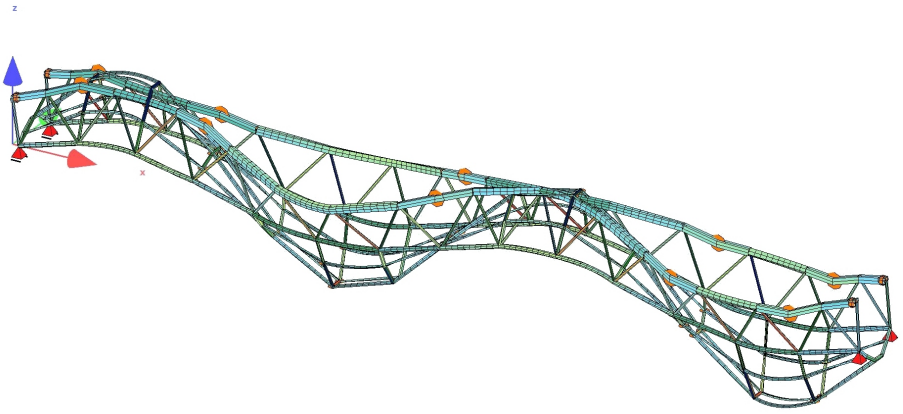

Figure D.74: Fourteen-bay bridge: 37.74 Hz

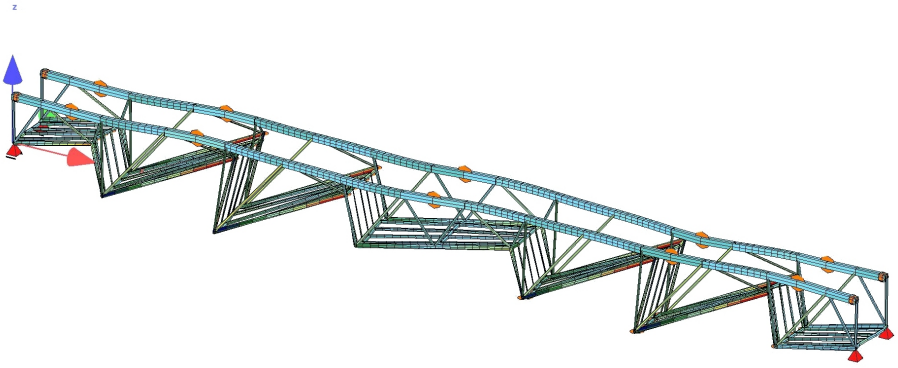

Figure D.75: Fourteen-bay bridge: 37.94 Hz

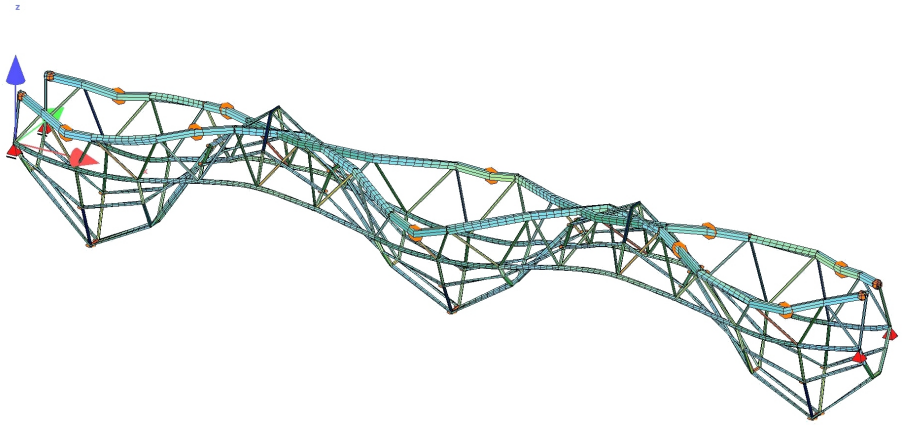

Figure D.76: Fourteen-bay bridge: 42.32 Hz

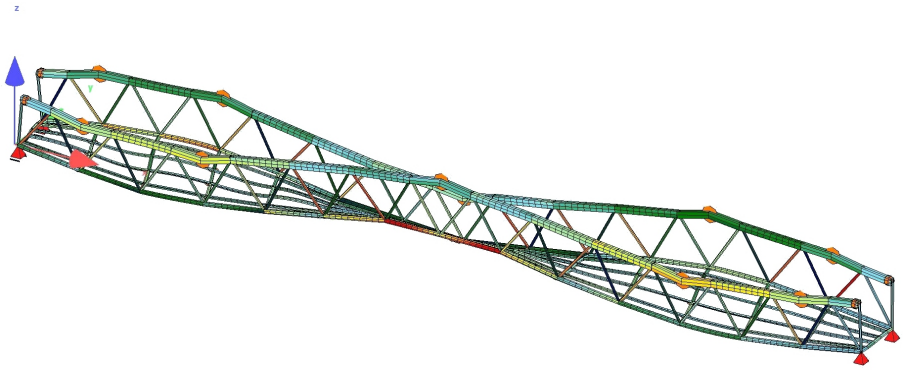

Figure D.77: Fourteen-bay bridge: 42.87 Hz

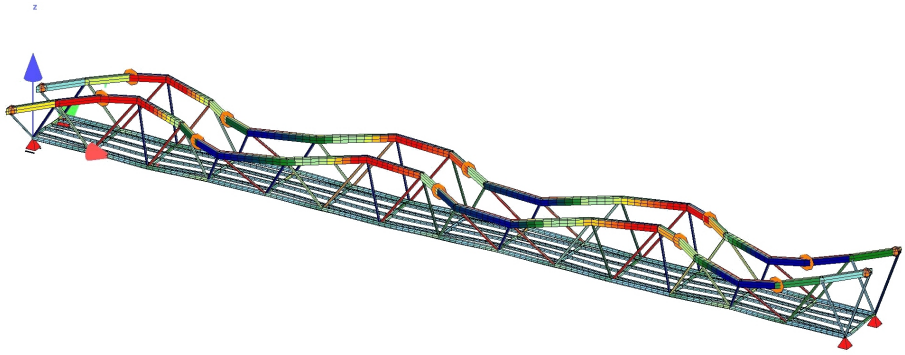

Figure D.78: Fourteen-bay bridge: 46.94 Hz

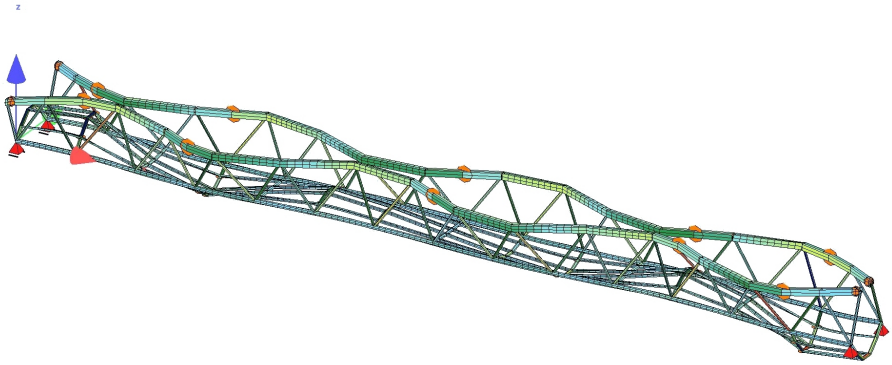

Figure D.79: Fourteen-bay bridge: 47.17 Hz

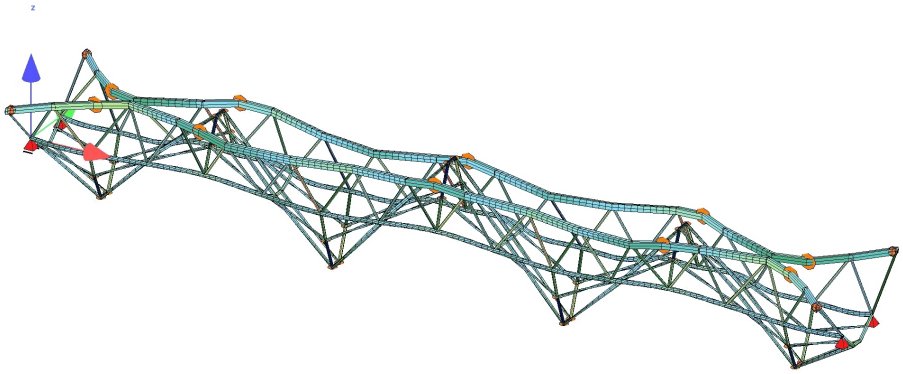

Figure D.80: Fourteen-bay bridge: 47.37 Hz

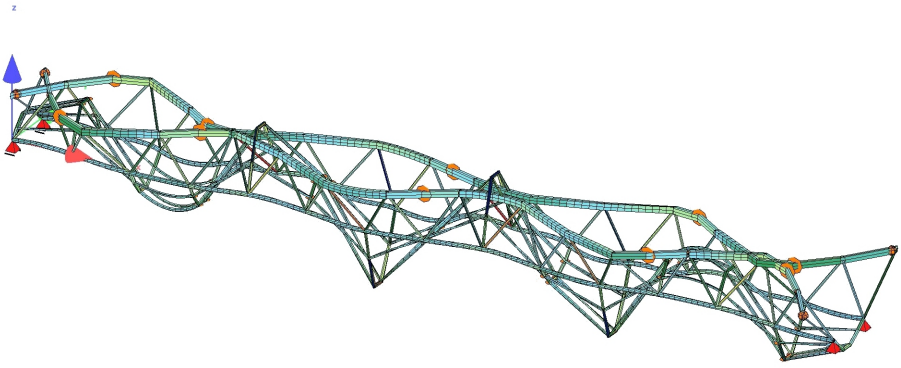

Figure D.81: Fourteen-bay bridge: 51.33 Hz

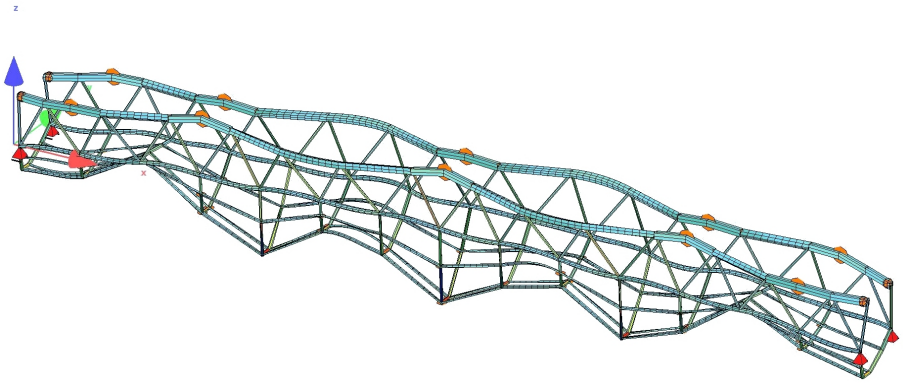

Figure D.82: Fourteen-bay bridge: 52.38 Hz

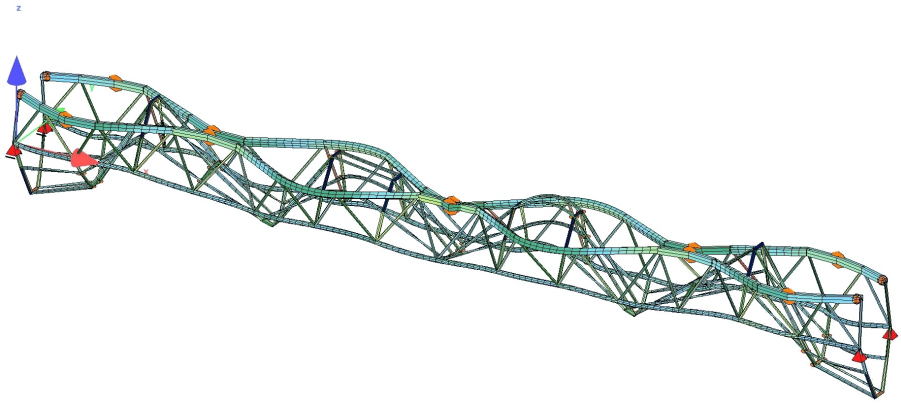

Figure D.83: Fourteen-bay bridge: 53.01 Hz

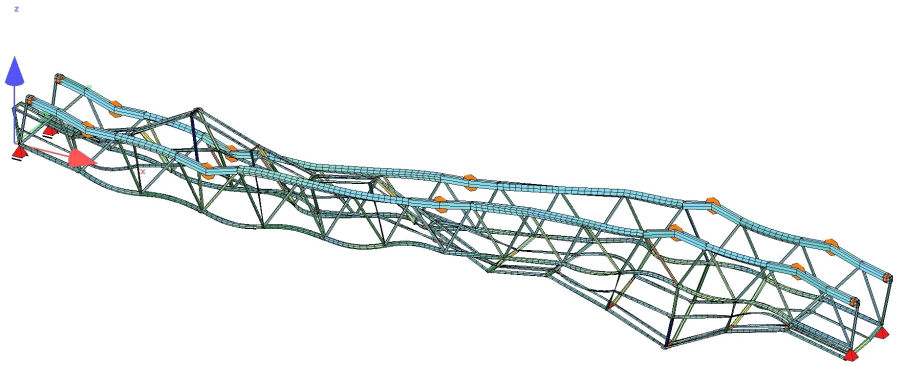

Figure D.84: Fourteen-bay bridge: 54.50 Hz

Figure D.85: Fourteen-bay bridge: 56.70 Hz

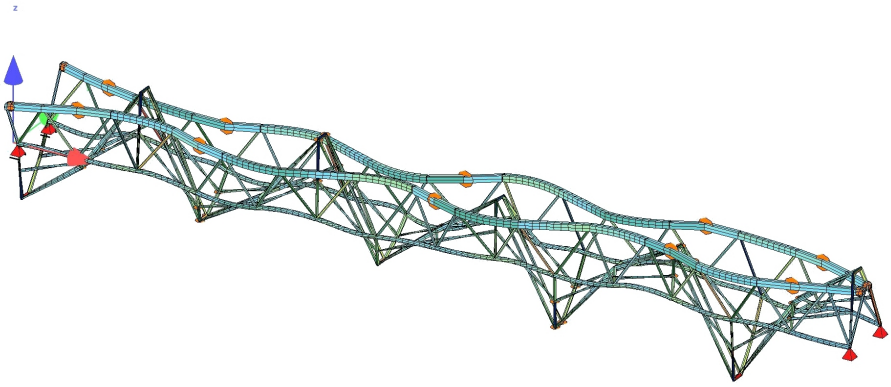

Figure D.86: Fourteen-bay bridge: 57.24 Hz

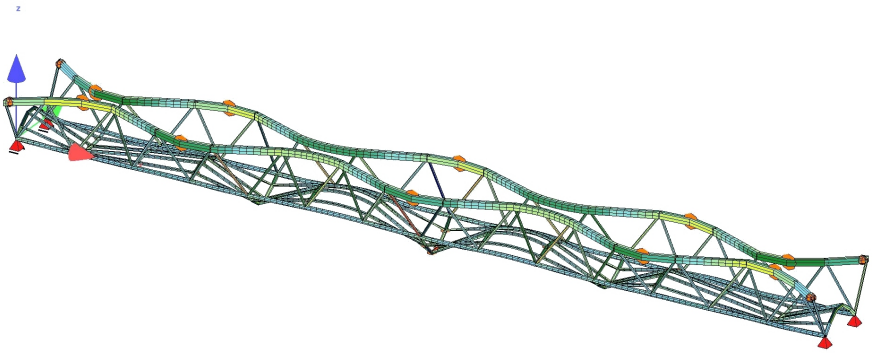

Figure D.87: Fourteen-bay bridge: 58.35 Hz

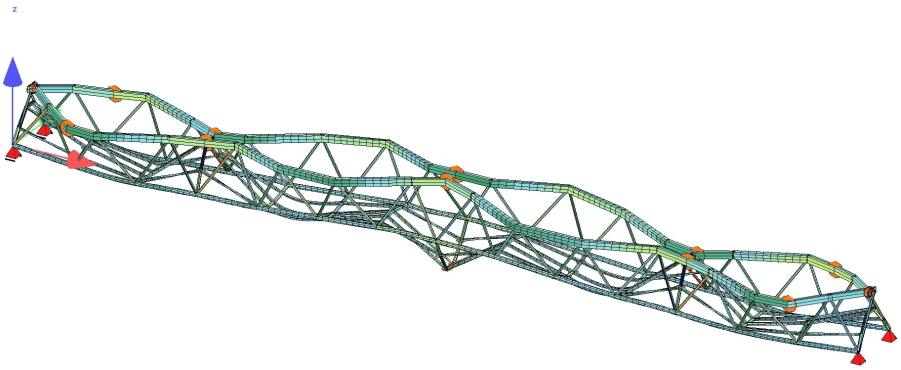

Figure D.88: Fourteen-bay bridge: 61.19 Hz

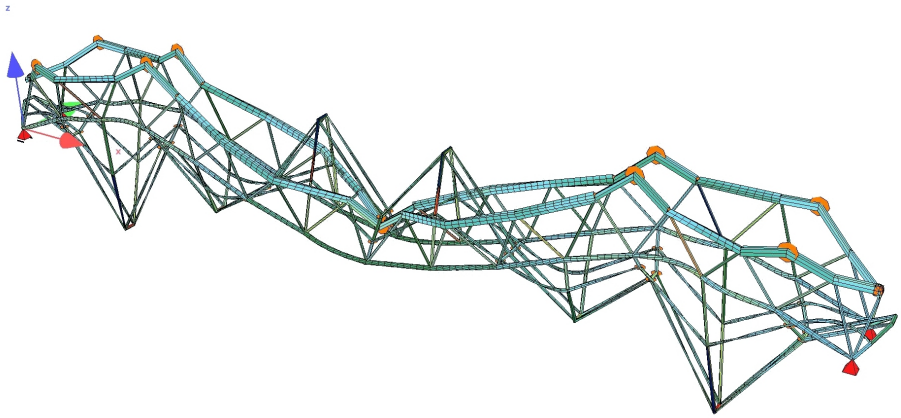

Figure D.89: Fourteen-bay bridge: 62.20 Hz

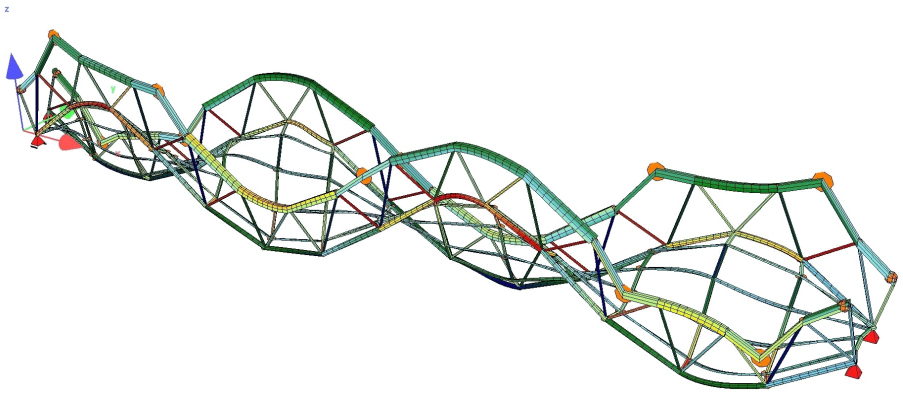

Figure D.90: Fourteen-bay bridge: 62.60 Hz

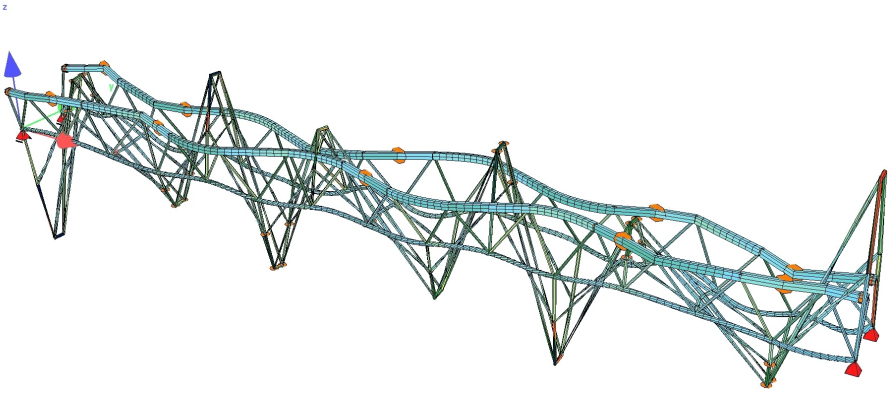

Figure D.91: Fourteen-bay bridge: 63.41 Hz

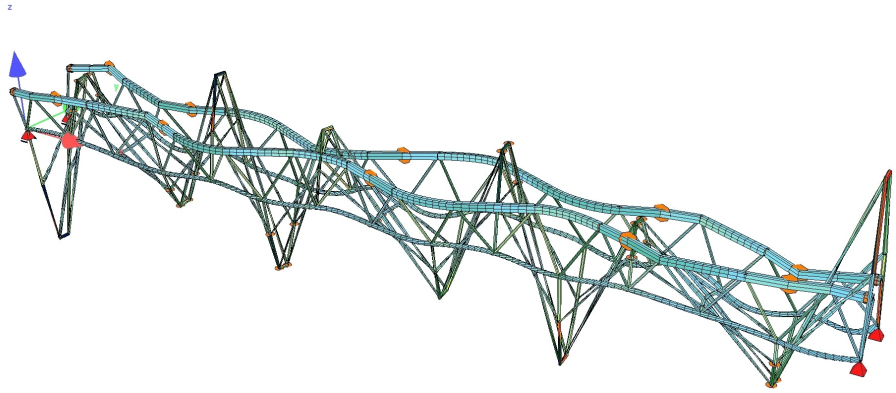

Figure D.92: Fourteen-bay bridge: 63.41 Hz

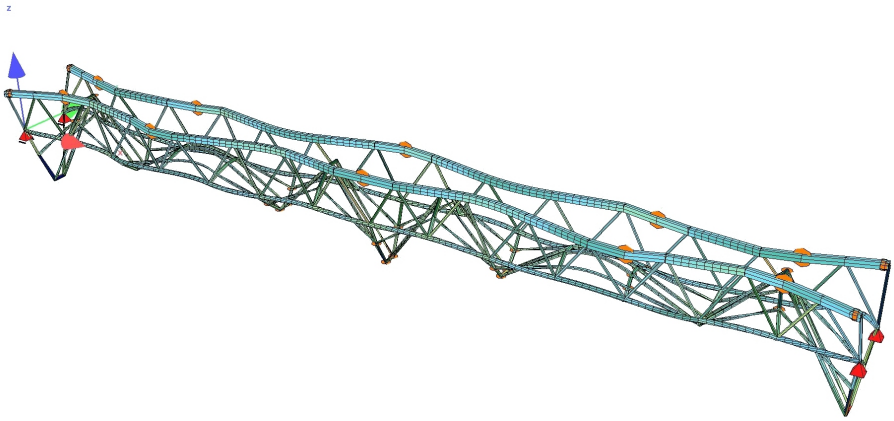

Figure D.93: Fourteen-bay bridge: 66.18 Hz

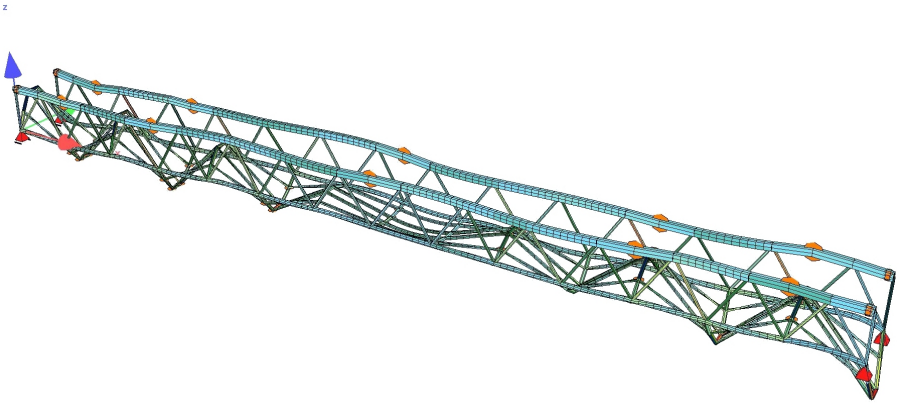

Figure D.94: Fourteen-bay bridge: 67.60 Hz

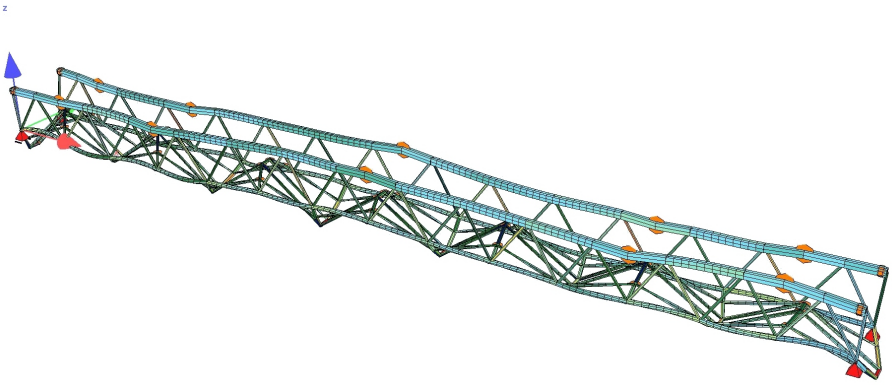

Figure D.95: Fourteen-bay bridge: 69.03 Hz

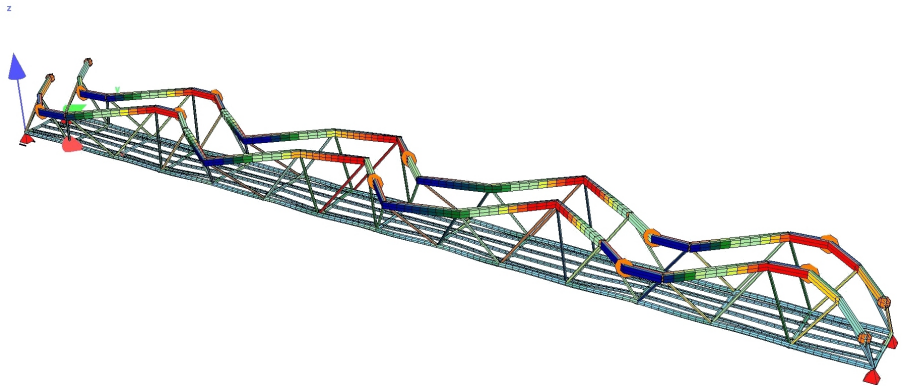

Figure D.96: Fourteen-bay bridge: 76.42 Hz

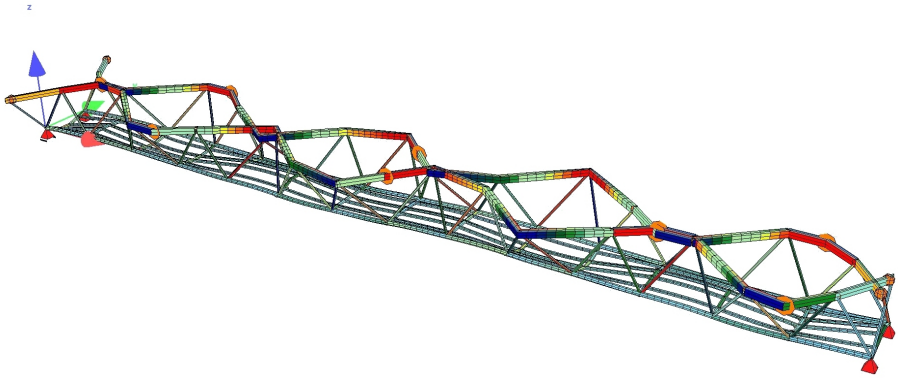

Figure D.97: Fourteen-bay bridge: 76.86 Hz

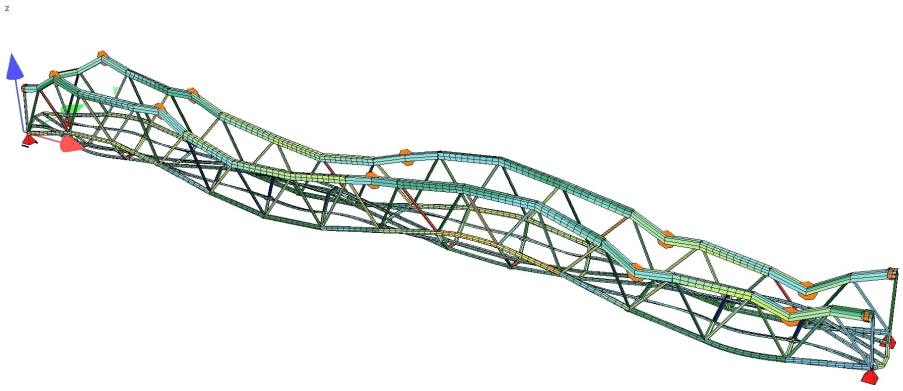

Figure D.98: Fourteen-bay bridge: 78.14 Hz

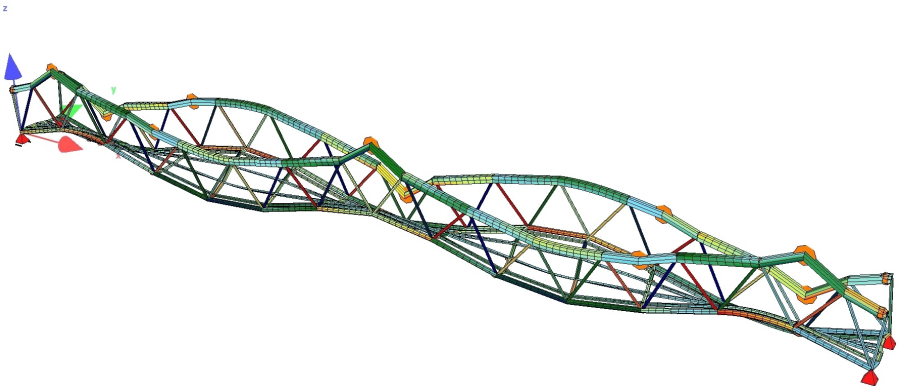

Figure D.99: Fourteen-bay bridge: 81.57 Hz